TRIQUETRA

Toolbox for assessing and mitigating Climate Change risks and natural hazards threatening cultural heritage

TRIQUETRA E-Handbook

Risk Methodology

Mitigation measures

Table of Contents

List of Figures

List of Tables

1. Overview

Climate change and other natural and human-related hazards are increasingly impacting cultural heritage properties. Rising temperatures, altered precipitation patterns, sea-level rise, extreme weather events, floods, erosion, and biological or chemical deterioration are all impacting the stability, integrity, and authenticity of cultural heritage properties. In addition, many of these properties are situated in regions where vulnerability to hazards is high and the budget for risk management is low.

Under these circumstances, there is not only the need for better-informed, more timely, and evidence-based decision-making for cultural heritage institutions, but there are also challenges for these institutions regarding access to data, availability of modeling tools, the ability for capacity building for interpretation regarding complex science, as well as the inclusion of climate and hazard effects on management.

To address these, the TRIQUETRA project tackles this issue by providing a toolbox of models and decision-support tools to support identification, assessment, and mitigation of climate and geo-hazards related to various cultural heritage. The TRIQUETRA project integrates climate and environmental data, hazard and impact models, monitoring and Earth observation, digital twins, web-based Decision Support System, and participatory tools such as an Augmented Reality application.

This e-handbook is an activity within TRIQUETRA's training and capacity building agenda. It translates scientific and technical work into practical guidance for cultural heritage professionals and stakeholders, with a focus on understanding risks, selecting appropriate response strategies, and using digital tools in a realistic and effective way.

2. Chemical and Biological Hazards – Chemical Analysis

2.1. Overview

Within the framework of the TRIQUETRA project, an attempt was made to create a chemical risk assessment based on existing water quality data. Due to the limited amount of data and the few water sampling stations around the cultural heritage sites (CHs), only sporadic trends in water quality are currently available. For an accurate assessment, more data at shorter measurement intervals are needed to clearly identify dependencies and influences of chemicals on the CHs. Therefore, pure water quality data of nutrients and physical water parameters are shown as the currently accessible chemical and biological hazards – chemical analysis section and should be collected there in future to enable more accurate long-term assessments.

2.2. Methodological Description

Only larger water quality data sets from Roseninsel in Germany and Les Argilliez in Switzerland were accessible. The data set from Lake Starnberg comes from the Bavarian Water Survey Service (GKD). The data set from Lake Neuchatel can be

accessed via the die3Seen website (https://www.die3seen.ch/category/chemie/aktuelle-wasserchemie/). Since the CHs are mainly located in shallow waters, the data plots focus primarily on shallow depths. Regarding chemicals, the focus was on the nitrate, sulphate and phosphate concentrations in water, since these are nutrients that should allow conclusions on potential eutrophication. Since the temperature generally plays a major role during chemical reactions, the water temperature was included as a vital parameter that could potentially be linked to direct climate changes in the future.

2.3. Outputs and Interpretation of Results

The water quality data for Lake Neuchatel and Lake Starnberg show that phosphate levels have decreased in recent decades indicating that preventing water pollution can have a significant impact on the nutrient content of the water body. The installation of a ring canal around the Lake Starnberg in 1979 (Melzer, 1999) and their effect on water quality is evident in the GKD's Starnberg water quality data. Conversely, this also shows that the concentrations of pollutants can vary greatly (compare 1980's and nowadays). Since the current phosphate levels of the CHs Roseninsel and Neuchatel are frequently below the detection limit, variations in these values have to be considered with caution. It is therefore difficult to determine the influence of nutrient levels on the corresponding CH sites. In addition, it can be concluded that low phosphate levels result in a lower risk of eutrophication, as phosphate/phosphorous is available at smaller quantities in nature vs. nitrate/nitrogen or sulphate/sulfur. Therefore, the addition of CH sites at or above critical water quality levels would be advantageous, as it would be possible to compare different water quality levels for identifying the influence of various chemicals/nutrients on the CHs.

2.4. References

Melzer, A. Aquatic macrophytes as tools for lake management. Hydrobiologia 395, 181–190 (1999). https://doi.org/10.1023/A:1017001703033

2.5. Contributors

Developed by: UULM

Lead Contributors:

- Boris Mizaikoff
- Patrick Krebs

3. Remote Sensing Model for Quagga Mussel Detection at Les Argilliez

3.1. Overview

This risk model describes the methodology for detecting and monitoring the proliferation of invasive quagga mussels on the bottom of Lake Neuchatel,

specifically near the Les Argilliez UNESCO World Heritage site. The model leverages multitemporal Earth Observation data, primarily Sentinel-2 satellite images (Cerra, 2024), to identify areas where mussel colonization is occurring, providing a non-invasive, cost-effective tool for heritage site monitoring. Inputs include multitemporal Sentinel-2 imagery (focusing on the green band reflectance). The model assesses the feasibility of detection based on the spectral properties of mussels and the site's average depth of 2 m to 3 m. The output is the identification and mapping of critical areas (anomalies) where quagga mussels are likely spreading, as confirmed by underwater surveys (OARC in autumn 2024, as reported in Bosch 2025).

3.2. Methodological Description

3.2.1. Feasibility Study using Spectral Simulation

The initial phase involved a feasibility study to determine if quagga mussels are spectrally separable from the natural lake bottom environment, which includes sand and macrophytes. This was achieved by simulating spectra of mixtures of mussels, typical sand samples, and macrophytes at a specific depth of 2.5 m, considering that the Cultural Heritage (CH) site is found at an average depth between 2 m and 3 m. This simulation used the WASI software (Gege, 2014). Simulations clearly demonstrated that detection is only feasible in shallow waters because spectral features become more difficult to separate and quantify as depth increases.

Spectral Separability and Range

The simulations established that mussels appear to be separable from both sand and macrophytes at the bottom of such shallow inland waters, particularly in the green range of the spectrum, which corresponds to the range from 500 nm to 600 nm. This range is represented by Band 3 in Sentinel-2 data. The spectral mixtures were resampled to the relevant bands of the Sentinel-2 multispectral satellite to assess the impact of these three components on the measured water spectra.

Comparison with Underwater Materials

The spectral library used in the simulation reported typical reflectance spectra for the three key underwater components: mussels, macrophytes, and sand, allowing for a comparative analysis of their spectral signatures.

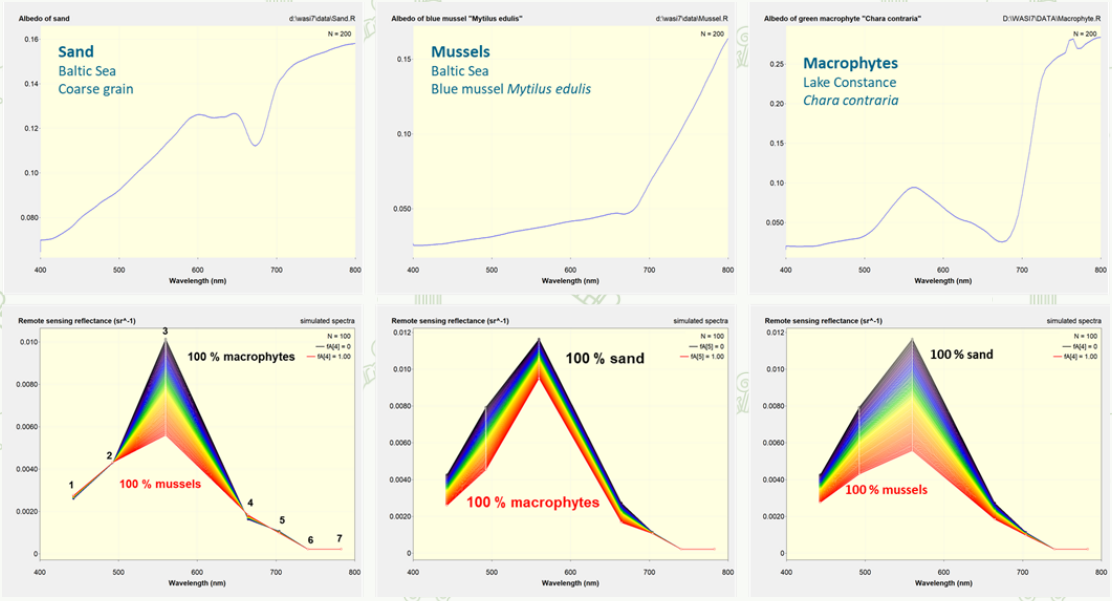

Figure 1: Spectral separability analysis reporting simulated mixtures for typical reflectance spectra of mussels, macrophytes, and sand.

3.2.2. Multitemporal Sentinel-2 Analysis

The core method involves a multitemporal analysis of satellite imagery to detect changes in spectral reflectance over time. This technique was first validated in a similar case study at Unteruhldingen in Lake Constance, Germany, for which spatial extent of mussels spread was derived from an underwater survey. That study established a strong correlation between the presence of quagga mussels and a decrease in green reflectance. This key finding was directly transferred to the study of the area surrounding Les Argilliez on Lake Neuchatel.

Application to Lake Neuchatel Sites

Satellite images acquired by Sentinel-2 in the proximities of the site were used to compute the estimated anomaly in the green band. The model analyses areas near Concise (approximately 5 km south of Les Argilliez) and Saint-Aubin (2 km south, partially covering the site). The primary change detection metric employed was the anomaly in the green band, computed as a normalized difference between the median reflectance of images acquired over the month of April in 2018 and 2022. A manually adjusted threshold of 0.2 has been applied to this anomaly map to delineate critical areas.

3.3. Outputs and Interpretation of Results

The model's output is a map of anomalies indicating the spatial extent and intensity of the suspected quagga mussel spread. Interpretation relies on linking the detected spectral changes (darker areas/decreased green reflectance) to the physical presence of the mussels.

3.3.1. Detection of Anomalies at Concise and Saint-Aubin

Multitemporal analysis of Sentinel-2 data revealed areas near Concise and Saint-Aubin (adjacent to Les Argilliez site) that exhibited a decrease in green reflectance in the 2022 image composite compared to 2018. This manifested as a darker appearance in true color representations, consistent with the spectral features observed in the feasibility study. The band ratio analysis then highlighted these changes in Fig. 2, providing a first identification of critical areas.

Figure 2: Anomalies detected between April 2018 and April 2022 in Concise (5 km from Les Argilliez), overlaid on the April 2022 image.

3.3.2. Validation and Impact Assessment

The results from the satellite analysis were assessed through an underwater survey carried out by the project partner OARC (formerly OPAN) in August 2024 (Bosch, 2025).

Underwater Survey

The survey successfully validated the remote sensing model's findings, confirming the presence of quagga mussels in all sites marked as anomalous, including both Concise and Saint-Aubin. Observations at Concise showed colonization intensifying, with mussels colonizing pebbles and, in general, found on piles, stones, and sandy bottoms.

Mussels Spread at Les Argilliez

The most critical finding from the underwater survey was the assessment of the mussels spread at the heritage site itself. The OARC report specifically concluded that “the evolution is much more marked on the site of Gorgier / Les Argilliez where the development since 2022 is very strong”. This confirms the urgency of the phenomenon and validates the model's ability to identify it.

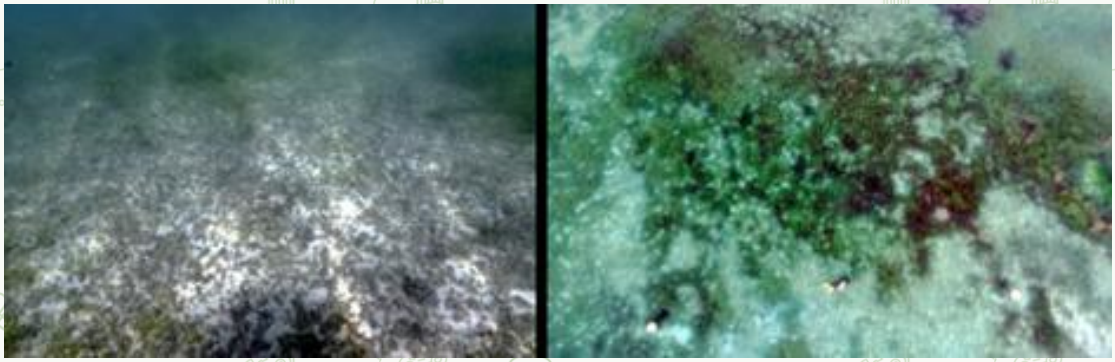

Figure 3: Sample photographs from underwater surveys carried out by OARC in 2024. The density of mussels has been confirmed to increase in the sites of Concise and Saint-Aubin, as observed in satellite images.

3.4. References

Cerra, D., Gege, P., Plattner, S., Langenegger, F., Wüthrich, S., Roulet, J.-C., & Droz, F. (2024). Assessing the Spread of Invasive Mussels in Lake Neuchâtel as a Potential Threat to the Les Argilliez Heritage Site with Sentinel-2. In IGARSS 2024 - 2024 IEEE International Geoscience and Remote Sensing Symposium (pp. 3376–3379). IEEE.

Gege, P. (2014). The water colour simulator WASI: an underwater model for the simulation and analysis of the water-leaving radiance. Computers & Geosciences, 67, 22–35.

Bosch, E., Langenegger, F., Gege, P., Roulet, J.C., Nguyen, D., Holzer, J., Cerra, D., Wuethrich, S., Pache, C. (2025). Preserving underwater cultural heritage: combining satellite images with a novel flash lidar platform. Italian Journal of Engineering Geology and Environment, 25–33. https://doi.org/10.4408/IJEGE.2025-01.S-02

3.5. Contributors

Developed by: DLR

Date of last update: 24.10.2025

Lead contributors:

- Cerra Daniele
- Gege Peter
- Langenegger Fabian

4. Heritage Outdoor Microclimate Risk and Predicted Risk of Damage (PRD) indices

4.1. Overview

To assess the suitability of climates hosting heritage and to quantify the damage risk due to climatic conditions, the Heritage Outdoor Microclimate (HMRout) and Predicted Risk of Damage (PRD) indices were applied following the approach of Tringa and Tolika (2023). According to the literature the Heritage Outdoor

Microclimate (HMRout) index is defined as the outdoor microclimate risk of the cultural heritage and makes it possible to assess the risk related to the microclimate. To assess both current and potential future effects of climate change on the selected cultural heritage sites, meteorological data from weather stations (observations) and simulations from regional climate models (RCMs) were analyzed. The model uses as input the main climatic variables, including temperature and relative humidity, derived from both observational datasets and climate projections. The indices were applied to inorganic materials at the CH sites made of stone and marble for temperature. The outputs include distributed values of the HMRout and PRD indices, representing the potential risk level for heritage degradation under current and future climatic conditions. These results are integrated into the TRIQUETRA DSS Risk Severity Quantification Module, supporting users in evaluating the vulnerability of heritage sites and identifying regions at higher climatic risk.

4.2. Methodological Description

The HMR_{out} index is defined as the outdoor microclimate risk of the cultural heritage and makes it possible to assess the risk related to the microclimate (Tringa and Tolika 2023). HMR_{out} is calculated according to the formula:

$$\mathrm{HM}R_{out} = \frac{HMR_{env.out} + HMR_{fluc}}{2}$$

where:

$$\mathrm{HM}R_{env.out} = 1 - \left[\left(\frac{H\_HMR_{env.out} - HMR_{env.out.data}}{H\_HMR_{env.out} - H\_HMR_{env.out}}\right) * 2\right]$$

where:

$$\mathrm{HMR}_{\mathrm{env.out.data}} = \frac{\mathrm{M}_{\mathrm{env.out.data}}}{\mathrm{N}}$$

$M_{env.out.data}$ represents the total sum of the outdoor time series data, for each considered variable (e.g., temperature and RH).

N is the total of the values of the outdoor time series data for each variable considered.

Regarding the higher and lower thresholds ($H\_HMR_{env.out}$ and $L\_HMR_{env.out}$), we consider that the cultural objects have adapted to the historical microclimate and these thresholds are derived from the maximum and minimum values of the outdoor time series data (temperature, RH). In this work, to examine the change in HMR_{out} and PRD indices in the future under three emission scenarios (RCP2.6, RCP4.5, RCP 8.5), the thresholds were derived from the emission scenario RCP2.6 for the period 1971-2100. The RCP2.6 scenario was chosen because it is considered a very stringent mitigation scenario. Based on the $H\_HMR_{env.out}$ and $L\_HMR_{env.out}$ derived from the RCP2.6 scenario for the period 1971-2100, the indices were applied to the other two scenarios.
The "high" and "low" limit values of the HMR_{out} are defined as follows: $L\_HMR_{env.out} = -1$ (the risk condition relative to the "lower threshold") and $H\_HMR_{env.out} = +1$ (the risk condition relative to the "higher threshold").

Therefore, in this study the H_$HMR_{env.out}$ (L_$HMR_{env.out}$) is the maximum (minimum) value from the outdoor data series from the RCP2.6 scenario for the period 1971-2100 (excluding the "scattered values") (Fabbri and Bonora 2021).

$$HMR_{fluc} = 1 - \left[\left(\frac{H\_\Delta_{fluc} - HMR_{fluc.data}}{H\_\Delta_{fluc} - L\_\Delta_{fluc}}\right) * 2\right]$$

The H_Δ_{fluc} (L_Δ_{fluc}) is the maximum (minimum) value of hourly fluctuation from the outdoor data series from the RCP2.6 scenario for the period 1971-2100 (excluding the "scattered values".

$\Delta Mf_{luc.data}$ is defined as:

$$\Delta M_{fluc.data} = \sum_{k=1}^{n}\sum_{j=1}^{24}\left[X_{day,k,hourj} - X_{day,k,hour(j+1)}\right]$$

According to the literature, if $HMR_{env.out} > 0$, then the sign of the HMR_{out} index will be "+" (positive), while if the $HMR_{env.out} < 0$, the sign will be "−" (negative), with $HMR_{env.out}$ as the predominant risk factor between $HMR_{env.out}$ and HMR_{fluc} (Figure 1) (Fabbri and Bonora 2021). In this study, when the index takes a value lower than 0, we interpret this as indicating no change compared to the lower threshold, signifying minimal risk, which is defined as $HMR_{out} = 0$. Accordingly, when the HMR_{out} exceeds the value 1, it indicates high risk and is defined as $HMR_{out} = 1$. This is based on maintaining the thresholds set for the RCP2.6 scenario and applying them also to the RCP4.6 and RCP8.5 scenarios.

Respectively, PRD index is defined as a "forecast" of damage and assesses the ability of damage caused by the microclimatic conditions (Fabbri and Bonora 2021). It mainly depends on the microclimate, the HMR index, and the type of material. The values of "a" and "b" are exponents that define the risk of damage. Specifically, "a" defines the risk of damage due to the persistence of the cultural asset in environments where maximum or minimum HMR values are present (higher risk), while "b" defines the absence of risk due to the persistence of the cultural asset in environments where average or zero HMR values are present (lower or no risk). Their values have been empirically determined based on the standards reported by UNI 10829:1999 and EN 15757:2010 and differ by the type of material (inorganic, organic, etc.).

For the outdoor environment, the PRD index is calculated according to the formula:

$$PRD = 1 - 0.95 \times e^{(-a \times HMR_{env.out}^{4} - b \times HMR_{env.out}^{2})}$$

Further details about HMR_{out} and PRD indices are also provided in the works of Tringa et Tolika (2023) and Fabbri and Bonora (2021).

HMR	−1.00	−0.80	−0.60	−0.40	−0.20	0.00	+0.20	+0.40	+0.60	+0.80	+1.00
Risk Level	Maximum	High	Medium	Moderate	Low	Minimum	Low	Moderate	Medium	High	Maximum

Figure 4: The risk level of the Heritage Outdoor Microclimate Risk index.

4.3. Outputs and Interpretation of Results

The model provides two main outputs for the selected cultural heritage sites: the Heritage Outdoor Microclimate (HMRout) index and the Predicted Risk of Damage (PRD) index. The HMRout index represents the level of risk posed by the outdoor microclimate, integrating both the environmental (HMRenv.out) and fluctuation

(HMRfluc.) components. It indicates whether the local microclimatic conditions are likely to pose a stress to heritage materials, with higher values reflecting increased microclimatic risk. The index is bounded between –1 and +1, corresponding respectively to the “low” and “high” thresholds of the outdoor climatic variables. The PRD index, on the other hand, provides a quantitative forecast of potential damage to heritage materials based on the HMRout values and the type of material (e.g., inorganic, organic). Therefore, while HMRout describes the climatic risk level, PRD translates this risk into the likelihood of material deterioration. Users can interpret higher PRD values as a greater likelihood of material degradation or damage, whereas lower values indicate more stable and suitable conditions for heritage preservation. The outputs are presented both as continuous indices and as categorized risk levels (e.g., Minimum-Low, Moderate-Medium, High-Maximum), allowing users to identify areas or periods of higher risk, compare the vulnerability of different sites, and prioritize conservation measures. For example, higher HMRout or PRD values indicate an increased probability that temperature or humidity fluctuations may exceed the tolerance limits of materials, potentially accelerating decay or surface damage. Conversely, low or negative values suggest stable microclimatic conditions that favor long-term preservation.

In the context of the TRIQUETRA DSS, these outputs support evidence-based decision-making by enabling users to assess how climatic variability influences heritage stability, compare different sites or time periods, and prioritize conservation actions. The results are designed to inform heritage managers, conservators, and policymakers about which sites or materials are most at risk under present and projected climatic conditions. However, it is important to note that the results should be interpreted as indicative assessments rather than absolute predictions, as they depend on the accuracy of input datasets, the resolution of climate data, and the assumptions applied within the modeling framework.

4.4. References

Tringa, E., & Tolika, K. (2023). Analysis of the outdoor microclimate and the effects on Greek cultural heritage using the Heritage Microclimate Risk (HMR) and Predicted Risk of Damage (PRD) indices: Present and future simulations. Atmosphere, 14, 663.

Fabbri, K., & Bonora, A. (2021). Two new indices for preventive conservation of the cultural heritage: Predicted risk of damage and Heritage Microclimate Risk. Journal of Cultural Heritage, 47, 208–217.

Ente Nazionale Italiano di Unificazione. (1999). UNI 10829: Works of art of historical importance—Ambient conditions for the conservation—Measurement and analysis. UNI.

iTeh Standards. (2010). EN 15757: Conservation of cultural heritage—Specifications for temperature and relative humidity to limit climate-induced mechanical damage. iTeh Standards.

4.5. Contributors

Developed by: Department of Meteorology and Climatology, School of Geology, Aristotle University of Thessaloniki, 54124 Thessaloniki, Greece

Date of last update: 10/11/2025

Lead contributors:

- Efstathia Tringa
- Aristeidis K. Georgoulias
- Dimitris Akritidis
- Haralambos Feidas
- Prodromos Zanis

5. Regional Climate Model (RCM) Simulations

5.1. Overview

Within the framework of the TRIQUETRA project, regional climate model (RCM) high-resolution simulation data from the EURO-CORDEX initiative (https://www.euro-cordex.net/) (Vautard et al., 2013; Jacob et al., 2014; 2020) were processed in order to assess future changes in various climate-related parameters. In total, 11 model simulation sets (Table 1) were acquired through https://esgf-data.dkrz.de/search/cordex-dkrz/ (currently available at https://esgf-metagrid.cloud.dkrz.de/search/cordex-dkrz/) covering both the historical period (1950–2005) and three different Representative Concentration Pathways (RCPs) of the Intergovernmental Panel on Climate Change (IPCC) for the future period (2006–2100), resulting in 44 RCM simulations in total (see Georgoulias et al., 2021). RCP2.6 corresponds to a strong mitigation scenario, with greenhouse gas (GHG) concentrations decreasing by approximately 70% between 2010 and 2100. RCP4.5 represents a moderate mitigation scenario, in which GHG concentrations begin to decline after 2040, while RCP8.5 assumes no further climate mitigation policies and continued increases in GHG concentrations (Moss et al., 2010; Riahi et al., 2011; Thomson et al., 2011; van Vuuren et al., 2011a,b). The daily raw data cover a wide European domain (~27°N–72°N, ~22°W–45°E) at a fine horizontal spatial resolution of 0.11° (~12.5 km).

Table 1: List of 11 RCM simulations within EURO-CORDEX used in the analysis.

	RCM	Driving model	Realization	Historical	RCP2.6	RCP4.5	RCP8.5
1	ALADIN63.v2	CNRM.CNRM-CERFACS-CNRM-CM5	r1i1p1	x	x	x	x
2	CCLM4-8-17.v1	CLMcom.ICHEC-EC-EARTH	r12i1p1	x	x	x	x
3	HIRHAM5.v2	DMI.ICHEC-EC-EARTH	r3i1p1	x	x	x	x
4	RACMO22E.v1	KNMI.ICHEC-EC-EARTH	r12i1p1	x	x	x	x
5	RACMO22E.v2	KNMI.MOHC-HadGEM2-ES	r1i1p1	x	x	x	x
6	RACMO22E.v2	KNMI.CNRM-CERFACS-CNRM-CM5	r1i1p1	x	x	x	x

7	RCA4.v1	SMHI.MOHC-HadGEM2-ES	r1i1p1	x	x	x	x
8	RCA4.v1	SMHI.MPI-M-MPI-ESM-LR	r1i1p1	x	x	x	x
9	RCA4.v1	SMHI.ICHEC-EC-EARTH	r12i1p1	x	x	x	x
10	REMO2009.v1	MPI-CSC.MPI-M-MPI-ESM-LR	r1i1p1	x	x	x	x
11	REMO2009.v1	MPI-CSC.MPI-M-MPI-ESM-LR	r2i1p1	x	x	x	x

5.2. Methodological Description

Approximately 4 TB of data were processed using the high-performance computing (HPC) infrastructure of the Aristotle University of Thessaloniki (AUTH) (Aristotelis). For each of the eight TRIQUETRA cultural heritage (CH) pilot sites, namely, Aegina, Epidaurus, and Kalapodi in Greece, Choirokoitia in Cyprus, Les Argilliez in Switzerland, Roseninsel in Germany, Smuszewo in Poland, and Ventotene in Italy (Table 2), the grid cell closest to the corresponding site was extracted, producing datafiles covering the period 1951-2100. Seven basic climatic parameters were analyzed: precipitation (PR), near-surface temperature (TAS), daily maximum and minimum near-surface temperature (TASMAX/TASMIN), specific humidity (HUSS), downwelling solar radiation (RSDS), and near-surface wind speed (WS) (see also Table 3 for details). However, the focus of the analysis is primarily on the period 1971–2100. The future changes along with the related inter-model variability (±1σ) have been calculated for the near-future (2021-2050) and end-of-the-century (2071-2100) periods relative to the baseline period 1971-2000.

Table 2: Location (coordinates) of the TRIQUETRA CH sites.

	CH site	Country	Longitude (°E)	Latitude (°N)
1	Aegina	Greece	23.4236	37.7501
2	Choirokoitia	Cyprus	33.3439	34.7964
3	Epidaurus	Greece	23.1576	37.6259
4	Kalapodi	Greece	22.8954	38.6365
5	Les Argilliez	Switzerland	6.7898	46.9032
6	Roseninsel	Germany	11.3086	47.9413
7	Smuszewo	Poland	17.4045	52.8932
8	Ventotene	Italy	13.4300	40.8013

Table 3: Basic climatic parameters included in the TRIQUETRA database.

	Basic climatic parameter	Abbreviation	Units
1	Precipitation	PR	mm day^{-1}
2	Near-surface air temperature	TAS	°C
3	Daily surface maximum temperature	TASMAX	°C
4	Daily surface maximum temperature	TASMIN	°C
5	Near-surface specific humidity	HUSS	gkg^{-1}
6	Downwelling surface solar radiation	RSDS	Ws^{-1}
7	Near-surface wind speed	WS	ms^{-1}

5.3. Outputs and Interpretation of Results

For each TRIQUETRA CH site, columnar daily, monthly, and annual CSV files were generated, containing all basic climatic parameters for each simulation set over the period 1950–2100. A separate dataset was created for each RCP, although it should be noted that the historical period (1950–2005) is common across all RCP datafiles. Additional monthly and annual files were also produced for the ensemble of all 11

RCM simulation sets. Examples of daily, monthly, and annual files are shown in Figs. 1–3. The data form part of the TRIQUETRA database, which is operated by Geosystems Hellas A.E. (https://www.geosystems-hellas.gr/). These datafiles (Figs. 1–3) have been used to assess future climate change over the CH sites for the identification of potential risks (Ioannidis et al., 2024; Tringa et al., 2025). The projected future changes from the model ensemble, presented in the form of heatmaps (Fig. 6) in Ioannidis et al. (2024), along with the corresponding inter-model variability (±1σ), are also reported in the TRIQUETRA DSS Platform.

	A	B	C	D	E	F	G	H	I	J	K	L	M
1	Date	Year	Month	Day	DOY	pr(mm)	tas(C)	tasmax(C	tasmin(C)	huss(gkg-	rsds(Wm-	ws(ms-1)	
2	1/1/1950	1950	1	1	1	NaN	NaN	NaN	NaN	NaN	NaN	NaN	
3	2/1/1950	1950	1	2	2	0.003238	13.69479	15.70987	11.86298	6.703432	81.74639	7.165157	
4	3/1/1950	1950	1	3	3	0	12.70731	14.88513	10.83722	5.347498	89.81438	7.487136	
5	4/1/1950	1950	1	4	4	0.008033	11.85379	13.79056	10.49603	5.502615	36.67127	7.558497	
6	5/1/1950	1950	1	5	5	0.013876	12.48908	14.7001	10.91382	5.857583	39.57192	4.8222	
7	6/1/1950	1950	1	6	6	2.234164	13.29025	15.63181	11.27554	6.650983	9.796973	1.585487	
8	7/1/1950	1950	1	7	7	0.404355	11.71042	13.74756	10.41098	6.684163	44.239	2.002026	
9	8/1/1950	1950	1	8	8	1.921197	13.93918	14.60812	12.33041	8.2689	5.524926	5.245316	
10	9/1/1950	1950	1	9	9	0.532508	12.93256	15.45923	11.4599	6.509134	50.41126	2.426046	
11	10/1/1950	1950	1	10	10	0.000011	12.858	16.08188	10.54901	5.097575	94.38577	1.385821	
12	11/1/1950	1950	1	11	11	0.001457	12.74793	15.10745	11.04718	6.836049	58.39148	3.601773	
13	12/1/1950	1950	1	12	12	0.003125	13.94473	15.98236	12.32587	4.980445	27.86787	3.768934	
14	13/1/1950	1950	1	13	13	12.05443	14.14713	15.07221	13.3523	6.101851	8.62458	3.709356	
15	14/1/1950	1950	1	14	14	7.662857	13.90689	15.31754	12.80432	6.788763	17.58431	3.762631	
16	15/1/1950	1950	1	15	15	27.24782	12.74371	13.63751	12.08084	7.046807	3.409052	1.864308	
17	16/1/1950	1950	1	16	16	2.323626	13.07837	15.48087	11.60275	6.219741	73.03651	3.546769	
18	17/1/1950	1950	1	17	17	0.831541	12.42816	13.89197	11.42313	5.555156	14.70615	3.254885	
19	18/1/1950	1950	1	18	18	0.000654	12.60852	15.24353	10.86307	6.188186	98.65459	2.102346	
20	19/1/1950	1950	1	19	19	0	12.9494	15.76636	10.32733	4.923591	98.85096	2.299633	
21	20/1/1950	1950	1	20	20	0.000181	13.98984	16.1481	12.86545	4.942666	35.08842	3.54904	
22	21/1/1950	1950	1	21	21	0.000092	13.89746	16.37628	12.69922	6.72998	70.03883	3.695118	
23	22/1/1950	1950	1	22	22	0	14.83829	17.22858	13.21652	7.315888	100.6243	6.216924	
24	23/1/1950	1950	1	23	23	0.000004	15.03174	17.14053	13.91104	7.238153	44.60923	6.76581	
25	24/1/1950	1950	1	24	24	0.255989	14.26398	17.0632	11.68515	5.400297	107.0593	4.642051	
26	25/1/1950	1950	1	25	25	0.000784	10.95938	12.00287	9.561554	4.920624	18.22514	5.250721	
27	26/1/1950	1950	1	26	26	1.62552	10.0679	13.09076	7.76474	4.529954	108.454	4.356286	
28	27/1/1950	1950	1	27	27	0.038513	9.71344	12.75415	6.951996	4.784182	86.17558	2.331581	
29	28/1/1950	1950	1	28	28	0.016768	12.78644	14.84244	10.07758	6.032817	45.02937	8.024178	
30	29/1/1950	1950	1	29	29	0.000063	11.38699	13.16025	8.786804	4.651435	116.2785	8.263658	
31	30/1/1950	1950	1	30	30	0.040678	13.11264	15.85782	9.162689	5.981878	102.5188	7.149087	
32	31/1/1950	1950	1	31	31	3.37499	12.36923	14.13043	10.62378	5.403992	32.8884	1.467385	
33	1/2/1950	1950	2	1	32	0.021442	14.75491	17.41394	12.2493	5.661224	115.6226	4.229236	
34	2/2/1950	1950	2	2	33	0.000457	16.38736	17.73413	14.80841	4.377072	79.2579	5.918926	
35	3/2/1950	1950	2	3	34	0.000837	16.47049	18.37894	14.85013	4.794648	91.87178	6.575878	
36	4/2/1950	1950	2	4	35	0.001134	16.71024	18.02612	14.93677	4.505729	9.645352	7.846043	
37	5/2/1950	1950	2	5	36	0.032495	15.07111	17.39505	13.67133	6.343687	116.7773	7.120852	
38	6/2/1950	1950	2	6	37	0.000689	11.67224	13.66705	8.118591	4.399162	30.13088	9.509393	

REMO2009_MPI-M-MPI-ESM-LR_r1_

Figure 5: An example daily csv datafile with basic climatic parameters for the Epidaurus CH site for EURO-CORDEX simulations with the REMO2009.v1 RCM (set of simulations 10 in Table 1) driven by the historical emissions (1950-2005) and RCP8.5 (2006-2100).

	A	B	C	D	E	F	G	H	I	J	K	L	M	N	O	P	Q	R
1	Year	Month	Decyear	pr(mmd-1	std	tas(C)	std	tasmax(C	std	tasmin(C)	std	huss(gkg-	std	rsds(Wm-	std	ws(ms-1)	std	
2	1950	1	1950	1.973134	1.347474	9.309039	3.220391	12.43207	2.444262	7.142181	4.37345	5.347551	0.467554	90.07757	17.36939	3.356212	1.261106	
3	1950	2	1950.083	1.958956	0.789645	8.476288	2.857491	12.01008	2.197499	5.611816	4.235167	4.996889	0.215175	128.9013	23.14599	4.043814	0.839065	
4	1950	3	1950.167	1.88867	0.84507	9.877228	2.617095	13.04392	1.985572	7.546173	3.225405	5.139388	0.362047	172.0855	17.37651	3.235359	0.396705	
5	1950	4	1950.25	1.041501	0.928431	13.66873	3.508064	17.30189	3.148762	11.63586	3.194664	5.41144	0.407417	237.0421	35.3864	2.865991	0.668184	
6	1950	5	1950.333	0.911486	0.617365	17.89783	1.467492	21.47485	1.544364	14.61154	2.570753	6.977427	0.805167	268.2914	22.7759	2.51706	0.789712	
7	1950	6	1950.417	0.455209	0.432384	21.86653	1.601632	25.37741	1.630781	18.23047	3.109211	8.240048	0.66542	295.2215	17.42296	2.493438	0.71814	
8	1950	7	1950.5	0.216784	0.394685	25.20303	1.486655	28.83475	1.665449	21.79126	2.815969	8.902848	0.854396	309.7563	21.28814	3.436286	0.685851	
9	1950	8	1950.583	0.162868	0.1606	24.8002	1.961866	28.68253	2.11853	20.87973	2.69473	8.722689	0.890267	277.2058	22.26965	3.247467	0.546965	
10	1950	9	1950.667	0.783591	0.35483	21.16708	2.356219	24.75116	2.162652	18.26068	3.121269	8.33781	0.754611	217.0644	23.6799	3.822326	0.876607	
11	1950	10	1950.75	2.621604	2.786192	16.87262	2.150988	20.0596	1.905432	14.41312	3.037127	7.852214	0.760057	144.4754	29.80716	3.766686	1.244116	
12	1950	11	1950.833	5.669284	3.480165	12.62344	2.809455	14.96921	2.772482	10.63996	3.393826	6.95314	0.654148	79.11041	6.19994	3.908677	0.687715	
13	1950	12	1950.917	1.931155	2.019994	10.42691	2.23793	13.56267	1.70651	8.107391	3.297452	5.659947	0.557796	83.23566	14.81094	3.926408	0.698558	
14	1951	1	1951	2.69779	1.55516	7.886062	2.659911	10.50528	2.159713	5.486267	3.305683	4.789752	0.206687	89.52895	16.85902	4.146563	0.920317	
15	1951	2	1951.083	4.607083	1.931978	7.630859	2.860609	10.48019	2.695339	4.909515	3.738163	4.733124	0.575403	118.6547	19.21761	4.019564	1.332824	
16	1951	3	1951.167	1.6037	1.337201	10.73303	2.127778	14.1225	1.700877	7.550969	3.140941	5.104487	0.267185	182.6669	26.58801	3.218358	1.16736	
17	1951	4	1951.25	2.225535	1.433462	12.4447	1.814045	15.60971	1.936282	9.400757	2.493912	5.799457	0.585465	224.3148	26.53961	3.190969	1.049209	
18	1951	5	1951.333	1.206078	0.79115	16.68096	2.02787	19.73953	1.796272	13.5044	3.006955	7.02065	0.937695	271.2423	12.84907	2.14357	0.476146	
19	1951	6	1951.417	0.670313	0.614213	21.3833	1.949335	24.69062	2.132552	17.89945	2.665528	8.019574	0.967711	299.4854	19.08178	2.490054	0.580992	
20	1951	7	1951.5	0.325278	0.346876	24.15073	1.570042	27.42813	1.863855	20.80731	2.176767	9.199805	1.074317	301.5096	16.6127	2.936414	0.690249	
21	1951	8	1951.583	0.096673	0.082558	25.07349	1.711043	28.41788	2.075877	21.78406	2.235082	9.442943	1.039694	280.21	22.91368	3.396921	1.410188	
22	1951	9	1951.667	1.682238	2.211817	21.7106	2.011815	25.10803	1.966106	18.61133	2.625889	9.247356	0.788959	208.5511	20.21381	2.911939	0.992178	
23	1951	10	1951.75	2.046156	1.289757	16.51541	2.268984	19.41492	1.959057	13.82715	2.83382	7.711962	0.4206	145.0334	9.814517	3.229788	0.528837	
24	1951	11	1951.833	2.499923	1.899495	13.47	2.269148	16.26221	1.641473	10.97437	3.022477	6.945554	0.538439	101.8403	11.76176	3.606479	0.740199	
25	1951	12	1951.917	3.03931	1.796262	10.09692	1.648316	12.83475	1.636881	7.657196	2.421279	5.698327	0.494857	77.43969	14.63573	3.913682	0.834413	
26	1952	1	1952	1.706676	1.007707	10.0413	2.347023	13.13309	1.452307	7.318298	3.255688	5.346921	0.401193	96.26052	17.83305	3.490733	1.147412	
27	1952	2	1952.083	3.443246	2.092963	8.539215	2.751792	11.27069	2.452154	6.048645	3.308294	5.014189	0.576748	120.236	16.91447	4.016141	0.932529	
28	1952	3	1952.167	2.505668	1.691627	10.29416	2.49281	13.2894	1.806657	7.420044	3.467385	5.321814	0.415291	174.1228	18.54998	3.630585	0.754748	
29	1952	4	1952.25	1.854214	0.861571	12.91013	1.576628	16.19676	0.893713	9.731964	2.863076	6.034155	0.347392	227.4335	24.43312	2.976484	0.679185	
30	1952	5	1952.333	0.802688	0.4967	17.94153	1.25868	21.28968	1.363862	14.51758	2.5279	7.045988	0.78212	276.3884	20.24112	2.277349	0.496545	
31	1952	6	1952.417	0.514659	0.44313	21.78229	1.887761	25.17435	2.408146	18.29083	2.4091	8.221683	0.984549	301.3268	23.57306	2.514168	0.853617	
32	1952	7	1952.5	0.235754	0.267773	25.00122	1.493994	28.37085	1.97694	21.60773	2.161548	8.90916	0.879893	309.144	24.77925	3.346067	1.132085	
33	1952	8	1952.583	1.217762	2.017685	24.09158	1.687062	27.29703	1.879685	20.91824	2.134423	9.85081	0.843531	266.8459	16.28818	3.338955	1.018528	
34	1952	9	1952.667	2.597267	2.353798	20.66043	2.422351	23.61331	2.161651	17.68178	2.96186	9.495433	1.571596	194.5195	13.42764	2.424169	0.488664	
35	1952	10	1952.75	3.153141	2.195304	17.15485	2.490396	20.01337	2.066262	14.57178	2.988996	8.15022	0.761413	140.9218	13.92797	3.432724	1.051829	
36	1952	11	1952.833	3.149984	1.376572	13.11197	2.577255	15.76511	2.077302	10.77295	3.254029	6.947778	0.511944	95.23721	15.51047	4.156472	1.233658	
37	1952	12	1952.917	2.18024	1.724928	9.64798	3.408045	12.16229	2.912686	7.479584	3.882806	5.408013	0.617842	78.77486	12.38359	4.433449	0.972198	
38	1953	1	1953	1.689158	0.996489	8.403625	3.281242	11.16016	2.668167	5.914185	4.010482	4.96853	0.616885	89.79249	13.73216	3.64536	1.264668	

ENSEMBLE_rcp85_23.1576_37.6259_

Figure 6: An example monthly csv datafile with basic climatic parameters for the Epidaurus CH site for the ensemble of the 11 EURO-CORDEX sets of simulations driven by the historical emissions (1950-2005) and RCP8.5 (2006-2100).

	A	B	C	D	E	F	G	H	I	J	K	L	M	N	O	P
1	Year	pr(mmd-1	std	tas(C)	std	tasmax(C	std	tasmin(C)	std	huss(gkg-	std	rsds(Wm-	std	ws(ms-1)	std	
2	1950	1.63452	0.291801	16.01492	1.97011	19.37662	1.281848	13.23917	3.09524	6.878449	0.259251	191.8723	18.02162	3.384977	0.332947	
3	1951	1.89184	0.528208	15.64813	1.740625	18.71707	1.258152	12.70148	2.627151	6.976082	0.369077	191.7081	15.22229	3.266192	0.656944	
4	1952	1.946775	0.717474	15.9314	1.903031	18.96466	1.373337	13.04663	2.777632	7.145514	0.432747	190.1001	13.97618	3.336441	0.620443	
5	1953	1.659281	0.591604	15.81177	2.147567	18.90152	1.788237	12.85056	2.960899	7.027744	0.464449	191.7614	15.28514	3.33303	0.860445	
6	1954	1.618392	0.628971	15.81769	2.089915	18.97055	1.520912	12.82193	3.030789	6.964176	0.388523	194.2412	17.25321	3.258082	0.624554	
7	1955	1.453625	0.337194	15.87991	1.937138	19.05466	1.098641	12.85455	3.016251	6.907619	0.292643	193.615	17.72556	3.242303	0.560192	
8	1956	1.625449	0.244423	15.82874	1.995239	18.95233	1.41926	12.87088	2.905684	7.0686	0.291801	191.9764	16.15456	3.245296	0.601103	
9	1957	1.807682	0.337299	15.78021	1.854151	18.91013	1.34295	12.82797	2.7677	6.961734	0.34125	192.2159	16.36345	3.272822	0.580346	
10	1958	1.698385	0.349033	15.60352	1.951296	18.62968	1.340436	12.70114	2.851052	6.82087	0.402019	190.593	15.26357	3.461574	0.61366	
11	1959	1.929241	0.588634	15.9902	2.15829	19.04855	1.676468	13.09143	3.033491	7.01538	0.287745	192.4245	13.06288	3.267581	0.66169	
12	1960	1.779124	0.641403	15.42853	2.227255	18.46512	1.587566	12.54056	3.131444	6.784852	0.300297	192.0348	13.68787	3.46317	0.582258	
13	1961	1.935794	0.341392	15.41104	1.894924	18.43704	1.280065	12.50659	2.866891	6.940139	0.297096	188.8432	15.81363	3.425176	0.628521	
14	1962	1.826573	0.278109	15.64758	1.929681	18.72311	1.25991	12.72012	2.890459	6.93756	0.296002	190.318	16.43666	3.366351	0.62489	
15	1963	1.815884	0.827613	16.00583	1.460849	19.0679	0.840977	13.10391	2.448481	7.024324	0.466721	190.4906	18.18713	3.385923	0.621827	
16	1964	1.653949	0.738048	15.71652	2.09891	18.74939	1.47325	12.79709	3.011653	6.804296	0.351154	191.5954	11.74023	3.138382	0.577885	
17	1965	1.672083	0.337979	15.80734	1.815865	18.93164	1.208409	12.84961	2.769983	6.875133	0.296396	193.5773	13.5224	3.209929	0.456851	
18	1966	1.793088	0.49791	15.60904	2.16948	18.72363	1.483207	12.62839	3.158002	6.882974	0.186887	191.5421	12.86136	3.210757	0.799203	
19	1967	1.78485	0.481628	15.59836	2.051193	18.6785	1.5456	12.66205	2.932599	6.800323	0.286109	191.9998	13.83715	3.354974	0.644516	
20	1968	2.060938	0.637011	15.64258	1.845525	18.65463	1.313275	12.76065	2.73405	6.936202	0.278381	187.7247	14.43934	3.350073	0.570504	
21	1969	1.671276	0.416006	15.97037	2.024216	19.03546	1.525323	13.05176	2.875937	6.985361	0.343341	188.1133	14.69741	3.173851	0.536629	
22	1970	1.519125	0.392788	15.1918	1.868455	18.65012	1.400678	11.90537	2.760263	6.75778	0.230975	199.7151	18.82178	3.613373	0.511476	
23	1971	1.381173	0.407659	15.69486	1.449354	19.2609	1.07865	12.29089	2.486316	6.869675	0.269057	200.9985	20.79995	3.396456	0.661595	
24	1972	1.443745	0.568807	15.96713	1.949444	19.54749	1.621225	12.54623	2.862971	6.783171	0.375171	203.4185	20.05397	3.487109	0.542659	
25	1973	1.51396	0.639639	15.58029	2.106817	19.1022	1.627361	11.8067	2.593194	6.820544	0.460011	199.9604	19.63544	3.39321	0.473017	
26	1974	1.516987	0.499075	15.72885	1.772226	19.26749	1.280405	11.90186	2.462602	6.916819	0.425187	201.4139	18.25536	3.388888	0.528236	
27	1975	1.70211	0.610776	15.83533	1.632729	19.37796	1.176824	11.96951	2.419847	6.991421	0.360502	199.3599	19.93577	3.290484	0.567042	
28	1976	1.645038	0.662446	15.68716	1.835892	19.20389	1.510311	12.27429	2.782012	7.035894	0.375845	198.9869	21.04991	3.329026	0.544544	
29	1977	1.329673	0.460935	16.08875	1.627089	19.70761	1.343462	12.60669	2.600747	6.933138	0.345314	202.746	19.42494	3.330772	0.610207	
30	1978	1.591507	0.575102	15.86447	1.572713	19.38074	1.033376	12.47415	2.617103	6.901649	0.313704	199.5215	20.78433	3.452403	0.547988	
31	1979	1.487965	0.489654	15.95609	1.60036	19.48456	1.113512	12.5925	2.587843	6.992155	0.277861	200.1149	21.25466	3.314657	0.5703	
32	1980	1.511944	0.559403	15.91333	1.6517	19.46204	1.267417	12.4747	2.636661	6.938256	0.287707	200.8193	20.58239	3.404511	0.638533	
33	1981	1.544974	0.659403	15.80234	1.685273	19.30371	1.054519	12.48816	2.676144	6.995462	0.370168	200.0728	19.21325	3.471999	0.511333	
34	1982	1.703261	0.69906	15.73953	1.714763	19.24789	1.423002	12.38229	2.598029	6.962087	0.279748	199.1452	20.32024	3.360723	0.614541	
35	1983	1.566477	0.332832	15.75681	2.074057	19.21021	1.597073	12.45612	2.987446	6.932548	0.314473	198.2478	19.22528	3.316846	0.589208	
36	1984	1.527804	0.48198	15.84451	1.622892	19.36545	1.144301	12.47836	2.638379	6.881428	0.439014	201.0938	20.11607	3.351039	0.611522	
37	1985	1.460099	0.61921	15.69925	1.734206	19.22549	1.394239	12.33032	2.635447	6.907372	0.323838	202.4218	19.34837	3.391157	0.499171	
38	1986	1.235049	0.436638	15.90668	1.799798	19.45154	1.427349	12.50287	2.732323	6.844213	0.353613	201.8912	19.90226	3.509454	0.485044	

ENSEMBLE_rcp85_23.1576_37.6259_

Figure 7: The same as Fig 6 but for annual data.

5.4. References

Georgoulias, A. K., Akritidis, D., Kalisoras, A., Kapsomenakis, J., Melas, D., Zerefos, C. S., & Zanis, P. (2022). Climate change projections for Greece in the 21st century from high-resolution EURO-CORDEX RCM simulations. Atmospheric Research, 271, 106049. https://doi.org/10.1016/j.atmosres.2022.106049

Ioannidis, C., Verykokou, S., Soile, S., Istrati, D., Spyrakos, C., Sarris, A., Akritidis, D., Feidas, H., Georgoulias, A. K., Tringa, E., et al. (2024). Safeguarding our heritage—The TRIQUETRA project approach. Heritage, 7, 758–793. https://doi.org/10.3390/heritage7020037

Jacob, D., Petersen, J., Eggert, B., Alias, A., Christensen, O. B., Bouwer, L. M., Braun, A., Colette, A., Déqué, M., Georgievski, G., et al. (2014). EURO-CORDEX: New high-resolution climate change projections for European impact research. Regional Environmental Change, 14, 563–578. https://doi.org/10.1007/s10113-013-0499-2

Jacob, D., Teichmann, C., Sobolowski, S., Katragkou, E., Anders, I., Belda, M., Benestad, R., Boberg, F., Buonomo, E., Cardoso, R. M., et al. (2020). Regional climate downscaling over Europe: Perspectives from the EURO-CORDEX community. Regional Environmental Change, 20, 51. https://doi.org/10.1007/s10113-020-01606-9

Moss, R. H., Edmonds, J. A., Hibbard, K. A., Manning, M. R., Rose, S. K., van Vuuren, D. P., Carter, T. R., Emori, S., Kainuma, M., Kram, T., Meehl, G. A., Mitchell, J. F. B., Nakicenovic, N., Riahi, K., Smith, S. J., Stouffer, R. J., Thomson, A. M., Weyant, J. P., & Wilbanks, T. J. (2010). The next generation of scenarios for climate change research and assessment. Nature, 463, 747–756. https://doi.org/10.1038/nature08823

Riahi, K., Rao, S., Krey, V., Cho, C., Chirkov, V., Fischer, G., Kindermann, G., Nakicenovic, N., & Rafaj, P. (2011). RCP 8.5—A scenario of comparatively high greenhouse gas emissions. Climatic Change, 109, 33–57. https://doi.org/10.1007/s10584-011-0149-y

Thomson, A. M., Calvin, K. V., Smith, S. J., Kyle, G. P., Volke, A., Patel, P., Delgado-Arias, S., Bond-Lamberty, B., Wise, M. A., Clarke, L. E., & Edmonds, J. A. (2011). RCP4.5: A pathway for stabilization of radiative forcing by 2100. Climatic Change, 109, 77–94. https://doi.org/10.1007/s10584-011-0151-4

Tringa, E., Georgoulias, A. K., Akritidis, D., Feidas, H., & Zanis, P. (2025). Assessing the future risk of damage to European cultural heritage due to climate change. Heritage, 8(5), 175. https://doi.org/10.3390/heritage8050175

van Vuuren, D. P., Edmonds, J., Kainuma, M., Riahi, K., Thomson, A., Hibbard, K., Hurtt, G. C., Kram, T., Krey, V., Lamarque, J.-F., Masui, T., Meinshausen, M., Nakicenovic, N., Smith, S. J., & Rose, S. K. (2011a). The representative concentration

pathways: An overview. Climatic Change, 109, 5–31. https://doi.org/10.1007/s10584-011-0148-z

van Vuuren, D. P., Stehfest, E., den Elzen, M. G. J., Kram, T., van Vliet, J., Deetman, S., Isaac, M., Klein Goldewijk, K., Hof, A., Mendoza Beltran, A., Oostenrijk, R., & van Ruijven, B. (2011b). RCP2.6: Exploring the possibility to keep global mean temperature increase below 2 °C. Climatic Change, 109, 95–116. https://doi.org/10.1007/s10584-011-0152-3

Vautard, R., Gobiet, A., Jacob, D., Belda, M., Colette, A., Déqué, M., Fernández, J., García-Díez, M., Goergen, K., Güttler, I., Halenka, T., Karacostas, T., Katragkou, E., Keuler, K., Kotlarski, S., Mayer, S., van Meijgaard, E., Nikulin, G., Patarčić, M., Scinocca, J., Sobolowski, S., Suklitsch, M., Teichmann, C., Warrach-Sagi, K., Wulfmeyer, V., & Yiou, P. (2013). The simulation of European heat waves from an ensemble of regional climate models within the EURO-CORDEX project. Climate Dynamics, 41(9–10), 2555–2575. https://doi.org/10.1007/s00382-013-1714-z

5.5. Contributors

Developed by: Department of Meteorology and Climatology, School of Geology, Aristotle University of Thessaloniki, 54124 Thessaloniki, Greece

Date of last update: 10/11/2025

Lead contributors:

- Aristeidis K. Georgoulias
- Efstathia Tringa
- Dimitris Akritidis
- Haralambos Feidas
- Prodromos Zanis

6. Vegetation Condition

6.1. Overview

The Enhanced Vegetation Index (EVI) anomaly detection model processes MODIS MOD13Q1 16-day composite datasets (250 m spatial resolution) spanning the period 2000–2022 to calculate anomalies relative to phenologically adjusted, long-term median EVI reference values. These anomalies are derived by comparing each composite against its corresponding multi-year baseline, allowing the quantification of departures from expected seasonal patterns. The approach enables the detection of short-term fluctuations, interannual variability, and multi-decadal trends in vegetation activity. By capturing both abrupt deviations and gradual directional changes, the model supports detailed temporal analyses of vegetation dynamics under varying environmental and climatic conditions.

A key component of the model is the establishment of a temporally resolved baseline. For each 16-day composite period, the median EVI value across the full 2000–2022 record is computed. This median baseline represents expected vegetation conditions throughout the growing season and minimizes the influence of short-term weather anomalies or extreme events. Deviations from this baseline are calculated as EVI anomalies, which serve as the model output. Positive anomalies indicate vegetation activity above expected levels, while negative anomalies signify reduced activity due to stressors such as drought or heat (Grillakis 2019; Bento et al. 2018).

The model allows for temporal aggregation of anomalies at monthly, seasonal, or annual scales, enabling identification of periods of environmental stress or accelerated growth. By leveraging quality-controlled EVI composites, robust baseline calculations, and anomaly detection, the model provides a framework for interpreting vegetation responses to climatic and environmental variability. It is designed to be generalizable across diverse landscapes and can support applications in ecological monitoring, drought assessment, and long-term vegetation trend analysis.

6.2. Methodological Description

6.2.1. Data Sources

The analysis is based on satellite-derived vegetation index data from the MODIS MOD13Q1 Version 6 product, which provides 16-day composites of the Enhanced Vegetation Index (EVI) at a spatial resolution of 250 m. The MOD13Q1 product is generated from daily surface reflectance data after atmospheric correction and composited using a maximum value compositing algorithm to minimize the effects of clouds and atmospheric variability. Each composite contains not only spectral indices but also pixel reliability layers and quality assurance (QA) flags. These ancillary layers were used to exclude unreliable observations, such as those affected by cloud, aerosols, snow cover, or sensor anomalies. Only pixels flagged as “highest quality” were retained to ensure consistency of the time series.

The EVI, which incorporates blue, red, and near-infrared bands, offers improved performance over NDVI by reducing atmospheric and soil background effects. Corine Land Cover (CLC) change products were used to identify and mask non-vegetated areas and regions affected by recent land-use changes.

6.2.2. Data Preprocessing

Preprocessing was conducted to ensure the reliability and consistency of the MODIS EVI time series prior to analysis. First, pixel-level quality filtering was applied using the MODIS pixel reliability layer and associated Quality Assessment (QA) flags, retaining only observations classified as “good quality” and excluding low-reliability or contaminated pixels. Negative EVI values, which typically indicate non-vegetated or non-physical spectral responses, were masked out.

Subsequently, spatial masking was performed using CLC datasets to remove pixels outside vegetated zones or in areas affected by land cover changes during the 2000–2022 period (Reinermann et al. 2019). This step was essential for preventing false drought signals arising from land use conversion. The filtered time series was then temporally harmonized to maintain a consistent 16-day composite interval across all years, ensuring comparability in seasonal and interannual analyses.

All MODIS data processing and EVI calculations were implemented within the Google Earth Engine (GEE) environment (Gorelick et al. 2017), which provided direct access to the MOD13Q1 product and enabled large-scale computation across the full study period. The EVI values were derived using the standard MODIS formulation embedded in the dataset, and quality assurance layers were simultaneously accessed to filter out unreliable observations.

6.2.3. Enhanced Vegetation Index (EVI)

EVI was chosen instead of the more widely used NDVI because it offers improved sensitivity in areas with dense vegetation cover and high leaf area index, where NDVI tends to saturate. Furthermore, EVI reduces residual atmospheric influences by incorporating a blue band correction for aerosols and decouples the canopy background signal, which makes it particularly suitable for monitoring vegetation conditions across heterogeneous landscapes.

A. Comparison of EVI and NDVI

The Enhanced Vegetation Index (EVI) offers several advantages over the Normalized Difference Vegetation Index (NDVI) that are particularly relevant for monitoring vegetation dynamics across heterogeneous landscapes. NDVI is widely used due to its simplicity, but it tends to saturate in areas with dense vegetation, which reduces its sensitivity to variations in high biomass regions. EVI addresses this limitation by incorporating a canopy background adjustment and coefficients that correct for atmospheric aerosol scattering, including effects detectable in the blue spectral band. These modifications allow EVI to maintain a more linear response to vegetation cover and leaf area index, even in dense canopies. In addition, EVI reduces the influence of residual atmospheric effects, enabling more consistent temporal and spatial monitoring. This makes EVI especially suitable for detecting vegetation anomalies and analyzing long-term trends across regions with diverse vegetation types and structural heterogeneity.

B. Calculation

The Enhanced Vegetation Index is calculated according to the following formula (Huete et al. 2002):

$$EVI = G * \frac{(NIR - RED)}{(NIR + C1 * RED - C2 * BLUE + L)}$$

where NIR, RED, and BLUE are atmospherically corrected surface reflectances in the near-infrared, red, and blue bands, respectively. G is a gain factor (set to 2.5), L is a canopy background adjustment term (set to 1.0), and C1 and C2 are aerosol resistance coefficients (6.0 and 7.5, respectively). These parameterizations are designed to optimize sensitivity to canopy biophysical parameters while minimizing atmospheric and background noise effects.

6.2.4. Baseline Vegetation Activity Estimation

To establish a reference for expected vegetation conditions, long-term median EVI values were calculated over the 2000–2022 period. For each 16-day composite period, the median EVI value was calculated across all years, producing a temporally resolved baseline that captures typical seasonal patterns while minimizing the influence of outliers and extreme events. The median was used instead of the mean to ensure robustness against outliers and occasional data errors. The use of the median, rather than the mean, ensures robustness against occasional data errors or extreme vegetation disturbances.

The baseline allows for calculation of EVI anomalies, defined as the deviation of observed EVI from the median baseline value for the corresponding 16-day period. Positive anomalies indicate above-average vegetation activity, while negative anomalies signify below-normal conditions. To enhance comparability and reduce temporal noise, anomalies can be aggregated at monthly, seasonal, or annual scales. This approach provides a robust reference framework for detecting vegetation stress, unusual growth, or recovery patterns across diverse landscapes with varying vegetation types and canopy structures. By incorporating long-term temporal information, quality-controlled observations, and spatially explicit masking, the baseline serves as a reliable foundation for the detection and quantification of deviations in vegetation dynamics over time.

6.2.5. Anomaly Calculation and Temporal Analysis

Anomalies were computed by subtracting the long-term median EVI for a given composite from the observed EVI in that composite for each year. This generated a time series of positive and negative deviations, where negative anomalies indicate reduced vegetation activity relative to the baseline, potentially signaling drought stress, or other disturbances. Positive anomalies, conversely, reflect higher-than-expected vegetation vigor, which may result from favorable climatic conditions.

The anomaly time series was aggregated both spatially, to represent conditions over the entire Roseninsel site (Ottinger et al. 2025), and temporally, to evaluate seasonal and interannual patterns. The primary focus was on detecting sustained negative anomalies during summer (June–August) and autumn (September–November), as these periods are most sensitive to soil moisture deficits in temperate ecosystems.

6.3. Outputs and Interpretation of Results

The analysis of monthly Enhanced Vegetation Index (EVI) deviations provides detailed insights into temporal vegetation dynamics and the response of ecosystems to environmental stressors. By examining EVI anomalies over multiple years, key periods of vegetation stress and enhanced growth were identified, highlighting the influence of climatic variations on seasonal vegetation development.

Positive EVI anomalies indicate higher-than-expected vegetation activity for a given period. Such increases typically correspond to favorable growing conditions, such as sufficient soil moisture, optimal temperatures, or accelerated phenological development in spring. Conversely, negative EVI anomalies reflect reduced vegetation activity, which can be caused by environmental stressors including drought, heatwaves, early frost, or other adverse climatic events.

Seasonal patterns of anomalies often reveal periods when vegetation is particularly sensitive to environmental conditions. For example, late summer months frequently show negative anomalies, reflecting periods of water limitation or heat stress, while early spring may display positive anomalies associated with accelerated canopy development under favorable conditions.

By comparing observed EVI values with long-term baseline medians, it is possible to detect deviations from expected vegetation activity. This provides a robust framework for assessing ecosystem health, resilience, and vulnerability, as well as for monitoring the impacts of climatic extremes. Aggregating anomalies at monthly, seasonal, or annual scales enhances interpretability and helps identify broader temporal trends across different vegetation types and landscapes.

Overall, the EVI anomaly analysis provides a robust framework for interpreting temporal vegetation responses, highlighting both the vulnerability and resilience of ecosystems to interannual climate variations. This information is crucial for ecological assessment and climate impact studies, enabling identification of periods at CH sites most affected by environmental stress.

6.4. References

Bento, Virgílio A., Célia M. Gouveia, Carlos C. DaCamara, and Isabel F. Trigo. 2018. “A Climatological Assessment of Drought Impact on Vegetation Health Index.” Agricultural and Forest Meteorology 259 (September): 286–95. https://doi.org/10.1016/j.agrformet.2018.05.014

Gorelick, Noel, Matt Hancher, Mike Dixon, Simon Ilyushchenko, David Thau, and Rebecca Moore. 2017. “Google Earth Engine: Planetary-Scale Geospatial Analysis for Everyone.” Remote Sensing of Environment, Big Remotely Sensed Data: tools, applications and experiences, vol. 202 (December): 18–27. https://doi.org/10.1016/j.rse.2017.06.031

Grillakis, Manolis G. 2019. “Increase in Severe and Extreme Soil Moisture Droughts for Europe under Climate Change.” Science of The Total Environment 660 (April): 1245–55. https://doi.org/10.1016/j.scitotenv.2019.01.001

Huete, A, K Didan, T Miura, E. P Rodriguez, X Gao, and L. G Ferreira. 2002. “Overview of the Radiometric and Biophysical Performance of the MODIS Vegetation Indices.” Remote Sensing of Environment, The Moderate Resolution Imaging Spectroradiometer (MODIS): a new generation of Land Surface Monitoring, vol. 83 (1): 195–213. https://doi.org/10.1016/S0034-4257(02)00096-2

Ottinger, Marco, Felix Bachofer, Sophie Reinermann, Aristeidis Georgoulias, Prodromos Zanis, and Juliane Huth. 2025. Analyzing Climate Change Impacts on European Cultural Heritage Sites Using High-Temporal-Resolution Satellite Time Series. https://doi.org/10.13140/RG.2.2.17614.37449

Reinermann, Sophie, Ursula Gessner, Sarah Asam, Claudia Kuenzer, and Stefan Dech. 2019. “The Effect of Droughts on Vegetation Condition in Germany: An Analysis Based on Two Decades of Satellite Earth Observation Time Series and Crop Yield Statistics.” Remote Sensing 11 (15): 15. https://doi.org/10.3390/rs11151783

6.5. Contributors

Developed by: German Aerospace Center (DLR)

Date of last update: August 20, 2025

Lead contributors:

- Marco Ottinger
- Felix Bachofer

7. Sea Level Rise Prediction

7.1. Overview

The Sea Level Rise Risk model aims at assessing the threat of Sea Level Rise to coastal sites and cultural heritage assets located in coastal zones. The scope is to study the vulnerability of these areas based on their current elevation values, the recorded trends of vertical ground motion and sea level projections under different climatic scenarios, namely RCP 2.6, 4.5 and 8.5.RCP 2.6 refers to an assumption of below 2.0o C warming relative to 1850-1900 with implied net zero emissions in the second half of the century. RCP 4.5 scenario has a very mild differentiation from a “no-additional climate policy” scenario resulting in an estimated warming of 2.7o C. Finally, RCP 8.5 is the worst case scenario regarding the use of fossil fuels. To proceed with the Sea Level Rise risk model several key inputs are necessary, with the most important being a high-resolution Digital Elevation Model (DEM) that will provide information of the current elevation values of the coastal sites. The area of interest is depicted as a 2km buffer zone from the coastline provided by the

European Environment Agency (EEA). Vertical Ground motion is provided by the European Ground Motion Service as a media trend expressed in mm/year. Sea Level Rise scenarios are provided by NASA's Sea Level Projection tool (https://sealevel.nasa.gov/ipcc-ar6-sea-level-projection-tool). Finally, cultural heritage (CH) site locations are retrieved from UNESCO's website and OpenStreetMap (OSM)The data are preprocessed and through the application of the proposed new areas under flood threat for the target years 2050 and 2100 are produced for the three distinct RCP scenarios. The output consists essentially of digital elevation models of projected values that can be vectorized to perform spatial queries.

7.2. Methodological Description

7.2.1. Selecting and Retrieving the Datasets

A. Digital Elevation Models

Digital Elevation models (DEMs) are a core geospatial input for the risk model as they define the current terrain morphology including height values and slopes. Several global and regional models were reviewed in the frame of the risk model to assess their accuracy, spatial coverage and suitability. The Shuttle Radar Topography Mission (SRTM), produced by NASA and NGA, provides 30m resolution between 60oN and 56oS, with vertical errors ranging between 5-9m. The ASTER Global DEM (GDEM v.3), developed by NASA and METI, also offers a 30m resolution with near global coverage but suffers from higher vertical errors (15-17m). The DLR-SRTM X-band DEM (at a 25m resolution and approximately 16m vertical accuracy) and ALOS World 3D DEM (30m resolution, with RMSE of 4.4m) provide additional radar and optical-derived alternatives. At a European scale, the EU-DEM v.1.1 (25m resolution) which is hybrid product of SRTM and ASTER GDEM) recorded better vertical accuracy (around 2.9m), but it is no longer available. These DEMs provided a valuable benchmarking framework for selecting the most accurate and updated dataset for analysis in the region of the Mediterranean.

Copernicus GLO-30 DEM produced from the TanDEM-X mission and distributed by the European Space Agency and Airbus Defence and Space was selected as the most suitable elevation dataset. It provides global coverage at a spatial resolution of 30m (1 arc second), with a vertical accuracy better than 4m (90% linear error) and relative accuracies within 2–4m depending on slope. Unlike earlier DEMs, Copernicus DEM incorporates extensive editing to improve hydrological consistency, including flattening of water bodies, adjustment of river flows, and coastline correction. It is provided in standardized formats (GeoTIFF/DTED) and reference systems (horizontal datum WGS84, vertical datum EGM2008), ensuring interoperability across applications. Critically, the Copernicus DEM is openly accessible for research purposes, making it both technically robust and policy-aligned. Its combination of resolution, accuracy, and consistency led to its selection as the baseline elevation

model for assessing sea-level rise impacts on cultural heritage across the Mediterranean.

B. Coastline Data

Accurate coastline representation is crucial for linking terrestrial elevation models with marine inundation projections. Several open-access datasets were used to ensure reliability across different Mediterranean contexts. The Global Self-consistent, Hierarchical, High-resolution Geography Database (GSHHG), developed by NOAA and the University of Hawaii, provides multi-scale vector shorelines ranging from ~100m to 10km resolution, suitable for both global and regional analyses. The USGS Global Shoreline Vector (GSV), produced from Landsat imagery in 2014, offers 30m spatial precision and classifies mainland, small islands, and large islands, thereby supporting ecological and geomorphological studies. At the European scale, the European Environment Agency's (EEA) Polygon Coastline Dataset combines EU-Hydro (Pan-European Hydrographic and Drainage Database) with GSHHG, harmonized to support EU Nature, Water Framework, and Marine Strategy Directives; it is designed for analysis at a 1:100,000 scale and is available as WMS and ESRI services. By integrating these datasets into a hybridized coastline layer, the study ensures accurate boundary delineation across diverse coastal morphologies, thereby improving the precision of sea-level rise impact assessments on heritage assets.

C. Ground Motion Data

Vertical ground motion is a critical parameter for refining sea-level rise (SLR) projections, as local subsidence or uplift can significantly amplify or mitigate relative sea-level change. The primary source for this information in Europe is the European Ground Motion Service (EGMS), part of the Copernicus Land Monitoring Service. EGMS products are derived from Sentinel-1 Synthetic Aperture Radar Interferometry (InSAR) time series, providing consistent measurements of land displacement across Europe. Three data product levels are available: Basic (L2a), which provides relative line-of-sight velocity maps; Calibrated (L2b), which are anchored to GNSS reference points for absolute accuracy; and Ortho (L3), which includes vertical and horizontal motion components at 100m resolution. Accuracy assessments show that EGMS products achieve millimeter-per-year precision, with 3D geolocation errors under 10m, making them suitable for both regional-scale hazard mapping and site-specific risk assessments.

The EGMS datasets cover the periods 2015–2021 and 2018–2022, following a five-year moving update cycle, and are freely accessible via the Copernicus EGMS portal (https://egms.land.copernicus.eu/). Metadata and product descriptions are documented in the EGMS Product Description Document (EEA/Copernicus, 2021), which specifies product attributes such as mean velocity, acceleration, and seasonal displacement trends. These data are provided in CSV vector format and referenced to ETRS89/LAEA (EPSG:3035) and WGS84 (EPSG:4326). The combination of high

temporal resolution, broad geographic coverage, and open accessibility makes EGMS a unique and robust dataset for integrating vertical ground motion into SLR exposure assessments. By correcting sea-level projections with EGMS-derived subsidence or uplift rates, the methodology ensures that local dynamics are properly accounted for, particularly in Mediterranean deltas, urbanized coastlines, and tectonically active regions where ground motion strongly influences cultural heritage vulnerability.

D. Sea Level Rise Projections

Sea-level rise (SLR) projections were obtained from the NASA/IPCC AR6 Sea Level Projection Tool, which builds on the Intergovernmental Panel on Climate Change's Sixth Assessment Report (AR6, 2021). The tool provides both global and regionalized estimates of sea-level change, expressed in NetCDF format for integration into geospatial analyses. Projections are based on Representative Concentration Pathways (RCPs 2.6, 4.5, 8.5) and the corresponding Shared Socioeconomic Pathways (SSPs 1–1.9 to 5–8.5), which reflect different trajectories of greenhouse gas emissions, mitigation policies, and socioeconomic development. For each scenario, the tool supplies median values and uncertainty ranges of SLR, broken down into contributing components such as thermal expansion, ice sheet mass loss, glacier melt, and land water storage. The capacity to regionalize projections allows Mediterranean-specific adjustments, making them particularly relevant for assessing cultural heritage risks along European coastlines (NASA Sea Level Projection Tool: https://sealevel.nasa.gov/ipcc-ar6-sea-level-projection-tool).

At the regional scale, these data provide estimates for target years 2050 and 2100, enabling both mid-century and long-term scenario analysis. By integrating global circulation model outputs with localized factors, the tool refines projections to capture variations caused by ocean dynamics and gravitational effects of ice sheet mass redistribution. These datasets were complemented by scientific literature, including the IPCC AR6 Working Group I Report (Oppenheimer et al., 2019), which outlines historical SLR trends (1.4 mm/yr in 1901–1990, rising to 3.2 mm/yr in 1998–2015) and anticipated accelerations into the 21st century. Together, NASA's regionalized datasets and the broader IPCC assessments form the scientific backbone for scenario-based inundation modeling. When combined with elevation, bathymetric, coastline, and vertical land motion data, they allow for the creation of detailed hazard maps identifying at-risk Mediterranean cultural heritage sites under multiple climate scenarios.

7.2.2. Preprocessing stage

The present research used the EGMS L3 product as it provides a raster version of the intended dataset that is easier to process. In the Mediterranean Coastal Zone, the recorded vertical ground motion using SAR algorithms varies from −91 mm/year (in the southern parts of Greece) to +63 mm/year. The preprocessing stage included mosaicking the necessary tiles downloaded from the EGMS portal and converting

the mean velocity value from mm/year to m/year. The data were resampled from 100 m resolution to 30 m to match the pixel size of the GLO-30 DEM and clipped to the area of interest's extent, defined as a 2km buffer zone from the selected coastline. The annual mean values were considered constant and projected to the target years of study, i.e., 2050 and 2100, by applying a simple raster calculation.

The pre-processing of NASA's Sea Level Rise datasets involved reading the NetCDF files per scenario (RCP 2.6, 4.5, 8.5) and extracting information on SLR projections for 2050 and 2100 at each location point (expressed as the median value of the quantile intervals between 0.14 and 0.79), using Python scripts in Google Colab notebooks. The extracted data were saved in CSV format and converted into a raster mosaic of 30 m resolution using GIS software (QGIS v.3.28). The mosaic was re-projected from WGS84 to ETRS89-LAEA, and a raster calculation was performed to convert SLR units from mm/year to m/year. The outputs consisted of six raster files corresponding to the different RCP scenarios and target years, clipped to the area of interest boundaries to depict expected sea level rise in meters.

7.2.3. Data Processing and Algorithm Application

Once the pre-processing stage finishes, the algorithm proceeds to raster calculations to determine the AOI's elevation for target years 2050 and 2100 under the three RCP scenarios of interest. Through an automated raster calculation process, the algorithm adds GLO-30 DEM values and EGMS vertical land movement values and, finally, subtracts NASA's SLR Projection Values. This step provides six new raster layers depicting elevation values under RCP scenarios 2.6, 4.5, and 8.5 for the target years.

The next algorithmic step involves using raster calculations and Boolean algebra to select and extract the sub-areas in the AOI that are affected by the different RCP scenarios for target years 2050 and 2100—areas that currently have an elevation greater than zero but are projected to have a negative or zero value in the future. The output of this stage is six raster files delineating affected areas, which can then be converted into vector features for further processing such as area calculation, country-level statistics, proximity analysis to heritage sites, and spatial queries to identify coastal heritage assets at risk. These results are then organized per monument type (UNESCO WHS or other cultural heritage sites) and per country to assess vulnerability levels across the Mediterranean EU-27.

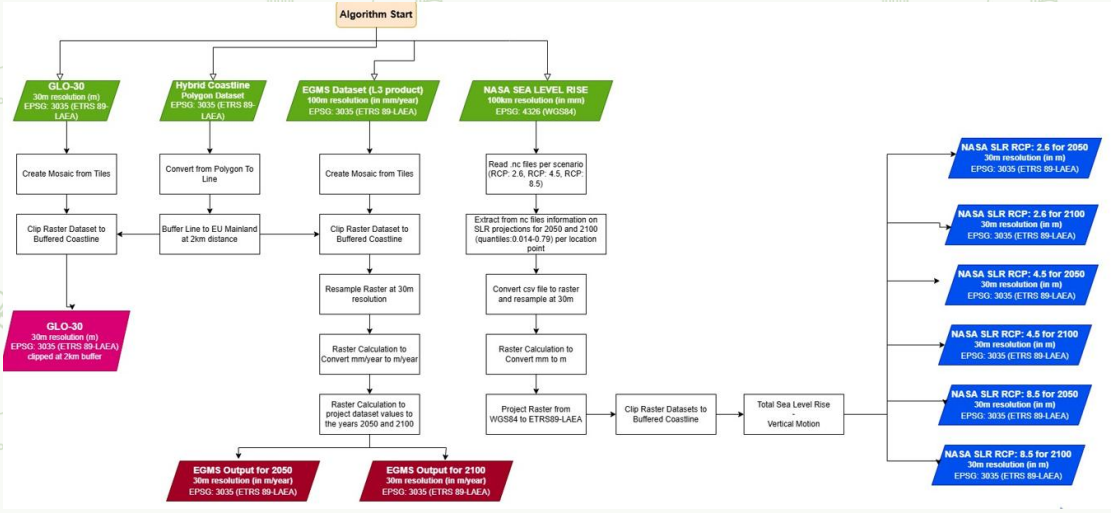

Figure 8: Algorithmic Representation of the preprocessing Steps.

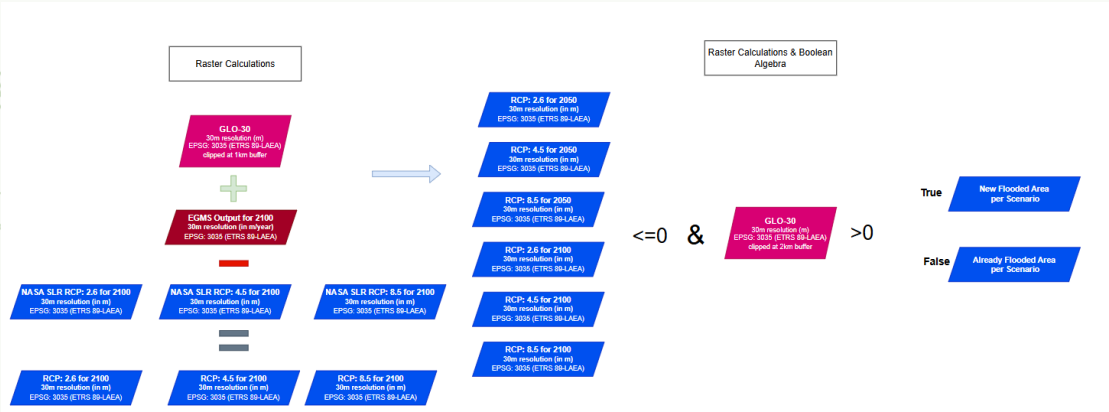

Figure 9: Raster Calculations for assessing new areas under SLR threat.

7.3. Outputs and Interpretation of Results

7.3.1. Affected Areas by SLR in the Mediterranean Region

The application of the algorithm led to the following calculation of affected areas by SLR per country expressed in hectares:

Table 4: Affected Area (in hectares) per country for each studied SLR scenario.

	2050			2100		
	RCP 2.6	RCP 4.5	RCP 8.5	RCP 2.6	RCP 4.5	RCP 8.5
Croatia	836,64	856,26	897,03	1588,14	1918,53	2606,31
Cyprus	354,42	365,04	400,77	1112,49	1348,29	1803,33
France	2536,92	2616,03	2720,79	5485,23	6799,86	8876,88
Greece	4833,90	4952,07	5254,38	12853,17	14859,81	18485,64
Italy	5941,44	6154,74	6487,65	13511,34	16747,29	22829,76
Malta	15,75	15,75	16,11	30,24	36,99	49,14
Monaco	1,80	2,97	3,06	4,14	4,41	5,94
Slovenia	51,03	52,56	55,80	125,73	155,34	206,73
Spain	2142,27	2219,94	2347,29	5466,69	7007,67	9773,64
Total:	**16714,17**	**17235,36**	**18182,88**	**40177,17**	**48878,19**	**64367,37**

7.3.2. Affected Cultural Heritage Monuments

The algorithmic results show that Greece, Italy, and France are the most exposed countries to future Sea Level Rise (SLR) scenarios by 2050 and 2100. For Greece and Italy, this is linked to their extensive coastlines and insular morphology, while France—despite ranking only fifth in coastline length—shows significant vulnerability due to its lowland coastal morphology and large river deltas such as the Rhône Delta in Camargue. Regarding UNESCO World Heritage Sites, five sites already exhibit negative minimum elevation values: the Amalfi Coast and Venice in Italy, and Delos, the Medieval City of Rhodes, and Pythagoreion and Heraion of Samos in Greece. These sites are projected to face even greater exposure to SLR in the coming decades.

For non-UNESCO cultural heritage assets identified through OpenStreetMap, the study found that currently 243 records are already below sea level, with most located in Greece (72), France (62), Italy (46), and Spain (40). By 2050 and 2100, an additional 215 cultural heritage assets are expected to be affected under the different RCP scenarios, the majority in Greece (102) and Italy (80). This growing risk underlines the urgent need for adaptation and mitigation strategies, as these monuments are not only irreplaceable historical resources but also central to local identity, tourism, and economic activity across the Mediterranean.

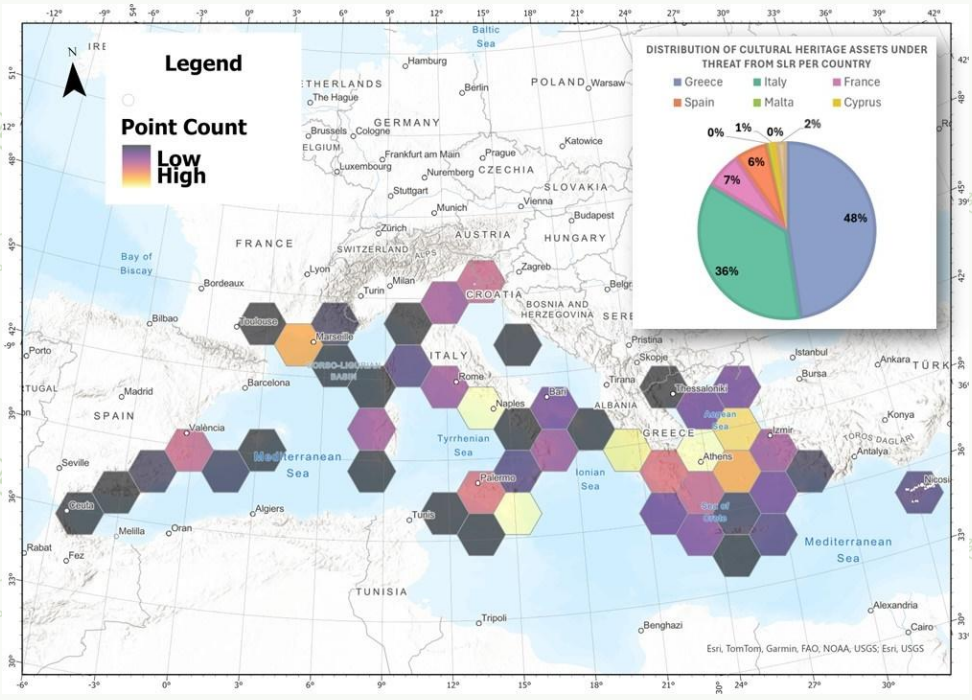

Figure 10: Density of CH sites under threat from SLR in the Mediterranean Region (Low:1-High:16) (Chalkidou et al, 2024).

7.3.3. Application of the Methodology in the pilot areas

Three pilot areas were selected for the application of the methodology, using very high resolution LiDAR derived DEMs instead of Copernicus GLO-30 DEM, namely Ventotene (Italy), Aegina and Epidaurus (Greece). Ventotene's archaeological site is

rather protected due to its rocky coastal morphology from SLR threats as can be seen in the Figures 4 and 5.

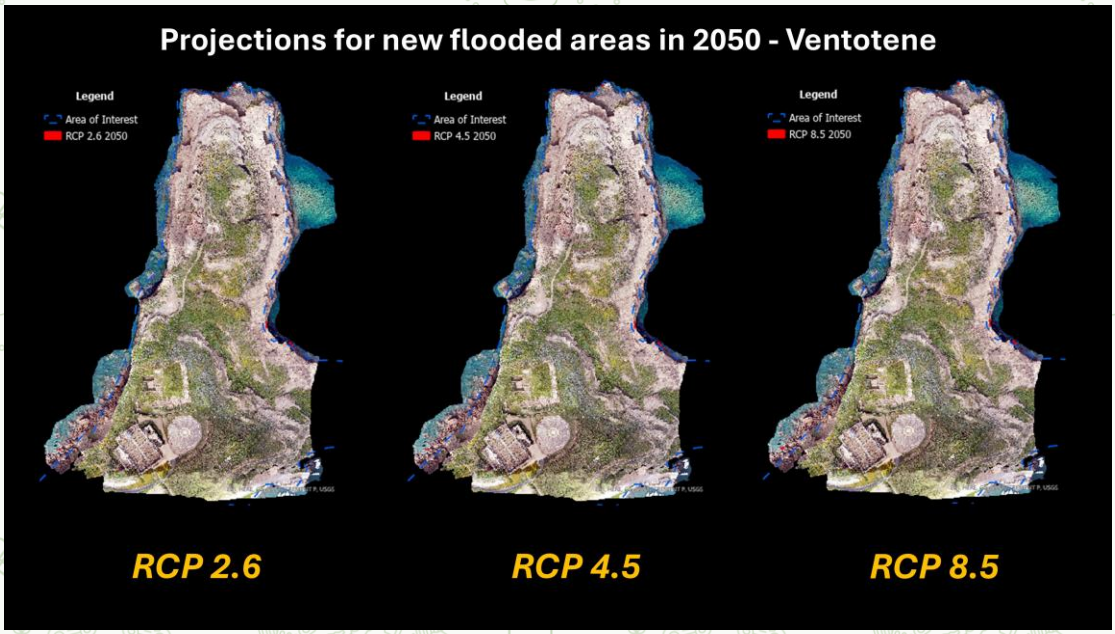

Figure 11: Projection for new flooded areas in 2050 (Ventotene, Italy).

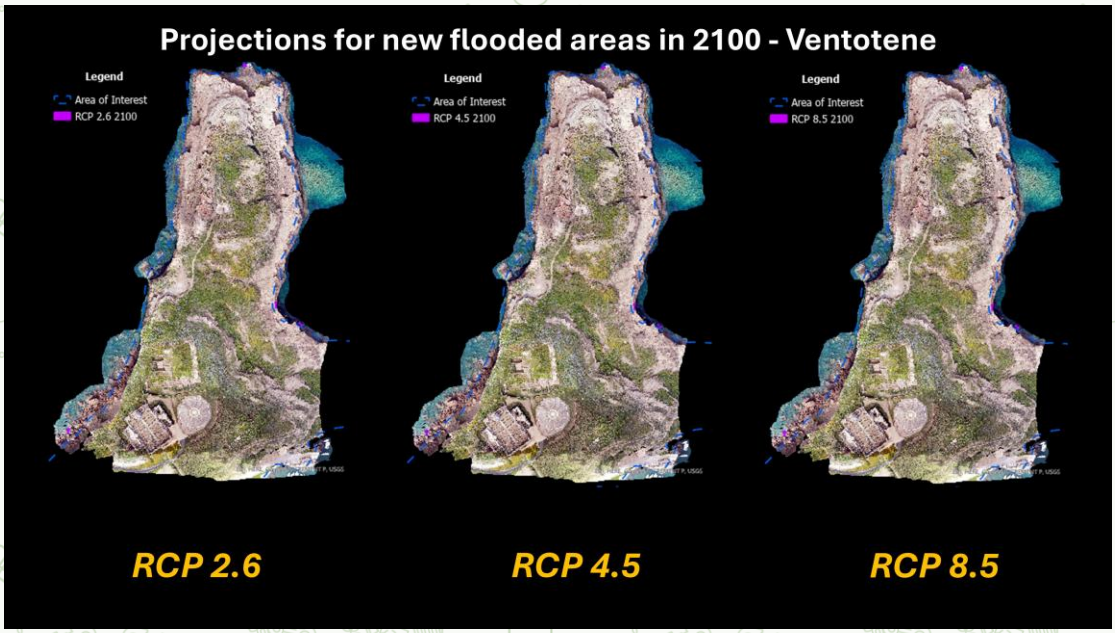

Figure 12: Projection for new flooded areas in 2100 (Ventotene, Italy).

The “Kolona” Archaeological site is located in the island of Aegina in Greece. The application of the proposed methodology calculated the following additional flooded areas per RCP scenario:

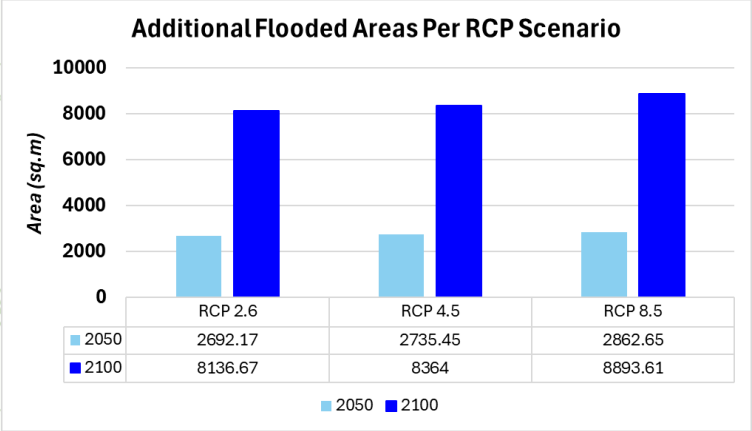

Figure 13: Areas under inundation threat from SLR per RCP scenario(Aegina, Greece).

Figure 14: Flooded areas in 2050 under different RCP scenarios (Aegina, Greece).

The archaeological site of Epidaurus is located in Southern Greece, and more specifically in the Northeastern part of Peloponnisos. It has been declared as a protected site under the Greek Legislation regarding Cultural Monuments in 1965. It covers an area of approximately 6 km2. According to the proposed methodology, we can see that, in contrast to Ventotene, the coastal area around Ancient Epidaurus appears more sensitive to Sea Level Rise under the different RCP scenarios for 2050 and 2100 with an escalating effect depending on the scenario and the year of study. The specific parts of the Epidaurus that face Sea Level Rise risk-related dangers under different RCP scenarios can be viewed in the following Figures:

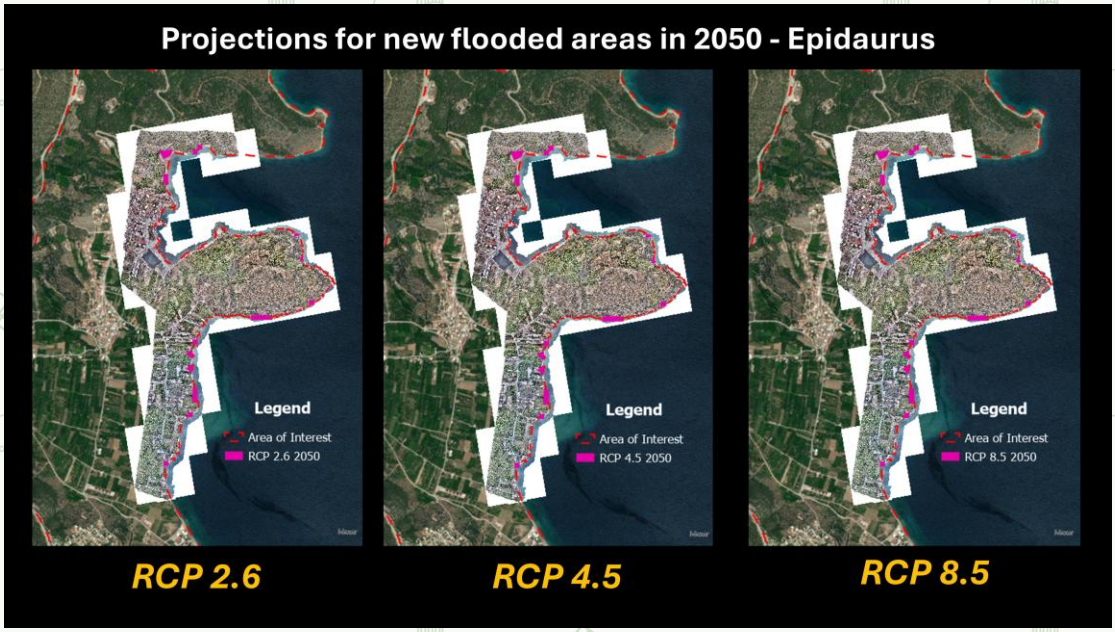

Figure 15: Projection for new flooded areas in 2050 (Epidaurus, Greece).

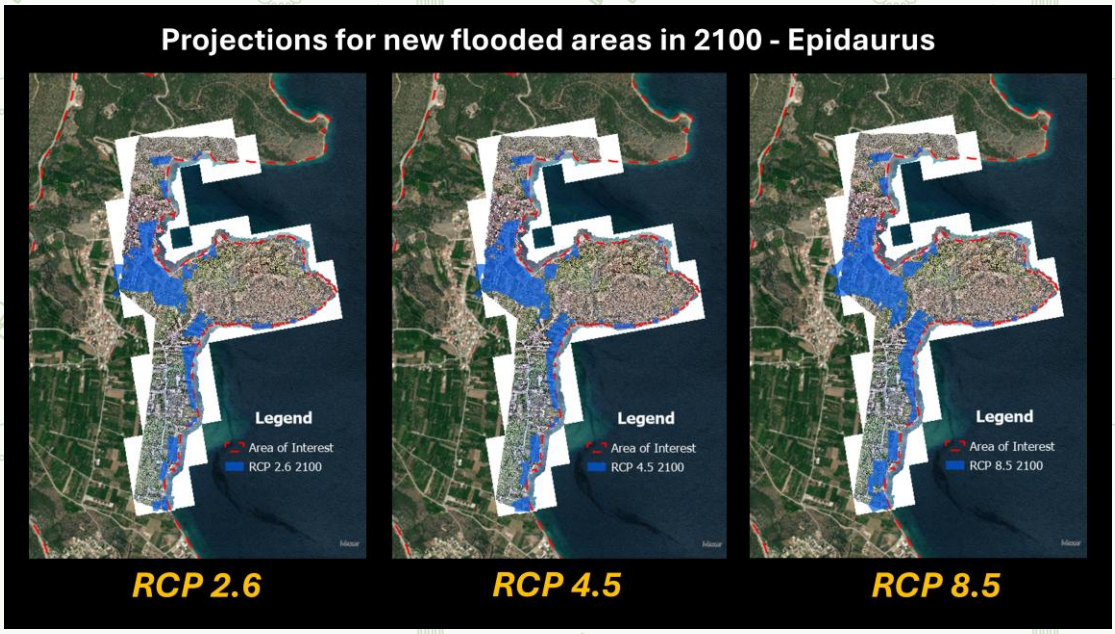

Figure 16: Projection for new flooded areas in 2100 (Epidaurus, Greece).

7.4. References

Chalkidou, S., Georgiadis, C., Roustanis, T., & Patias, P. (2024). A Methodology for Identifying Coastal Cultural Heritage Assets Exposed to Future Sea Level Rise Scenarios. Applied Sciences, 14(16), 7210. https://doi.org/10.3390/app14167210

7.5. Contributors

Developed by: Aristotle University of Thessaloniki, School of Rural and Surveying Engineering, Laboratory of Photogrammetry and Remote Sensing

Date of last update: 10/09/2025

Lead contributors:

- Charalampos Georgiadis
- Sevasti Chalkidou
- Petros Patias
- Themistoklis Roustanis

8. Seismic Fragility Assessment

8.1. Overview

The fragility analysis aims to quantify the probability of exceeding predefined damage states of the Temple of Apollo under varying seismic intensity levels. Following the nonlinear dynamic simulations, fragility curves were developed to express the conditional probability that the structural demand surpasses the corresponding capacity for different levels of ground shaking.

This probabilistic framework provides a direct means to assess seismic vulnerability and to identify critical intensity thresholds beyond which significant damage is expected to occur. In contrast to deterministic assessments, fragility analysis captures the inherent uncertainties in ground motion variability, structural response, and material properties. The resulting curves enable a performance-based interpretation of the monument's seismic resilience.

8.2. Methodological Description

8.2.1. Input Data and Damage States

The fragility assessment was conducted to estimate the probability of exceeding predefined damage states under varying seismic intensities. The procedure builds upon the nonlinear dynamic simulations previously described, where the Temple of Apollo was subjected to five real ground motion records scaled to four peak ground acceleration (PGA) levels: 0.2 g, 0.4 g, 0.6 g, and 0.8 g.

Given that the surviving monolithic column represents the most critical load-bearing element of the structure, it was selected as the primary focus of the fragility analysis. Two response parameters were used to quantify structural demand:

1. The maximum lateral displacement at the top of the column, representing the peak transient deformation during shaking.
2. The residual displacement after ground motion cessation, indicating permanent deformation and potential loss of stability.

These parameters were extracted from the time-history results of the dynamic analyses for each input motion and intensity level.

To characterize the structural performance, three limit states (LS) were defined, corresponding to increasing levels of damage severity:

- LS1 – Minor Cracking: Onset of superficial cracks and negligible stiffness degradation. This state corresponds to small reversible deformations and represents the transition from fully elastic to slightly damaged behaviour.
- LS2 – Moderate Damage: Visible cracking and partial stiffness loss, with localized nonlinearity in the column shaft. This state indicates limited structural distress but no overall instability.
- LS3 – Severe Damage: Extensive cracking and significant residual displacement, suggesting a potential collapse mechanism or loss of vertical load-bearing capacity.

Each limit state was associated with displacement-based thresholds that is presented in Table 1 derived from the nonlinear simulation outputs and engineering judgment, ensuring physical consistency with the observed behaviour of limestone masonry structures.

Table 5: Limitstates and associated damage for columns.

Limit State (LS)	Transverse dislocation (δ_{max})	Residual dislocation (δ_{res})	Damage state
LS1	0.25	0.15	Slight damage
LS2	0.50	0.3	Moderate damage
LS3	1.00	1.00	Severe (extensive) damage

Following Dasiou et al. (2024), the displacement thresholds were normalized with respect to the base diameter of the column (D). The damage criterion was expressed as:

$$P[\delta_{max} > \delta_{max,LS}\ OR\ \delta_{res} > \delta_{res,LS} | PGA] = f(PGA)$$

where δ_{max} denotes the ratio of the top column displacement to the column's base diameter, and δ_{res} denotes the ratio of the residual displacement to the base diameter. This normalization allows direct comparison between the numerical results and literature benchmarks, independent of geometric scale.

In practice, this condition was implemented through a classification algorithm that iterates over all ground motion records and evaluates whether the normalized displacement response exceeds each limit threshold. A binary indicator was assigned to each limit state (1 for exceedance, 0 for non-exceedance). The process was automated using a Python routine, as shown in Figure 17.

```python
# Classify states based on failure criteria
failures_LS1 = np.zeros(len(IM))  # Initialize minor damage
failures_LS2 = np.zeros(len(IM))  # Initialize moderate damage
failures_LS3 = np.zeros(len(IM))  # Initialize severe damage

for i in range(len(IM)):
    if abs(max_Us[i]) >= δmax_ls1 or abs(max_Us_res[i]) >= δres_ls1:
        failures_LS1[i] = 1  # Minor damage
    if abs(max_Us[i]) >= δmax_ls2 or abs(max_Us_res[i]) >= δres_ls2:
        failures_LS2[i] = 1  # Moderate damage
    if abs(max_Us[i]) >= δmax_ls3 or abs(max_Us_res[i]) >= δres_ls3:
        failures_LS3[i] = 1  # Severe damage
```

Figure 17: Python code shown the fragility criteria.

This procedure produced a vector of binary outcomes for each limit state and intensity level, which was subsequently used to compute the empirical probability of damage exceedance. These probabilities formed the input dataset for the statistical fitting of the fragility functions described in Section 8.3.

8.2.2. Intensity Measure and Structural Demand Modeling

The peak ground acceleration (PGA) was used as the seismic intensity measure (IM), while the displacements δ_{max} and δ_{res} served as structural demand parameters. For each intensity level, the computed displacements were compared with the threshold values associated with LS1, LS2, and LS3 to determine whether a given limit state had been exceeded.

The probability of exceeding each damage state was then calculated as the fraction of ground motion records that produced responses above the defined thresholds for each PGA level. This provided the empirical exceedance probability for each limit state and intensity level, forming the basis for subsequent curve fitting.

8.2.3. Lognormal Fitting and Fragility Curve Construction

To model the continuous relationship between seismic intensity and probability of exceedance, a lognormal cumulative distribution function (CDF) was used. The lognormal distribution is widely adopted in fragility analysis because it effectively represents the nonlinear increase in failure probability with seismic intensity while maintaining mathematical simplicity and interpretability.

The fragility function takes the general form:

$$P[DS \geq LSi \mid IM] = \Phi\left(\frac{ln(IM) - \mu_i}{\beta_i}\right)$$

where Φ denotes the standard normal cumulative distribution function, μ_i is the mean (logarithmic median) of the intensity measure corresponding to a 50% probability of exceedance for the *i*-th limit state, and β_i is the standard deviation in logarithmic space (dispersion).

The fitting process was carried out in Python using the SciPy curve fitting routine. The empirical exceedance probabilities derived from the nonlinear analyses were fitted to the lognormal CDF using the function in Figure 18.

```python
# Lognormal CDF function
def lognormal_cdf(IM, mu, beta):
    return norm.cdf((np.log(IM) - mu) / beta)

# Fit the function to empirical probabilities
popt_ls1, _ = curve_fit(lognormal_cdf, IM_values, damage_probs_ls1)
```

Figure 18: Indicative python code for lognormal distribution used for the curve fitting of the fragility curve.

In Figure 18 IM_values correspond to the PGA levels, and damage_probs_ls1 are the empirical exceedance probabilities for LS1. The fitted parameters mu and beta were used to define the median and dispersion of the fragility function for each damage state.

The fitted curves were then plotted to generate the fragility curves, which express the conditional probability of damage exceedance as a function of increasing seismic intensity. Separate sets of curves were produced for both maximum and residual displacement indicators, enabling a comparative interpretation of transient versus permanent deformation sensitivity.

8.3. Outputs and Interpretation of Results

Using the predefined damage states and the fitted lognormal functions, fragility curves were derived to represent the probability of exceeding each limit state (LS1, LS2, LS3) as a function of seismic intensity, expressed in terms of peak ground acceleration (PGA). The resulting curves are illustrated in Figure 19.

These curves demonstrate the progressive increase in structural vulnerability of the monolithic column under escalating seismic demand. For lower PGA values (below 0.2 g), only minor cracking (LS1) exhibits a notable probability of occurrence, indicating that the structure largely remains within the elastic range. As the intensity increases beyond 0.3 g, the probability of moderate damage (LS2) begins to rise sharply, signifying the onset of stiffness degradation and localized cracking.

A more critical transition is observed beyond approximately 0.6 g, where the probability of severe damage (LS3) escalates rapidly, approaching near-total exceedance at higher intensity levels. This indicates the emergence of potential collapse mechanisms and substantial loss of load-bearing capacity.

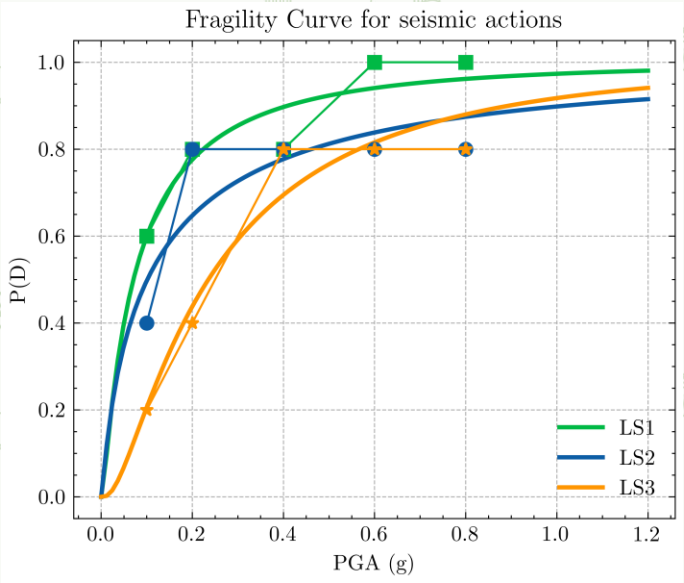

Figure 19: Fragility curves of the monolithic column at the Temple of Apollo, Aegina Kolonna, showing the probability of exceeding the three defined damage states (LS1: minor cracking, LS2: moderate damage, LS3: severe damage) as a function of peak ground acceleration (PGA).

The dispersion parameter (β) of the fitted lognormal models reflects the level of uncertainty in the structural response and the variability in damage initiation under different ground motion intensities. Lower β values correspond to steeper fragility curves, indicating a more consistent and predictable onset of damage, whereas higher β values produce flatter curves that suggest greater uncertainty in the structure's seismic response. In the case of the Temple of Apollo column, the moderate steepness observed for LS2 and LS3 indicates a relatively robust performance up to moderate intensities, followed by a rapid loss of capacity once the deformation limits are exceeded. This trend implies limited redundancy and a brittle transition from elastic to failure states, consistent with the behavior expected for ancient monolithic stone structures.

Overall, the fragility curves capture the nonlinear vulnerability trend of the column, reflecting the transition from elastic to inelastic behaviour as the seismic demand increases. The steeper slope of the LS1 curve compared to LS2 and LS3 highlights the structure's sensitivity to low-intensity excitations, while the convergence of LS2 and LS3 at higher intensities suggests a saturation of damage states once the material reaches its deformation capacity.

These results provide a quantitative basis for evaluating the seismic fragility of the Temple of Apollo's monolithic column, serving as a valuable input for broader risk assessment and preservation strategies within the Aegina Kolonna archaeological complex.

8.4. References

Dasiou, M.-E., Lachanas, C. G., Melissianos, V. E., & Vamvatsikos, D. (2024). Seismic performance of the temple of Aphaia in Aegina island, Greece. Earthquake

Engineering & Structural Dynamics, 53(2), 573–592. https://doi.org/10.1002/eqe.4032

8.5. Contributors

Developed by: National Technical University of Athens

Date of last update: 10/11/2025

Lead contributors:

- Paraskevi Modé
- Denis Istrati

9. Material Analysis

9.1. Overview

As part of an ongoing research programme, this study focuses on the investigation of the mechanical and chemical properties of building stone materials from the archaeological site of Kalapodi, located in Central Greece. The principal aim is to assess the provenance, usage history, and weathering behaviour of the stones employed in the ancient structures, in order to understand the factors influencing their long-term preservation.

A set of four representative stone samples was collected and submitted to the CCM Laboratory of NCSR “Demokritos” for detailed analytical examination. The research follows an integrated, multi-analytical methodology that combines complementary techniques to obtain a comprehensive characterization of the materials. X-ray Diffraction (XRD) was employed to determine the mineralogical composition and crystalline phases present in each sample, providing insights into raw material selection and diagenetic alterations. Scanning Electron Microscopy (SEM) coupled with Energy Dispersive X-ray Spectroscopy (EDS) was used to investigate the microstructure, surface morphology, and elemental composition of the samples, facilitating the identification of alteration layers, inclusions, and compositional heterogeneities. Petrographic analysis under polarized light microscopy was performed to observe the textural and fabric features of the stones, aiding in the differentiation of lithotypes and possible provenance indicators.

In parallel, porosity measurements were conducted to evaluate the pore network characteristics, which play a critical role in moisture transport and frost susceptibility, while uniaxial compression tests were carried out to determine the mechanical strength and assess the integrity of the material under stress conditions. Together, these methods provide a robust dataset for correlating mineralogical, microstructural, and mechanical parameters with environmental and deterioration factors.

The analytical results form part of a broader research framework concerned with the durability of ancient building materials under fluctuating environmental conditions. Particular emphasis is placed on frost-induced deterioration processes, which represent a major risk for the long-term stability of archaeological remains in temperate and mountainous regions. The study thus contributes to developing a systematic approach for evaluating material vulnerability and informing evidence-based conservation and preservation strategies for heritage sites such as Kalapodi.

9.2. Methodological Description

9.2.1. Scanning Electron Microscopy (SEM)

Scanning Electron Microscopy coupled with Energy Dispersive X-ray Spectroscopy (SEM–EDS) was employed to characterize the microstructural features and elemental composition of the ancient building stone samples. The analyses were performed using a FEI Inspect scanning electron microscope equipped with an OXFORD Instruments EDS system, housed at the Institute of Nanomaterials and Nanotechnology, NCSR “Demokritos” (Athens, Greece). The instrument was operated under high-vacuum conditions with an accelerating voltage (kV) of 25.00, a specimen tilt of 0.00°, and a take-off angle of 35.00°. The SUTW Sapphire detector provided high spectral resolution (130.69 eV) and reliable detection sensitivity for both major and minor elements. The amplifier time constant (AmpT) was set to 102.4 μs, and the live acquisition time (Lsec) to 151 s, ensuring adequate counting statistics for quantitative analysis.

Prior to analysis, the samples were mounted on aluminum stubs and coated with a thin conductive carbon layer to prevent surface charging and to enhance image and signal quality. Both secondary electron (SE) and backscattered electron (BSE) imaging modes were utilized to examine surface morphology, textural features, and compositional contrasts. The EDS spectra were processed using standard ZAF (atomic number, absorption, fluorescence) correction procedures to obtain semi-quantitative elemental data. These analytical conditions allowed for detailed characterization of the mineralogical heterogeneity and alteration features of the stone materials.

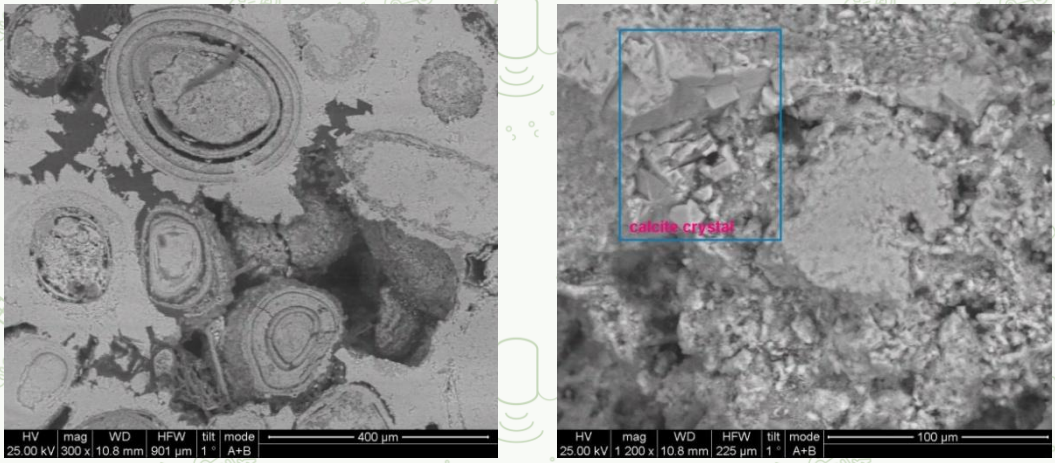

Figure 20: Backscattered Electron (BSE) micrographs of the KT1 sample obtained by SEM analysis, illustrating aragonite crystal formation and textural features of the calcareous sandstone matrix.

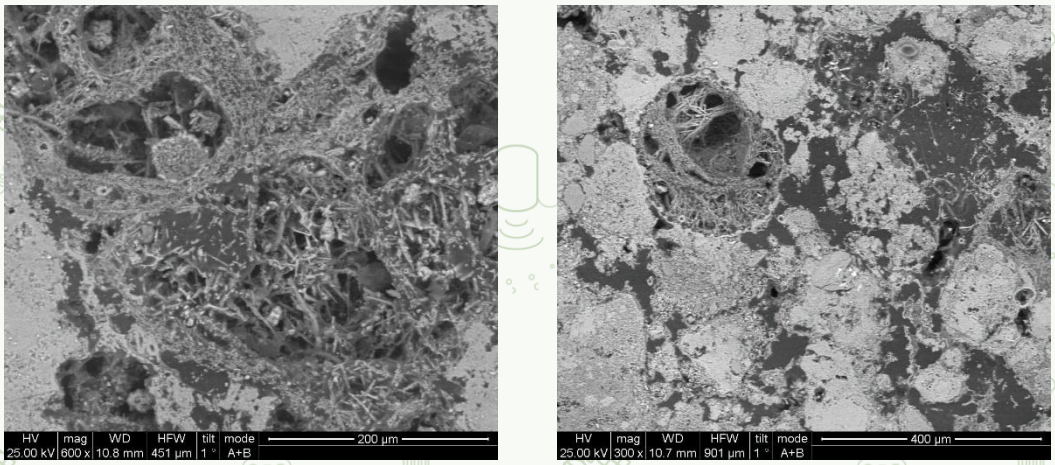

Figure 21: SEM–BSE micrographs of the KT2 sample illustrating organic calcite at 600× magnification (left) and a detailed 300× view (right) showing Ca- and C-rich areas within the limestone matrix.

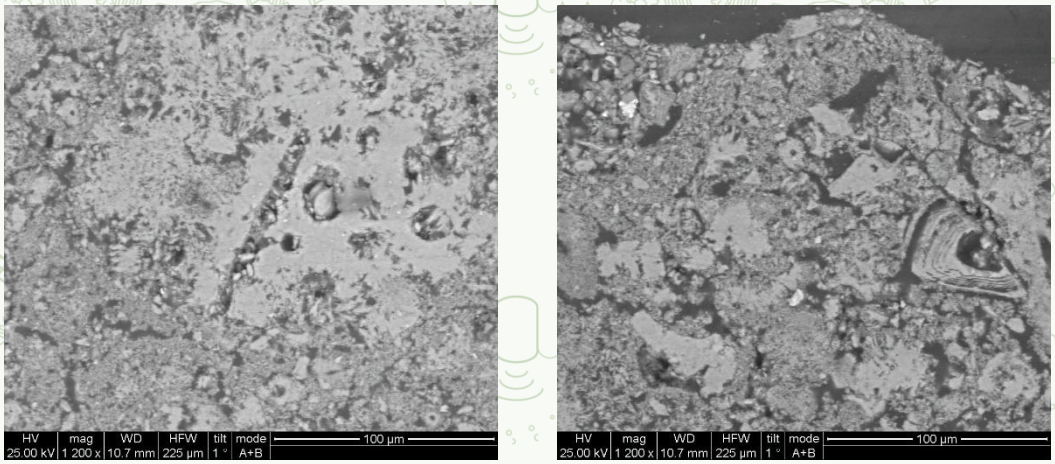

Figure 22: SEM–BSE micrographs of the SB1 sample at 1200× magnification illustrating surface features: (left) well-formed calcite crystals and dolomite phases and fossil inclusions close to the surface (right).

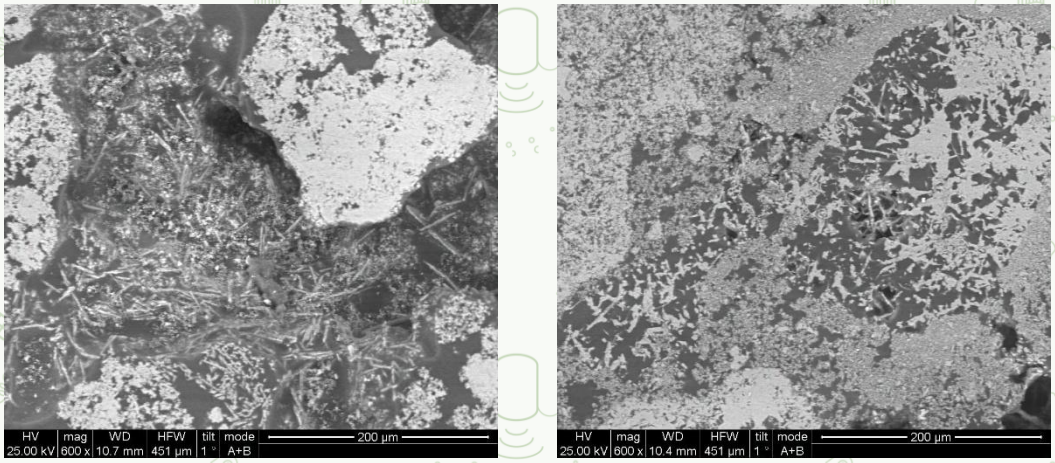

Figure 23: SEM–BSE micrographs of the SB2 sample at 600× magnification illustrating calcite crystal morphology (left) and areas containing organic matter near the surface (right).

The elemental composition of representative stone samples was determined through SEM–EDS analysis under the analytical conditions described above. The results indicate significant compositional differences between the examined specimens, reflecting variability in raw material sources and possible diagenetic or alteration processes.

Samples KT1 and KT2 are both characterized by high calcium oxide (CaO) contents (80.32 wt.% and 94.30 wt.%, respectively), confirming their calcareous nature. Minor amounts of silica (SiO_2: 10.34 wt.% in KT1 and 3.31 wt.% in KT2) and alumina (Al_2O_3: 2.92 wt.% in KT1) were also detected, together with traces of magnesium oxide (MgO: 1.63–1.46 wt.%) and phosphorus pentoxide (P_2O_5: 1.73 wt.% in KT1). The presence of sulfur trioxide (SO_3: 2.02 wt.%) and chlorine (Cl: 1.03–0.93 wt.%) may be associated with secondary alteration phases such as gypsum or soluble salts formed during weathering.

In contrast, samples SB1 and SB2 show a somewhat different compositional profile. Sample SB1 exhibits a mixed silicate–carbonate composition, dominated by CaO (55.15 wt.%) and SiO_2 (27.55 wt.%), with appreciable quantities of Al_2O_3 (6.91 wt.%), MgO (4.28 wt.%), and Fe_2O_3 (3.83 wt.%). The presence of minor K_2O (1.11 wt.%) and Cl (1.17 wt.%) further suggests the occurrence of aluminosilicate or feldspathic components, likely corresponding to clay or detrital impurities within the stone matrix. Sample SB2, by contrast, is predominantly calcareous, with CaO reaching 96.53 wt.% and only minor MgO (2.35 wt.%) and SiO_2 (1.12 wt.%), indicating a nearly pure limestone composition with limited silicate inclusions.

Overall, the SEM–EDS analyses confirm that the examined building stones primarily consist of calcitic materials, with variable proportions of silicate and aluminosilicate phases that may reflect local geological heterogeneity or weathering effects. The minor presence of sulfur and chlorine-bearing compounds suggests potential surface alteration related to environmental exposure and salt crystallization phenomena.

9.2.2. X-Ray Diffraction (XRD)

The mineralogical composition was determined by X-ray Diffraction (XRD) using a Siemens D500 diffractometer equipped with a Cu-Kα radiation source (λ=1.5406 Å). The measurements were carried out over a 2θ range of 2-60°, with a scanning step of 0.03° per 3 seconds.

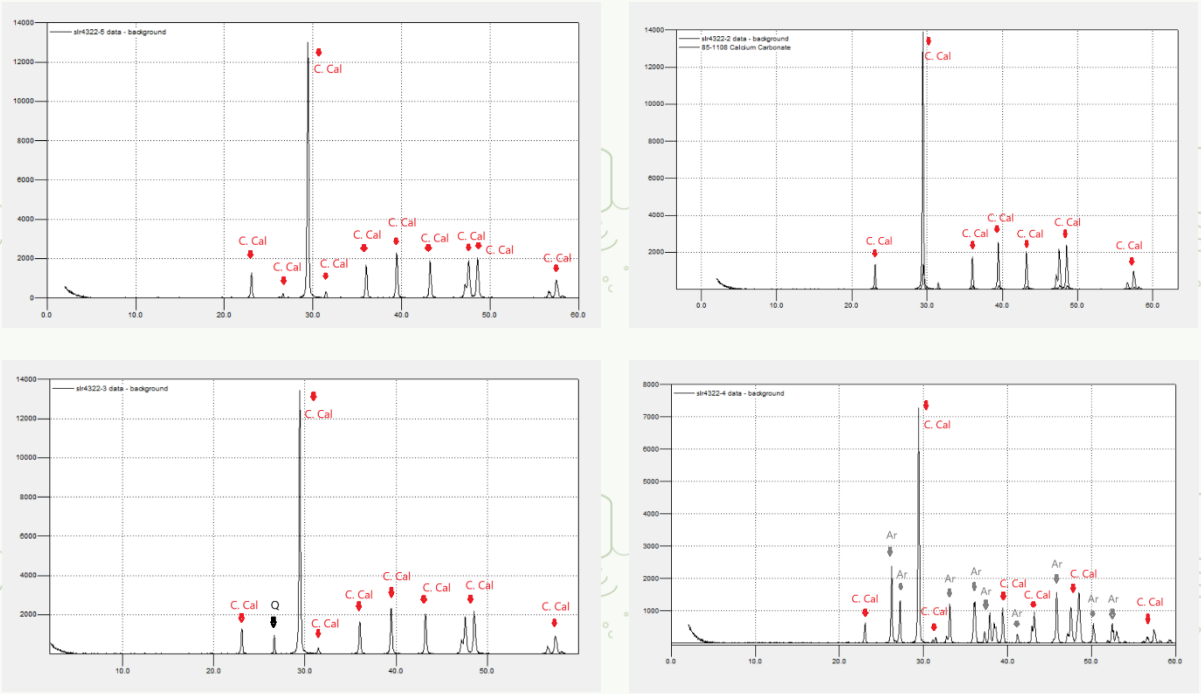

Figure 24: Characteristic diffractograms of the four stone samples analysed.

9.2.3. Stereomicroscopic Analysis

In addition to the analytical techniques described above, stereomicroscopic examination was conducted to obtain preliminary visual and morphological information on the stone samples prior to detailed microanalytical investigation. Observations were carried out using a stereomicroscope under reflected light, allowing for the assessment of surface features, textural heterogeneity, grain morphology, and visible alteration phenomena. This non-destructive method provided valuable insights into the macroscopic and mesoscale characteristics of the materials, such as fissures, cavities, inclusions, mineral aggregates, and weathering crusts. The stereomicroscopic study also served as a preparatory stage for subsequent analytical procedures, assisting in the selection of representative areas for SEM–EDS and petrographic analyses. By correlating the visual observations with the mineralogical and microstructural data obtained from other techniques, the stereomicroscopic examination contributes to a more comprehensive understanding of the physical condition and deterioration patterns of the Kalapodi stone materials.

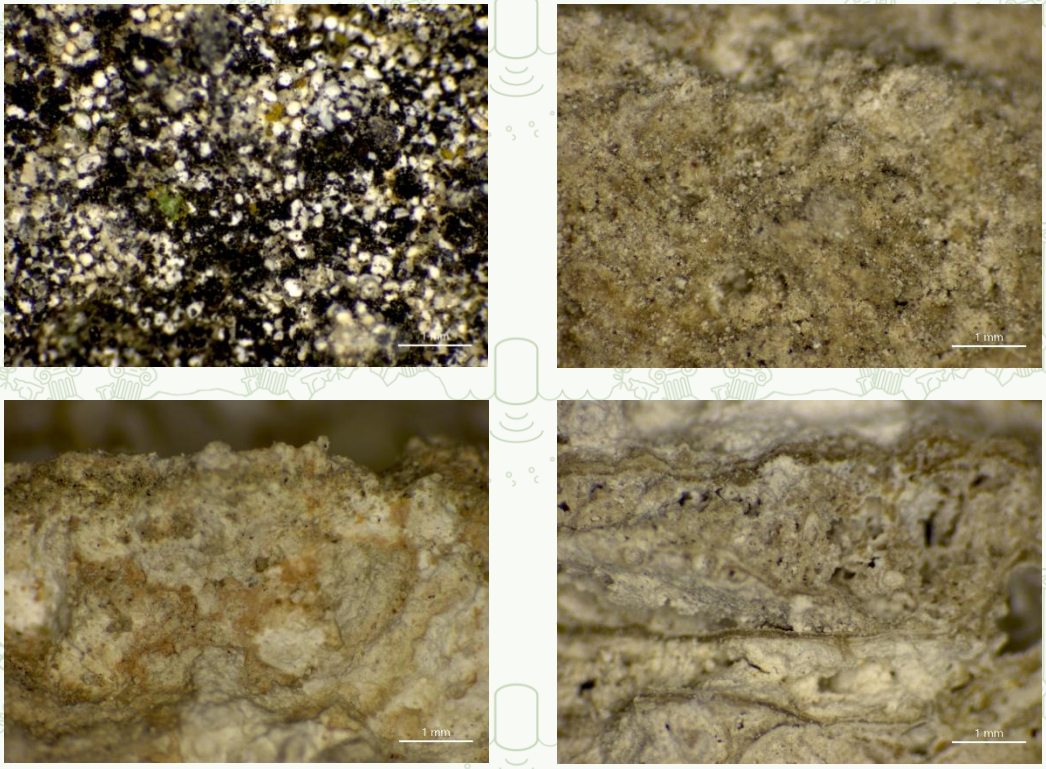

Figure 25: Characteristic stereomicroscope images of the samples. Clockwise from upper left: KT1, KT2, SB2, SB1.

9.2.4. Mechanical properties

To evaluate the mechanical performance and physical integrity of the building stones from the Kalapodi archaeological site, a series of tests were conducted to determine their total porosity and compressive strength. These parameters are critical for understanding the stones' durability, resistance to environmental stress, and overall suitability as construction materials. The total porosity was determined by the buoyancy method, which involves measuring the dry, saturated, and hydrostatic weights of the specimens to calculate the open pore volume and the percentage of interconnected porosity. This non-destructive test provides important information on the pore structure and water absorption capacity, both of which significantly influence the material's susceptibility to frost damage, salt crystallization, and other weathering mechanisms.

In parallel, uniaxial compression tests were performed to assess the mechanical strength and deformation behavior of the stones under applied stress. The samples were subjected to a steadily increasing axial load until failure, and the maximum load-bearing capacity was recorded. These measurements enable the determination of key mechanical properties such as compressive strength, elasticity, and fracture characteristics, providing a quantitative basis for evaluating the stones' performance in their architectural context. Together, the porosity and compression data contribute to a comprehensive understanding of the physical and mechanical stability of the materials, supporting the broader objective of assessing

their vulnerability to environmental degradation and informing conservation strategies for the site.

A. Porosity

The total porosity of the stone samples was determined using the buoyancy (water saturation) method, a standard procedure for evaluating the open pore volume and water absorption capacity of porous materials. This test provides critical information about the pore structure, which directly influences the durability, permeability, and mechanical behavior of the stones. The method is based on comparing the dry, saturated, and immersed weights of each specimen, from which the total porosity (Po) is calculated according to the following formula:

$$Po=100\%\times(Ws-Wd)/(Ws-Wi)$$

where W_d is the air-dry mass (g), W_s is the water-saturated mass (g), and W_i is the mass of the specimen when immersed in water (g). The difference between these values reflects the volume of interconnected pores accessible to water. This method allows for the assessment of open porosity, which is a key parameter in understanding the stone's susceptibility to moisture uptake, freeze–thaw cycles, and salt crystallization, all of which are major contributors to the deterioration of calcareous building materials.

Table 6: The results of the porosity test.

Samples	Dry mass	Saturated mass	Immersed in water	Po
SB1	189.24	226.79	113.03	0.33
Sb2	70.71	85.47	38.07	0.31
KT1	21.42	25.22	10.38	0.26
KT2	29.50	37.18	14.91	0.34

B. Compression testing

The uniaxial compressive strength of the stone samples was determined using an Instron universal testing machine with a maximum load capacity of 100 kN. The tests were carried out under controlled laboratory conditions in accordance with standard procedures for natural stone testing. Each specimen was positioned between two parallel steel platens, and a constant displacement rate of 150 µm/s was applied until mechanical failure occurred. During loading, both the applied force and axial deformation were continuously recorded, allowing for the determination of compressive strength and deformation behavior. This test provides a direct measure of the stone's load-bearing capacity and resistance to mechanical stress, parameters that are essential for evaluating its structural integrity and performance in situ. The resulting data were used to assess differences in mechanical behavior between lithotypes and to relate strength values to the stones' mineralogical composition, porosity, and weathering condition.

The compressive strength of the stone specimens was determined through uniaxial compression testing using a calibrated Instron 100 kN universal testing machine. Prior to testing, the dimensions of each cubic specimen were carefully measured on the top and bottom faces to ensure accuracy in cross-sectional area determination. Each specimen was then placed between the compression platens of the testing machine and aligned precisely, so that the load was uniformly distributed across the entire surface of contact.

The load was applied gradually and without shock, at a controlled and continuous rate, ensuring that failure occurred within 30 to 90 seconds, in accordance with standard testing protocols for natural stone. During the test, the maximum load (F_{max}) applied at failure was recorded in newtons (N). After the test, the fractured specimens were removed and their surfaces cleaned to allow for further examination of fracture morphology and failure behavior.

The compressive strength ($\sigma_{c,max}$) of each sample was calculated using the following equation:

$$\sigma_{c,\max} = \frac{F_{\max}}{b \times d}$$

where F_{max} is the maximum applied load (N), and b and d are the specimen's width and depth (mm), respectively. This parameter represents the material's maximum load-bearing capacity under uniaxial stress and provides a key indicator of the mechanical integrity and durability of the stone.

The compressive strength results provide valuable insight into the mechanical performance and deterioration behavior of the stone materials from Kalapodi. Variations in strength values among the different lithotypes reflect differences in mineralogical composition, porosity, and textural characteristics. Stones with higher calcite content and more compact microstructures generally exhibited greater load-bearing capacity, whereas samples with elevated porosity or microcracking showed reduced mechanical strength, consistent with their higher susceptibility to environmental decay. The observed correlation between porosity and compressive strength highlights the critical role of the pore network in governing mechanical stability, moisture migration, and frost resistance. These findings not only elucidate the material's current preservation state but also provide essential data for assessing the long-term structural performance of the architectural remains. Ultimately, the mechanical characterization contributes to the development of targeted conservation strategies, ensuring that any intervention or restoration work is compatible with the physical properties of the original materials.

Table 7: The results of the compression stress.

Samples	Meas. 1	Meas. 2	Meas.3	Meas. 4	Meas. 5	Average
KT1	19	19.5	26	-	-	1.73 MPa
KT2	7	-	-	-	-	0.11 MPa

SB1	22	27	28	Invalid	Invalid	2.27 MPa
SB2	21	20	10	12	-	1.14 MPa

9.3. Outputs and Interpretation of Results

At the Kalapodi sanctuary, X-ray Diffraction (XRD) and Scanning Electron Microscopy (SEM) analyses reveal that the classical temple drum (KT1) is composed of calcareous sandstone, dominated by calcite and aragonite. The surface shows advanced weathering features and clear evidence of biological colonization, including lichens observed under the optical microscope, indicative of prolonged environmental exposure and biochemical alteration. The high carbonate content of this lithotype makes it particularly prone to chemical dissolution and biogenic weathering, processes commonly intensified under fluctuating moisture and temperature conditions.

Sample KT2 corresponds to a porous limestone, also rich in calcite, whose elevated porosity enhances water absorption and salt crystallization, leading to progressive microcracking and mechanical fatigue. Similarly, the spolia samples SB1 and SB2, derived from earlier construction phases and later reused, are porous biogenic limestones, composed primarily of calcite and biogenic calcite. Their texture and inclusions suggest sedimentary deposition and subsequent reworking, reflecting both geological variability and the adaptive reuse of locally available materials in ancient construction practices.

Pending petrographic analysis is expected to refine the mineralogical interpretation, identifying potential shell fragments, organic residues, or minor mineral inclusions that could provide further evidence for provenance and depositional environment. Preliminary correlations with regional geological mapping strongly support the local sourcing of building stones, consistent with the abundance of limestone and sandstone formations in the surrounding area.

Overall, the building materials of Kalapodi exhibit high calcite content and significant porosity, characteristics that critically influence their susceptibility to moisture-related decay, frost action, and biological colonization. These findings highlight the complex interplay between mineralogical composition, microstructural properties, and environmental stressors, providing essential insights into the mechanisms of stone degradation in archaeological contexts. From a conservation perspective, this understanding supports the development of targeted preservation strategies that prioritize moisture management, biological control, and the use of compatible repair materials. More broadly, the study underscores the value of integrating material science with environmental assessment to inform sustainable conservation planning, contributing to the long-term protection and interpretation of cultural heritage sites such as Kalapodi.

9.4. References

Cappai, M., Casti, M., & Pia, G. (2024). Salt Crystallization in Limestone: Materials Decay and Chemomechanical Approach. Materials, 17(16), 3986. https://doi.org/10.3390/ma17163986

Gomez-Heras, M., McCabe, S. (2015). Weathering of stone-built heritage: A lens through which to read the Anthropocene. Anthropocene, Volume 11, 1-13, https://doi.org/10.1016/j.ancene.2015.12.003

Negishi, N., Inaba, T., Miyazaki, Y. et al. (2021). Aqueous mechano-bactericidal action of acicular aragonite crystals. Sci Rep 11, 19218 (2021). https://doi.org/10.1038/s41598-021-98797-w

Rives, V., & Talegon, J. G. (2006). Decay and Conservation of Building Stones on Cultural Heritage Monuments. Materials Science Forum, 514–516, 1689–1694. https://doi.org/10.4028/www.scientific.net/msf.514-516.1689

Smith, B. J., Gomez-Heras, M., & McCabe, S. (2008). Understanding the decay of stone-built cultural heritage. Progress in Physical Geography: Earth and Environment, 32(4), 439-461. https://doi.org/10.1177/0309133308098119

Smith, B.J., McCabe, S., McAllister, D. et al. A commentary on climate change, stone decay dynamics and the 'greening' of natural stone buildings: new perspectives on 'deep wetting'. Environ Earth Sci 63, 1691–1700 (2011). https://doi.org/10.1007/s12665-010-0766-1

9.5. Contributors

Developed by: German Archaeological Institute at Athens, DAI, Artemios Oikonomou

Date of last update: 10/11/2025

Lead contributors:

- Artemios Oikonomou
- Kely Christodoulou
- Themistoklis Bilis

10. Shoreline Changes

10.1. Overview

Coastal zones are among the most dynamic landscapes on Earth, constantly shaped by natural processes such as tides, waves, sediment transport, and human activities. Monitoring shoreline changes is crucial for understanding coastal dynamics, managing erosion, protecting infrastructure, and supporting ecosystem conservation. High-resolution satellite imagery, combined with advanced image processing techniques, offers a powerful approach to quantify these dynamics with unprecedented spatial and temporal precision.

This model focuses on shoreline extraction for Triquetra Cultural Heritage (CH) sites, leveraging high resolution multispectral satellite time series data, deriving Normalized Difference Water Index (NDWI) images to map subpixel coastline positions. PlanetScope data, accessible through Planet's Explorer platform, provide high-temporal, high-spatial resolution optical imagery suitable for detailed shoreline change analysis. The model developed in this study not only extracts subpixel shorelines but also generates shore-normal transects to quantify coastline changes along perpendicular profiles.

The model's primary objective is to derive accurate coastline positions over time and provide metrics to assess shoreline dynamics, including dynamic changes (which might refer to erosion and accretion). The methodology integrates remote sensing preprocessing, NDWI calculation, subpixel contour extraction, and transect-based analysis, producing outputs that are both spatially precise and suitable for temporal comparison.

By employing these techniques, the study enables a fine-grained analysis of coastal processes at Triquetra CH sites, supporting long-term coastal monitoring and management initiatives.

10.2. Methodological Description

The methodological framework for shoreline extraction consists of several key stages: acquisition and preprocessing of high-resolution satellite imagery, NDWI computation, subpixel coastline extraction, transect generation, and analysis of coastal dynamics. Each step ensures data quality and maximizes the accuracy of the resulting shoreline positions (Lappe et al. 2022).

10.2.1. Data Sources

The primary data source for this study is PlanetScope imagery obtained through Planet's Explorer platform under a dedicated Planet data proposal. PlanetScope provides multispectral imagery at a spatial resolution of approximately 3–5 meters, with four spectral bands: blue, green, red, and near-infrared (NIR). The high spatial resolution is essential for capturing small-scale coastal features and allows for subpixel interpolation to improve the accuracy of shoreline delineation.

NDWI calculations are performed on the green and NIR bands, which are most sensitive to the presence of water. Additionally, ancillary data such as shoreline reference layers, and digital elevation models (DEMs) may be used for validation or to enhance transect analysis. Temporal stacks of PlanetScope images enable the assessment of shoreline dynamics over multiple acquisition dates.

A. PlanetScope 4-band bundle

PlanetScope imagery is provided by a constellation of CubeSats operated by Planet Labs, delivering high-frequency, high-resolution Earth observation data. PlanetScope's high temporal revisit frequency is critical for capturing short-term

coastal changes and for minimizing cloud coverage issues. The 4-band bundle includes 4 multispectral bands: Blue (455–515 nm), Green (500–590 nm), Red (590–670 nm), and Near-Infrared (780–860 nm); these spectral bands support the derivation of water indices such as NDWI. PlanetScope scenes are available at a spatial resolution of approximately 3–5 m, with near-daily global coverage depending on orbital characteristics and atmospheric conditions.

For the present study, only PlanetScope images with a reported cloud cover below 20% were selected in order to ensure sufficient data quality and minimize atmospheric contamination effects. The selected imagery, delivered as orthorectified surface reflectance products, includes all radiometric and geometric metadata necessary for subsequent calibration and analysis.

B. Auxiliary Data

Additional datasets such as base-shoreline was used to provide context for interpretation of coastal change rates. An OpenStreetMap (OSM) global shoreline dataset from 2020 is used, clipped to the CH sites extent and buffered by 10 km to ensure inclusion of nearshore environments.

10.2.2. Data preprocessing

Effective preprocessing is crucial for reliable shoreline extraction. The raw PlanetScope images undergo several standard procedures to correct radiometric distortions, remove noise, and enhance water-land separation.

A. Radiometric correction

Radiometric correction ensures that pixel values accurately represent surface reflectance. The acquired PlanetScope Level 3 imagery is already ortho-corrected and radiometrically calibrated.

B. Water Index Calculation

The Normalized Difference Water Index (NDWI) is calculated using the formula (Xu 2006; Gao 1996; McFeeters 1996):

$$NDWI = \frac{Green - NIR}{\text{Green} + \text{NIR}}$$

This index enhances the water signal while suppressing vegetation and soil reflectance. For this study, NDWI images are computed for each single PlanetScope scene to improve separation of water from land surfaces. The resulting NDWI rasters (TIFs) serve as the primary input for subpixel coastline extraction.

C. NDWI Cleaning and Noise Removal

Binarized NDWI rasters are further processed to remove small isolated pixel clusters that may cause spurious coastline detections. Morphological operations, such as opening and closing filters, are applied to produce clean water masks suitable for vectorization.

10.2.3. Subpixel Coastline Extraction

To increase the spatial accuracy beyond the native resolution of PlanetScope imagery, subpixel coastline extraction is performed. This approach estimates shoreline positions between discrete pixels using interpolation and thresholding techniques.

A. Thresholding

Based on the computed NDWI images (see 10.2.2 B), binary land–water masks were subsequently generated to delineate the boundary between terrestrial and aquatic surfaces. For this purpose, Otsu's adaptive thresholding method (Otsu 1979) is applied to each NDWI scene to automatically identify the optimal threshold value. Otsu thresholding is an automated, unsupervised technique that minimizes intra-class variance and ensures consistent classification between water and non-water pixels across images. The resulting binary masks were then used to extract the land–water interface, which we refer to as the shoreline in the context of this study.

B. Linear Interpolation

Once the water and land pixels are classified, linear interpolation is applied along the boundary of water and land pixels to locate the shoreline with subpixel precision. This technique considers the reflectance values of neighboring pixels to refine the estimated coastline position.

C. Smoothing and Polygon Generation

The extracted shorelines are converted into polygons representing land extent. A one-dimensional Gaussian filter is applied to smooth the land polygon and reduce local irregularities, ensuring the derived shorelines are suitable for transect analysis.

10.2.4. Shore-normal Transect Generation

To quantify shoreline change, shore-normal transects are generated perpendicular to the coastlines. Transects provide a consistent framework to measure spatial shifts along defined coastal profiles.

A. Transect Creation

Transects are generated with lengths of up to 3 km and sampling intervals of 10–100 meters, depending on the coastal morphology. These transects are anchored at the smoothed shoreline and extend offshore and inland to capture full water-land transitions.

B. Intersection with Shorelines

For each acquisition date, intersections between shorelines and transects are calculated. These intersection points provide spatial metrics of coastal position along each transect, enabling the computation of shoreline change rates.

C. Data Cleaning and Validation

Transects intersecting non-coastal features, such as islands or anthropogenic structures, are filtered out. Visual inspection and automated checks ensure the reliability of transect-based measurements.

10.2.5. Coastline Change Analysis

Coastline dynamics are quantified using temporal sequences of transect intersections. Key analyses include calculation of erosion or accretion rates, identification of hotspots of rapid change, and statistical summary of coastal behavior.

A. Change Metrics

The shoreline displacement along each transect is calculated as the difference between consecutive shoreline positions. Annualized change rates are derived for comparison with historical trends or to assess the impact of extreme events.

B. Uncertainty Assessment

Uncertainty in shoreline positions arises from image resolution, tidal variation, and threshold selection. Subpixel extraction reduces positional uncertainty, but residual errors are estimated using sensitivity analyses with varying thresholds and interpolation schemes.

C. Visualisation and Mapping

Shoreline changes are visualized as vector layers overlaid on base imagery, providing intuitive representation of erosion and accretion patterns. Transect-based plots show quantitative displacement along the coast, allowing identification of localized processes.

10.3. Outputs and Interpretation of Results

The outputs of this model are designed to provide actionable insights into coastal dynamics at Triquetra CH sites. They include vector and raster layers, quantitative metrics, and visualizations that collectively support coastal management and scientific analysis.

10.3.1. Vector and Raster Outputs

The primary outputs include subpixel shoreline vectors for each acquisition date, smoothed land polygons, and shore-normal transect layers. Raster outputs include NDWI and MNDWI images, cleaned water masks, and interpolated distance grids along transects.

10.3.2. Quantitative Metrics

Transect intersections allow calculation of key metrics such as shoreline displacement, erosion and accretion rates, and variability along the coast. Summary statistics provide insights into general trends and highlight areas experiencing significant changes. Temporal analysis enables identification of episodic events,

such as storm-driven erosion, and comparison with baseline conditions (Ottinger et al. 2025).

10.3.3. Interpretation of Coastal Processes

The derived data allow interpretation of both short-term and long-term coastal dynamics. For instance, areas showing repeated landward shifts indicate ongoing erosion, while seaward shifts may reflect sediment deposition or shoreline stabilization measures. Transect spacing enables capturing local heterogeneity in coastal processes, ensuring robust analysis even in complex coastal environments.

10.3.4. Applications

The outputs of this model can inform coastal zone management, infrastructure planning, hazard assessment, and ecosystem conservation. Accurate, high-resolution shoreline data support decisions related to erosion mitigation, habitat protection, and long-term monitoring of coastal resilience.

10.3.5. Limitations and Future Work

Despite the high spatial resolution and subpixel accuracy achieved with PlanetScope data, the methodology still has several limitations. PlanetScope imagery may be affected by cloud cover, tidal variability, and seasonal environmental factors, all of which can introduce noise into shoreline delineation. Subpixel interpolation improves positional accuracy, but residual uncertainties remain due to image resolution, reflectance variability, and threshold sensitivity. As part of the initial pre-work, longer-term shoreline analyses were conducted using Landsat (30 m) and Sentinel-1 SAR (10 m) time series data. These datasets provided valuable temporal depth — over 30 years for the Landsat archive and approximately 10 years for Sentinel-1 — enabling the investigation of long-term coastal trends. However, the relatively coarse spatial resolution of these sensors limited their ability to capture small-scale morphological changes, particularly at fine-grained cultural heritage sites where subtle shoreline dynamics are of critical importance.

The present PlanetScope-based approach therefore complements these earlier datasets by offering higher spatial precision, albeit over shorter temporal ranges. Future work could integrate multi-sensor approaches that combine the temporal richness of Landsat and Sentinel-1 with the spatial detail of PlanetScope or other very-high-resolution sensors. Additional improvements could include machine learning classifiers for enhanced water–land discrimination, data fusion with UAV or LiDAR surveys for validation, and coupling with hydrodynamic models to interpret shoreline dynamics more mechanistically.

10.4. References

Gao, BC. 1996. “NDWI—a Normalized Difference Water Index for Remote Sensing of Vegetation Liquid Water from Space.” Remote Sensing of Environment 58: 257–66.

Lappe, Ronja, Tobias Ullmann, and Felix Bachofer. 2022. “State of the Vietnamese Coast—Assessing Three Decades (1986 to 2021) of Coastline Dynamics Using the Landsat Archive.” Remote Sensing 14 (10): 2476. https://doi.org/10.3390/rs14102476

McFeeters, S. K. 1996. “The Use of the Normalized Difference Water Index (NDWI) in the Delineation of Open Water Features.” International Journal of Remote Sensing 17 (January 2015): 1425–32. https://doi.org/10.1080/01431169608948714

Otsu, Nobuyuki. 1979. “A Threshold Selection Method from Gray-Level Histograms.” IEEE Transactions on Systems, Man, and Cybernetics 9 (1): 62–66.

Ottinger, Marco, Felix Bachofer, Sophie Reinermann, Aristeidis Georgoulias, Prodromos Zanis, and Juliane Huth. 2025. Analyzing Climate Change Impacts on European Cultural Heritage Sites Using High-Temporal-Resolution Satellite Time Series. https://doi.org/10.13140/RG.2.2.17614.37449

Xu, Hanqiu. 2006. “Modification of Normalised Difference Water Index (NDWI) to Enhance Open Water Features in Remotely Sensed Imagery.” International Journal of Remote Sensing 27 (14): 3025–33. https://doi.org/10.1080/01431160600589179

10.5. Data Specification

PlanetScope data for this study was part of a Planet Data proposal. Attribution: Planet Team (2022). Planet Application Program Interface: In Space for Life on Earth. San Francisco, CA. https://api.planet.com

10.6. Contributors

Developed by: German Aerospace Center (DLR)

Date of last update: August 20, 2025

Lead contributors:

- Marco Ottinger
- Felix Bachofer

11. Flood Model

11.1. Overview

This risk model provides a scalable framework for pluvial flood risk assessment, specifically applied to cultural heritage sites. It integrates field data acquisition with hydrological and hydraulic modelling at both catchment and local scales. The model quantifies flood hazards by generating synthetic design hyetographs, which serve as primary input for two-dimensional (2D) Rain-on-Grid (RoG) hydraulic simulations. Key inputs include spatially distributed rainfall data, high-resolution Digital Elevation Models (DEMs), land cover information for deriving infiltration parameters (Soil Conservation Service Curve Number) and Manning's roughness

coefficient. The primary outputs are detailed inundation maps that provide the main hydraulic properties, namely water depths and flow velocities.

11.2. Methodological Description

The methodological framework systematically integrates data acquisition and hydrological/hydraulic modelling to assess pluvial flood risk.

11.2.1. Design Hyetograph Generation

Design rainfall curves are fundamental tools in hydrological design and flood risk assessment, establishing the relationship between rainfall intensity, timescale, and return period to estimate design rainfall events.

A. Probabilistic Model for Design Rainfall

The probabilistic model for design rainfall, specifically for Greece, is based on the revised methodology of Iliopoulou et al. (2024). This model quantifies the relationship between rainfall intensity x (in mm/h), the timescale k (in hours), and the return period T (in years) as follows:

$$x = \lambda * \cdot \frac{\left[\left(\frac{T}{\beta *}\right)^{\xi} - 1\right]}{\left(1 + \frac{k}{\alpha}\right)^{\eta *}} \quad (1)$$

In this equation, α = 0.18 h and ξ = 0.18 are dimensionless constants applied uniformly across the country. The parameters $\lambda *$ (mm/h), $\beta *$ (years), and $\eta *$(dimensionless) vary spatially, derived from a 5 km resolution grid covering the entire country (Koutsoyiannis et al., 2024). Catchment-specific parameter values are obtained through an area-weighted averaging of these grid parameters within a Geographic Information System (GIS) environment.

B. Construction of Design Rainfall Events

For a specified return period, such as 100 years, design rainfall events are constructed using the Alternating Blocks method, which partitions the total rainfall depth into sequential sectional depths with the maximum depth centrally located. Remaining blocks are allocated alternately in descending order to the left and right of the central block.

Design rainfall events are constructed for a total duration of 12 or 24 hours depending on the area, selected to exceed the catchment's concentration time. Equation (2) provides point rainfall intensities. For hydrological analyses, these point intensities are converted to catchment-average surface intensities using an Areal Reduction Factor (ARF). The ARF, ϕ, for timescales from 1 minute to 25 days and areas between 1 and 30,000 km^2, is expressed as:

$$\varphi = \max\left\{1 - \frac{\left[0.048 \cdot A^{0.36 - 0.01\cdot\ln(A)}\right]}{k^{0.35}}, 0.25\right\} \quad (2)$$

where A is the area in km^2, and k is the timescale in hours.

C. Infiltration Loss Estimation

The estimation of infiltration losses, and the separation of active or excess rainfall from the total hyetograph, employs the method developed by the US Soil Conservation Service (SCS). This method is predicated on specific assumptions:

During an initial period, τ_0, all rainfall, h_{a0}, is entirely absorbed as an initial deficit, resulting in no excess runoff.

Beyond the initial deficit, h_{a0}, the additional deficit during heavy rainfall cannot exceed a maximum value known as potential maximum retention, S. The initial deficit, h_{a0},, is expressed as h_{a0} = 0.1S. A value of 0.1, instead of the textbook 0.2, is adopted for consistency with regional literature findings (Baltas et al., 2007), which indicate a lower actual initial abstraction ratio, representing a realistic yet conservative approach.

For any time $t > \tau_0$, the ratio of the excess rainfall depth to the additional deficit ($h_a - h_{a0}$) is equal to the ratio of these values to their potential counterparts (h - h_{a0}) and S, respectively.

Based on these assumptions, the empirical equation for estimating excess rainfall, h_e, is:

$$h_e = \begin{cases} 0 & h \le 0.1S \\ \dfrac{(h - 0.1S)^2}{h + 0.9S} & h > 0.1S \end{cases} \quad (3)$$

Equation (3) is applied to both total and partial (block) rainfall depth values to determine the temporal evolution of the event. The SCS Curve-Number (CN) method is modified by applying the runoff equation block-wise to derive a time-distributed excess-rainfall hyetograph compatible with the RoG solver. Other steps align with the standard CN procedure during model computation.

The parameter S (in mm), representing potential maximum retention, is linked to the runoff and can be estimated from existing literature if runoff data are unavailable. The relationship between S and CN is:

$$S = 254\left(\frac{100}{CN} - 1\right) \quad (4)$$

The CN value, ranging from 0 to 100, is determined by factors such as soil type, land use, and antecedent moisture conditions. For this study, a layer of CN values is

derived from the European Space Agency's (ESA) land cover typology, specifically ESA World Cover 2020 (10 m resolution).

11.2.2. Rain-on-Grid Hydraulic Modeling

RoG is a hydraulic modelling technique that integrates rainfall-runoff processes directly within the hydraulic model, applying measured or remotely sensed rainfall data as a spatially distributed boundary condition. This contrasts with traditional methods that rely on pre-computed runoff hydrographs. RoG facilitates a cohesive simulation of rainfall-runoff dynamics and flood propagation by applying rainfall uniformly or spatially varied across the domain. HEC-RAS 2D, developed by the United States Army Corps of Engineers, is the platform utilized for these hydraulic simulations.

A. Hydraulic Equations and Numerical Solvers

HEC-RAS 2D offers multiple computational methods, including the Diffusion Wave Equations (DWE) and two forms of the Shallow Water Equations (SWE): SWE-ELM (Eulerian-Lagrangian Method) and SWE-EM (Eulerian Method). The SWE-EM solver employs a finite difference approach to solve the 2D shallow water equations. These equations, derived under the shallow-water assumption (horizontal scales $\gg$ vertical scales), constitute a set of hyperbolic partial differential equations that describe the conservation of mass and momentum in surface water flows.

The continuity equation, encapsulating the principle of mass conservation, is given as:

$$\frac{\partial h}{\partial t} + \nabla(Vh) = q \qquad (5)$$

$$\frac{\partial V}{\partial t} + (V\nabla)V = -g\nabla(h+z) + \mathrm{v_t}\nabla^2\mathrm{V} - \mathrm{c_f}V \qquad (6)$$

where h is the water depth, u and v are velocity components in x- and y-directions, V is the velocity vector, q is a compound source term accounting for water balance (e.g., precipitation, infiltration), g is the acceleration of gravity, z is the bed elevation, and C_f is the bottom friction coefficient.

The solver's numerical stability necessitates compliance with the Courant-Friedrichs-Lewy condition. The Courant number, Cr, is defined as:

$$Cr = \frac{u\Delta t}{\Delta s} \qquad (7)$$

where u is the characteristic wave propagation speed, Δt is the computational time step, and Δs is the spatial discretization length. For explicit time-integration

schemes, stability is governed by $Cr \leq 1$. Maintaining Cr close to or below unity is generally recommended to avoid numerical instability and oscillations. The solver enforces $Cr \leq 1$ by automatically reducing Δt upon any violation, starting with a base step and iteratively halving it. Fine-tuning Cr through iterative adjustments ensures stable and accurate simulations across terrain, flow conditions, and grid resolution.

B. Sub-Grid Bathymetry and Computational Mesh

HEC-RAS employs a sub-grid bathymetry approach. This method uses a relatively coarse computational grid while incorporating finer-scale information about the underlying topography. The mass conservation equation is discretized using a finite volume technique, factoring fine grid details as parameters representing multiple integrals over volumes and face areas. This ensures that fluid mass transport accounts for fine-scale topography within each discrete cell. This approach is appropriate as the free water surface is typically smoother than the bathymetry, allowing a coarser grid to effectively compute spatial variability in free surface elevation.

The computational mesh, which can be structured or unstructured, is generated within a defined 2D flow area perimeter. HEC-RAS supports polygonal cells with up to 8 sides, allowing a mixture of shapes and sizes. The creation of the 2D computational mesh involves:

1. Defining the 2D flow area perimeter: A polygon is drawn to define the boundary.
2. Generating computation points: Nominal cell center spacing (DX and DY) is entered to generate a base mesh, with options to include breaklines.
3. Refinement regions and breaklines: Breaklines are used to enforce cell faces along linear features such as high ground. Refinement regions modify cell spacing in specific areas, increasing or decreasing computational point density.
4. Mesh editing: Manual editing tools allow adding, moving, or deleting points to improve mesh quality and capture critical topographic features.

The underlying terrain and computational mesh are preprocessed to develop detailed elevation-volume relationships for each cell and hydraulic property curves (elevation vs. wetted perimeter, area, roughness) for each cell face. This "subgrid" technology allows for larger computational cells while retaining hydraulic detail.

C. Geospatial Layers and Parameters

The RoG model relies on several spatially distributed geospatial layers to define model parameters.

a) Digital Elevation Model

An accurate terrain model is essential for a detailed and accurate hydraulic model. This study utilizes DEMs provided from the government institutions, combined with Digital Surface Models (DSMs) of below-meter resolution that capture micro-topography, governing local pooling and flow routes.

HEC-RAS Mapper supports various gridded data formats (e.g., floating-point grid, GeoTIFF, ESRI grid files) for terrain models. These are converted to GeoTIFF format, which supports tiled and pyramided data, for efficient storage and dynamic mapping.

b) Land Cover and Infiltration

Land cover data informs infiltration parameters. A spatially varying land cover layer, derived from the European Space Agency's (ESA) land cover typology (ESA World Cover 2020 at 10 m resolution), is used. This layer is used to determine the aforementioned CN values for infiltration calculations.

The CN method is employed for infiltration. CN values range from approximately 30 for permeable soils to 100 for impervious surfaces. As discussed in Section 2.1.3, the method adopted an initial abstraction ratio of 0.1, where $h_{a0} = 0.1S$.

c) Spatially Distributed Manning's Roughness Coefficient

Manning's roughness coefficient *n* is spatially distributed based on land cover, providing a critical parameter for hydraulic calculations. This is achieved by building a table of land cover types versus Manning's n values within HEC-RAS Mapper.

The Manning's *n* value for each cell face is derived from these layers during the 2D flow area pre-processing stage. HEC-RAS can compute a composite Manning's n value as a function of elevation for each cell face using the formula:

$$n_c = \left(\frac{1}{P} \sum_{i=1}^{N} P_i n_i^{3/2} \right)^{2/3} \qquad (8)$$

The composite Manning's roughness coefficient n_c is calculated using a weighted average approach that accounts for the varying roughness characteristics along different segments of a channel or surface. The total wetted perimeter $P = \sum_{i=1}^{N} P_i$ represents the sum of all individual segment perimeters, where each local wetted perimeter P_i corresponds to a specific segment along a face with its own roughness properties. The local Manning's roughness coefficient n_i for each segment is raised to the power of 3/2 and weighted by its corresponding perimeter length, ensuring that segments with larger wetted perimeters have proportionally greater influence on the overall composite roughness value. This formulation provides a physically meaningful method for combining multiple roughness values into a single representative coefficient for hydraulic calculations.

d) Input Boundary Condition: Rainfall

The synthetic design hyetographs generated are directly applied as uniformly distributed input boundary conditions across the 2D flow area within the RoG framework. This method utilizes a time series of rainfall excess (rainfall minus losses) applied equally to all cells within the 2D flow area, or as spatially varying precipitation data (gridded or point gage data).

e) Output Boundary Condition: Normal Depth

For locations where flow exits a 2D flow area, a Normal Depth boundary condition is applied. This boundary condition requires specifying the energy grade slope (or friction slope), which is utilized to compute a flow at each computation face. The friction slope is used within Manning's equation to compute a Normal Depth water surface elevation for each given flow, based on the cross-section data along the boundary condition line.

11.3. Outputs and Interpretation of Results

The pluvial flood risk model provides precise, location-specific data on water depths and flow velocities through detailed inundation maps, which are important for understanding the immediate flood hazard at cultural heritage sites. The interpretation of these outputs is highly specific: higher water depths directly correlate with potential structural vulnerabilities and prolonged saturation of materials, while elevated flow velocities indicate significant erosive potential and dynamic pressure impacts on historical structures. This detailed understanding is greatly enhanced by the use of high-resolution DSMs, often derived from UAV photogrammetry, which accurately capture micro-topographical features that govern local water pooling, flow routes, and, consequently, site-specific patterns of material decay.

The model assesses different return periods (e.g., 100-, 500-, and 1000-year events), which represent the probability of a flood of a given magnitude occurring in any single year. These return periods reveal scale-dependent differences in inundation extents, site-specific inundation percentages, and water volumes, with impacts generally amplifying with longer return periods. For instance, a 500-year event would show a more extensive inundation and intensified flow accumulation compared to a 100-year event. While some areas might exhibit consistent depth and velocity distributions due to flat site morphology or functioning as isolated basins, variations in depth and velocity are evident across different return periods and locations, driven by factors like micro-topography and local drainage impedance.

11.4. References

Baltas, E. A., Dervos, N. A., & Mimikou, M. A. (2007). Technical note: Determination of the SCS initial abstraction ratio in an experimental watershed in Greece. Hydrology and Earth System Sciences, 11(6), 1825–1829. https://doi.org/10.5194/HESS-11-1825-2007

Iliopoulou, T., Koutsoyiannis, D., Malamos, N., Koukouvinos, A., Dimitriadis, P., Mamassis, N., Tepetidis, N., & Markantonis, D. (2024). A stochastic framework for rainfall intensity–time scale–return period relationships. Part II: point modelling and regionalization over Greece. Hydrological Sciences Journal, 69(8), 1092–1112. https://doi.org/10.1080/02626667.2024.2345814

Koutsoyiannis, D., Iliopoulou, T., Koukouvinos, A., & Malamos, N. (2024). A stochastic framework for rainfall intensity–time scale–return period relationships. Part I: theory and estimation strategies. Hydrological Sciences Journal, 69(8), 1082–1091. https://doi.org/10.1080/02626667.2024.2345813

11.5. Contributors

Developed by: National Technical University of Athens

Date of last update: 12/09/2025

Lead contributors:

- Marcos Julien Alexopoulos
- Theano Iliopoulou
- Denis Istrati

12. Random Waves Impacts on the coastline

12.1. Overview

This section presents the coastal impact models developed to evaluate hydrodynamic hazards on coastlines and heritage sites resulting from random wave interactions under realistic sea conditions. It quantifies the intensity and spatial extent of wave-induced runup and pressures to support risk assessment and resilience planning along exposed coastlines. The model focuses on the physical hazard component of coastal risk, assessing potential exposure and loading due to extreme wave events derived from long-term offshore data. The model is based on a three-dimensional non-hydrostatic framework that propagates irregular wave fields -generated from 35-year hindcast data and represented by JONSWAP spectra- across realistic bathymetry and topography. Wave height scenarios correspond to average return periods of 5, 10, and 130 years, obtained through Peak-Over-Threshold (POT) extreme value analysis. Key input parameters include offshore wave spectra, bathymetric and topographic data, and boundary conditions representing the selected return-period scenarios. Main outputs comprise time-dependent free-surface elevations, pressure distributions, and runup heights along the coastal domain, which together quantify wave-induced loading and exposure under random sea states.

12.2. Methodological Description

12.2.1. Governing equations

The coastal impact model is based on a three-dimensional non-hydrostatic numerical framework implemented in REEF3D::NHFLOW, which solves the incompressible Navier–Stokes equations in a single-phase formulation where only the water domain is resolved. The governing equations are:

$$\frac{\partial u_i}{\partial t} + u_j \frac{\partial u_i}{\partial x_j} = -\frac{1}{\rho}\frac{\partial p}{\partial x_i} + g_i + \nu \frac{\partial^2 u_i}{\partial {x_j}^2}$$

$$\frac{\partial u_i}{\partial x_i} = 0$$

Where u_i are the velocity components, p the pressure, ρ the water density, g_i the gravitational acceleration, and ν the kinematic viscosity.

The free surface is computed through a depth-integrated continuity equation that advances the surface elevation η by integrating vertical fluxes over the water column:

$$\frac{\partial \eta}{\partial t} + \nabla . \int_{-h}^{\eta} u dz = 0$$

This formulation efficiently resolves dispersive and nonlinear wave motions while maintaining the vertical dynamics required for simulating breaking and runup. A σ–coordinated grid follows both the seabed and the free surface, enabling realistic bathymetry and topography to be represented through a dynamically deforming mesh.

The non-hydrostatic solver has been validated against laboratory experiments (Bihs et al., 2024; Bihs & Wang, 2025), confirming its ability to reproduce free-surface evolution and transient impact pressures.

12.2.2. Bathymetry

The computational domain represents a realistic coastal segment extending up to 2 km offshore. Bathymetric data are derived from fine-resolution nearshore surveys, complemented by open-source regional datasets to ensure complete and continuous coverage. Topographic data describing the coastal slope and near-shore elevation are interpolated onto the same σ-coordinate grid, allowing accurate representation of coastal morphology within the model.

12.2.3. Boundary conditions

The model includes four main boundary types:

Inlet: Random wave trains generated from spectral input over a relaxation zone and are imposed as time-varying velocity and surface elevation boundary conditions, .

Seabed and topography: A no-slip condition is applied to represent bottom and coastline.

Lateral Boundaries: Treated as symmetry with relaxation zone planes to minimize lateral confinement effects.

Free Surface: The non-hydrostatic pressure correction ensures smooth propagation and realistic wave deformation near breaking zones.

12.2.4. Wave scenario and offshore forcing

Offshore boundary conditions are defined using wave spectra derived from a 35-year hindcast analysis (Lavidas & Venugopal, 2017), parameterized through the JONSWAP spectrum. Representative sea states are selected using Peak-Over-Threshold (POT) extreme value analysis, which identifies exceedances above a significant-wave-height threshold and fits them to a Generalized Pareto Distribution (GPD). From this analysis, three wave scenarios are derived, corresponding to average return periods (ARPs) of approximately 5, 10, and 130 years (Lechner et al., 1993). Each scenario defines a random wave field at the model inlet characterized by its significant wave height Hm0 and peak period Tp, ensuring statistical realism of the simulated sea states.

Table 8: Wave scenarios.

Return period (year)	significant spectral wave height (m)	Peak period (s)
5	1.75	5.14
10	1.86	5.14
130	2.1	5.14

12.3. Output and Interpretation of Results

The model outputs include three-dimensional fields of free-surface elevation and pressure across the computational domain, representing the spatial and temporal evolution of wave motion along the coastline. From these fields, key indicators such as wave runup height and impact pressure temporal and spatial distribution along the coastal boundary are derived. Time-dependent outputs are stored at selected monitoring points on the coastline surface nodes. The results quantify how wave energy and impact intensity vary with scenario severity (corresponding to 5-, 10-, and 130-year return periods). Higher runup levels indicate greater potential inundation and exposure, while elevated pressure and force values correspond to stronger hydrodynamic loading on the coastal boundary. Spatial visualization of pressure and runup provides direct insight into the areas most affected by random wave events, supporting the assessment of physical hazard levels and vulnerability of cultural heritage assets. Users should interpret the results as hydrodynamic hazard indicators, not as direct damage estimates. Structural response, material resistance, and secondary effects (e.g., sediment transport or long-term erosion) are not included in this modeling stage. The non-hydrostatic model resolves the water phase only and assumes incompressible, Newtonian flow without wind or tidal effects. Consequently, results represent instantaneous hydrodynamic exposure under idealized random sea states and realistic bathymetry, serving as input for

subsequent risk evaluation and impact correlation analyses within the DSS framework.

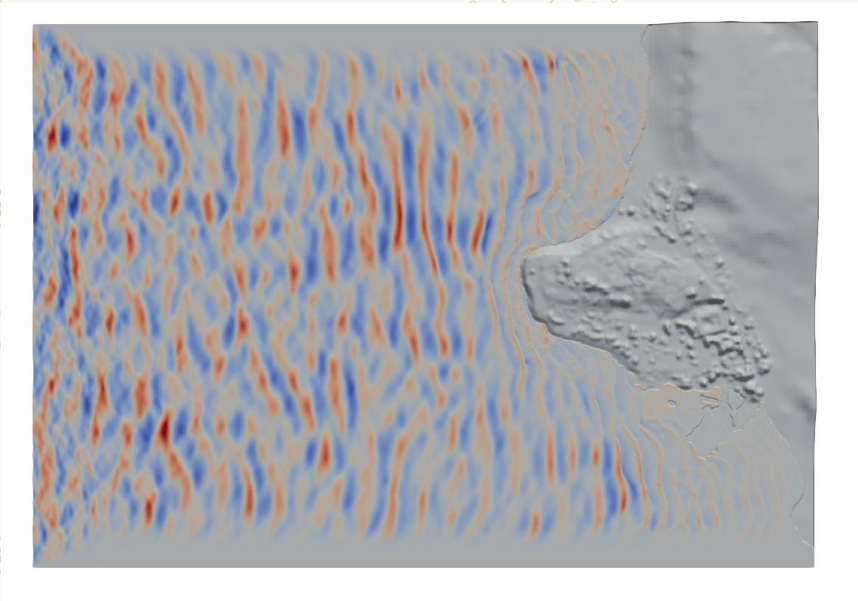

Figure 26: Wave generation and propagation over the computational domain until hitting the coastline.

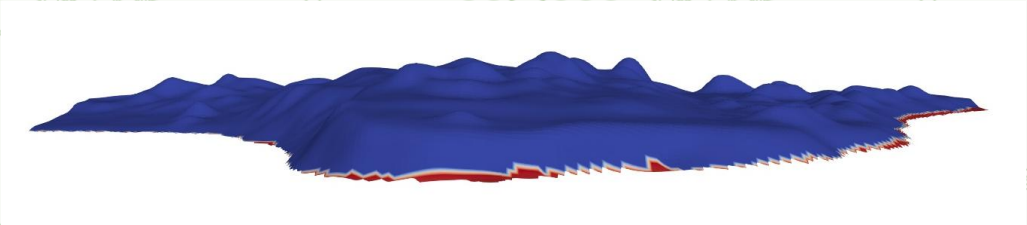

Figure 27: 3D distribution of runup and the corresponding pressure along the coastline on the cliff.

12.4. References

Bihs, H., Ehlers, R., & Wang, W. (2024, June). A Shock-Absorbing Non-Hydrostatic Navier-Stokes Solver on σ-GRIDS for Wave Modeling Over Irregular Topography. In International Conference on Offshore Mechanics and Arctic Engineering (Vol. 87844, p. V006T08A016). American Society of Mechanical Engineers.

Bihs, H., & Wang, W. W. (2025). REEF3D:: NHFLOW—A high-performance non-hydrostatic solver for coastal wave propagation. Coastal Engineering, 104819

Lavidas, G., & Venugopal, V. (2017). A 35 year high-resolution wave atlas for nearshore energy production and economics at the Aegean Sea. Renewable Energy, 103, 401-417.

Lechner, J. A., Simiu, E., & Heckert, N. A. (1993). Assessment of ‘peaks over threshold’methods for estimating extreme value distribution tails. Structural Safety, 12(4), 305-314.

12.5. Contributors

Developed by: National Technical University of Athens

Date of last update:

Lead contributors:

- Raouf Sobhani
- Denis Istrati

13. Snow Cover Dynamics

13.1. Overview

Snow cover is a dynamic component of the Earth system, influencing the climate, hydrological cycles, and ecosystems. Understanding its temporal and spatial variability is essential for assessing climate impacts, water resources, and ecosystem services. At the same time, snow cover dynamics pose substantial challenges for cultural heritage (CH) preservation, especially at archaeological sites that are often composed of fragile materials. Rapid snowmelt, intensified by extreme weather events, can destabilize built remains. Climate change is introducing new complexities to snow cover regimes. Projections indicate significant reductions in snow cover duration, earlier onset of snowmelt, and increasing variability in depth and extent. Even slight shifts in temperature near the freezing point can profoundly influence whether precipitation falls as snow or rain. As a result, snow-dependent systems, including ecosystems, water resources, and archaeological landscapes, are increasingly vulnerable to climate change.

The snow cover model provides a framework for monitoring, analyzing snow cover dynamics at CH sites (Ottinger et al. 2025; Ioannidis et al. 2024). It integrates Earth Observation (EO) data derived from satellite sensors with advanced processing algorithms to produce daily and seasonal snow cover metrics, allowing for continuous assessment of snow extent and duration. At its core, the model leverages operational MODIS snow cover products, applying cloud correction, interpolation, and quality assurance steps to generate a globally consistent dataset of snow cover extent (SCE). Beyond the observational component, additional work been done based on the model outputs, incorporating climate projections to simulate potential changes in snowfall and snow cover under different Representative Concentration Pathways (RCPs). This integration enables the comparison of historical and projected snow cover dynamics, supporting both scientific research and practical applications in areas such as hydrology, ecosystem management, and climate adaptation planning.

The following chapters detail the methodology applied to process and analyze snow cover data, the workflows for integrating climate projections, and the interpretation of results in the context of archaeological site management.

13.2. Methodological Description

The methodological approach to analyzing snow cover extent and its implications for cultural heritage management integrates Earth Observation (EO) time series data, advanced pre-processing techniques, and climate model projections. This section outlines the entire workflow, starting from data sources and acquisition, followed by data preprocessing and aggregation, the calculation of long-term statistical measures, the integration of climate model outputs for future projections, and finally, the comparative analysis of historical and modeled data.

13.2.1. General Analytical Framework

The analytical framework of this study is built on three key steps:

1. **Acquisition of EO-based snow cover datasets** through the DLR Global SnowPack processor, using MODIS Terra and Aqua satellite data.
2. **Preprocessing and aggregation of data** into daily and monthly composites to derive long-term temporal statistics of snow cover extent.
3. **Integration of modeled snowfall projections** based on EURO-CORDEX climate models and RCP scenarios to contextualize observed changes and explore future dynamics.

13.2.2. Data Sources

Snow cover monitoring relies primarily on optical satellite missions that provide long-term, consistent, and high-frequency observations. The primary data source for this model is the Moderate Resolution Imaging Spectroradiometer (MODIS), which delivers daily global coverage at a spatial resolution sufficient to capture regional snow dynamics. MODIS snow cover products are derived using the Normalized Difference Snow Index (NDSI), an established metric for differentiating snow from other land cover types based on spectral reflectance properties. The strength of MODIS lies in its long time series and temporal density, making it suitable for identifying seasonal and inter-annual variability in snow cover. The MODIS snow cover products are derived from the Terra (MOD10A1.006) and Aqua (MYD10A1.006) satellites. These datasets were processed through the Global SnowPack processor, developed at the German Aerospace Center (DLR). MODIS data were selected due to their high temporal resolution and reliable snow detection capabilities, offering daily global coverage at a spatial resolution of 500 meters.

To complement satellite observations, modeled datasets of snowfall and precipitation are integrated. These are commonly generated within the framework of coordinated climate modeling initiatives such as EURO-CORDEX, which provides downscaled regional projections based on multiple global climate models. Climate model outputs include essential meteorological variables such as precipitation, temperature, and snow water equivalent, all of which are critical drivers of snow cover dynamics. By combining satellite-derived snow cover extent and modeled snowfall data. The latter were provided by the Aristotle University of Thessaloniki

(AUTH. Snowfall simulations included 11 climate models and three Representative Concentration Pathways (RCPs), which span a wide range of possible future greenhouse gas emission scenarios. These projections formed the basis for simulating potential future snow dynamics under different climate change trajectories.

A. MODIS Snow Cover Data

The core dataset is derived from the MODIS MOD10A1.006 (Terra) and MYD10A1.006 (Aqua) daily snow cover products. These datasets provide the Normalized Difference Snow Index (NDSI) at 500 m resolution, enabling a consistent distinction between snow and non-snow surfaces.

B. Global SnowPack Data

At the German Aerospace Center (DLR), the Global SnowPack processor (A. J. Dietz et al. 2012; A. Dietz et al. 2012; A. J. Dietz et al. 2015)was developed to transform MODIS NDSI products into cloud-free binary snow masks. The processor employs adaptive thresholding, cloud screening, temporal interpolation, and topographic adjustment to ensure reliable daily snow cover maps. Combining Terra and Aqua reduces cloud contamination, while residual cloudy pixels are interpolated. The Global SnowPack dataset represents a refined, globally consistent resource for monitoring snow dynamics. The dataset provides two main parameters: daily snow cover extent (SCE) and seasonal snow cover duration (SCD. With a spatial resolution of 500 meters, continuous global coverage, and ongoing expansion, Global SnowPack constitutes a unique basis for analyzing snow cover at multiple scales.

C. Modeled Snowfall Data

To simulate future snow cover dynamics, 11 climate models were used, providing outputs for three greenhouse gas concentration pathways, namely RCP2.6, RCP4.5, and RCP8.5. These datasets, supplied by the TRIQUETRA partner Aristotle University of Thessaloniki (AUTH), include high-resolution temperature and precipitation simulations suitable for deriving snowfall scenarios.

13.2.3. Data Processing

Before snow cover datasets can be analyzed, extensive preprocessing is required to ensure reliability and comparability. For optical satellite products, a key challenge lies in cloud contamination, which frequently obscures snow-covered surfaces. Advanced processing systems address this issue by merging data from multiple sensors, applying temporal interpolation across consecutive days, and incorporating topographic information to infer snow presence in persistently cloudy areas.

A central product in this context is the Global SnowPack dataset, which provides globally consistent information on daily snow cover extent (SCE). This dataset is

derived from the operational MODIS snow cover products, available since February 2000, and has been specifically designed to close data gaps caused by cloud cover conditions. Through a sequence of interpolation steps, all missing values are filled, resulting in a continuous and gap-free snow cover record. The Global SnowPack system produces a near-real-time snow cover extent product (NRT_SCE), updated daily with a processing lag of about three days. To ensure long-term consistency and reliability, the entire annual dataset is reprocessed after the end of each calendar year, leading to a quality-controlled SCE product. Each daily snow cover dataset is accompanied by a quality layer (SCE_Accuracy), which quantifies the confidence of snow detection based on the temporal distance to the next cloud-free observation, the seasonality of snow occurrence, and the topographic or geographic context. This quality indicator enables users to assess the robustness of snow cover information in different regions and time periods.

13.2.4. Aggregation and Statistical Analysis of Daily SnowPack Data

The processed datasets provide a foundation for detailed statistical analysis of snow cover dynamics at CH sites. Continuous satellite observations allow the construction of time series of fractional snow cover at daily, monthly, and annual scales. Aggregating these data over multiple decades enables the identification of long-term averages, variability patterns, and seasonal cycles, including the timing of snow onset, peak accumulation, and melt (Uereyen et al. 2022; Rößler et al. 2021). These metrics offer insights into the stability and potential shifts of snow regimes. Daily snow cover observations derived from MODIS products are converted into monthly composites, enabling the model to track changes across both seasonal and interannual scales. Aggregation of these data allows the calculation of multidecadal statistics, including daily and monthly averages, providing a detailed understanding of temporal variability and long-term trends over the period from 2000 to 2022. Over the 22-year period, a total of 8,748 daily observations were processed, and more than 274 monthly means were calculated, visualized, and analyzed using R software. These aggregated statistics form the basis for identifying patterns, assessing interannual variability, and understanding the persistence and spatial extent of snow cover. By systematically compiling EO-derived data in this way, the model delivers a robust and continuous record of snow dynamics, which can be further compared with modeled snowfall projections to evaluate potential changes under different climate scenarios.

13.2.5. Integration of Climate Model Projections and Comparative Analysis

The integration of satellite-based snow observations with regional climate model projections provides a comprehensive perspective that links past, present, and future snow conditions. Earth observation data deliver robust empirical evidence of snow cover dynamics over the last two decades, while climate models extend this understanding by simulating future scenarios under varying greenhouse gas emission pathways.

This approach involves comparing observed snow cover patterns with modeled snowfall. Cross-validation ensures that models reproduce the variability captured in the satellite record, thereby strengthening their reliability for projecting future conditions. By combining observational baselines with modeled projections, the analysis clarifies whether recent trends are likely to persist, intensify, or stabilize. It highlights the relative influence of natural variability and anthropogenic climate change, pointing to potential risks such as shorter snow seasons, reduced snow depth, or shifts from snowfall to rainfall. This integrated perspective not only advances scientific understanding of snow dynamics but also provides actionable insights for sectors that rely on snow cover information, including water resource management, hydropower, agriculture, and the preservation of cultural and natural heritage.

13.3. Outputs and Interpretation of Results

The analysis of the processed datasets highlights the variability of snow cover across spatial and temporal scales. Time series data allow both short-term fluctuations and long-term developments to be examined. A key feature is the pronounced interannual variability, with some years showing more extensive and persistent snow cover while others display considerably reduced conditions. These variations reflect broader climate influences that affect precipitation patterns and temperature regimes, contributing to the observed diversity in snow dynamics.

By aggregating daily snow cover observations into seasonal and annual indicators, broader temporal patterns become apparent. In several regions, changes in the duration of the snow season can be observed, often reflected in an earlier onset of snowmelt during spring and shifts in the snowline at different elevations. While higher altitudes tend to retain relatively stable snow cover, mid-elevation zones increasingly exhibit shorter or more intermittent snow seasons. These transitional areas are particularly sensitive, as even minor temperature changes can strongly affect snow persistence.

Comparisons between observed snow cover records and regional climate model simulations show general agreement in large-scale seasonal patterns but also highlight differences in the intensity and persistence of snow cover in specific regions. These deviations can be linked to simplified model representations of topography and land-surface processes, though improvements are achieved through bias correction and the use of high-resolution datasets such as Global SnowPack.

The combined use of satellite-based observations and climate model projections suggests that previously observed trends—such as shorter snow seasons, reduced continuous snow cover, and an upward shift of the snowline—are likely to continue and intensify under future climate scenarios. These findings underscore the

dynamic character of snow cover within the climate system and its sensitivity to variations in temperature and precipitation.

13.4. References

Dietz, Andreas Jürgen, Claudia Kuenzer, and Stefan Dech. 2015. “Global SnowPack: A New Set of Snow Cover Parameters for Studying Status and Dynamics of the Planetary Snow Cover Extent.” Remote Sensing Letters 6 (11): 844–53. https://doi.org/10.1080/2150704X.2015.1084551

Dietz, Andreas Jürgen, Claudia Kuenzer, Ursula Gessner, and Stefan Dech. 2012. “Remote Sensing of Snow – a Review of Available Methods.” International Journal of Remote Sensing 33 (13): 4094–134. https://doi.org/10.1080/01431161.2011.640964

Dietz, Andreas, Christoph Wohner, and Claudia Kuenzer. 2012. “European Snow Cover Characteristics between 2000 and 2011 Derived from Improved MODIS Daily Snow Cover Products.” Remote Sensing 4 (8): 8. https://doi.org/10.3390/rs4082432

Ioannidis, Charalabos, Styliani Verykokou, Sofia Soile, et al. 2024. “Safeguarding Our Heritage—The TRIQUETRA Project Approach.” Heritage 7 (2): 2. https://doi.org/10.3390/heritage7020037

Ottinger, Marco, Felix Bachofer, Sophie Reinermann, Aristeidis Georgoulias, Prodromos Zanis, and Juliane Huth. 2025. Analyzing Climate Change Impacts on European Cultural Heritage Sites Using High-Temporal-Resolution Satellite Time Series. https://doi.org/10.13140/RG.2.2.17614.37449

Rößler, Sebastian, Marius S. Witt, Jaakko Ikonen, Ian A. Brown, and Andreas J. Dietz. 2021. “Remote Sensing of Snow Cover Variability and Its Influence on the Runoff of Sápmi’s Rivers.” Geosciences 11 (3): 3.

Uereyen, Soner, Felix Bachofer, and Claudia Kuenzer. 2022. “A Framework for Multivariate Analysis of Land Surface Dynamics and Driving Variables—A Case Study for Indo-Gangetic River Basins.” Remote Sensing 14 (1): 197. https://doi.org/10.3390/rs14010197

13.5. Contributors

Snow cover extent developed by: German Aerospace Center (DLR)

Modeled Snowfall data provided by Aristotle University of Thessaloniki (AUTH)

Date of last update: August 20, 2025

Lead contributors:

- Marco Ottinger (DLR)
- Felix Bachofer (DLR)
- Aristeidis Georgoulias (AUTH)

- Prodromos Zanis (AUTH)

14. Tsunami Hazard Estimation

14.1. Overview

This methodology estimates tsunami hazard at coastal sites using Geographic Information System (GIS)-based inundation mapping derived from probabilistic tsunami hazard assessment data. The method takes offshore tsunami hazard curves as input. It produces spatially explicit maps of inundation depth and flow velocity as output. The approach provides a computationally efficient screening tool for site-scale tsunami hazard assessment.

14.2. Methodological Description

14.2.1. Data Sources and Probabilistic Hazard Assessment

A. Tsunami Hazard Database

Tsunami inundation scenarios derive from the NEAM Tsunami Hazard Model 2018 (NEAMTHM18) regional Probabilistic Tsunami Hazard Assessment (PTHA) dataset. The dataset covers the Northeast Atlantic, Mediterranean, and connected seas. It provides tsunami hazard assessments at multiple offshore Points of Interest (POIs). Offshore hazard is quantified via exceedance probabilities for maximum inundation heights (MIH).

The NEAMTHM18 hazard curves present results as percentile series (p02 to p98). These percentiles represent epistemic uncertainty bounds in the tsunami hazard assessment. They quantify the range of credible tsunami wave heights. The range results from alternative assumptions in seismic source characterization, tsunami generation models, and propagation scenarios. The 98th percentile (p98) represents a conservative upper bound. This bound accounts for uncertainties in earthquake rupture parameters.

B. Return Period Selection

The methodology analyzes three distinct Average Return Periods (ARP): 2,475 years, 9,975 years, and 24,975 years. The probability of exceedance is expressed over a 50-year time window. This aligns with standard infrastructure design life considerations. The 50-year reference period reflects the typical service life of critical structures. It enables conversion to annual exceedance probabilities through Poissonian assumptions. A 2% probability of exceedance in 50 years corresponds to an ARP of 2,475 years. This framework differs from the annual return period convention commonly used in hydrological applications.

C. Digital Elevation Model Requirements

The methodology requires a Digital Elevation Model (DEM) or Digital Surface Model (DSM) that extends beyond the coastline. The model must capture both terrestrial

topography and underwater bathymetry. High-resolution terrain data derived from UAV photogrammetry provides sub-meter accuracy at monument scale. Coarser resolution DEMs (5 m) serve for catchment-scale analysis. The accuracy of hazard modeling depends fundamentally on the quality and resolution of the DEM used.

14.2.2. Hazard Parameter Extraction and Calculation

A. Maximum Inundation Height Extraction

The MIH represents the maximum wave height recorded at the nearshore POI. Extraction of the 98th percentile MIH (MIHp98) for the selected ARPs follows established procedures. The nearshore POI is selected based on proximity to the study site and availability of hazard data. Hazard curves display the probability of exceedance versus MIH. The curves enable selection of scenario magnitudes that leverage site-specific hazard projections.

B. Design Run-up Computation

The design run-up (R_d) is computed through application of a conversion factor to the MIHp98. The calculation applies an empirical amplification factor of three. This adheres to the hydrodynamic conversion established for Mediterranean coastal sites. The amplification accounts for coastal topography effects. Local conditions can amplify tsunami heights significantly beyond open-ocean values.

The design run-up is calculated using:

$$R_d = 3 \times MIH_{p98} \qquad (2)$$

The value Rd represents the maximum elevation the water achieves onshore due to run-up.

C. Maximum Inland Inundation Distance

The theoretical maximum inland inundation distance (D_{MAX}) is estimated using an empirical relation. Physical and computational constraints require limiting the analysis extent to reasonable distances inland. The maximum distance is calculated as:

$$D_{MAX} = 200 \times R_d \qquad (3)$$

This D_{MAX} value delineates the maximum extent of the hazard footprint. In practice, this provides only a theoretical upper bound. Inland propagation is constrained by local topography. When ground elevations exceed the design run-up, tsunami inundation does not extend further inland.

14.2.3. GIS-Based Inundation Mapping Workflow

A. Coastline Processing

The coastline serves as the starting boundary for tsunami propagation analysis. Coastline data are extracted from OpenStreetMap using GIS software. The coastline is converted to points with specified spacing to ensure adequate transect density. Typical spacing intervals range from 2 m to 50 m, depending on coastal complexity. The points are reconstructed into a densified coastline layer.

B. Perpendicular Transect Generation

Perpendicular transects represent pathways along which tsunami waters flow inland from the coast. Transects are generated using GIS tools with the densified coastline as input. Length is set to the maximum Rd distance (200 × Rd). Angle is set to 90 degrees for perpendicular orientation to the coast. Transects are filtered to retain only those extending landward. Transects over marine areas are removed via spatial selection based on the land polygon.

C. Point-Based Elevation Sampling

Transect lines are converted to points to allow precise elevation sampling. Points are generated along the transect geometry at regular intervals. The intervals match the spacing used for coastline densification. Each point is assigned elevation data through sampling from the DEM. Points inherit distance information representing their position along each transect from the coast.

D. Elevation-Based Screening

Points are filtered using elevation criteria to identify potentially inundated locations. The screening retains points where elevation is below the design run-up threshold (Rd) and above zero. The modeled scenario cannot inundate points above the amplified MIH threshold. Points touching or intersecting the coastline are removed to avoid analytical artifacts.

E. Gap Correction for Topographic Barriers

After filtering by elevation criteria, some transects may include unrealistic inland points beyond the first elevation barrier. This occurs when the elevation drops below Rd further inland after initially exceeding it. Such configurations do not accurately simulate topographic blocking of tsunami run-up. Each transect is truncated at the first gap in the distance sequence. All points beyond the first barrier are removed even if they meet elevation criteria. This ensures a continuous inundation profile per transect.

F. Inundation Polygon Generation

The furthest inland points along each transect define the tsunami inundation boundary. A concave hull algorithm connects these points into a continuous polygon. Alpha values for the concave hull are calibrated (typically 0.005 to 0.03) to balance geometric accuracy with coastal complexity. The hull polygon is intersected

with the land polygon. This removes areas extending over water where no actual inundation occurs.

14.2.4. Inundation Depth Calculation

The water depth analysis utilizes static mapping. Local inundation depth h(x,y) is calculated at each DSM cell. This elevation-based method estimates water depth by subtracting local ground elevation z(x,y) from the design run-up height R_d.

The calculation is performed using:

$$h(x,y) = \max[0, R_d - z(x,y)] \qquad (4)$$

The non-negative constraint ensures that inundation depth remains zero where ground elevation exceeds the design run-up elevation. The resultant depth maps produce scenario-specific extents necessary for assessing the hazard. Maximum simulated water depths can reach 17 m near the shoreline in severe ARP projections.

14.2.5. Flow Velocity Derivation

A. Critical Flow Assumption

Flow velocity analysis estimates the design flow velocity (u) from local inundation depth (h) using the Froude relation. The estimation assumes critical flow conditions. The Froude number (Fr) is fixed at 1.0. This assumption aligns with critical flow conditions. It falls within the typical tsunami bore range reported in the literature (Fr range 0.7-2 for tsunamis).

The Froude number is defined as:

$$Fr = \frac{u}{\sqrt{gh}} \qquad (5)$$

where u is flow velocity (m/s), g is gravitational acceleration (9.81 m/s^2), and h is water depth (m).

B. Velocity Calculation

Design flow velocity is calculated by rearranging the Froude relation. Under the critical flow assumption (Fr = 1.0), velocity becomes:

$$u = \sqrt{gh} \qquad (6)$$

The resultant flow velocity is thus governed primarily by the calculated water depth. This critical flow assumption aligns with tsunami design standards established in ASCE 7-16 Chapter 6. The approach intentionally maintains computational feasibility for initial hazard quantification. Maximum tsunami flow velocities can reach 15 m/s in extreme scenarios.

14.2.6. Methodological Justification and Limitations

A. Computational Efficiency

GIS-based tsunami inundation mapping functions as a computationally efficient, first-order screening tool. The method simplifies tsunami hazard assessment. It offers computational feasibility for initial hazard quantification. Full site-specific seismic probabilistic tsunami hazard analysis simulations are computationally demanding. Coupling precomputed offshore hazard products with static onshore mapping reduces runtime. This supports timely risk screening.

B. Inherent Simplifications

The elevation-based mapping provides only a first-order screening. It omits dynamic flow simulation. Associated wave-energy dissipation mechanisms would be captured through full hydrodynamic modeling. GIS-based mapping overlooks dynamic factors. These include nonlinear interactions between waves and complex coastal morphology. The method may not capture exact critical flow dissipation mechanisms. These include wave energy loss due to turbulence at obstacles and infiltration-induced water loss during overland propagation.

The methodology might lead to some overestimation of inundation depths. Actual depths are expected to be lower than the estimated outputs. The method does not account for processes such as fill-spill dynamics in topographic depressions. Low-lying areas are expected to accumulate water through ponding. A GIS approach may be appropriate along relatively straight coastlines. It might prove unsuitable along highly curvilinear coastlines.

C. Applicability Context

Dynamic numerical simulations consistently yield substantially larger tsunami runup hazard compared to static models. The GIS approach provides conservative estimates. These are suitable for preliminary site screening. Results identify areas requiring detailed hydrodynamic investigation. The methodology establishes exposure footprints. It supports prioritization of resources for more refined modeling efforts.

14.3. Outputs and Interpretation of Results

14.3.1. Spatial Hazard Maps

The methodology produces georeferenced raster datasets. These represent maximum water depth and flow velocity across the study area. Outputs are generated for each analyzed return period scenario. Maps identify specific zones where water accumulates. They provide a basis for linking hydrodynamic exposure to site vulnerability.

14.3.2. Inundation Extent Polygons

Inundation extent polygons delineate the spatial footprint of the tsunami impact. These polygons define areas subject to estimated flooding. The extents vary by

return period. Longer return periods produce larger inundation footprints. The extents are controlled by coastal topography and local relief.

14.3.3. Decision Support Parameters

Results provide quantifiable physical parameters essential for developing targeted risk mitigation strategies. High-resolution hazard data support subsequent development of risk indices. Decision-makers can prioritize resources based on identified hazard intensities. The outputs directly inform the exposure assessment of coastal assets. They enable systematic comparison across multiple hazard scenarios.

14.4. References

American Society of Civil Engineers. Minimum Design Loads and Associated Criteria for Buildings and Other Structures (ASCE/SEI 7-16). American Society of Civil Engineers, 2017.

Basili, Roberto, et al. "The Making of the NEAM Tsunami Hazard Model 2018 (NEAMTHM18)." Frontiers in Earth Science, vol. 8, 2021, Article 616594, https://doi.org/10.3389/feart.2020.616594

Gibbons, Steven J., et al. "Probabilistic Tsunami Hazard Analysis: High Performance Computing for Massive Scale Inundation Simulations." Frontiers in Earth Science, vol. 8, 2020, article 591549, https://doi.org/10.3389/feart.2020.591549

Glimsdal, S., Løvholt, F., Harbitz, C. B., Romano, F., Lorito, S., Orefice, S., Brizuela, B., Selva, J., Hoechner, A., Volpe, M., Babeyko, A., Tonini, R., Wronna, M., & Omira, R. "A New Approximate Method for Quantifying Tsunami Maximum Inundation Height Probability." *Pure and Applied Geophysics*, vol. 176, no. 7, 2019, pp. 3227–3246. Springer, https://doi.org/10.1007/s00024-019-02091-w

Matsutomi, Hideo, and Kensuke Okamoto. "Inundation Flow Velocity of Tsunami on Land." Island Arc, vol. 19, no. 3, 2010, pp. 443-457, https://doi.org/10.1111/j.1440-1738.2010.00725.x. Accessed 11 Nov. 2025.

Tonini, Roberto, et al. "Testing Tsunami Inundation Maps for Evacuation Planning in Italy." Frontiers in Earth Science, vol. 9, 2021, p. 628061, https://doi.org/10.3389/feart.2021.628061. Accessed 11 Nov. 2025.

14.5. Contributors

Developed by: National Technical University of Athens

Date of last update: 12/11/2025

Lead contributors:

- Marcos Julien Alexopoulos
- Denis Istrati

15. Water Fluxes

15.1. Overview

Extreme precipitation events are becoming more frequent and intense due to climate change, posing significant risks to cultural heritage sites through flash floods and surface runoff (Ioannidis et al. 2024). Studies such as the IPCC Sixth Assessment Report (IPCC, 2021) document increases in short-term heavy rainfall in Central Europe by 3 to 19% over the past two decades, with further intensification expected. This trend emphasizes the urgent need for reliable flood hazard mapping tailored to the protection of vulnerable cultural heritage locations (United Nations 2020; Kreienkamp et al. 2021; Masson-Delmotte et al. 2021). Protecting cultural heritage from pluvial and fluvial flooding requires detailed hazard assessments combining multiple spatial scales. This report outlines a multi-disciplinary methodology, focusing on integrating terrain-based hazard indices, catchment runoff modeling, and advanced hydrodynamic simulations to provide actionable flood risk maps for heritage conservation.

The Water Fluxes model is a hydrological tool designed to simulate the spatial and temporal dynamics of surface water movement within a catchment or landscape. It estimates water fluxes by integrating terrain information, meteorological inputs, and land surface characteristics to quantify runoff generation, flow accumulation, and fluxes through river networks and drainage paths.

This model is essential for understanding hydrological processes at various scales and provides critical information for flood forecasting, water resource management, ecological studies, and infrastructure planning. The primary goal of the Water Fluxes model is to accurately represent the transport of water from precipitation through surface runoff, subsurface flow, and stream channels to catchment outlets. The model focuses on spatially explicit calculation of water movement by leveraging high-resolution Digital Elevation Models (DEMs) for terrain representation, combined with precipitation inputs and hydrological parameters governing infiltration and runoff.

15.2. Methodological Description

The model applies a multi-method approach to map strong rain and flood danger at selected cultural heritage sites, integrating terrain analysis and hydrological runoff modeling.

15.2.1. Data Sources

The accuracy and reliability of the Water Fluxes model depend heavily on the quality and resolution of input data. The following datasets form the core of the model inputs:

1) Digital Elevation Model (DEM)

The DEM provides a gridded representation of the terrain surface, typically with a spatial resolution ranging from a few meters to tens of meters depending on data availability. Elevation data is critical for defining flow directions, flow paths, slope gradients, and catchment delineations. Common DEM sources include airborne LiDAR, satellite-based systems like SRTM, or national elevation datasets.

2) Precipitation Data

Precipitation inputs are essential drivers of runoff generation. The model accepts both point-based rainfall data from meteorological stations and spatially distributed precipitation from radar or satellite estimates (e.g., TRMM, GPM). Temporal resolution can range from hourly to daily, depending on the model application and data availability.

3) Land Use and Land Cover (LULC)

Land surface characteristics influence infiltration rates, surface roughness, and runoff coefficients. LULC maps derived from remote sensing (e.g., Landsat, Sentinel-2) classify the landscape into categories such as forest, urban, agriculture, and bare soil, each associated with specific hydrological properties.

4) Soil Characteristics

Soil texture and structure affect infiltration capacity and subsurface flow. Soil maps provide parameters such as hydraulic conductivity, porosity, and field capacity. These parameters are used to adjust runoff coefficients and estimate soil water retention.

5) Streamflow Data (Optional)

For model calibration and validation, observed discharge data from hydrological gauging stations are used to compare modeled water fluxes with actual streamflow.

15.2.2. Data Processing

The data processing framework integrates terrain analysis, hydrological modeling, and runoff simulation to produce spatially explicit flood risk indicators. This multi-stage approach begins with catchment delineation, followed by runoff estimation, calibration against observed data, and water level profiling to inform flood hazard assessment. The model workflow consists of several key processing steps that transform raw input data into hydrologically meaningful outputs.

A. Terrain Positioning Index (TPI) Calculation

The initial step in hazard estimation involves calculating the Terrain Positioning Index (TPI) based solely on the Digital Elevation Model (DEM) of the area surrounding the site of interest. The Terrain Positioning Index (TPI) is computed from high-

resolution DEM data by comparing the elevation of each grid cell to the mean elevation of its surrounding neighborhood. This relative elevation metric allows classification of the terrain into ridges, slopes, valleys, and flat depressions, which are critical for identifying areas prone to water accumulation during intense rainfall events. This classification underpins the identification of potential flood hotspots and pathways for surface runoff (Krauß and Fischer, 2016). Automated mapping of vulnerable zones using TPI provides a scalable approach applicable across large landscapes encompassing multiple heritage sites. This relative measure normalizes elevation differences, allowing classification of terrain positions independently of absolute heights. To compute the TPI, for each DEM cell z_0, the average elevation $\bar{z}$ and standard deviation σ of elevations are calculated within an annular ring defined by an inner radius r_i and outer radius r_o. The TPI is then defined as:

$$TPI = \frac{(z^0 - \bar{z})}{\sigma_z}$$

Based on calibrated thresholds, TPI values classify each DEM cell into distinct terrain classes (e.g., ridge, slope, valley, sink), which correlate with varying probabilities of being affected by strong rainfall-induced runoff and flooding. This classification was validated using historical insurance loss data over a decade in North Rhine-Westphalia, Germany, showing a clear increase in flood risk probability from ridges to sinks. Thus, TPI serves as a valuable first indicator of local flood hazard based on topographic predisposition.

B. Water Runoff Estimation

Runoff estimation begins with delineating catchment areas by analyzing the DEM to determine upstream contributing regions. Building on the terrain classification, this stage delineates catchment areas that define the upstream regions contributing runoff to the site. Flow direction algorithms are applied to the DEM to assign flow paths from each pixel to its downstream neighbor, enabling aggregation of all upstream pixels draining into specific outlets. This hydrological partitioning ensures that precipitation inputs from the entire contributing area are accounted for in runoff estimates.

Runoff is computed by applying spatially distributed runoff coefficients that reflect infiltration and land surface characteristics:

$$Q_i = P_i \times C_i$$

Where Q_i is runoff at cell i, P_i is precipitation, and C_i is the runoff coefficient dependent on soil, land cover, and antecedent moisture conditions.

Flow direction is assigned to each cell, enabling identification of pixels draining into specific catchments. For every pixel, the total number of upstream pixels is calculated to derive the cumulative contributing area. Multiplying the upstream area by precipitation intensity produces the theoretical maximum runoff volume at

that location. This runoff map is then calibrated against measured hydrological data to improve prediction accuracy. Extracting elevation profiles perpendicular to flow allows estimation of maximum flood water levels based on runoff volume.

15.2.3. Danger Estimation For Cultural Heritage Sites

The heavy rainfall hazard model integrates both topographic and hydrodynamic components to assess flood-related risks to cultural heritage sites. A Terrain Position Index (TPI) is employed to characterize terrain morphology, capturing local elevation differences to identify depressions and ridges. This morphological information is combined with a physics-based runoff simulation, which computes spatially explicit water levels and surface flow velocities under different rainfall scenarios.

Hazard classification is then derived from predefined thresholds of ≥ 50 cm inundation depth and ≥ 0.25 m/s flow velocity, resulting in a color-coded hazard map ranging from high risk (dark blue) to no risk (light yellow). This integrated approach provides a detailed spatial understanding of flood dynamics and enables the identification of vulnerable heritage sites, supporting targeted protection and mitigation strategies.

15.3. Outputs and Interpretation of Results

The primary output of the hazard modelling framework is a comprehensive danger map that spatially delineates flood risk to cultural heritage sites under heavy rainfall scenarios. This map synthesizes information from several key inputs, including the Terrain Position Index (TPI), which characterizes local terrain morphology by identifying depressions, ridges, and slopes that influence water accumulation and flow pathways.

While the TPI itself is not an output product, it serves as an essential component in the modelling process, providing critical context for interpreting hydrodynamic runoff simulations. These simulations estimate spatially explicit water depths and surface flow velocities resulting from rainfall events, which are then integrated into the hazard classification.

Using threshold criteria of ≥ 50 cm inundation depth and ≥ 0.25 m/s flow velocity, the model classifies flood hazard levels across the landscape. The resulting danger map employs a clear color-coded scheme ranging from high hazard zones (dark blue) to areas of no or minimal risk (light yellow). This visualization allows stakeholders to quickly identify vulnerable cultural heritage sites and prioritize risk management actions.

By condensing complex hydrological and topographic data into an accessible and actionable format, the danger map supports effective decision-making for heritage conservation, emergency planning, and climate adaptation. Comparative analysis of danger maps generated from different rainfall scenarios further enables

assessment of site sensitivity to varying precipitation intensities, aiding long-term resilience strategies.

In summary, the integration of TPI-derived terrain insights with hydrodynamic simulation results provides a robust basis for hazard identification, with the danger map serving as a vital tool to safeguard cultural heritage from flood impacts exacerbated by climate change.

15.4. Conclusion and Outlook

The integration of terrain morphology and hydrodynamic runoff simulations enables a detailed spatial assessment of flood hazards affecting cultural heritage sites under heavy rainfall. The Terrain Position Index (TPI) serves to characterize landforms such as depressions and ridges that influence water flow and accumulation. Heavy rain danger classification based on thresholds of inundation depth and flow velocity produces a clear, color-coded danger map identifying areas of varying flood risk.

This hazard mapping approach effectively highlights vulnerable zones, supporting prioritization for risk management and conservation efforts. The resulting outputs provide a foundation for understanding spatial flood risk patterns and their potential impacts on cultural heritage.

Further work may focus on incorporating additional hydrological factors, such as soil infiltration and land use changes, as well as considering future climate scenarios to enhance hazard prediction. Integration with monitoring and early warning systems could improve responsiveness to extreme weather events.

Overall, the presented methodology offers a practical framework for flood hazard identification, with potential to inform protection strategies and contribute to resilient management of cultural heritage sites under changing environmental conditions.

15.5. References

Ioannidis, Charalabos, Styliani Verykokou, Sofia Soile, et al. 2024. “Safeguarding Our Heritage—The TRIQUETRA Project Approach.” Heritage 7 (2): 2. https://doi.org/10.3390/heritage7020037

Intergovernmental Panel On Climate Change (Ipcc). 2023. Climate Change 2021 – The Physical Science Basis: Working Group I Contribution to the Sixth Assessment Report of the Intergovernmental Panel on Climate Change. 1st ed. Cambridge University Press. https://doi.org/10.1017/9781009157896

Krauß, T., and Fischer, P., 2016, “Automatic Detection and Vulnerability Analysis of Areas endangered by Heavy Rain,” Proceedings of European Space Agency, Living Planet Symposium, 5, vol. 2016.

Kreienkamp, F. et al., 2012. “Rapid attribution of heavy rainfall events leading to the severe flooding in Western Europe during July 2021,” Tech. Rep., World Weather Attribution.

United Nations. 2023. "The human cost of disasters: an overview of the last 20 years (2000-2019)”, Tech. Rep., UN, 10 2020, (accessed 3/2023).

V. Masson-Delmotte et al., 2021. “Climate Change 2021: The Physical Science Basis. Contribution of Working Group I to the Sixth Assessment Report of the Intergovernmental Panel on Climate Change,” Tech. Rep., IPCC, 2021.

15.6. Contributors

Developed by: German Aerospace Center (DLR), Earth Observation Center (EOC)

Date of last update: November 10, 2025

Lead contributors:

- Thomas Krauß
- Daniele Cerra

16. Wave Impacts

16.1. Overview

The numerical framework assesses the impacts of different waves including periodic and solitary waves, which represent extreme and hight energy events, on various cliff configuration observed in the sites such vertical, inclined and notched (partially damaged) cliff. The model is focused on runup and loading that may compromise structural stability and accelerate erosion. Its purpose is to quantify the hazard posed to coastal cliffed environments and heritage sites under waves action. The model requires input offshore wave characteristics, together with site specific cliff geometry. The outputs include maximum runup elevations, time–dependent pressure distributions, and hydrodynamic forces on the cliff, providing a basis for evaluating exposure and potential damage.

16.2. Methodological Description

Offshore wave conditions integrated with site–specific bathymetry and cliff geometry to assess wave impacts on coastal cliffs.

Offshore wave conditions are represented by wave height and period, but extreme events are described by solitary wave profiles, which capture high–energy impact scenarios. Wave data is obtained from open sources or long–term analyses and used as input for the model. When simplified geometries are used, variations observed at the site can be studied parametrically, for example the presence of a notch existence or inclination in the cliff. Offshore wave conditions are introduced and propagated through the computational domain, where the solvers resolve transformation, runup, and impact processes. Model outputs are post-processed to extract water

surface variations along structural boundaries and time histories at selected monitoring stations, enabling a detailed assessment of hydrodynamic loading and wave–induced response.

In this computational framework, a two–phase is used that rely on Navier-stokes equations and resolve wave transformation, runup, and impact processes:

$\nabla . \boldsymbol{u} = 0$ (conservation of mass)

$\frac{\partial \boldsymbol{u}}{\partial t} + \boldsymbol{u} \cdot \nabla \boldsymbol{u} = -\frac{1}{\rho}\nabla p + \nu \nabla^2 \boldsymbol{u} + \boldsymbol{g}$ (conservation of momentum)

Where $\boldsymbol{u}$ is the velocity vector, p is the pressure, ρ is the fluid density, ν is the kinematic viscosity, and $\boldsymbol{g}$ is the gravitational acceleration vector.

16.2.1. Three–Dimensional Two–Phase Solver

This approach is implemented using the OpenFOAM framework, specifically the interFoam solver, which resolves two–phase incompressible flow through the Volume of Fluid (VOF) method. The free surface is tracked by advecting a phase–fraction field α:

$$\frac{\partial \alpha}{\partial t} + \boldsymbol{u} \cdot \nabla \alpha = 0$$

Where $\alpha = 1$ denotes the water phase, $\alpha = 0$ denotes the air phase, and intermediate values represent the interface region.

The governing Navier-Stokes equations are discretized with a finite–volume scheme on both structured and unstructured meshes, allowing flexibility in capturing complex cliff and structure geometries. Pressure–velocity coupling is handled by PISO algorithm for transient simulations.

Turbulence closure can be introduced through either RANS models or LES approaches, depending on the spatial resolution of the grid and objectives of the simulation. Viscosity is explicitly included in the momentum equation and can be specified as constant, laminar, or modeled through turbulence formulations.

A. Computational Domain

In this study, the two–phase solver is applied for local wave–cliff interactions, where high spatial resolution is required to resolve spikes and transient pressures. The most important boundary conditions are the inlet, where prescribed wave conditions are imposed; the opposite boundary, which represents a solid surface where a no–slip condition is assigned, similar to the seabed boundary at the bottom; and the outlet, where wave energy is allowed to dissipate. Although the solver is 3D inherently, it is possible to employ a 2D configuration, achieved by assigning empty condition on the sides of the domain. This setup reduces computational cost while retaining the ability to reproduce the key hydrodynamic processes governing local loading on cliffs and structures. In the present application, the computational domain extends over several hundred meters, which is sufficient to generate and

propagate waves within the domain without reflections at the inlet boundary, while still allowing mesh refinement to capture rapid transient phenomena.

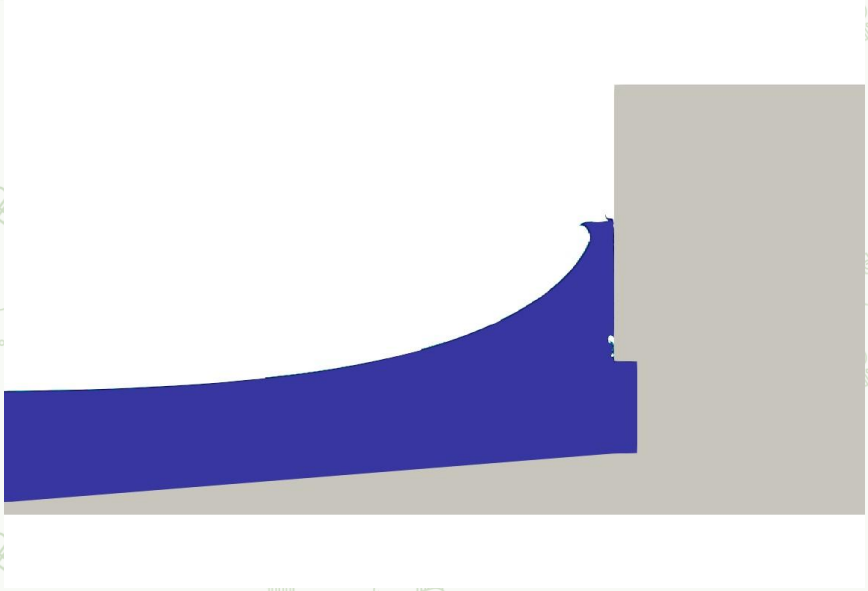

Figure 28: Modeling wave–cliff local interactions in Ventotene using OpenFOAM (Two–phase solver).

16.2.2. Modeling Procedure

The modeling procedure follows a consistent sequence for both solvers, comprising validation, sensitivity, parametric simulations, and post–processing of results.

For the two–phase solver, the procedure begins with validation against experimental data despite the considerable number of previous studies that have already validated this solver (L. F. Chen et al., 2014; Pablo Higuera et al., 2014). This step ensures that the model configuration can accurately reproduce wave runup and impact pressure on coastal structures. Validation is particularly important here because wave impact on walls can generate very sensitive and highly transient pressure spikes, so it is necessary to confirm that the solver performs reliably under these conditions. Following validation, a sensitivity analysis is performed to examine the influence of mesh resolution, time step size, turbulence closure, and boundary condition implementation. Once model robustness is confirmed, parametric study is conducted by systematically varying wave conditions and bathymetric configurations. The outputs are then post–processed to extract runup elevations, free–surface variations at monitoring stations, and pressure/force distribution on the cliff face.

In this solver, the time step is automatically adjusted according to a fixed Courant–Friedrichs–Lewy (CFL) criterion, supporting numerical convergence, accuracy, and stability.

16.3. Output and Interpretation of Results

This module produces outputs that describe the interaction between waves and cliffs. The primary results are maximum runup elevations along the cliff face, time–

dependent pressure distributions, and hydrodynamic forces exerted on the structure. These outputs are presented in graphical format within the DSS platform.

Interpretation of the results is based on the magnitude and spatial distribution of the outputs. For example, higher runup elevations indicate a greater exposure height and more likelihood of water penetration, leading to a bigger area of impact. Localized peaks in pressure diagrams correspond to impulsive impacts that may accelerate surface degradation or structural instability. Hydrodynamic force estimates represent the cumulative loading on the cliff, which can be compared against known thresholds for material resistance and stability.

The results should be interpreted with awareness of the underlaying assumptions and simplifications. Offshore wave conditions are represented by characteristic parameters and solitary waves, which capture high–energy scenarios. The geometry of the cliff is based on available bathymetry and survey data, introducing local–scale irregularities that influence wave impacts. Users should therefore consider the outputs as indicators of relative exposure and potential damage, rather than as absolute predictions.

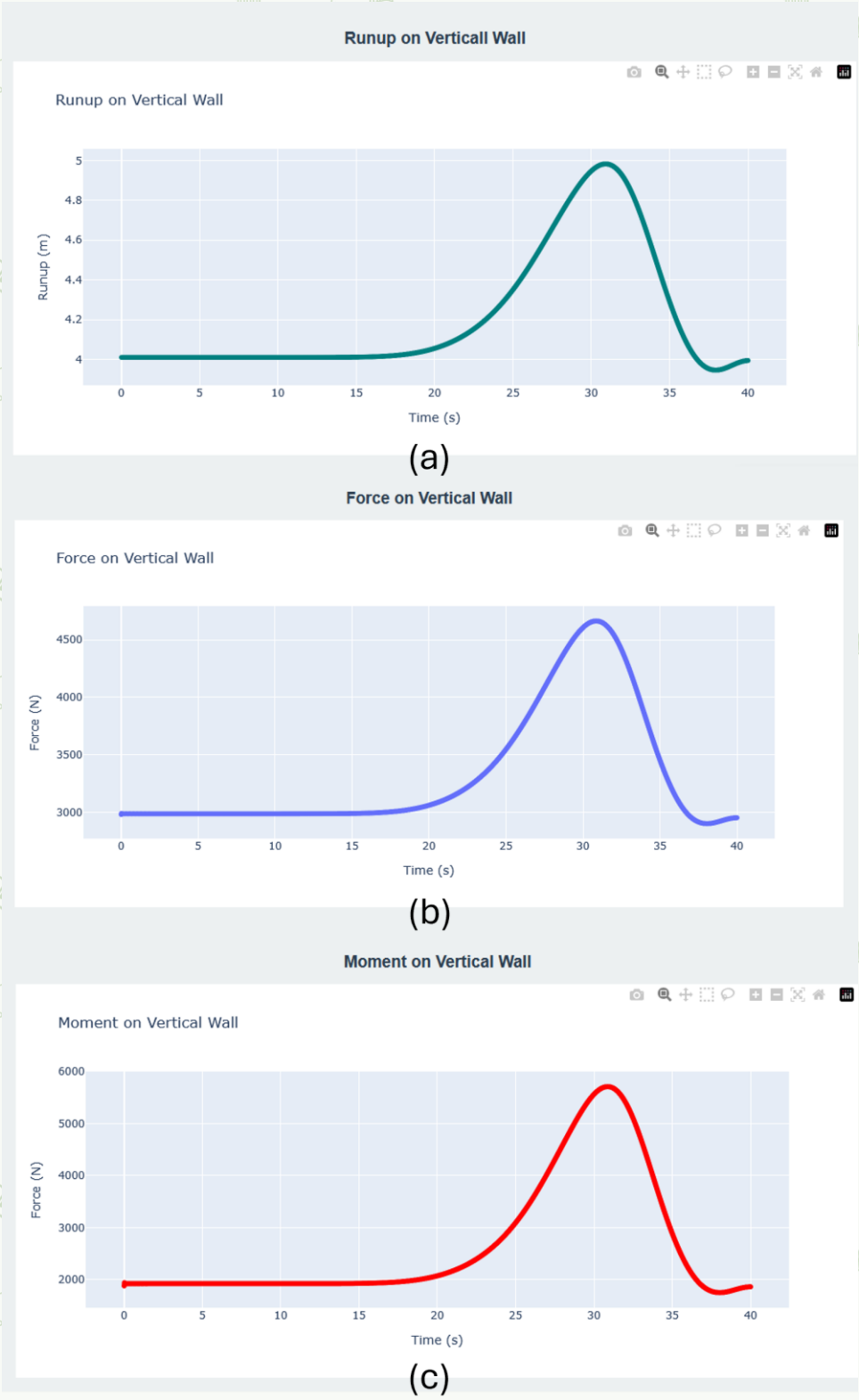

Figure 29: An example of presented outputs by the platform that shows moment (a)Runup, (b) Force, and (c) Moment time history on a cliff under a certain scenario.

16.4. References

Chen, L. F., Zang, J., Hillis, A. J., Morgan, G. C., & Plummer, A. R. (2014). Numerical investigation of wave–structure interaction using OpenFOAM. Ocean Engineering, 88, 91-109.

Higuera, P., Lara, J. L., & Losada, I. J. (2014). Three-dimensional interaction of waves and porous coastal structures using OpenFOAM®. Part I: Formulation and validation. Coastal Engineering, 83, 243-258.

16.5. Contributors

Developed by: National Technical University of Athens

Date of last update:

Lead contributors:

- Raouf Sobhani
- Denis Istrati

17. Geomorphological Maps (GM)

17.1. Overview

Geomorphology can be understood as a branch of Earth and Environmental Sciences that investigates landforms, the processes that shape them, and the evolution of the Earth's surface. Geomorphology aims at providing the physical and genetic framework through which surface processes can be interpreted in space and time. By analyzing the relationship between topography, geology, and climate, geomorphology explains why certain areas are more prone to specific natural hazards—such as landslides, erosion, or flooding—and how these processes can evolve under stable or changing environmental conditions.

In the context of cultural heritage (CH), geomorphology assumes a dual importance. First, it helps identify the natural factors that influence landscape stability, supporting conservation strategies for archaeological and historical sites. Second, it can provide information required to interpret the interaction between natural, dynamic systems and anthropogenic pressure. The geomorphological framework thus becomes a bridge between geological and natural systems and risk analysis, helping to distinguish long-term evolutionary trends from short-term hazardous events.

In this context, geomorphological maps are a thematic cartographic product that describe the distribution, shape, and genesis of landforms, together with the processes that created or modified them. It is not merely a morphological description, but rather an interpretative synthesis that combines geological, structural, and climatic information to represent the active surface processes in their spatial context-

The core function of a geomorphological map is to illustrate:

- The morphogenetic domains that dominate the terrain (e.g., geostructural, gravitational, fluvial, coastal, volcanic, anthropogenic);
- The state of activity of each landform (active, inactive, relict);
- The chronological relations among landforms.

Through these elements, geomorphological maps enable the direct identification of causal relationships between terrain morphology and natural hazards.

For instance, active gravitational landforms correspond to potential instability sources, fluvial terraces may constrain flood extents, and coastal notches mark the transition between marine and subaerial processes.

While geological maps describe the lithological and geostructural characteristics of the subsurface, geomorphological maps depict the surface expression of those structures and the processes acting upon them. Together, they form a two-tiered system: the geological layer provides the mechanical and stratigraphic context, and the geomorphological layer expresses its morphological and dynamic characteristics. This complementarity is fundamental for multi-hazard analysis, because geological data alone cannot capture the active processes and their temporal variability. In contrast, geomorphological data cannot be interpreted without geological constraints.

Within the TRIQUETRA Project, geomorphological maps serve as a foundational dataset for the Geohazard Severity Charts (GSCs) and the Risk Quantification Module of the Decision Support System (DSS). They provide the morphological basis required to interpret hazard indices and scenario maps described in Deliverable D2.2 – Report on Geological Risk Identification.

Specifically, geomorphological maps contribute to the Risk Quantification Module of the TRIQUETRA DSS Platform by:

- Defining the geomorphological context of each pilot site, identifying slopes, valleys, terraces, and coastal segments that control hazard distribution;
- Delineating process domains (erosional, depositional, geostructural);
- Supporting susceptibility analysis for landslides, floods, coastal erosion, and subsidence;
- Enabling potential temporal comparisons through successive updates, supporting the dynamic assessment of evolving hazard scenarios.

Their inclusion in the DSS, therefore, ensures that risk quantification is not limited to static indicators but also integrates the spatial and morphological dimensions of the processes affecting CH sites.

17.2. Methodological Description

17.2.1. Landforms Origin and State of Activity

Every geomorphological map is founded on the recognition that landforms are the visible outcome of dynamic processes acting on geological materials. The interpretation of these forms therefore requires a genetic classification of landforms according to their morphogenetic domain, their state of activity, and their chronological relation. Morphogenetic domains represent the principal process environments responsible for shaping the landscape:

- The **geostructural domain** encompasses landforms controlled by tectonic or lithological structures, such as fault scarps, joint-controlled ridges, cuestas, and folded reliefs;
- The **gravitational domain** includes all slope processes driven by gravity, from large-scale mass movements to slow deformations;
- The **fluvial domain** comprises landforms generated by running water—channels, terraces, alluvial fans, and erosional scarps;
- The **coastal domain** refers to landforms shaped by marine dynamics, including cliffs, beaches, and shore platforms;
- The **volcanic domain** is characterised by cones, lava flows, pyroclastic deposits, and collapse structures;
- The **anthropogenic domain** includes forms produced or heavily modified by human activity, such as embankments, excavations, terraces, and archaeological features.

Each landform is also classified according to its state of activity, which expresses the current intensity of the controlling process. Active forms display morphological freshness, bare surfaces, or direct evidence of movement. Inactive forms represent dormant processes that may be reactivated. Relict forms are abandoned features that record past morphogenetic environments.

Finally, chronological relations describe the relative temporal succession among landforms, allowing reconstruction of landscape evolution. Distinguishing active, recent, and ancient generations provides a temporal hierarchy that supports hazard evaluation and the prioritisation of conservation measures. This conceptual framework underlies the geomorphological mapping approach adopted in the TRIQUETRA project, guiding the field and remote-sensing analyses described below.

17.2.2. Data Sources and Pre-Mapping Analysis

Geomorphological mapping combines multiple data sources of complementary scales and resolutions. The procedure integrates desk-based compilation, remote-sensing analysis, and field validation.

A. Desk-based sources:

- National geological and topographical maps:

- ISPRA Geoportale Nazionale (http://www.pcn.minambiente.it/mattm/servizi-ogc/);
- Swisstopo (https://www.swisstopo.admin.ch/en/satellite-images) ;
- BGR Geoportal (https://geoportal.bgr.de) (Fig. 2-1) ;
- PGI Poland (https://www.pgi.gov.pl/en/services.html);

- Land cover data:
  - Copernicus Land Monitoring Service (https://land.copernicus.eu/);
  - CORINE Land Cover (https://land.copernicus.eu/pan-european/corine-land-cover) (Fig. 2-2);
- DEMs:
  - TINITALY (https://tinitaly.pi.ingv.it);
  - EU-DEM v1.1 (https://dataspace.copernicus.eu/explore-data/data-collections/copernicus-contributing-missions/collections-description/COP-DEM);
- Thematic hazard maps:
  - ELSUS v2 Landslide Susceptibility (https://esdac.jrc.ec.europa.eu/content/european-landslide-susceptibility-map-elsus-v2);

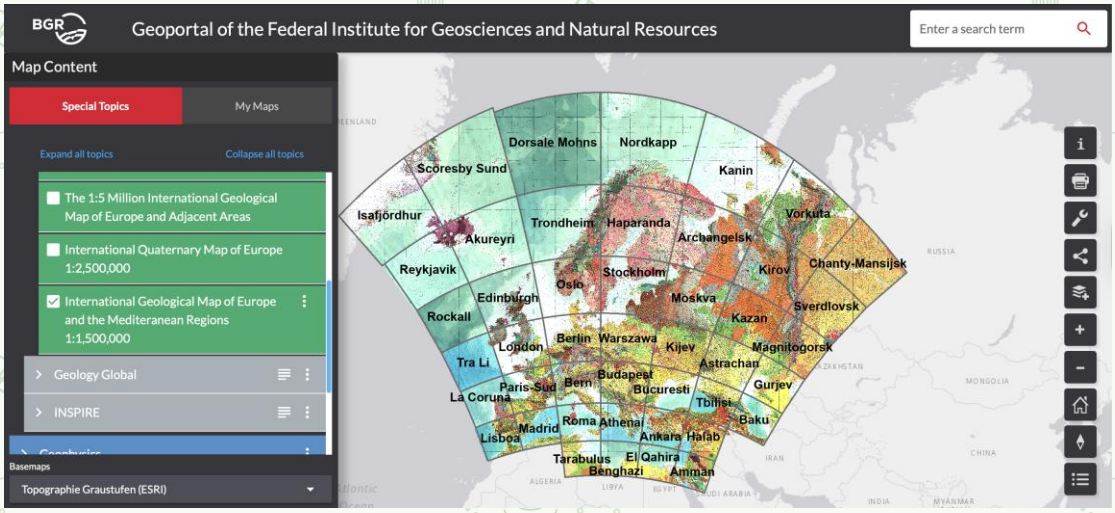

Figure 30: Example from the BGR Geoportal for consulting European-scale geological maps.

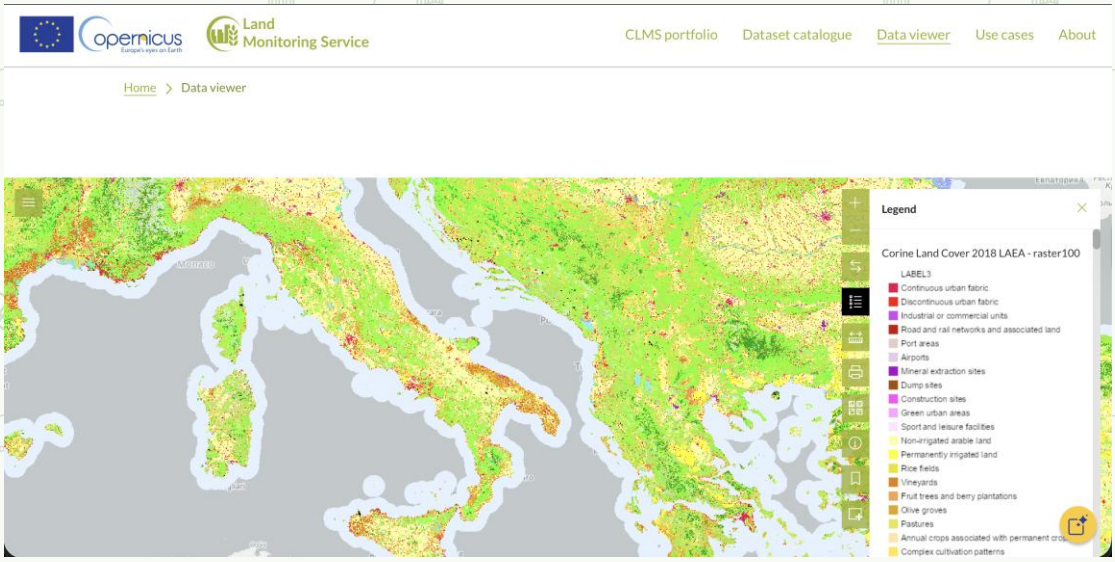

Figure 31: Example from the Copernicus Land Monitoring Service for consulting Land Cover features at the European-scale.

B. Remote-Sensing Analysis

- Optical imagery (Sentinel-2, PlanetScope, UAV orthophotos);
- Morphometric parameters derived from DEMs (slope, aspect, curvature, drainage network);
- Ground-motion data from Copernicus EGMS (https://egms.land.copernicus.eu/);
- Historical aerial imagery for multi-temporal assessment.

C. Field Validation

Targeted field surveys can confirm the nature, geometry, and activity of mapped landforms and geomorphological features. Field observations encompass lithological contacts between different geological formations, geomechanical surveys of outcropping rock masses, identification of slope and ground instabilities, erosion, or accumulation, as well as anthropogenic modifications.

D. Mapping Scale, Legend, and Symbology

The selection of mapping scale and the use of a consistent legend are essential to ensure interpretative precision and interoperability between sites. Geomorphological information is inherently hierarchical: large-scale processes (tectonics, drainage, and coastal evolution) condition medium-scale landforms (slopes, valleys, and fluvial terraces), which in turn control small-scale features (scarps, notches, and debris cones). The scale must therefore reflect the intended level of analysis and the available data resolution.

Table 9: Simplified scheme of the recommended scales of investigation and representation according to the specific objective.

Purpose	Scale	Typical Application

Regional mapping	1:50k – 1:25k	Physiographic settings, drainage and geostructural domains
Local mapping	1:10k – 1:5k	Mapping slope units and single landforms
Detail–monitoring	1:2k – 1:1k	Detailed instability features affecting archaeological sites

For example, in terms of cartographic base-layer, detailed geomorphological reconstructions require high-resolution orthophotos or hillshades generated from a Digital Elevation Model (DEM) with a spatial resolution of at least 2–5 m (e.g., UAV-derived, LiDAR, or photogrammetric DSM) (Fig. 2-3). For steep or coastal sites, oblique orthophotos and 3D perspective views can enhance the perception of complex morphologies.

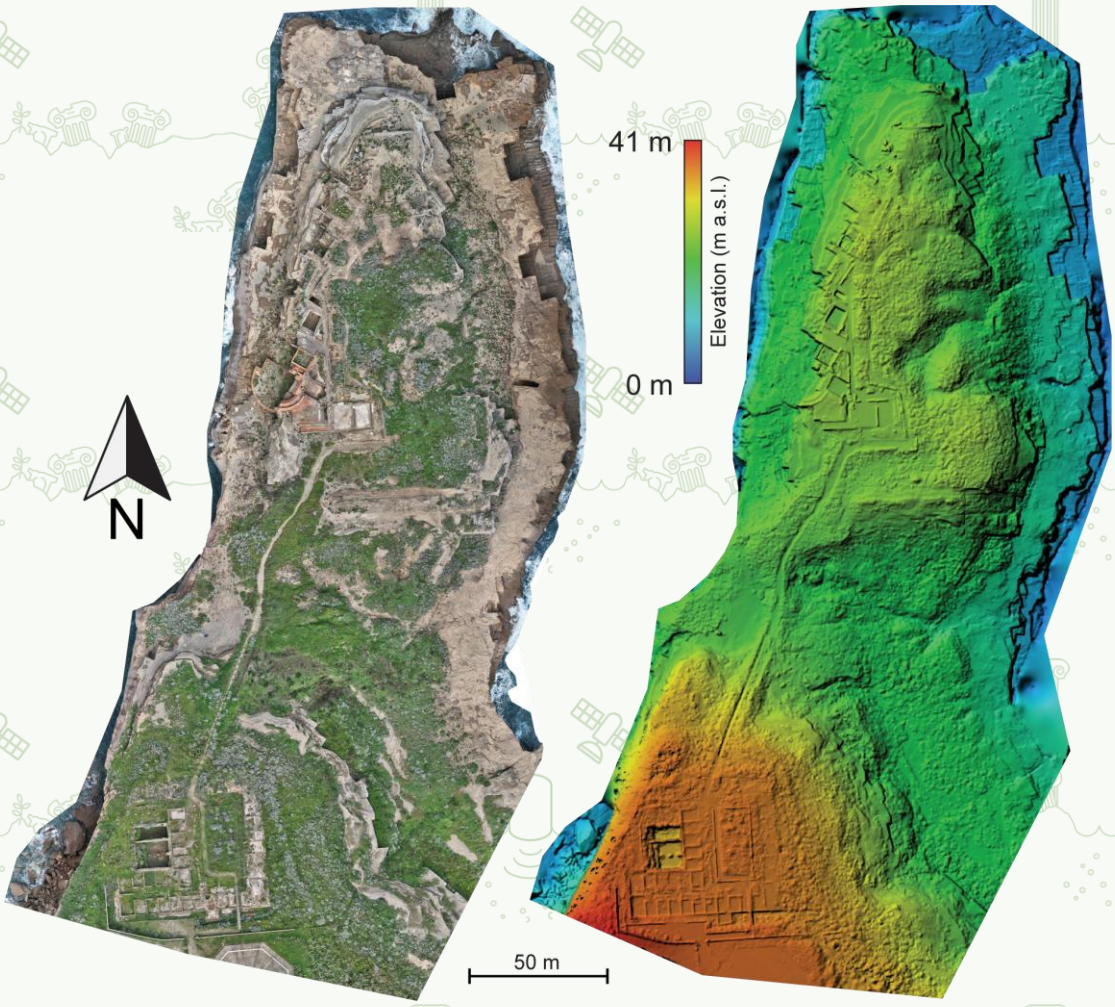

Figure 32: Example of high-resolution UAV-based orthophoto and DEM for the pilot site of Ventotene.

E. Legend and classification scheme

Geomorphological map legends are generally structured according to three fundamental descriptors:

1. Morphogenetic domain and process type – each landform is classified according to the prevailing morphogenetic process:

- Structural: controlled by tectonic and lithological structures.
- Gravitational: resulting from slope mass movements.
- Fluvial: due to running water and sediment transport.
- Coastal–marine: shaped by wave and tidal action.
- Volcanic: originating from volcanic construction or collapse.
- Anthropogenic: produced or modified by human activity.

2. Geological features and involved lithologies; this attribute is critical for assessing mechanical behaviour and susceptibility to erosion or general instability.
3. Activity and chronology to describe the state and evolutionary trends of the process:

- Active: showing ongoing deformation or erosion;
- Inactive or dormant: no current activity but potential reactivation;
- Relict or fossil: produced under past morphoclimatic conditions.

F. Symbology

To guarantee interoperability among sites, the following conventions are generally adopted:

- Line features: solid lines for active scarps and channels; dashed or dotted lines for relict or uncertain boundaries.
- Polygon fill: colour hues indicate morphogenetic.
- Point symbols: used for localised forms such as sinkholes, collapse pits, or spring heads.
- State of activity: colour saturation can sometimes be used to differentiate active (saturated hue) from inactive (pale hue) features.

All symbols must be documented in a legend table accompanying each digital map, ensuring direct translation into the TRIQUETRA database schema (Fig. 33).

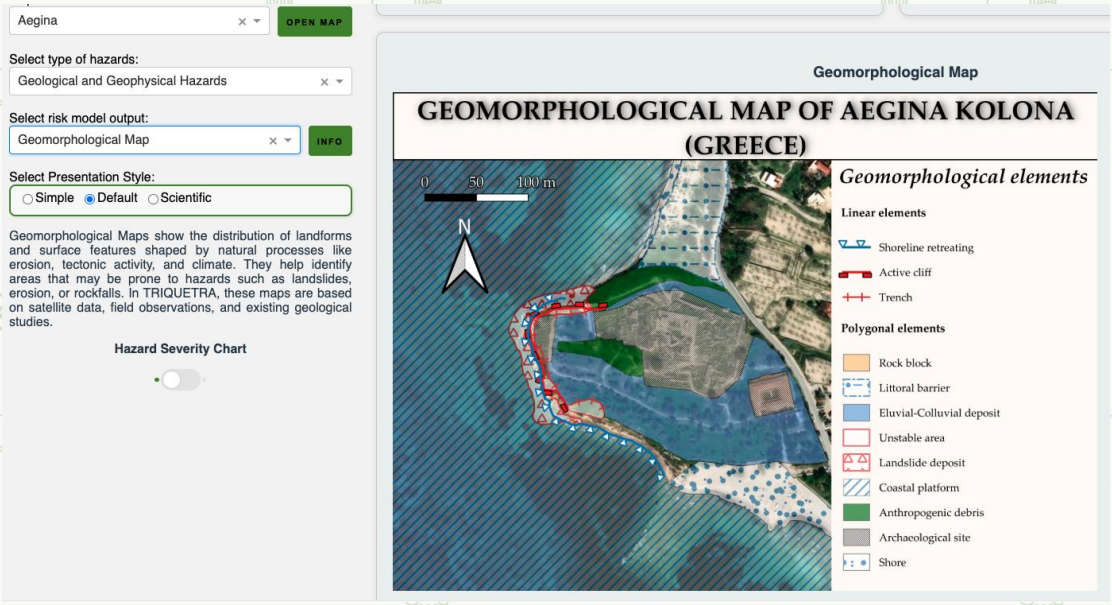

Figure 33: Example of the geomorphological map reconstructed for the pilot site of Aegina. Linear and polygonal elements describe the geomorphology of the area by presenting local landforms useful for investigating geological and natural hazards.

17.2.3. Surveying and Mapping Workflow

A. Definition of the Area of Interest (AoI)

The AoI is delineated based on physiographic boundaries such as watershed divides, coastal segments, or archaeological site perimeters (Fig. 33). The same delineation is used across all modules (e.g., GSCs) to maintain spatial consistency.

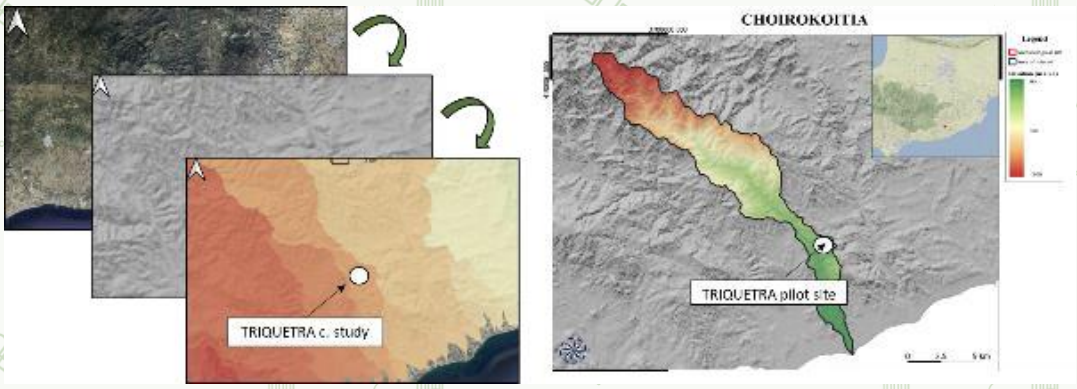

Figure 34: Physiographic unit analysis for the pilot site of Choirokoitia.

B. Database Compilation

All relevant datasets are imported into a GIS environment, including geological maps, orthophotos, DEMs, geostructural data, and existing hazard inventories.

As previously mentioned, primary sources include (but are not limited to):

- Copernicus Land Monitoring Service – https://land.copernicus.eu/
- EU-DEM – https://land.copernicus.eu/imagery-in-situ/eu-dem/
- TINITALY DEM – https://tinitaly.pi.ingv.it/

- ISPRA Geoportale Nazionale – http://www.pcn.minambiente.it/mattm/servizi-ogc/
- European Ground Motion Service (EGMS) – https://egms.land.copernicus.eu/

C. Morphometric Analysis

Digital terrain analysis is conducted to extract quantitative parameters: slope, aspect, curvature, flow accumulation, and relative relief. These parameters reveal morphological discontinuities that may correspond to faults, scarps, or drainage boundaries. Outputs are stored as raster layers and used to guide manual interpretation.

D. Remote Interpretation and Landform Delineation

Using high-resolution imagery (Sentinel-2, PlanetScope, UAV orthophotos), landforms are manually delineated within the GIS. Polygon and line features are classified by domain and activity state following the legend defined in the previous paragraphs. This phase emphasises geomorphic reasoning—formes, processes, and geological features must be consistent.

E. Field validation and survey

Targeted field campaigns verify ambiguous features and document evidence of recent or past activity. Measurements can include:

- Geological field mapping (rock mass discontinuities, lithological contacts, tectonic elements);
- Kinematic indicators of instabilities (shear zones, active scarps, landslide deposits, etc…);
- Surface characteristics (weathering, vegetation cover, soil development).

Field data can be recorded using differential GNSS or mobile GIS apps to ensure metric to centimetric accuracy. Each mapped feature is assigned standard attributes, such as ID, geomorphic domain, dominant process, geology, state of activity, source, and date.

F. Quality Control, Harmonization, and Export

Maps undergo systematic review to ensure internal consistency and adherence to accepted standards. Topological checks (no overlaps, closed polygons, consistent boundaries) are mandatory before export.

Final products are exported as Shapefile and GeoPackage formats, accompanied by metadata for allowing easy sharing across different users and platforms. Metadata can generally include information such as author, institution, data sources, scale, coordinate system, and versioning.

17.3. Conclusion and Recommendations

Geomorphological mapping, when embedded within a digital decision-support infrastructure, transcends its traditional descriptive role and becomes a diagnostic and predictive instrument. By standardising mapping procedures, adopting interoperable legends, and linking field observations with digital analyses, the TRIQUETRA methodology establishes a robust framework for multi-hazard risk assessment in cultural heritage environments.

17.4. Contributors

Developed by: Sapienza University of Rome (SUR)

Date of last update: 10/11/2025

Lead contributors:

- Federico Feliziani
- Gian Marco Marmoni
- Mattia Montagnese
- Salvatore Martino
- Stefano Rivellino
- Guglielmo Grechi
- Francesca Bozzano
- Gabriele Scarascia Mugnozza

18. Geohazard Severity Charts (GSC)

18.1. Overview

The Geohazard Severity Charts (GSCs) were developed within the framework of Deliverable D2.2 - Report on Geological Risk Identification to systematize and compare the main geological and climatic hazards affecting Cultural Heritage (CH) sites investigated by the TRIQUETRA project. The GSCs constitute a semi-quantitative, harmonized framework for assessing the relative severity of natural processes at the European scale. This methodology aims to ensure a consistent representation of the spatial variability, recurrence, and potential impact of natural hazards on CH assets, allowing both intra-site and inter-site comparison. The GSCs were conceived as a synoptic visualization tool to express hazard severity through standardized Intensity Levels (ILs), combining both quantitative parameters (e.g., ground acceleration, wave height, frost days) and qualitative expert-based evaluations.

The GSC approach integrates heterogeneous data sources derived from European and national hazard repositories, combined with site-scale geological and geomorphological analyses. This enables the derivation of hazard indicators even in

contexts characterized by limited in-situ data availability, ensuring comparability across the project's pilot sites.

The resulting products are organized into two complementary families:

- Natural Hazard-Specific Charts (NH-Specific): matrices illustrating hazard severity for each Type of Process (ToP) as a function of the Time of Recurrence (ToR);
- Cultural Heritage-Specific Charts (CH-Specific): integrated charts summarizing all relevant ToPs for a single CH site, thus providing an overall view of the multi-hazard framework affecting it.

18.2. Methodological Description

18.2.1. Conceptual framework

The Geohazard Severity Charts (GSCs) are structured using a matrix-based approach. Each matrix represents the intersection of two main parameters:

1. Type of Process (ToP) – defining the natural or geological process under consideration;
2. Time of Recurrence (ToR) – defining the time interval considered for the probability of occurrence of that process.

The intersection between the two parameters allows defining the Intensity Level (IL) associated with the expected magnitude or effect of the process over the chosen time frame. The IL is represented using a chromatic semaphoric scale (green → low; red → very high), as shown in Figure 35.

Figure 35: Intensity Level semaphoric scale.

This methodological design allows the comparison of hazard severity across both different processes and sites, while maintaining a consistent conceptual basis. Each ToP is characterized by a Severity Index (SI), representing either a quantitative or qualitative parameter that best describes the intensity or susceptibility of the process. The GSCs therefore translate complex hazard data into an interpretable format that expresses, for each ToP and ToR, the degree of expected geological or climatic impact on a given CH site.

18.2.2. Types of Processes (ToP)

Nine principal Types of Processes were analyzed within TRIQUETRA, reflecting the dominant geological, hydrological, meteorological and climatic hazards relevant to CH sites:

1. Seismic hazard
2. Tsunami hazard
3. Sea-wave hazard
4. Wind hazard
5. Flood hazard
6. Landslides
7. Geotechnical subsidence (Static and Dynamic components)
8. Wildfires
9. Weather events (Heat waves and Frost events)

Certain ToPs were further disaggregated into secondary categories to better represent their internal variability (Fig. 36). For instance, Landslides were subdivided into “Falls,” “Slides,” and “Flows,” while Geotechnical Subsidence was split into Static (long-term ground displacement) and Dynamic (liquefaction-related) types. Similarly, Weather Events were treated as “Heat” or “Frost” events.

Each ToP was selected through a preliminary physiographic and geological assessment of the CH sites, ensuring relevance to local processes. Climatic and meteorological ToPs were included to reflect the role of climate change in modifying hazard occurrence and intensity.

TRIQUETRA
Toolbox for assessing and mitigating Climate Change risks and natural hazards threatening cultural heritage

Severity Geo-Hazard Chart

Geohazard Identification

Case study	Type of processes																					
	Seismic	Floods	Landslides				Geotechnical subsidence		Wildfires	Weather event			Sea Waves	Wind	Tsunami
			Type of landslide				Type of subsidence			Type of weather event					
			Fall	Slide	Flow		Static Load	Dynamic Load		Heat wave	Freezing				
Aegina	X		X				X		X	X			X	X	X
Choirokoitia	X		X				X	X	X	X				X	
Epidauro	X						X	X					X	X	X
Les Argilliez	X	X					X	X			X			X	
Kalapodi	X						X		X	X	X			X	
Roseninsel	X						X				X			X	
Smuszewo	X						X		X	X	X			X	
Ventotene	X		X				X		X	X			X	X	X

Figure 36: Geohazard identification table.

18.2.3. Time of Recurrence (ToR)

The Time of Recurrence (ToR) represents the time window considered in the hazard analysis. It expresses the expected recurrence period of a process of given magnitude and is directly related to its probability of occurrence.

In the TRIQUETRA framework, four main ToR intervals were adopted:

- 1–10 years,
- 10–100 years,
- 100–1,000 years,
- >1,000 years.

By integrating ToRs of different duration, it becomes possible to define multiple hazard scenarios and understand how severity evolves as the recurrence interval increases.

For most processes, the longer the ToR, the higher the expected intensity and thus the hazard severity. The ToR parameter therefore introduces a temporal dimension into the GSCs, enabling users to compare hazard severity not only spatially (among sites) but also temporally (across recurrence scales).

18.2.4. Intensity Level (IL) and Severity Index (SI)

The Intensity Level (IL) expresses the relative magnitude of a natural process over a specified ToR. It is derived directly from the Severity Index (SI), which quantifies the characteristic property of the process. Depending on the nature of the hazard, the SI can be:

Quantitative, expressed in physical units (e.g., Peak Ground Acceleration (PGA) in g, wind speed in knots, frost days in number per period, displacement rate in mm/year);

Qualitative, based on expert judgment when a numerical indicator cannot be defined (e.g., Dynamic Subsidence susceptibility).

Each SI was classified into four IL classes:

- Low (green)
- Medium (yellow)
- High (orange)
- Very High (red)

Two additional categories were introduced for cases with missing or non-applicable data:

- Not Considerable (white): process not active or not relevant for the site.
- Not Detectable (grey): process not quantifiable with available information.

An additional marking (*) identifies cases in which the hazard acts indirectly on the CH site (e.g., process active within the AoI but not on the archaeological area itself).

Severity Index						
Peak Ground Acceleration (PGA) [g]						
Not considerable	Not detectable	Low	Medium	High	Very High	Indirectly
		0 - 0.2	0.2 - 0.4	0.4 - 0.6	> 0.6	
						*

Figure 37: Example of Severity Index table for seismic hazard.

18.2.5. Input Data and Sources

A. Public data repositories and databases

The GSCs were produced by integrating open-access and institutional datasets that describe natural hazard conditions at European and national scales.

These datasets were selected for their reliability, update frequency, and spatial coverage.

Table 1 of D2.2 lists all sources used for each Type of Process (ToP).

The primary data providers include:

- EFEHR – European Facilities for Earthquake Hazard and Risk (Seismic models) – http://www.efehr.org/start/.
- INGV – National Institute of Geophysics and Volcanology, Italy (Seismic model MPS04-S1) – http://www.ingv.it.
- GFZ – German Research Centre for Geosciences (Seismic hazard model) – https://www.gfz.de.
- Swiss Seismological Service, ETH Zürich (Seismic hazard model for Switzerland) – http://seismo.ethz.ch/en/home/.
- JRC-EFAS – European Flood Awareness System (Flood hazard maps) – https://data.jrc.ec.europa.eu/collection/id-0068.
- EMODnet – European Marine Observation and Data Network (Sea-wave height) – https://emodnet.ec.europa.eu/en.
- Copernicus EGMS – European Ground Motion Service (Static subsidence) – https://egms.land.copernicus.eu.
- LIQUEFACT / ECLiq – European catalogues for liquefaction hazard (Dynamic subsidence)

- ELSUS v2 – European Landslide Susceptibility Map (JRC) – https://esdac.jrc.ec.europa.eu/content/european-landslide-susceptibility-map-elsus-v2.
- EFFIS – European Forest Fire Information System (Fire Weather Index) – https://forest-fire.emergency.copernicus.eu.
- ThinkHazard – Platform for meteorological and climatic hazard likelihood (Heat, Frost, and general climate hazards) – https://thinkhazard.org/en/
- TSUMAPS-NEAM – Probabilistic tsunami hazard maps for the NEAM region – https://tsumaps-neam.eu

These sources were complemented by national geological surveys, Copernicus-derived thematic layers, and site-specific geomorphological surveys.

B. Data Integration and Harmonization

Each dataset exhibits different spatial resolutions, reference systems, and hazard descriptors. To ensure comparability across all TRIQUETRA sites, the following harmonization procedures were applied:

- Adoption of common SI classes: All processes were normalized to four IL classes (Low, Medium, High, Very High).
- Expert-based classification: Where quantitative thresholds were unavailable (e.g., for qualitative hazards), class limits were defined through expert judgment.
- Consistency checks: Results from European-scale databases were verified against national or site-specific data to validate their representativeness.
- AoI-based extraction: For each CH site, hazard values were extracted within the corresponding Area of Interest rather than at a single coordinate, ensuring a realistic representation of local variability.

This integration approach enabled the creation of coherent datasets that describe seismic, hydrological, geomorphological, and climatic processes in a standardized manner.

18.3. Workflow

The preparation of the Geohazard Severity Charts involved a sequence of structured steps ensuring consistency and reproducibility across sites.

18.3.1. Delineation of the Area of Interest (AoI)

A physiographic unit approach was adopted to define the spatial boundaries within which each hazard was evaluated. For every CH site, a watershed analysis was conducted in a GIS environment, producing an Area of Interest (AoI) that encompasses the entire drainage network and local topographic catchment (Fig. 38).

This step is essential because many hazards (e.g., floods, landslides) are controlled by broader physiographic factors that extend beyond the archaeological boundaries.

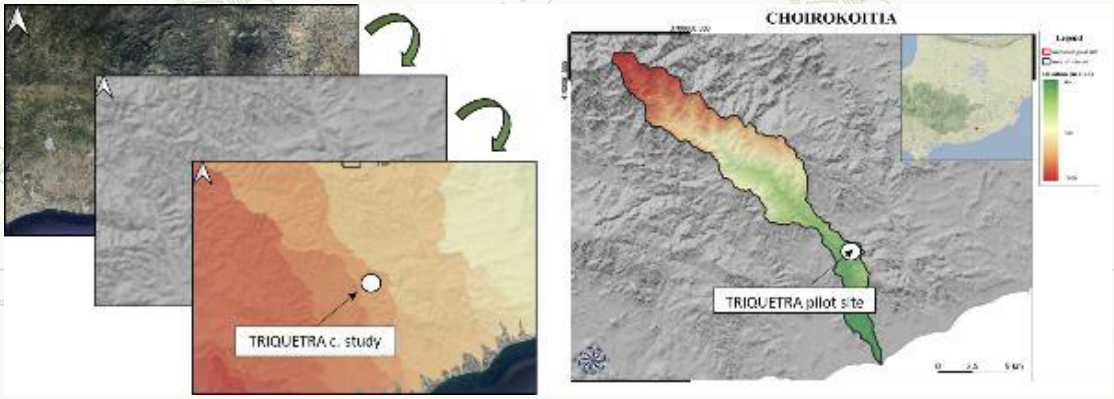

Figure 38: Example of the AoI for the pilot site of Choirokoitia.

18.3.2. Selection and Extraction of Hazard Parameters

Within each AoI, hazard parameters corresponding to each ToP were extracted from the relevant datasets. For quantitative processes, direct numerical indicators were retrieved (e.g., PGA for seismic hazard, mm/year displacement for subsidence, wind speed for wind hazard). For qualitative processes, categorical indices from susceptibility maps were used (e.g., ELSUS classes for landslides). Each value was then converted into a Severity Index (SI) class according to the corresponding classification tables (Fig. 39).

Severity Index						
Frost Days (n. of T<0° days in the 1971-2020 period)						
Not considerable	Not detectable	Low	Medium	High	Very High	Indirectly
		<100	100-120	120-140	>140	
						*

Figure 39: Example of Severity Indexes for Frost Hazard.

18.3.3. Construction of Natural Hazard (NH) Specific Charts

Each Natural Hazard–Specific Chart presents a two-dimensional matrix where:

- The x-axis represents the Time of Recurrence (ToR),
- The y-axis represents the Cultural Heritage sites.

The IL (derived from SI) is plotted in each cell, defining a color-coded representation of severity.

NH-Specific Charts were prepared for all nine ToPs, providing an overview of each hazard type across all sites (Fig. 40).

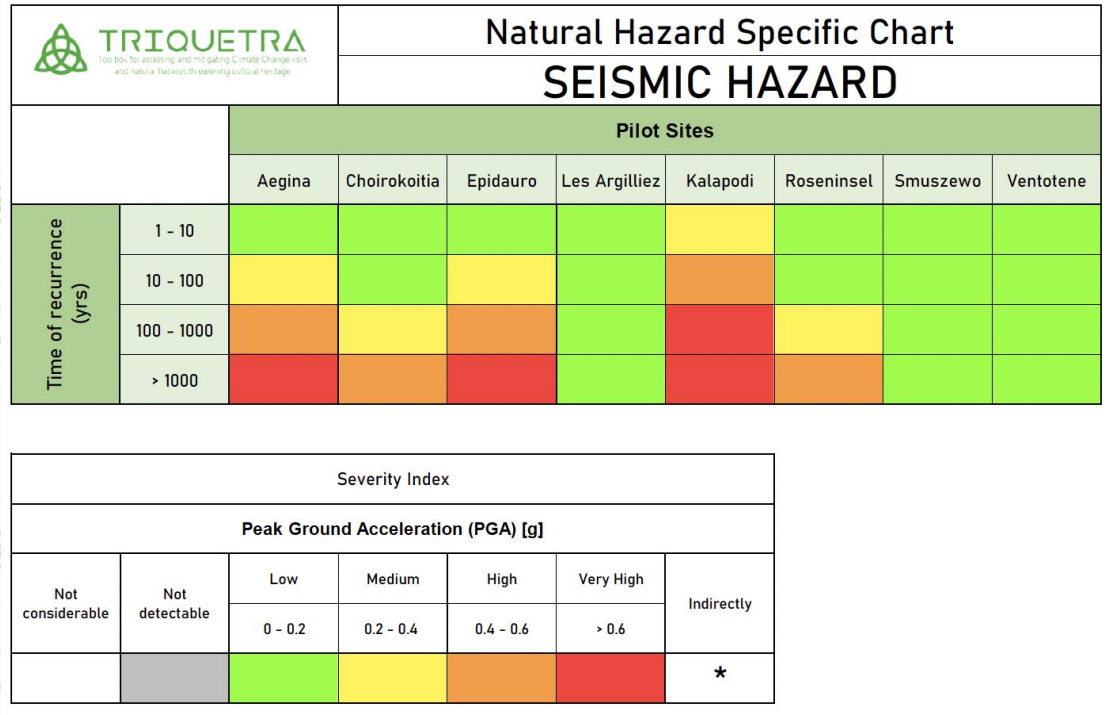

Figure 40: Natural hazard-specific chart for Seismic Hazard across all pilot sites.

18.3.4. Compilation of Cultural Heritage (CH) Specific Charts

The CH-Specific Charts synthesize the results of all NH-Specific Charts for each CH site. They display all ToPs in a single matrix and express, for each, the IL class corresponding to the defined ToR intervals. The use of color coding (green to red) enables an immediate visual identification of the dominant hazards at each site.

Additional conventions adopted in the CH-Specific Charts:

- ***White cells*** indicate processes not applicable to the site (Not Considerable)
- ***Grey cells*** indicate hazards not quantified due to insufficient data (Not Detectable).
- ***Asterisk**** denotes processes indirectly affecting the site (Indirectly).

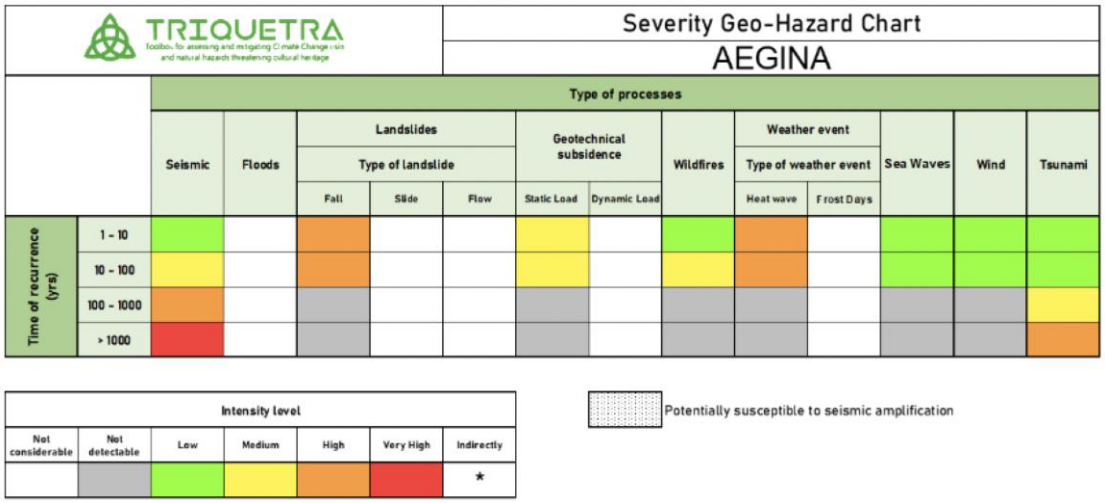

Figure 41: CH-specific Geohazard Severity Chart for the pilot site of Aegina.

18.3.5. Comparative Analysis

The final step involved the comparative analysis of all CH-Specific Charts. For each ToP and recurrence time, the corresponding ILs were compared across all CH sites to identify the most critical hazards. This overview was visualized with histograms showing the distribution of geohazard priorities. The resulting GSC framework offers a unified basis for prioritizing subsequent detailed studies, numerical simulations, and conservation efforts strategies.

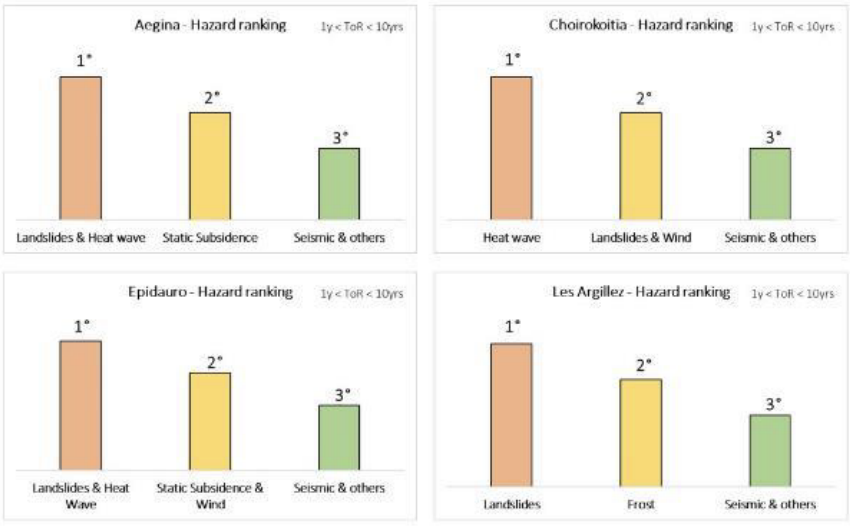

Figure 42: Histograms representing the distribution of geohazard priorities in the individual project CHs.

18.4. Conclusive Remarks and Perspectives

This work represents the first integrated attempt within the TRIQUETRA project to synthesize and compare the main geohazards affecting the Cultural Heritage (CH) sites through the construction of Geohazard Severity Charts (GSCs).

The methodology adopted in Deliverable D2.2 merges data, catalogues, and bibliographic information available from technical–scientific sources and previous European projects, harmonizing them within a unified analytical framework. The

primary advancement introduced by the GSC approach lies in its synoptic restitution of the natural hazards affecting each CH site. By classifying the intensity of individual geohazards into standardized Intensity Levels (ILs), it becomes possible to preserve the quantitative meaning of each hazard indicator while enabling direct comparison among different processes and sites.

This indexing criterion ensures that both local-scale and continental-scale information can be interpreted coherently, supporting a harmonized multi-hazard assessment. The analysis was extended to multiple recurrence times, covering where possible time windows up to the order of thousands of years. This temporal dimension allows not only an evaluation of the present hazard conditions but also a first approximation of their evolution in long-term geological and climatic scenarios—thus preparing the basis for subsequent risk-oriented analyses within the project.

Building upon these results, several research directions can be pursued in the continuation of TRIQUETRA activities:

1. Focused investigations on hazard severity, to refine the evaluation of processes most relevant for the vulnerability of specific archaeological contexts;
2. Quantification of dominant stressors, for those geohazards exerting significant forcing on CH sites, enabling a quantitative assessment of their effects on both the surrounding environment and the exposed artefacts;
3. Direct integration of established hazard models into quantitative risk analyses, where existing datasets already provide harmonized parameters at European scale.

This latter approach is particularly suitable for seismic hazards, whose basic action parameters—such as Peak Ground Acceleration—have already been standardized across Europe through probabilistic models (e.g., ESHM20). Nevertheless, site-specific factors such as local seismic amplification, controlled by stratigraphic or topographic conditions, may require targeted investigations at sites where seismic risk is a priority. Conversely, hazards driven by meteorological or climatic forcing (e.g., heat, frost, intense rainfall, or wind) demand additional studies, as the available datasets typically provide hazard estimates limited to centennial recurrence windows. For such cases, and especially for sites exposed to marine or atmospheric processes—like Aegina Kolona and Ventotene—the coarse spatial resolution of continental datasets cannot capture the fine-scale variability of local instability phenomena.

Future analyses will therefore require the integration of physically based, quantitative models capable of scaling external forcing actions to their effects at the archaeological-site level. In this perspective, the application of new monitoring technologies and experimental detection methods—including in-situ sensors,

remote sensing platforms, and ambient vibration measurements—will be crucial to fill existing knowledge gaps and validate model outcomes. Finally, for certain geohazards such as snow cover, data currently available at European level do not allow direct quantification of hazard intensity from climatic parameters alone. For these processes, statistical or physically based atmospheric models should be implemented to derive reliable forcing indicators.

In conclusion, the Geohazard Severity Charts provide a foundational framework for the comparative evaluation of natural hazards across TRIQUETRA Cultural Heritage sites. They represent a first step towards the quantitative risk analysis phase, serving as a technical and conceptual basis for future project discussions and working tables. The transition from identification to quantification of geohazards will enable a more robust assessment of site-specific risks and the design of effective mitigation and conservation strategies aligned with the objectives of the TRIQUETRA project.

18.5. References

Bozzoni, F., Bonì, R., Conca, D., Lai, C. G., Zuccolo, E., & Meisina, C. (2021). Megazonation of earthquake-induced soil liquefaction hazard in continental Europe. Bulletin of Earthquake Engineering, 19, 4059-4082.

Bozzoni, F., Cantoni, A., De Marco, M. C., & Lai, C. G. (2021). ECLiq: European interactive catalogue of earthquake-induced soil liquefaction phenomena. Bulletin of Earthquake Engineering, 19(12), 4719-4744.

Danciu L., Nandan S., Reyes C., Basili R., Weatherill G., Beauval C., Rovida A., Vilanova S., Sesetyan K., Bard P-Y., Cotton F., Wiemer S., Giardini D. (2021) - The 2020 update of the European Seismic Hazard Model: Model Overview. EFEHR Technical Report 001, v1.0.0, https://doi.org/10.12686/a15

Dottori, Francesco; Alfieri, Lorenzo; Bianchi, Alessandra; Skoien, Jon; Salamon, Peter (2021): River flood hazard maps for Europe and the Mediterranean Basin region. European Commission, Joint Research Centre (JRC)

Grünthal, G., Stromeyer, D., Bosse, C., Cotton, F., & Bindi, D. (2018). The probabilistic seismic hazard assessment of Germany—version 2016, considering the range of epistemic uncertainties and aleatory variability. Bulletin of Earthquake Engineering, 16, 4339-4395.

Hungr, O., Leroueil, S., & Picarelli, L. (2014). The Varnes classification of landslide types, an update. Landslides, 11, 167-194.

Stucchi, M., Akinci, A., Faccioli, E., Gasperini, P., Malagnini, L., Meletti, C., ... & Valensise, G. (2004). Redazione della Mappa di Pericolosità Sismica prevista dall'Ordinanza PC del 20 marzo 2003, n. 3274, All. 1 Rapporto Conclusivo.

Wilde, M., Günther, A., Reichenbach, P., Malet, J. P., & Hervás, J. (2018). Pan-European landslide susceptibility mapping: ELSUS Version 2. Journal of maps, 14(2), 97-104

18.6. Contributors

Developed by: Sapienza University of Rome (SUR)

Date of last update: 30/09/2023

Lead contributors:

- Federico Feliziani
- Gian Marco Marmoni
- Mattia Montagnese
- Salvatore Martino
- Stefano Rivellino
- Guglielmo Grechi
- Francesca Bozzano
- Gabriele Scarascia Mugnozza

19. Local Seismic Response Analysis (LSRA)

19.1. Overview

The purpose of this document is to present the methodological approach, computational principles, and interpretative framework used to assess the local seismic amplification effects arising from stratigraphic and topographic characteristics of the selected pilot sites. These effects represent a key component of the geological risk assessment performed across the TRIQUETRA pilot sites.

Analyses were conducted using the licensed LSR2D numerical code, which enables the simulation of wave propagation in two-dimensional geological cross-sections under the assumption of linear elastic or viscoelastic behavior. The software enables the quantification of the expected amplification of ground motion relative to an outcropping bedrock reference condition, thus allowing the identification of critical zones prone to local seismic amplification.

The primary objectives of LSRA are to assess how local geological settings, surface morphology, and structural discontinuities affect the propagation of seismic wavefields, thereby determining modifications in the amplitude, spectral content, and duration of ground shaking, and ultimately contributing to an increase in the related seismic hazard.

The main outputs of LSRA consist of:

- Amplified seismic ground-motion and displacement fields along the modelled cross-sections;
- Local amplification factors, expressed as ratios between surface and reference site responses;

- Amplification functions describing the frequency-dependent response in different areas of the model due to local ground motion modifications.

These results provide a refined quantification of seismic hazard at the site scale and constitute the basis for integrating local effects into the broader hazard framework defined by European and national-scale seismic hazard models (e.g., ESHM20, MPS04) (Fig. 43).

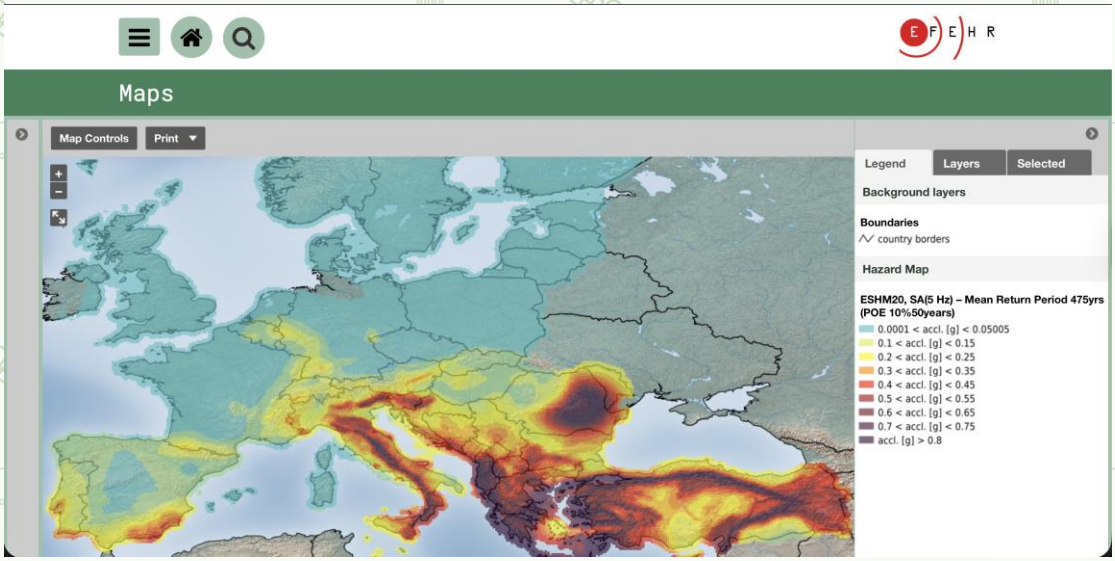

Figure 43: Example of the European Seismic Hazard Model (EHSM20) considering a mean return period of earthquakes of 475 yrs.

19.2. Methodology

19.2.1. Background and Rationale

The amplitude, frequency content, and duration of seismic ground motion are strongly affected by local geological structures and morphological conditions. Variations in shear-wave velocity, seismic impedance contrasts between geological structures and formations, and topographic irregularities may significantly modify the amplitude, duration, and spectral characteristics of ground motion relative to a reference seismic bedrock condition. These phenomena, commonly referred to as local seismic response, can be of particular interest for the correct management and definition of targeted conservation strategies of Cultural Heritage assets. Many archaeological sites are situated in complex geomorphological settings—such as coastal terraces, volcanic islands, or alluvial basins—where local amplification effects may significantly influence and increase the local seismic hazard.

In this framework, the Local Seismic Response Analysis (LSRA) provides an essential complement to probabilistic seismic hazard models, which are typically defined on regional scales and assume average seismic bedrock conditions, therefore lacking all information on local geological and topographic settings. By explicitly modeling the stratigraphic and morphological configuration of each site, LSRA enables the identification of areas where amplification can significantly increase the action of expected ground motion, thus allowing for the refined definition of site-specific

seismic hazard (Antonielli et al. 2021; Martino et al. 2015; Sonmezer et al. 2019; Tallini et al. 2020; Tunar Özcan et al. 2019).

Within the TRIQUETRA project, LSRA contributes to the understanding, identification and quantification of geological risks by translating the regional, probabilistic seismic hazard framework—derived from regional large-scale models—into local amplification metrics that account for the detailed reconstruction of local surface and subsurface conditions. This nontrivial step aims to bridge the gap between large-scale hazard datasets and the specific conditions that can control the seismic vulnerability of CH sites.

The LSRA represents a methodological advancement that complements and refines the geological risk identification conducted in Deliverable D2.2. While that deliverable relied primarily on open-access databases (e.g., EFEHR, EGMS, ELSUS v2, INGV), these products typically neglect site-specific stratigraphic and topographic effects. Through the integration of LSRA, TRIQUETRA achieves a higher-resolution quantification of seismic hazard at the scale of cultural heritage sites. The resulting seismic amplification maps and frequency-dependent amplification functions can be directly correlated with the local geological units defined in the engineering-geological models and with the geomorphological processes described by thematic maps. Consequently, LSRA outputs provide a bridge between regional hazard information and local ground-motion characteristics, supporting a more realistic evaluation of the seismic loadings on CH structures.

19.2.2. Theory and Background

A. Nature of Earthquakes

Earthquakes result from the sudden release of elastic strain energy accumulated in the Earth's crust. This release occurs when the stress acting on tectonic elements (e.g., pre-existing fault plane) exceeds their shear strength, producing a rupture that can propagate within the Earth's crust toward the surface (Fig. 44). The rupture initiates at the focus (or hypocentre) and radiates seismic energy in all directions. The surface projection of this point is known as the epicentre. The energy generated from this rupture then propagates through the crust in the form of elastic waves. These include body waves—P-waves (primary, compressional) and S-waves (secondary, shear)—and surface waves, which travel along the ground–air interface. More in particular, P-waves involve volumetric deformation, whereas S-waves induce shear deformation that is perpendicular to the direction of wave propagation. As seismic waves travel away from the source, their amplitude tends to decrease because of a mechanism known as energy dissipation (intrinsic and scattering attenuation).

The overall energy radiated by an earthquake is related to the fault area, the average slip, and the rigidity of the rocks involved, expressed by the seismic moment M_0:

$$M_0 = \mu A D$$

Where μ is the shear modulus of the rock involved in the rupture, A is the rupture area, and D is the average slip displacement. The earthquake magnitude—such as the moment magnitude M_w—is a logarithmic measure of M_0 and provides a consistent scale for comparing seismic sources:

$$M_w = \frac{2}{3}(log_{10} M_0 - 9.1)$$

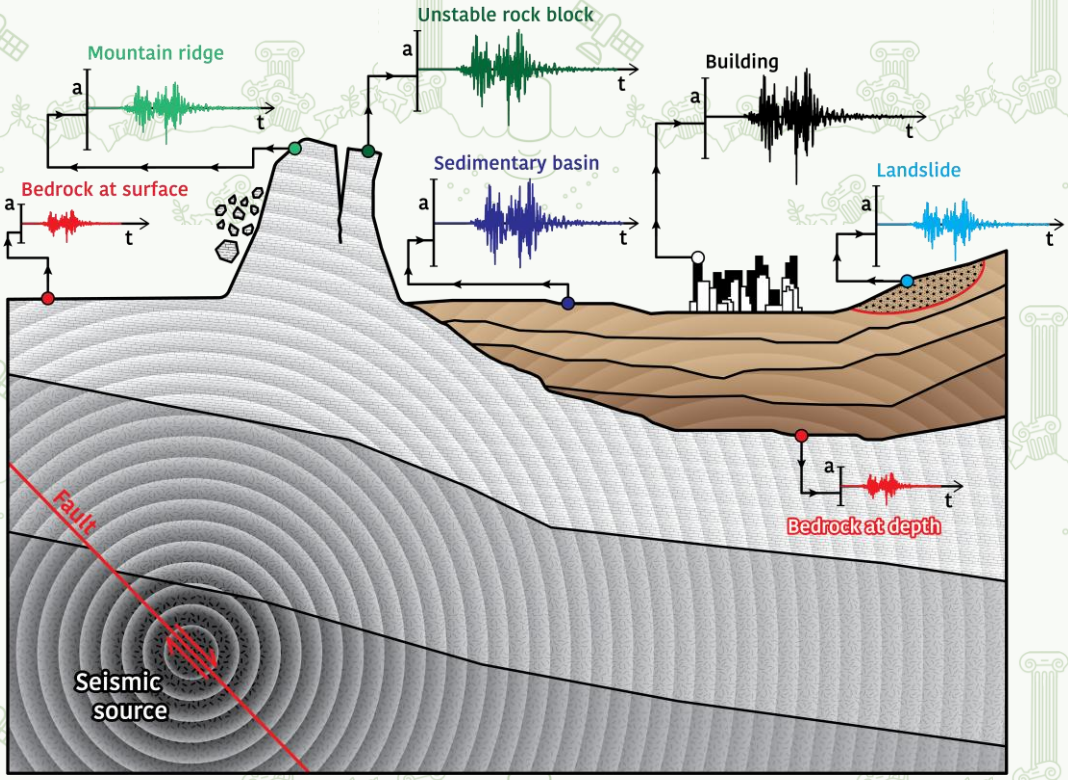

Figure 44: Simplified sketch describing the propagation of seismic waves from the seismic source (hypocentre) toward the surface.

Among the different seismic phases, S-waves play a dominant role in ground shaking and structural damage. Their particle motion is perpendicular to the propagation direction, producing strong horizontal displacements that interact with the dynamic response of surface layers and built structures. The velocity of shear waves depends on the mechanical properties of the medium and can be expressed as:

$$V_s = \sqrt{\frac{G}{\rho}}$$

Where V_s is the shear-wave velocity, G the shear modulus, and ρ the average medium density. Since G increases rapidly with confining pressure and depth, V_s it provides a direct indicator of the stiffness of the soil or rock media. In unconsolidated deposits (e.g., alluvial or landslide deposits), the low V_s values can produce high seismic impedance contrasts with the underlying bedrock, leading to wave trapping and amplification. For this reason, V_s is the key parameter for classifying ground typologies in seismic design codes such as Eurocode 8 or the Italian NTC 2018.

Average $V_{s\,30}$ values, computed over the top 30 m from the surface, are widely used to define site categories and to estimate the expected seismic amplification level.

Therefore, accurate knowledge of the shear-wave velocity profile is fundamental for modelling seismic wave propagation and evaluating the frequency-dependent amplification at the site scale.

B. Local Seismic Response Analysis

The goal of local seismic response analysis is to quantify the variation of surface ground motion with respect to the reference bedrock condition, expressed in terms of amplified accelerations and amplification factors. From a physical standpoint, Local Seismic Response Analysis (LSRA) refers to the quantitative evaluation of the modifications in amplitude, duration, and frequency content experienced by a seismic motion—defined on a reference bedrock formation (R), as it propagates through the overlying soil layers up to the ground surface (S) (Fig. 45).

From a technical perspective, it is often more meaningful to assume as a reference motion the one recorded or computed at a hypothetical—or real—outcropping bedrock site (A) (Lanzo et al., 1999). The quantitative evaluation of the local response is therefore obtained by comparing representative parameters of the seismic motion at the surface of the deposit with those corresponding to the reference rock motion, either in the time domain or in the frequency domain (Fig. 45).

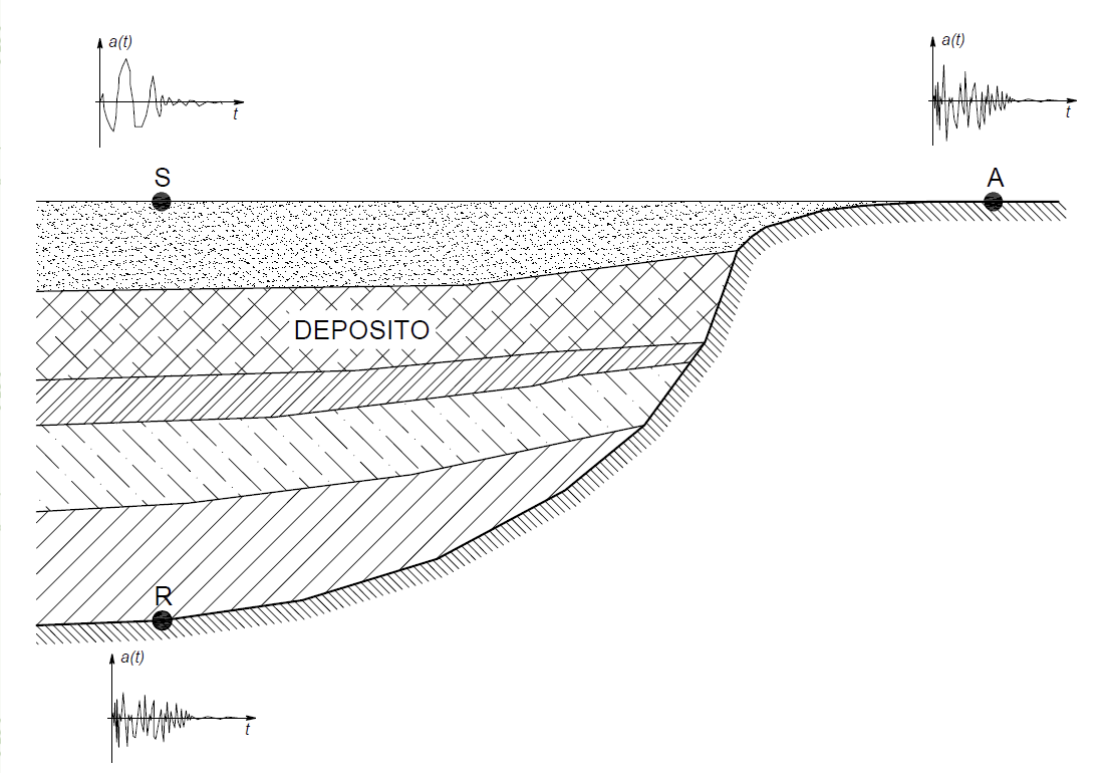

Figure 45: Simplified sketch representing the role of local seismic response in modifying ground motion characteristics (From the LSR2D User Manual).

In the time domain, a frequently adopted parameter is the amplification factor F_A defined as:

$$F_A = \frac{a_{max,S}}{a_{max,A}}$$

where $a_{max,S}$ is the peak acceleration recorded (or computed) at the surface of the soil deposit, and $a_{max,A}$ is the peak acceleration at the outcropping bedrock (Fig. 2-2). Values of F_A greater than unity indicate seismic amplification, whereas values lower than unity indicate seismic attenuation. This parameter provides a concise measure of the relative increase (or decrease) of motion amplitude but does not account for the filtering effect exerted by the soil deposit on the input motion; it therefore describes only the amplitude modification, not the frequency redistribution.

To overcome this limitation, analyses are often performed in the frequency domain, where the soil deposit is treated as a linear system characterized by its transfer function. Let $F_S(f)$ and $F_A(f)$ be the complex Fourier spectra of the ground motion at the surface and at the outcropping rock, respectively.

The transfer function H(f) is defined as:

$$H(f) = \frac{F_S(f)}{F_A(f)}$$

The amplification function is then expressed as the modulus of the transfer function:

$$A(f) = |H(f)|$$

This function quantifies, for each discrete frequency, the ratio between the surface and reference spectral amplitudes, thus identifying which components of the seismic motion are amplified or attenuated by the soil layer. Physically, A(f) describes the filtering behavior of the local site stratigraphy: it enhances certain frequency bands and dampens others according to the geometry of the deposit and the mechanical properties of its materials. It should be emphasized that the use of Fourier transforms and the principle of superposition are valid only when linear constitutive laws can approximate the mechanical response of the soil system. Under this assumption, the amplification function A(f) becomes an intrinsic property of the site, depending solely on its geometry and elastic–viscous parameters. Once the transfer function is known, the surface motion can be computed from the reference motion through the convolution operation:

$$F_S = H(f)F_A(f)$$

This expression indicates that the surface motion is governed by the spectral content of the input motion, $F_A(f)$, which in turn depends on the source mechanism, magnitude, and propagation path of the earthquake. Therefore, both the site

properties and the characteristics of the incoming seismic waves determine the final amplification.

However, in real conditions, the mechanical behavior of soils is nonlinear: shear modulus and damping change with the strain level. Therefore, the transfer function cannot be considered fixed but depends on the strain amplitude caused by seismic excitation. Low-energy motions (i.e., weak motion) produce small deformations and exhibit quasi-linear behavior; high-energy events (i.e., strong motion) can cause larger strains, reducing stiffness and increasing damping, which alters the shape and amplitude of A(f). Consequently, the effective amplification depends on both ground-motion intensity and local material properties.

From an engineering-geological perspective, the ultimate goal of LSRA is to derive site-specific acceleration response spectra, local amplification factors, and expected ground motion shakings that can be considered representative of a given earthquake scenario, thereby incorporating the filtering and amplification effects of local geological and topographic conditions.

19.3. Workflow

For the reader's ease, the following workflow is described through the application case of the Aegina pilot site. This example illustrates all principal steps of the Local Seismic Response Analysis (LSRA) and demonstrates the methodology adopted within the TRIQUETRA project. The same procedure is transferable to other pilot sites, with minor adaptations to local geological and seismotectonic conditions.

19.3.1. Definition of the Engineering-Geological Model and Cross Section

The first step in the LSRA consists in reconstructing the engineering–geological model of the investigated subsoil, which forms the basis for subsequent numerical simulations.

At the Aegina site, geological and geophysical field surveys were conducted across the promontory to characterize the subsurface stratigraphy and identify the primary lithotechnical units (Fig. 46).

Two representative engineering-geological cross-sections were reconstructed to represent the local subsurface conditions (Fig. 3-2). For each distinct layer (engineering–geological unit), the relevant physical properties (i.e., unit weight) and geophysical parameters (shear-wave velocity, Vs) were assigned by combining results from field measurements, laboratory tests, and literature data for comparable lithologies.

These parameters define the stiffness and damping behavior of the materials and directly control the propagation of seismic waves through the modelled stratigraphy.

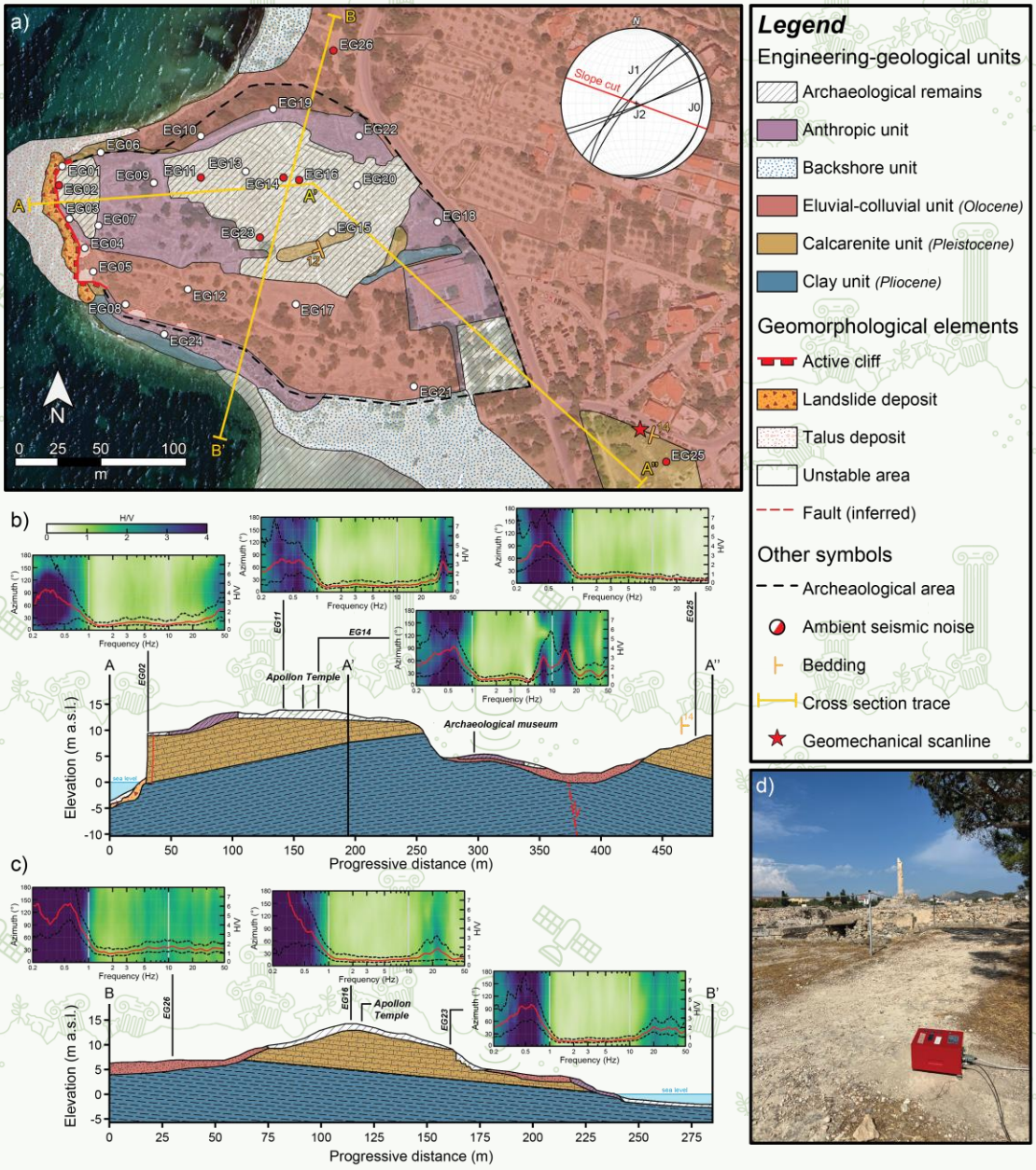

Figure 46: Engineering-geological map of Aegina, showing the main geological units, geomorphological elements, and ambient seismic noise measurement stations. The cross-section traces A-A'-A''(b) and B-B' (c) are indicated in yellow, while the location of the geomechanical scanline is marked with a red star. (d) Example of an ambient seismic noise measurement station, showing the field setup used for recording ambient vibrations to infer local site response characteristics (from Sokolicek et al., 2025).

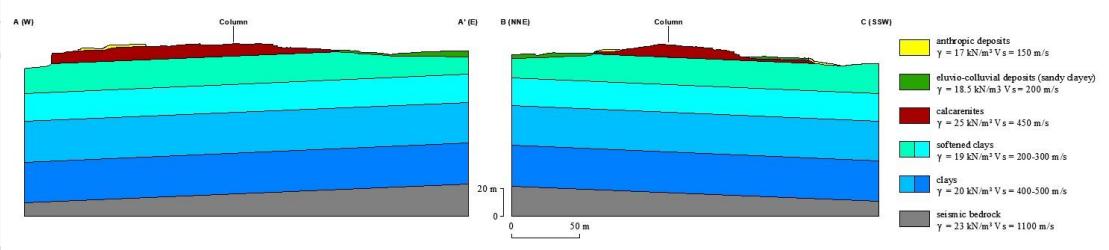

Figure 47: Example of the engineering-geological cross sections modelled for Aegina.

19.3.2. Extraction of the Seismic Inputs

To evaluate the expected local seismic response under medium-to-high seismic hazard conditions, two hazard levels were considered, corresponding to return periods of 475 and 2000 years. These levels represent, respectively, the design earthquake for ordinary structures according to the European EUROCODE standards. The corresponding Peak Ground Acceleration (PGA) values at the seismic bedrock were derived from probabilistic seismic hazard analyses (PSHA). Based on these reference PGA values, Pseudo-Spectral Acceleration (PSA) targets were computed for both return periods.

For each target, a set of seven real earthquake records was selected from the Engineering Strong Motion Database (ESM) and the Italian Accelerometric Archive (ITACA) using the REXELweb tool (Sgobba et al., 2021) (https://esm-db.eu/#/rexel). The selection criteria included:

- Spectral compatibility within a 0.15–2.0 s period range;
- Tolerances of −10% / +30% between the target spectrum and the mean spectrum of the selected recordings;
- Consistency in source mechanism and site class with the investigated area.

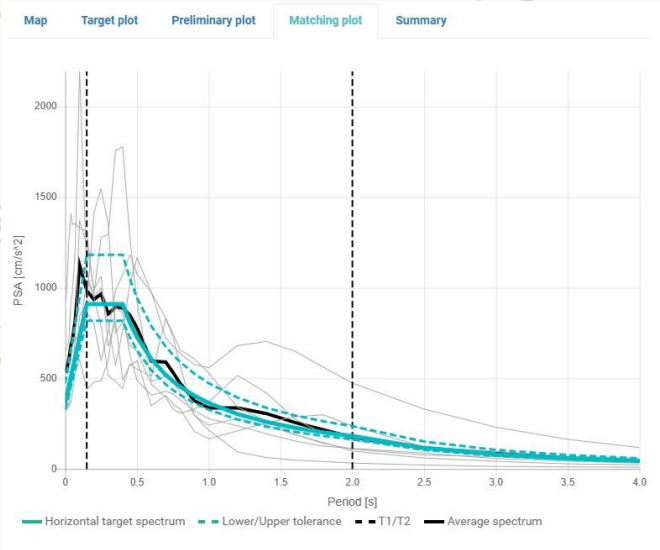

Figure 48: Example of spectral compatibility between the spectrum target and the mean spectrum of the extracted records for a 475 return period.

These time histories were used as input accelerograms for the numerical simulations, enabling the evaluation of local amplification effects for both design and maximum seismic amplification scenarios.

19.3.3. Numerical Modelling

The numerical simulations were performed using the LSR2D software (STACEC s.r.l.), which enables two-dimensional modelling of seismic-wave propagation through an equivalent linear analysis based on the finite element method in the time domain under total stress conditions. The rheological behavior of each geological layer was represented using the Kelvin–Voigt viscoelastic model, which accounts for both the

elastic (stiffness) and viscous (damping) components of the material response. The reconstructed geological cross-sections were imported into LSR2D as .dxf files. For each unit, the assigned physical, geophysical, and decay parameters—including shear stiffness and damping degradation curves—were defined based on available field and laboratory data. The model domain was discretized into a quadrangular finite-element mesh with an approximate grid spacing of 2 m, automatically refined according to the local Vs values and the maximum analysis frequency of 20 Hz (Fig. 49).

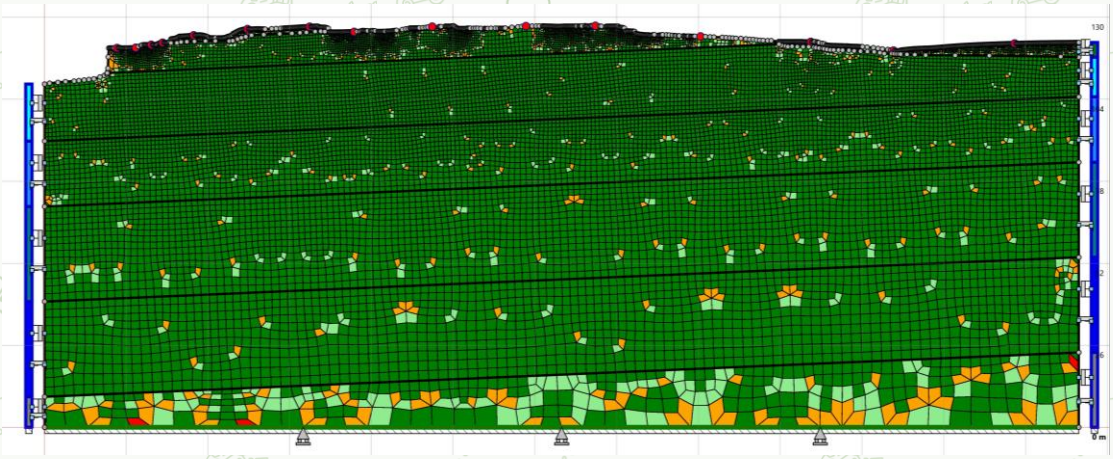

Figure 49: Example of model discretization using quadrangular meshes.

Boundary conditions were defined as follows (Fig. 50):

- Free-field conditions were applied along the lateral boundaries to absorb outgoing waves and avoid spurious reflections;
- A kinematic constraint was imposed on the vertical motion at the base of the model, representing the interface with the infinite half-space corresponding to the seismic bedrock;
- The input motions (for the 475- and 2000-year return periods) were applied at this base, following the criteria established by the ICMS (2008) guidelines for seismic microzonation studies.

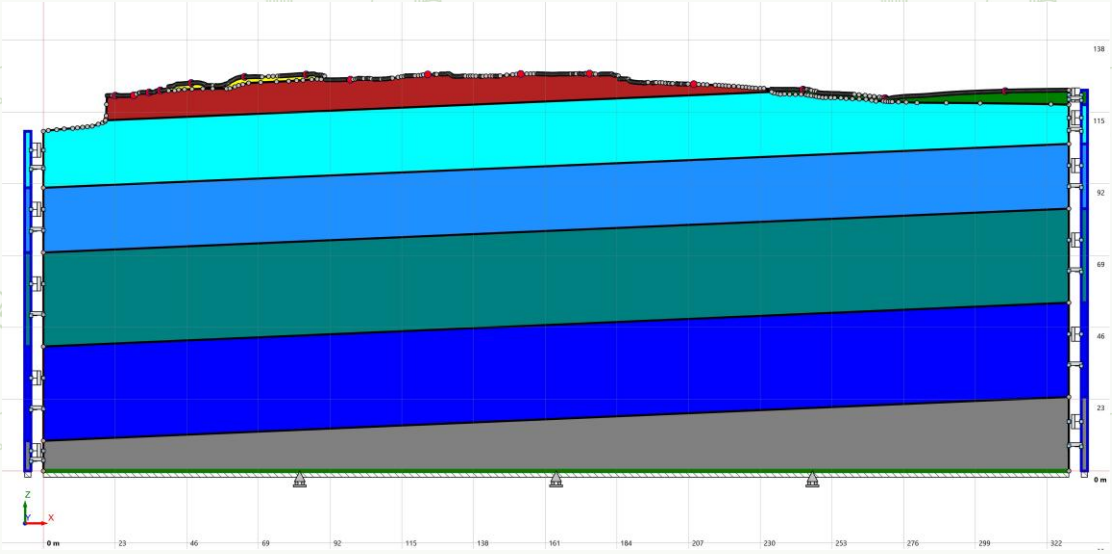

Figure 50: Cross-section for the Aegina site as imported in the software LSR2D with assigned boundary conditions and control points (red circles).

The numerical simulations were conducted independently for each selected accelerogram, allowing the analysis of the propagation of seismic waves from the bedrock to the surface and the identification of local amplification patterns. During the analysis, control points were defined along the modelled cross-sections—typically corresponding to surface and subsurface observation sites—to extract the acceleration time histories and compute the amplification factors (AF) according to ICMS (2008) standards. Furthermore, elastic response spectra (with 5% damping) were calculated for each return period, together with the corresponding horizontal acceleration and displacement fields.

19.3.4. Outputs and Results Interpretation

For each return period considered (475 and 2000 years), the numerical simulations produced a series of quantitative outputs describing the local amplification of ground motion along the modelled geological cross-sections.

A. Distribution of Earthquake-Induced Horizontal Accelerations

The first class of results comprises the spatial distribution of horizontal accelerations induced by the input seismic motions. These maps display the propagation of acceleration amplitudes from the seismic bedrock to the surface, highlighting areas where the dynamic response is intensified due to impedance contrasts or topographic effects (Fig. 51).

High acceleration zones typically correspond to superficial layers characterized by low shear-wave velocity or to morphological irregularities (e.g., ridges, slopes, or buried interfaces) that locally concentrate seismic energy. In contrast, low acceleration amplitudes may indicate energy dissipation or wave scattering caused by stiffer or more homogeneous materials. In a comparative framework, these maps allow users to identify zones of enhanced shaking potential within the cross-section, offering a spatially resolved representation of the local amplification phenomena.

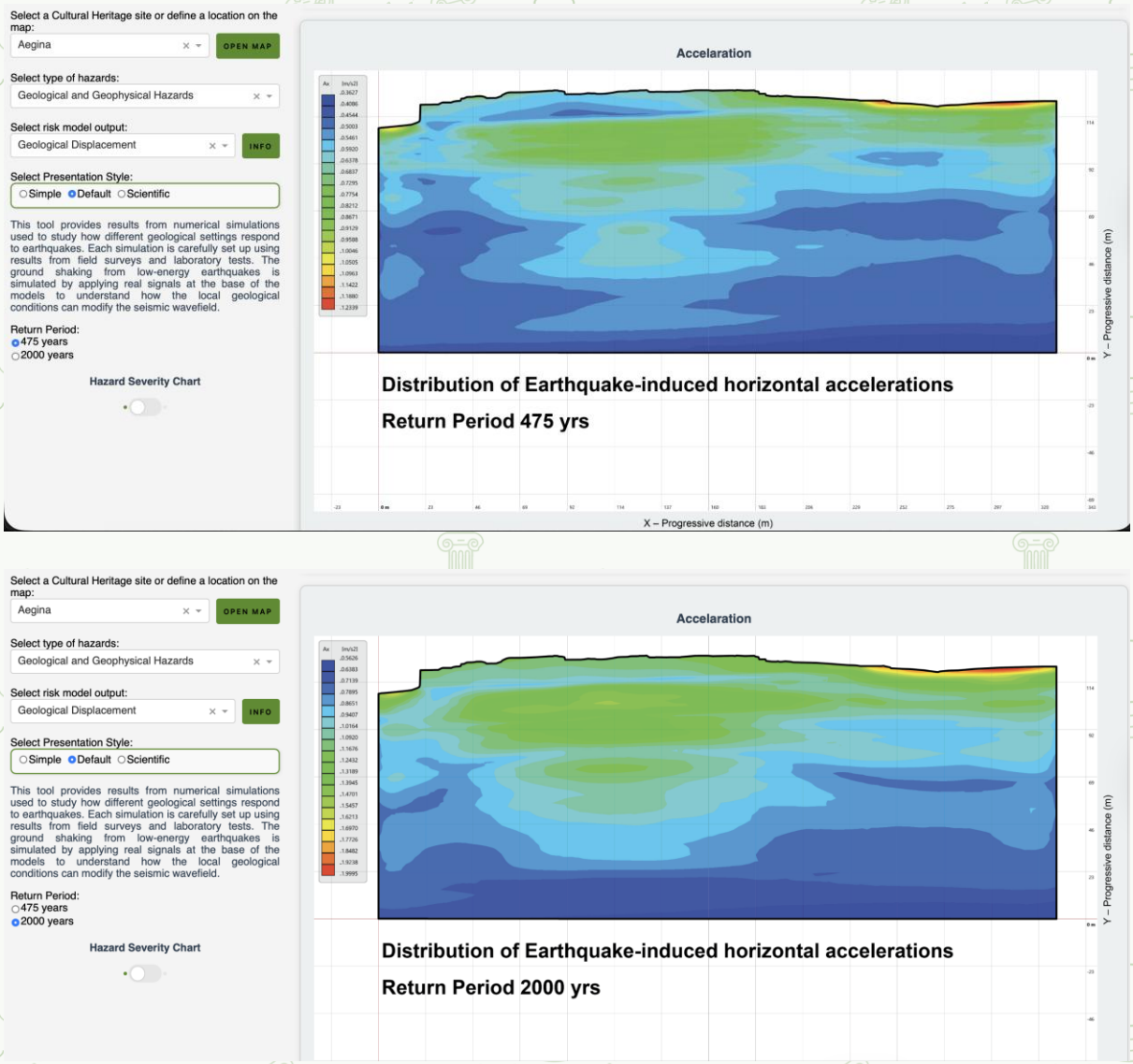

Figure 51: Distribution of earthquake-induced horizontal accelerations for earthquakes with a return period of 475 years (top panel) and 2000 years (bottom panel).

B. Distribution of Earthquake-Induced Horizontal Displacements

The second class of results refers to the distribution of horizontal displacements, which describes the cumulative ground deformation induced by the seismic excitation (Fig. 52). While acceleration reflects the instantaneous intensity of motion, displacement maps provide a measure of the overall kinematic response of the system, integrating both amplitude and duration effects. Higher displacements are generally associated with soft and thick sedimentary layers that are capable of storing and releasing seismic energy over longer oscillation periods. These distributions are particularly relevant for evaluating differential movements across the model and for identifying portions of the subsoil where structural deformations or surface ground strains may be more significant.

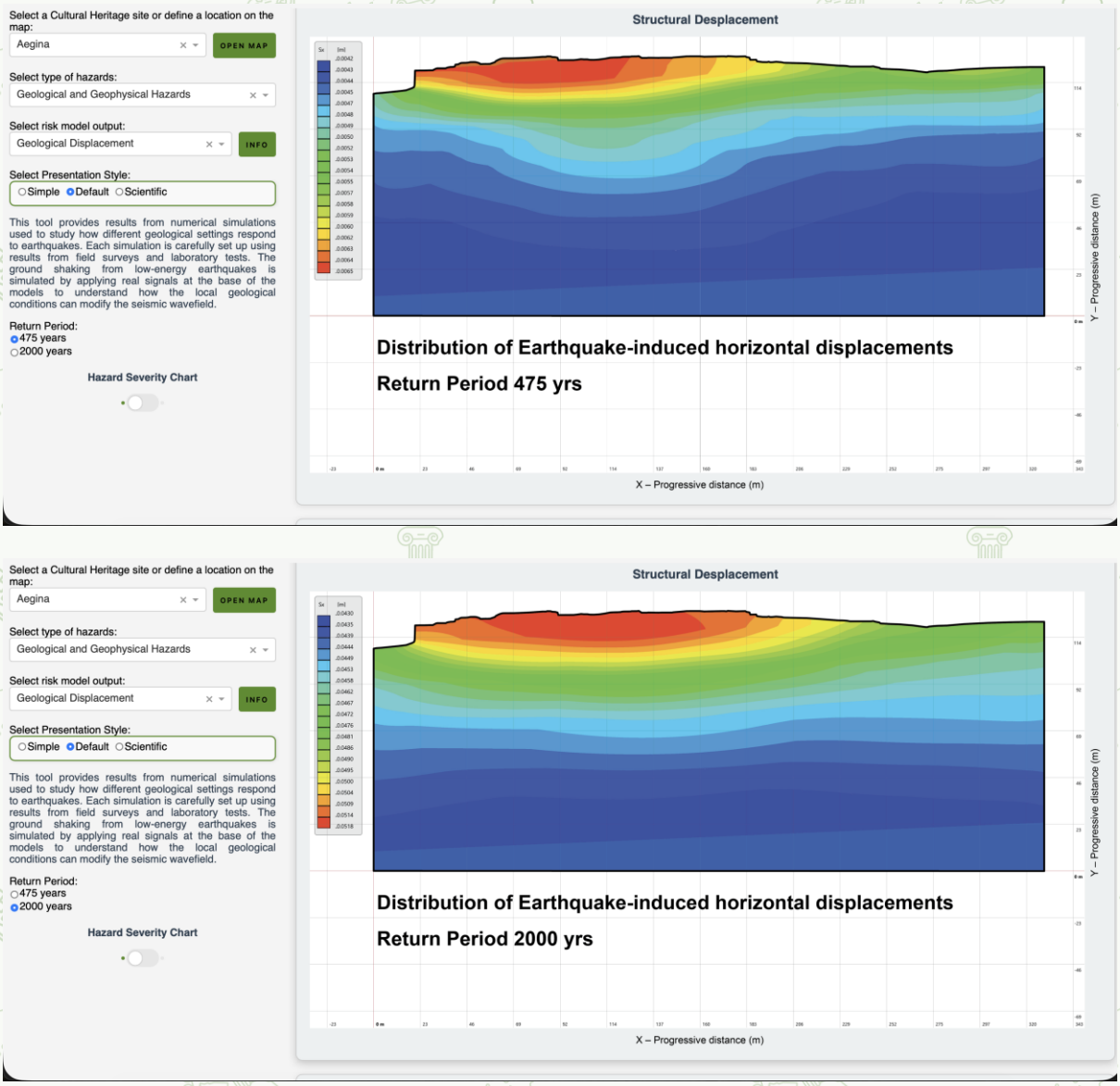

Figure 52: Distribution of earthquake-induced horizontal displacements for earthquakes with a return period of 475 years (top panel) and 2000 years (bottom panel).

C. Amplification Factors

The third class of results is represented by the amplification-factor profiles, which quantify the ratio between the maximum acceleration at the ground surface and the reference acceleration at the seismic bedrock (as defined by the ICMS 2008 standard). In the plots, the X-axis corresponds to the progressive distance along the cross-section, while the Y-axis indicates the amplification factor (AF) values (Fig. 53). Values greater than one identify areas where seismic motion is amplified, whereas values close to or below one correspond to non-amplified response conditions. The amplification-factor plots are divided into three period intervals to show how local ground response varies with both the frequency content of the seismic motion and the dynamic characteristics of potentially affected structures. The short-period range reflects high-frequency components that influence small and stiff structures or shallow deposits; the intermediate-period range corresponds to the typical

resonance periods of medium-sized buildings or archaeological remains; and the long-period range represents low-frequency motions relevant to large or flexible structures and thick sedimentary sequences. This subdivision, consistent with ICMS (2008) guidelines, enables correlating the frequency-dependent ground amplification with the expected dynamic response of exposed cultural heritage assets. These profiles provide a concise and quantitative representation of the frequency-integrated amplification behaviour of the subsoil. The observed variability along the section reflects the interplay between stratigraphic heterogeneity, geometric effects, and local boundary conditions. When compared across different return periods, the amplification-factor plots enable the identification of recurring amplification patterns, indicating which areas of the site are persistently more sensitive to ground-motion intensification.

Figure 53: Amplification factors for different period of intervals considering earthquakes with return periods of 475 and 2000 years (top and bottom panel, respectively).

D. Conclusive Remarks

Although the presented results refer to the Aegina pilot site, the same outputs and interpretative criteria can be applied to any other TRIQUETRA pilot site where LSRA was conducted:

- Acceleration maps indicate where seismic energy is locally concentrated.
- Displacement maps highlight zones potentially affected by larger ground deformations.
- Amplification-factor plots summarize the degree of motion enhancement along the model.

Together, these products provide a consistent framework for assessing local seismic amplification and for integrating site-specific information into the broader hazard models of the TRIQUETRA platform.

19.4. References

Antonielli, B., Bozzano, F., Fiorucci, M., Esposito, C., Martino, S., & Scarascia Mugnozza, G. (2021). Engineering-geological features supporting a seismic-driven multi-hazard scenario in the Lake Campotosto area (L'Aquila, Italy). Geosciences, 11(3), 107. https://doi.org/10.3390/geosciences11030107

ICMS Working Group. (2008). Indirizzi e criteri per la microzonazione sismica – Guidelines for seismic microzonation. Conferenza delle Regioni e delle Province autonome, Dipartimento della Protezione Civile. Retrieved from https://www.centromicrozonazionesismica.it/it/download/category/3-linee-guida

Martino, S., Lenti, L., Gélis, C., Bozzano, F., & Bonilla, L. F. (2015). Influence of lateral heterogeneities on strong-motion shear strains: Simulations in the historical center of Rome (Italy). Bulletin of the Seismological Society of America, 105(5), 2604–2624. https://doi.org/10.1785/0120150023

Sgobba, S., Felicetta, C., Russo, E., D'Amico, M., & Luzi, L. (2021, June 22–24). The online graphical user interface of REXELweb for the selection of accelerograms from the engineering strong motion database (ESM). In Proceedings of the 39th National Conference of the Gruppo Nazionale di Geofisica della Terra Solida (GNGTS) (Online).

Sonmezer, Y. B., Celiker, M., & Bas, S. (2019). An investigation on the evaluation of dynamic soil characteristics of the Elazig City through the 1-D equivalent linear site-response analysis. Bulletin of Engineering Geology and the Environment, 78(7), 4689–4712. https://doi.org/10.1007/s10064-019-01427-7

Tallini, M., Lo Sardo, L., & Spadi, M. (2020). Seismic site characterisation of Red Soil and soil-building resonance effects in L'Aquila downtown (Central Italy). Bulletin of Engineering Geology and the Environment, 79(8), 4021–4034. https://doi.org/10.1007/s10064-020-01827-2

Tunar Özcan, N., Ulusay, R., & Işık, N. S. (2019). Assessment of dynamic site response of the peat deposits at an industrial site (Turkey) and comparison with some seismic design codes. Bulletin of Engineering Geology and the Environment, 78(5), 2215–2235. https://doi.org/10.1007/s10064-018-1258-3

19.5. Contributors

Developed by: Sapienza University of Rome (SUR)

Date of last update: 10/11/2025

Lead contributors:

- Stefano Rivellino
- Guglielmo Grechi
- Federico Feliziani
- Gian Marco Marmoni
- Mattia Montagnese
- Salvatore Martino
- Francesca Bozzano
- Gabriele Scarascia Mugnozza

20. Seismic Analysis Toolbox

20.1. Overview

The Seismic Analysis Toolbox (SAT) is a MATLAB Livescript that has been developed to investigate single-station ambient vibration measurements for site characterization (HVSR analysis) and preliminary modal analysis of freestanding elements (Time-Frequency Polarization analysis). In other words, this toolbox is capable of characterizing i) local seismic amplification effects and ii) the vibrational behavior of freestanding elements, such as partially detached rock blocks prone to landslide. The main outputs are in form of plots and tables, and correspond to

- Time histories of ambient vibration recordings;
- Power spectral densities and spectrograms of the recorded ambient vibratio signals;
- Results of HVSR analysis in the form of multi-panel figure including a) Fourier Amplitude Spectra, Spectrum rotate plot, HVSR plot, HVSR rotate plot;
- Results of Time-Frequency polarization analysis including 9 panels describing the spectral content, polarization attributes and phase relations of all three components of ambient vibrations.

20.2. Methodological Description

This MATLAB Livescript enables the basic and advanced processing of three-component ambient vibration recordings (i.e., HHN/HHE/HHZ or HHY, HHX, HHZ). Seismic data must be provided in SAC or miniseed file format (1C for SAC and 3C for mseed). The user will be able to visualize and inspect waveform time series, spectrograms, power spectral densities, as well as compute horizontal-to-vertical spectral ratios (HVSR) and frequency-dependent polarization analysis (FDPA) of ambient vibration recordings. The following paragraph is divided into three sections introducing the theory and background of spectral processing, HVSR, and FDPA analyses. Furthermore, a practical example is provided at the end of this chapter to introduce the user to common applications of the SAT.

20.2.1. Spectral Analysis

Spectral analysis is a well-known signal processing technique used to investigate the frequency content of any type of signal. By transforming a time-domain signal into the frequency domain, it allows us to identify the different spectral attributes composing the signal and analyze their amplitude and phase. The most common method used for this time-frequency transformation is the Fast Fourier Transform (FFT), which is a mathematical operator that converts a time-based signal into its constituent frequencies.

For spectral analysis, this toolbox implements a modified version of Welch's periodgram for computing Power Spectral Densities (PSD) of ambient seismic noise signals (Welch, 1967). This method is widely used in seismic applications as it can reduce noise variance deriving from FFT of a finite-length signal via segment overlap. The main steps of the implemented spectral analysis routine can be summarized following McNamara and Buland (2004) worflow:

- **Segmentation**: the input signal is divided into partialy overlapping segments of length L;
- **Windowing**: signal segments are windowed using a Hamming window function to minimize spectral leakage at the segment boundaries;
- **Fast Fourier Transform (FFT)**: FFT is applied to each windowed segment to obtain spectral components;
- **Power Spectral Density (PSD) computation**: each FFT is squared and divided by the frequency resolution (which is the inverse of segments length) to obtain the periodgram;
- **Spectral Averaging**: The periodograms of all segments are averaged to produce the final PSD estimate. This averaging reduces the variance of the spectral estimate, resulting in a smoother and more reliable PSD.

Similar to PSD computation, this toolbox enables investigating how spectral attributes vary in time via spectrograms. A spectrogram is a graphical

representation of the amplitude or power spectrum of frequencies that provides a means to analyze the time-varying spectral content of non-stationary signals.

Therefore, spectrograms can offer a detailed observation of signals behavior in the time-frequency domain, while PSDs can provide more robust spectral information. The combined analysis of these signal processing techniques provides a comprehensive understanding of ambient seismic noise (or any type of ambient vibration signals) characteristics.

20.2.2. Horizontal to Vertical Spectral Ratio (HVSR)

Ambient seismic noise derives from surface or near-surface sources and consists mostly of elastic surface waves. Low frequency waves (below 1 Hz) are commonly called microseisms and high frequency waves (above 1 Hz) are called microtremors . Primary sources of seismic waves include human activities (such as transportation or industrial activities), winds and other atmospheric phenomena, rivers, and ocean waves (Wathelet et al., 2020).

The horizontal-to-vertical spectral ratio (HVSR) is a passive and non-invasive seismic analysis technique commonly used for site characterization, particularly in assessing local site effects and identifying resonance frequencies of low shear-velocity layers of soft-soil at a point location (Larose et al., 2015).From a general perspective, every natural element or geological structure vibrate at a fundamental resonance frequency that is a function of physical and mechanical properties of the vibrating system. This phenomenon (i.e., resonance) can be excited by seismic noise encountering the overburden-bedrock interface, at which a seismic impedance contrast generally exists. Seismic impedance is a measure of seismic wave transmittance (i.e., the measure of how much of the incident seismic wave is transmitted at the interface from one medium to another) and depends on seismic velocity and density of the soil or rock medium. In this framework, the HVSR technique enables the identification of the fundamental resonance frequency (f_0) at a given location when a marked seismic impedance contrast exists at the bedrock-sediment interface.

The HVSR technique can identify the fundamental resonance frequency (f_0) of overburden sediments by measuring three components of seismic noise over time (HHN = North-South component, HHE = East-West component, HHZ = vertical component). This fundamental resonance frequency is related to the sediment layer thickness (H) (i.e., depth to seismic bedrock) and average shear-wave seismic velocity (Vs) of the corresponding layered or massive sedimentary deposits through the expression:

$$f_0 = \frac{V_s}{4H}$$

Thus, the HVSR method can be effectively used to estimate the thickness or shear-wave velocity of the sediments that sharply overlie bedrock.

The main processing steps are hereafter briefly described:

- **Data Collection**: Record continuous seismic data (for at least 1-hour) from a single station using a three-component seismometer. The seismometer records three orthogonal components of ground motion: two horizontal components (H1 and H2) and one vertical component (V).
- **Data segmentation**: Segment seismic data into overlapping or non-overlapping time windows (e.g., 40–100 seconds each). The length of the window depends on the frequency range of interest and the characteristics of the recorded data.
- **Windowing**: Apply a window function (e.g., Hamming window) to each time segment to reduce spectral leakage effects.
- **Spectral Analysis**: Calculate the amplitude spectra via FFT of the horizontal (H1 and H2) and vertical components for each subwindow.
- **Horizontal components averaging**: Combine the two horizontal components to obtain a single representative horizontal spectrum. This can be done by averaging the spectra of H1 and H2:

$$H(f) = \sqrt{H1(f)^2 + H2(f)^2}$$

where $H1(f)$ and $H2(f)$are the amplitude spectra of the two horizontal components at frequency f.

- **HVSR computation**: Compute the Horizontal to Vertical Spectral Ratio for each time window by dividing the averaged horizontal spectrum by the vertical spectrum:

$$HVSR(f) = \frac{H(f)}{V(f)}$$

where $H(f)$is the averaged horizontal spectrum and $V(f)$ is the vertical spectrum at frequency f.

- **Smoothing and averaging**: Each HVSR window is smoothed by applying a Konno-Ohmachi filter and then averaged across all time windows to obtain a stable estimate of the spectral ratio.
- **Identify Peaks**: Analyze the HVSR curve to identify significant peaks. These peaks often correspond to the natural resonance frequencies of the site, which can also be indicative of local site effects and subsurface structures.

The identified resonance frequencies and associated HVSR values can effectively be used to infer geological properties and characteristics of the site, such as soft-soil layer thicknesses and potential amplification effects due to seismic excitation.

For a more comprehensive understanding of ambient seismic noise physics and HVSR technique, users are encouraged to consult the literature sources provided in the references section.

20.2.3. Frequency Dependent Polarization Analysis

Ambient vibration measurements represent a widely used technique employed in structural health monitoring (SHM) to assess the integrity and dynamic characteristics of freestanding structures, such as buildings, bridges, towers as well as natural landforms. These measurements capture the dynamic response of a structure to natural and random excitations such as wind, traffic, and ambient seismic noise, providing crucial data without the need for invasive testing or artificial loading conditions (Clinton et al., 2006). In the field of engineering-geology, recent studies have highlighted that ambient vibration modal analysis can be used to reveal mechanical and dynamic material properties of ground and slope instabilities, as well as their extent and structure, by identifying natural resonance frequencies, local site amplification and polarization attributes (Bessette-Kirton et al., 2022; Geimer et al., 2022; Kleinbrod et al., 2019).

In this framework, resonant modes can be preliminary characterized in their frequencies and shapes using the frequency dependent polarization analysis (FDPA), which describes vibrational particle motion through incidence and azimuth angles and a nondimensional degree of polarization across the range of recorded frequencies at the active sensor location. This latter parameter varies from 0 to 1 and measures the extent to which seismic noise is organized and can be described by fewer than three degrees of freedom(Koper & Hawley, 2010). Highly-polarized frequencies correspond to well-organized and coherent particle motion, which is often associated with resonance.

The here proposed code for FDPA represents a MATLAB-compiled version of the IRIS Polarization toolkit originally compiled in Python (https://ds.iris.edu/ds/products/noise-toolkit-polarization/), which is based on the work published by Koper and Hawley in 2010 (https://doi.org/10.1007/s11589-010-0743-5). TFPA is based on the eigendecomposition of the spectral covariance matrix of the three components of ground motion (HHX, HHY and HHZ) to retrieve polarization attributes from eigenvalues and eigenvectors. For a more detailed and exhaustive description of this technique please refer to the Koper and Hawley (2010) and therein references.

20.3. Workflow

In this section, the main info for selecting input data and running the Seismic Analysis Toolbox (SAT) are provided along with code samples and snippets for the ease of the reader/user. The SAT is divided into nine sections, some of which also feature subsections:

1. Introduction

2. Input section
3. Preprocessing steps
4. Preprocessing
5. Waveform plotting
6. Spectral analysis
7. Horizontal to vertical spectral ratio analysis (HV)
8. Polarization analysis
9. Extract polarization attributes

To effectively run the Toolbox, the user must correctly select input data files and formats. Input data and files must be given for sections 2, 3, 6, 7 and 8.

20.3.1. Input Section

In this section the user can modify and select multiple parameters to customize preprocessing and analysis steps. In this section, the main input required are related to the seismic monitoring station name, frequency range of interest for the analysis (Fig. 54) and path to the working directory where data are stored (Fig.55).

Specify station name and select a frequency range of interest

Station Name/Code (*do not use a number at the name beginning*)

```
2  option.STname = 'CBR';
```

Select if cutting to a specific a frequency range of interest (**'y' recommended – I'd say mandatory**)

```
3  option.F.frange = 'y'; % y = yes - n = no
```

Specify frequency range limits

```
4  option.F.fmin = 0.3; % Hz
5  option.F.fmax = 30; % Hz
```

Figure 54: Code sample for selecting input parameters.

Select working directory

Select working directory between the current folder and a specific path – ***current/gui/specific***.
If you want to manually select the working directory type ***gui***. You need to specify ***mypath*** only if you want to set the working directory to a specific folder.

```
6  option.workingdir.folder = 'gui'; % current/specific/gui
```

Specify folder path if needed (only if ***specific*** is selected)

```
7  option.mydir = '';
8  option.workingdir.path = SetWorkingDir_v1(option.workingdir.folder,option
```

```
Selecting working directory...
Working directory: /Users/guglielmogrechi/Documents/Postdoc/CaseStudies/UUtah/C
```

Figure 55: Code sample for selecting the working directory.

20.3.2. Preprocessing and waveform plotting

The preprocessing step is optional (Fig. 56), and it allows the user to:

- Remove instrument response (IRC);
- Trim data to a time interval of interest;
- Downsample data.

In particular, the instrument response needs to be removed to convert from the native instrument output (i.e., counts) into physical units of velocity/acceleration or displacement. To do this correctly, the user must specify the fullpath to the nominal instrument response file (NIR) of the employed seismometer and a frequency range of interest. NIR files can be retrieved from the IRIS DMC Nominal Response Library (https://ds.iris.edu/ds/nrl/) for most instruments on market. It is important to note that IRC is performed using pole and zero files only.

A bandpass pre-filter is applied before the instrument correction to prevent the amplification of undesired low- or high-frequency noise. This filter is defined by four corner frequencies:

- f1: absolute lowest frequency you want included;
- f2: lowest frequency fully preserved;
- f3: highest frequency fully preserved (set to ~40-45% of the sampling rate);
- f4: absolute highest frequency you want included (can't be more than 50% of the sampling rate).

Frequencies between f1 and f2, and f3 and f4 are only partially preserved.

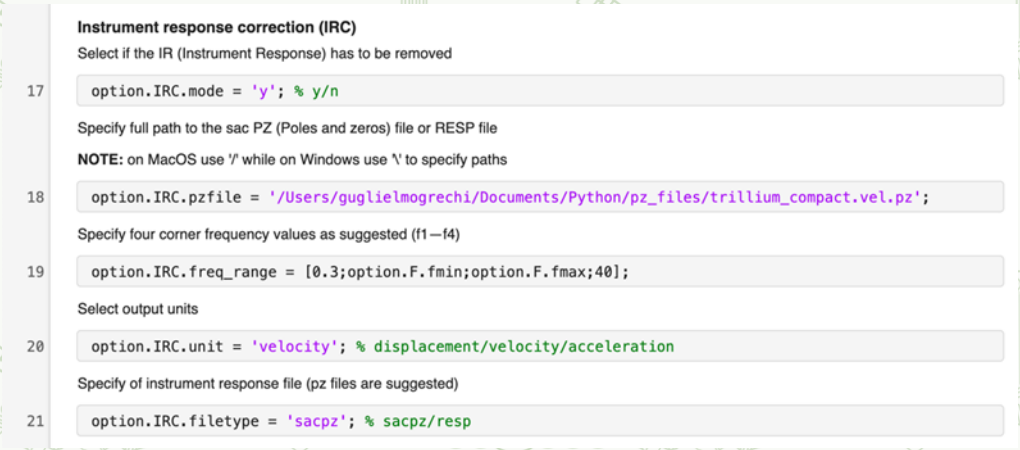

Data downsampling

Select if data have to be downsampled. Downsampling will increase speed while removing high-frequency information (Nyquist frequency is lowered)

```
25  option.downsample.mode = 'y';
```

Select downsampling factor (integer).

```
26  option.downsample.value = 2;
```

Figure 56: Code sample for preprocessing steps and user's inputs.

Once all the parameters for preprocessing have been selected, the user can run the preprocessing section (Fig. 57) and obtain the desired output for the following analysis steps.

Preprocessing

Instrument Response Correction (IRC), data trimming and data downsampling

```
27  [TT,fs] = Data_preprocessing_v1(TT,fs,option);
```

```
Removing Instrument Response | Data converted to velocity
Data not trimmed
Data downsampled by a factor of 2 | New sampling frequency is 125 Hz
```

Figure 57: Data preprocessing consists in IRC, data trimming and data downsampling.

Before proceeding with the analysis, the user can plot the preprocessed time-histories (or the raw ones in case preprocessing was avoided) to check for noisy or disturbed time windows (Fig 58). In case the user decides to avoid particularly noisy time windows, data can be trimmed around windows of interest characterized by less disturbed waveforms.

Waveform plotting

Plot seismic time histories before spectral and HV analysis

```
28  p0 = PlotTimeHist_v1(TT,option);
```

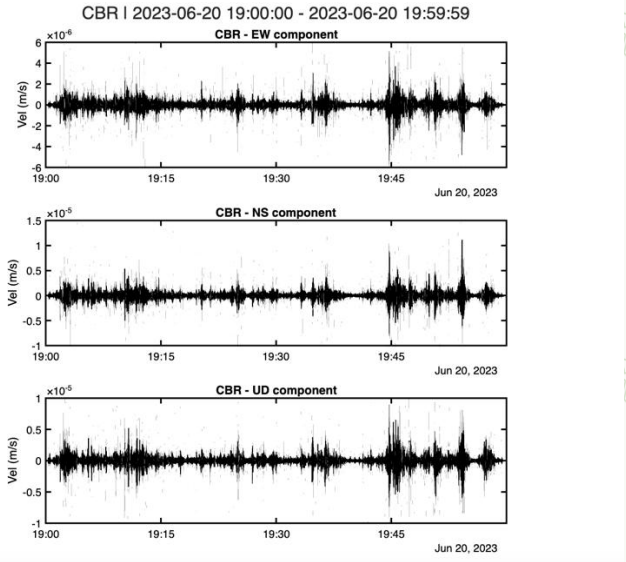

Figure 58: Waveform plots for the three components of ambient vibration recorded by the seismometer.

20.3.3. Spectral Analysis

In this section the user can select the main parameters for spectral processing and analysis (Power spectral density and spectrogram computation) (Fig. 59). Prior to

the analysis, the user can also select to rotate horizontal components to align with a defined orientation (e.g., to obtain transverse and longitudinal components with respect to a geometric element, rather than using North-South and East-West components).

Spectral analysis

Rotate horizontal components

Select if you want to rotate horizontal components

```
37 option.PSD.Rotate.mode = 'n'; % y/n: 'y' horizontal components are rotated for spectral analysis
```

Specify rotation angle for horizontal components (SHX, SHY)

```
38 option.PSD.Rotate.Theta = -10; % degrees. If positive, the rotation is counterclockwise.
```

Select inputs for spectral processing and plots

PSD processing parameters

FFT (Fast Fourier Transform) window length

```
39 option.PSD.win = 60; % in seconds
```

FFT window overlap

```
40 option.PSD.over = .5; % from 0 to 1 (0 = 0% and 1 = 100%)
```

Select PSD visualization scale

```
41 option.PSD.magnitude = 'dB'; % dB/linear
```

Select if PSD will be smoothed

```
42 option.PSD.smoothing.mode = 'y'; % y/n
```

Select smoothing method (*simple - can be refined*)

```
43 option.PSD.smoothing.type = 'movmed'; % movmed/movmean
```

Select smoothing window in Hz

```
44 option.PSD.smoothing.bandwidth = 0.1; % in Hz
```

Figure 59: Code block for spectral analysis.

Once all parameters have been selected, the next section will allow the user to obtain PSDs and spectrogram plots for all components of ground motion (Fig. 60). After generating PSD and spectrograms, the user can easily export them as raster or vector files.

Processing

```
52  [p1,p2] = SpectralAnalysis_v1(TT,fs,option);
```

```
Spectrogram computation | NS component
Spectrogram computation | EW component
Spectrogram computation | UD component
```

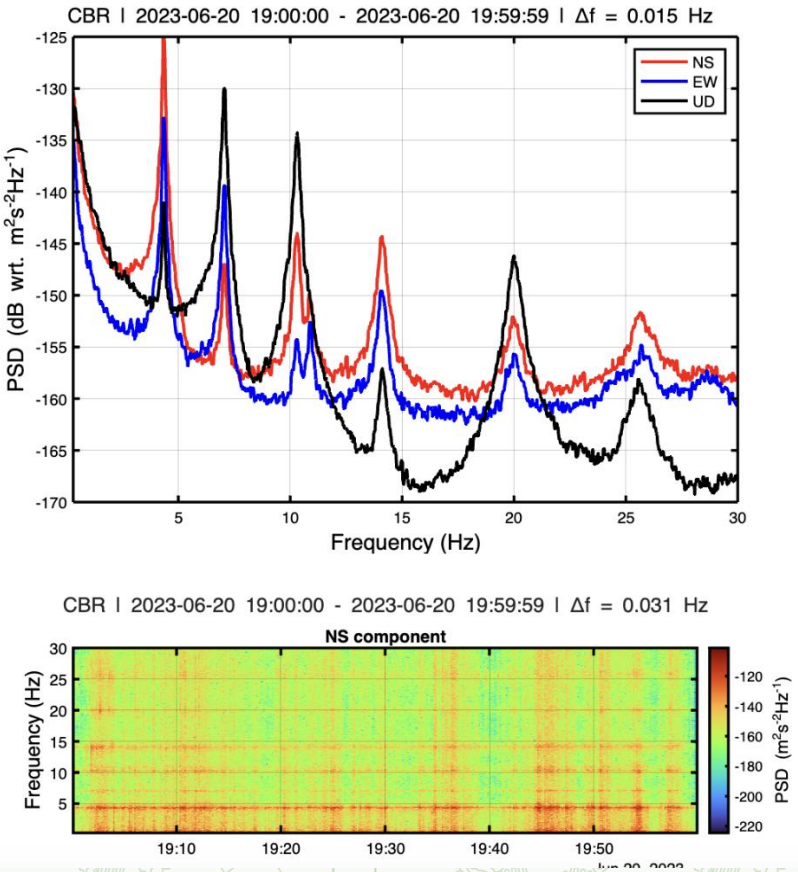

Figure 60: Example of spectral analysis results with PSD (upper plot) and spectrograms (lower plot – only the North-South component spectrogram is here displayed).

20.3.4. Horizontal to Vertical Spectral Ratio Analysis (HVSR)

In this section the user can select the main parameters for performing HVSR analysis, modifying several aspects controlling data segmentation, windowing, processing and graphics appearance (Fig. 61). In order to obtain stable and consistent results from HVSR analysis, it is highly recommended that at least 1-hour long seismic recordings are used.

Horizontal to vertical spectral ratio analysis (HV)

Select inputs for HV processing and plot

Select window length in seconds for spectral processing

```
option.HV.win = 60; % in seconds
```

Select window overlap for spectral processing

```
option.HV.over = 0.5; % from 0 to 1 (0 = 0% and 1 = 100%)
```

Select X axis type

```
option.HV.scale = 'log'; % log/linear
```

Select if you want to set X axis ticks manually or automatically

```
option.HV.xtick.Mode = 'auto'; % manual/auto
```

If X ticks are set manually, specify X tick values

```
option.HV.xtick.Values = [option.F.fmin,1,2,4,6,8,10,...
    option.F.fmax];
```

Select colormap for Spectrum and HV rotate plots - the user can also

```
option.HV.cmap = 'viridis_white';
```

select the colormap direction

```
option.HV.cmap_direction = 'reverse';
```

Figure 61: Code block for HVSR analysis.

Once all parameters have been selected, the next section will allow the user to perform the HVSR analysis (Fig. 62). The code implemented here not only computes the H/V spectrum, but it also performs the HV Rotate analysis (Fig. 63), which is used to obtain the H/V in the horizontal plane as a function of azimuth (https://www.geopsy.org/wiki/index.php/H/V_Rotate).

Processing

```
74  [p3,HVr,STD,freq] = HVprocessing_v1(TT,fs,option);
```

```
rotate horizontal components - 0
Computing HV for NS and EW horizontal components...
rotate horizontal components - 5
rotate horizontal components - 10
rotate horizontal components - 15
rotate horizontal components - 20
rotate horizontal components - 25
rotate horizontal components - 30
rotate horizontal components - 35
rotate horizontal components - 40
rotate horizontal components - 45
rotate horizontal components - 50
rotate horizontal components - 55
rotate horizontal components - 60
rotate horizontal components - 65
rotate horizontal components - 70
rotate horizontal components - 75
rotate horizontal components - 80
rotate horizontal components - 85
```

Figure 62: Example of HVSR analysis performed by the SAT.

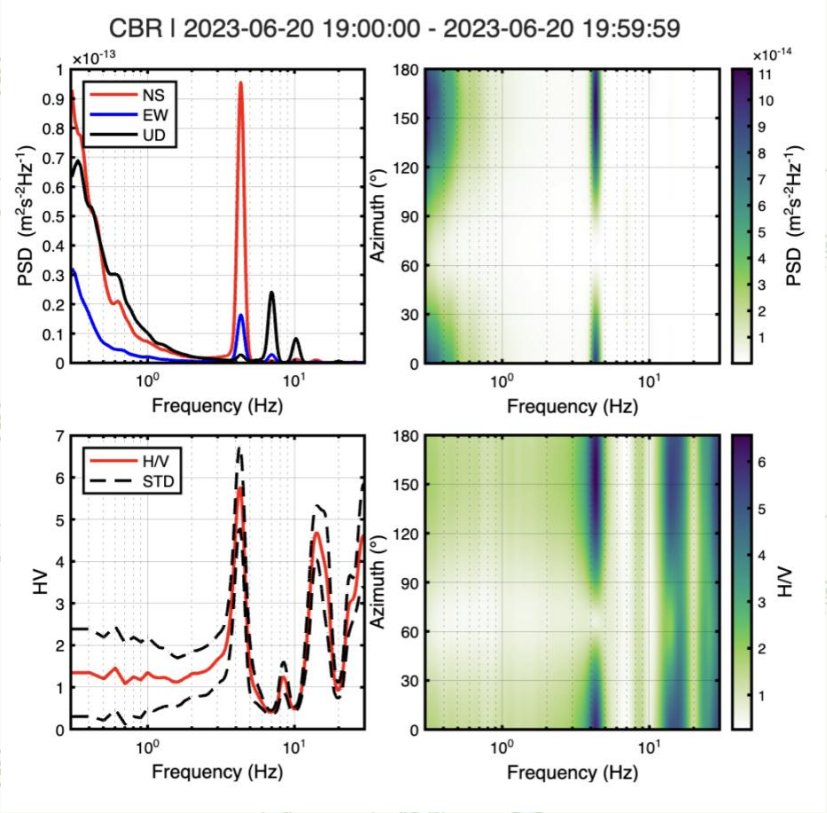

Figure 63: Results of the HVSR analysis; PSD plot (upper left panel), Spectrum rotate plot (upper right panel), HV spectrum plot (lower left panel), HV rotate plot (lower right panel).

20.3.5. Time-Frequency Polarization Analysis (TFPA)

This section is devoted to TFPA, and the user, similar to the previous sections, can freely modify the analysis parameters to obtain the desired results (Fig. 64). In order to get stable and consistent results from TFPA, it is highly recommended that at least 1-hour-long seismic recordings are used.

Select inputs for polarization analysis

Select the window length. The input signal will be divided into segments of that length

```
83  option.Pol.Time.Segment = 300; % seconds
```

Select window overlap

```
84  option.Pol.Time.Over = 0.5; % from 0 to 1
```

Select the window length in seconds for computing CPSDs (cross-power spectral densities) and reconstructing the averaged spectral matrix

```
85  option.Pol.CPSD.win = 40; % seconds
```

Select the window overlap (from 0 to 1) for computing CPSDs

```
86  option.Pol.CPSD.over = 0.5; % from 0 to 1
```

Processing

```
87  option = PolarizationAnalysis_v1(TT,fs,option);
```

```
********** START POLARIZATION ANALYSIS **********
CBR.EW | 2023-06-20 19:00:00.000 - 2023-06-20 19:59:59.992 | 125 Hz | 450000 samples
CBR.NS | 2023-06-20 19:00:00.000 - 2023-06-20 19:59:59.992 | 125 Hz | 450000 samples
CBR.UD | 2023-06-20 19:00:00.000 - 2023-06-20 19:59:59.992 | 125 Hz | 450000 samples
********** END POLARIZATION ANALYSIS **********
```

Figure 64: Input and processing section code block for TFPA.

Results from TFPA are represented by two main plots, each composed of nine panels. The first plot presents the mean and standard deviation values for each spectral and polarization attribute of the analyzed data. In contrast, the second plot displays probability density functions (PDFs) for the same spectral and polarization attributes (Fig. 65). More in detail, each figure will show power spectra for the horizontal and vertical components (left column), the principal eigenvalue spectrum (λ), the degree of polarization (β^2) and the azimuth of polarization ellipsoid (θ_H) (central column), and the incidence angle of the polarization ellipsoid (θ_V), along with phase differences between the vertical and principal horizontal components (ϕ_{VH}) and the two horizontal components (ϕ_{HH}) (left column).

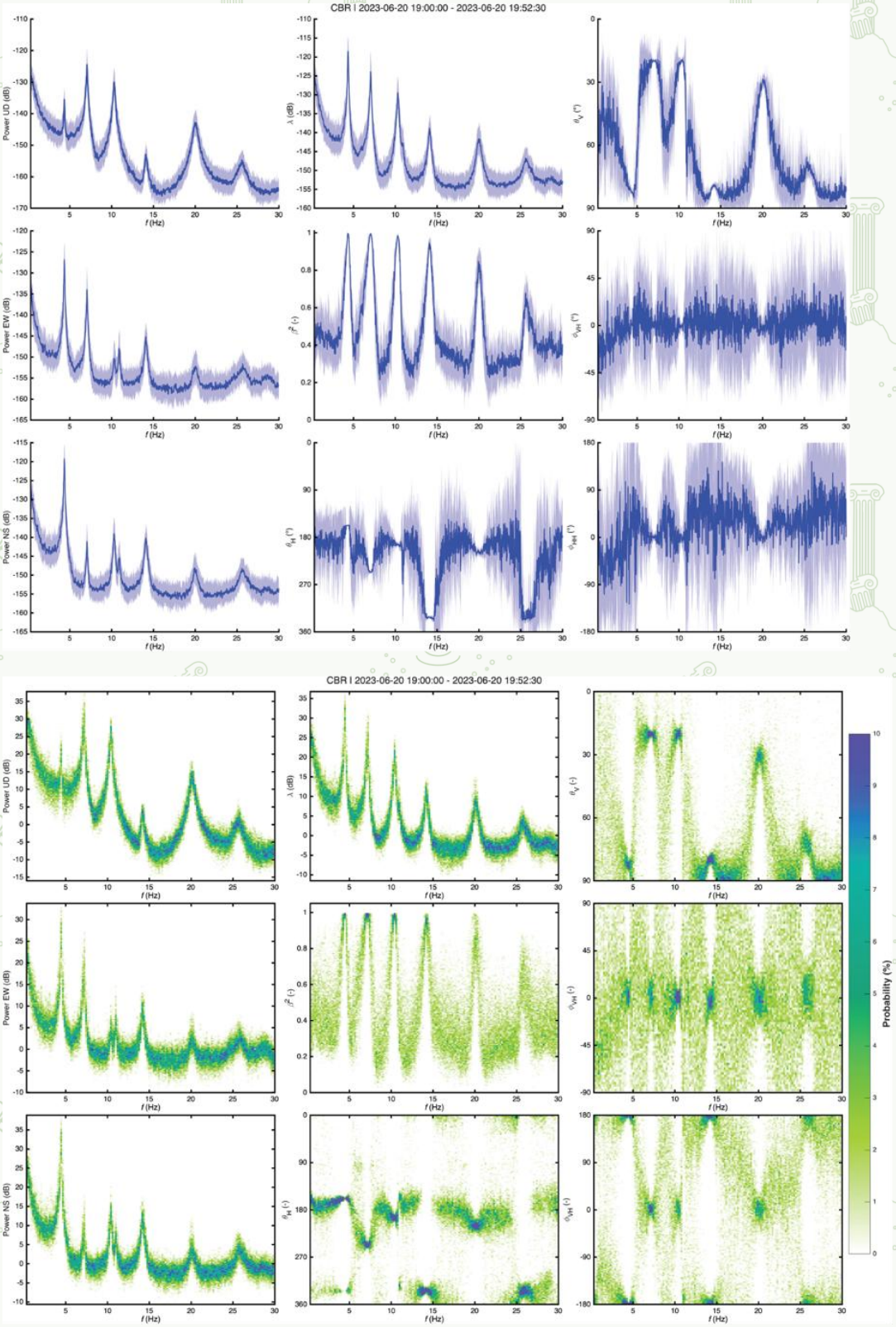

Figure 65: Example of TFPA results. Mean and standard deviation values (upper plots) and PDFs for the same attributes (lower plots).

20.4. Application Example

In this chapter, we present a practical application of the MATLAB-implemented SAT designed for analyzing single-station ambient seismic noise measurements. The

SAT enables users to employ two primary analysis techniques: Horizontal-to-Vertical Spectral Ratio (HVSR) and Time-Frequency Polarization Analysis (TFPA). The HVSR technique is widely used for estimating site effects and identifying subsurface structures. In contrast, the TFPA technique can be effectively employed to investigate the directionality of seismic noise and characterize resonance modes of vibrations of potentially unstable rock blocks and freestanding objects. To this aim, we briefly present the results obtained at two of the more than fifty single-station ambient vibration measurements performed at the promontory of Punta Eolo (Ventotene) (Fig. 66).

These two specific stations were selected as their outcomes represent clear examples of the potential of the SAT in retrieving crucial information for improving site-specific engineering-geological models and characterizing the resonance modes of vibration of a potentially unstable rock block. In fact, while HVSR analyses can successfully describe the local stratigraphic and geostructural setting, the TFPA significantly enhances the spectrum of ambient vibration measurement applications by enabling the identification of resonance frequencies along with their degrees and angles of polarization.

Hence, the application of the HVSR and TFPA techniques significantly improves the ability to perform quantitative geological risk assessment. By employing these methodologies, robust models for seismic hazard scenarios and dynamic stresses on unstable elements can be developed. This result is crucial in the framework of geological risk assessment, as it allows for the necessary calibration of forward-scenario analyses, thereby representing the basis for implementing reliable strategies of geological risk prediction and mitigation.

20.4.1. The pilot site of Ventotene

Among the several single-station ambient vibration measurements performed at the promontory of Punto Eolo in the framework of the TRIQUETRA project, two of them were selected to highlight the potential of the SAT:

- VTN.R, located in the southern sector of the promontory (i.e., near the service area of Villa Giulia), 50 m far from the western coastline;
- VTN.B, located in the western sector of the promontory and in proximity to a rock block that juts out the coastline and is prone to instability;

Ambient vibration data were acquired at VTN.R and VTN.B with a sampling frequency of 250 Hz for two hours to avoid the influence of transient disturbs (mainly deriving from strong wind). The collected dataset was then analyzed with the SAT:

- VTN.R was analyzed using the HVSR technique to identify peaks related to the local stratigraphic setting;
- VTN.B was analyzed using the TFPA technique to preliminary characterize its modal behavior by identifying clear resonance modes of vibration.

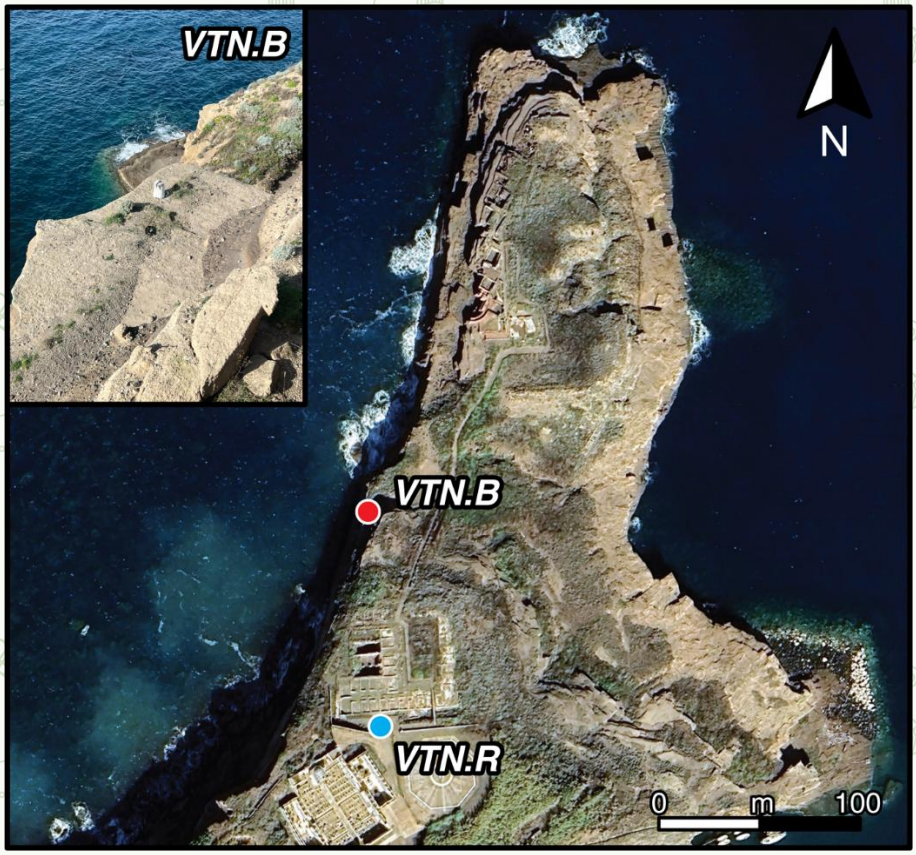

Figure 66: Location of the two single-station ambient vibration measurements VTN.R and VTN.B. The small inset in the upper-left corner shows the details of station VTN.B.

20.4.2. HVSR Results

HVSR plots exhibit two distinct, narrow peaks within the investigated frequency range (1–30 Hz), with the first centered at approximately 3 Hz and the second at 12 Hz (Fig. 67). The 3 Hz peak can be considered the site's fundamental resonance frequency (f_0), which is related to the local stratigraphic setting characterized by the contact between the Tuffs Unit (TU) and the basal Lava Unit (LU) (Feliziani et al., 2024). Differently, the second HVSR peak has been interpreted as deriving from the contact between the TU and the overburden (i.e., soil cover layers). The interpretation of these peaks as local fundamental resonance frequencies related to 1D stratigraphic conditions is strengthened by the absence of a clear polarization effect (e.g., the directionality of seismic surface waves), as observed in HVSR rotation plots (Fig. 67).

Hence, given a Vs (S-wave velocity) estimate for the involved layers, HVSR peaks can be used to constrain the elevation of the investigated stratigraphic contacts through the equation:

$$f_0 = \frac{V_s}{4H}$$

Where f_0 is the fundamental resonance frequency identified by the HVSR peak, V_s is the S-wave velocity within the layer of thickness H. Knowing f_0 and V_s, this equation can be rearranged to derive H:

$$H = \frac{V_s}{4f_0}$$

Considering Vs values of 310 and 740 ms^{-1} for the surface deposit and tuff unit, respectively, the 3 Hz peak indicates a TU-LU contact elevation of approximately 60 m from ground surface, whereas the 12 Hz peak marks a 6.5 m deep contact between TU and surface soil coverage.

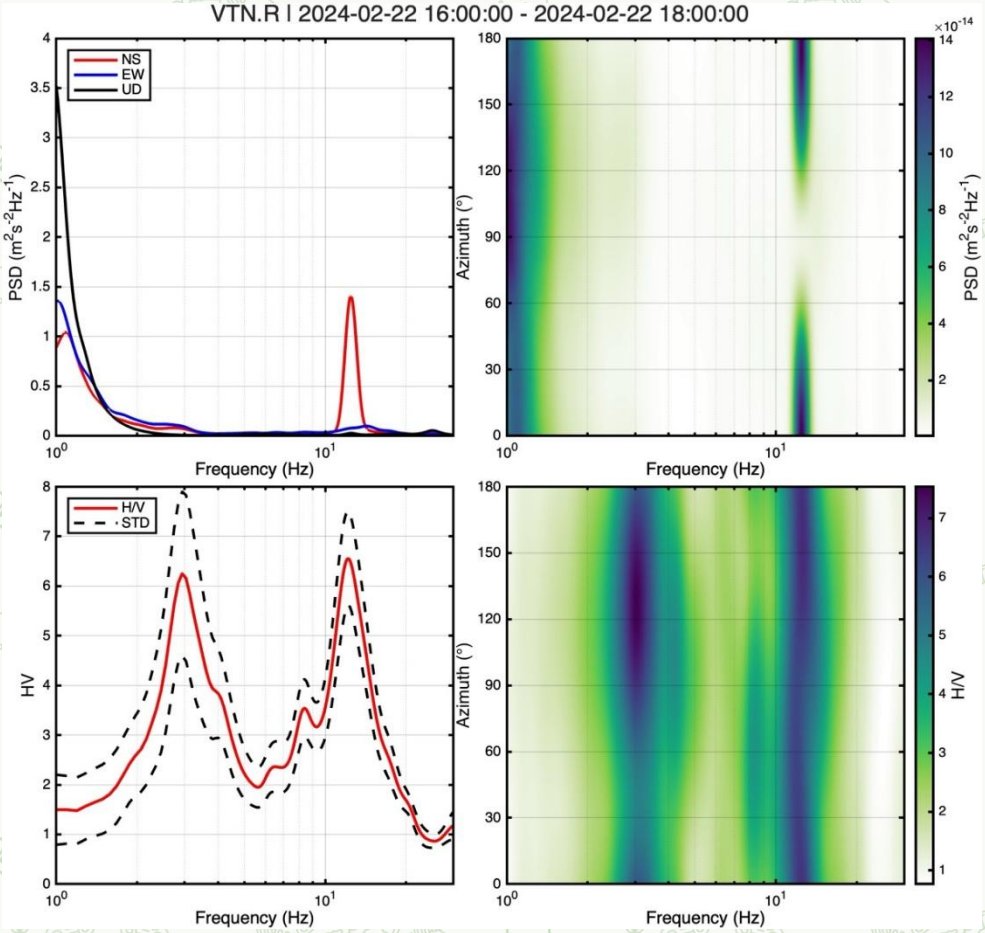

Figure 67: Results of the HVSR analysis at station VTN.R. Power spectral density (PSD) plot of all components of ground motion (upper-left panel) and relative power spectral density rotate plot (upper-right panel). Horizontal-to-vertical spectral ratio (HVSR) plot (lower-left panel) and relative HVSR rotate plot (lower-right panel). All frequency axes are logarithmically-scaled and limited to the range 1–30 Hz.

20.4.3. Results of TFPA Analysis

TFPA technique was employed at station VTN.B to characterize the dynamic behavior of a potentially unstable rock block jutting out the subvertical tuff cliff in the western sector of the promontory of Punta Eolo (Fig. 66). Before proceeding with TFPA, spectral analysis was conducted and highlighted the existence of two prominent peaks at 37 and 65 Hz (Fig. 68). These two peaks clearly emerge from

background noise, as it can also be observed from spectrograms (Fig. 69), supporting their interpretation as resonance modes of the investigated rock block.

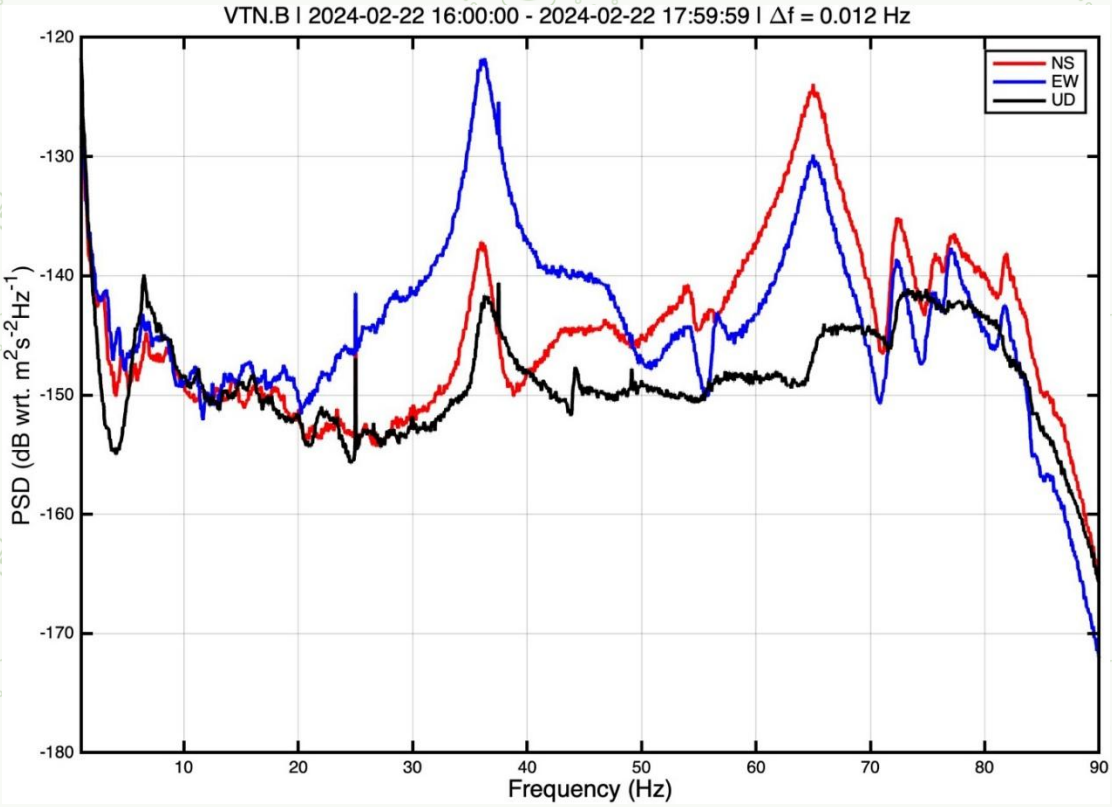

Figure 68: Power spectral density (PSD) plot for station VTN.B.

Based on this preliminary result, TFPA was applied to the ambient vibration dataset, and the main polarization attributes of the two identified spectral peaks were derived (Fig. 70). From the observation of the probability density plots, the two previously identified peaks are markedly visible and feature degrees of polarization close to 1 (i.e., strongly polarized particle motion). Within the frequency range of interest (1–100 Hz), no other polarized peaks emerge at station VTN.B, leading to the hypothesis that those identified frequencies can be considered as first-order resonance modes of the investigated rock block.

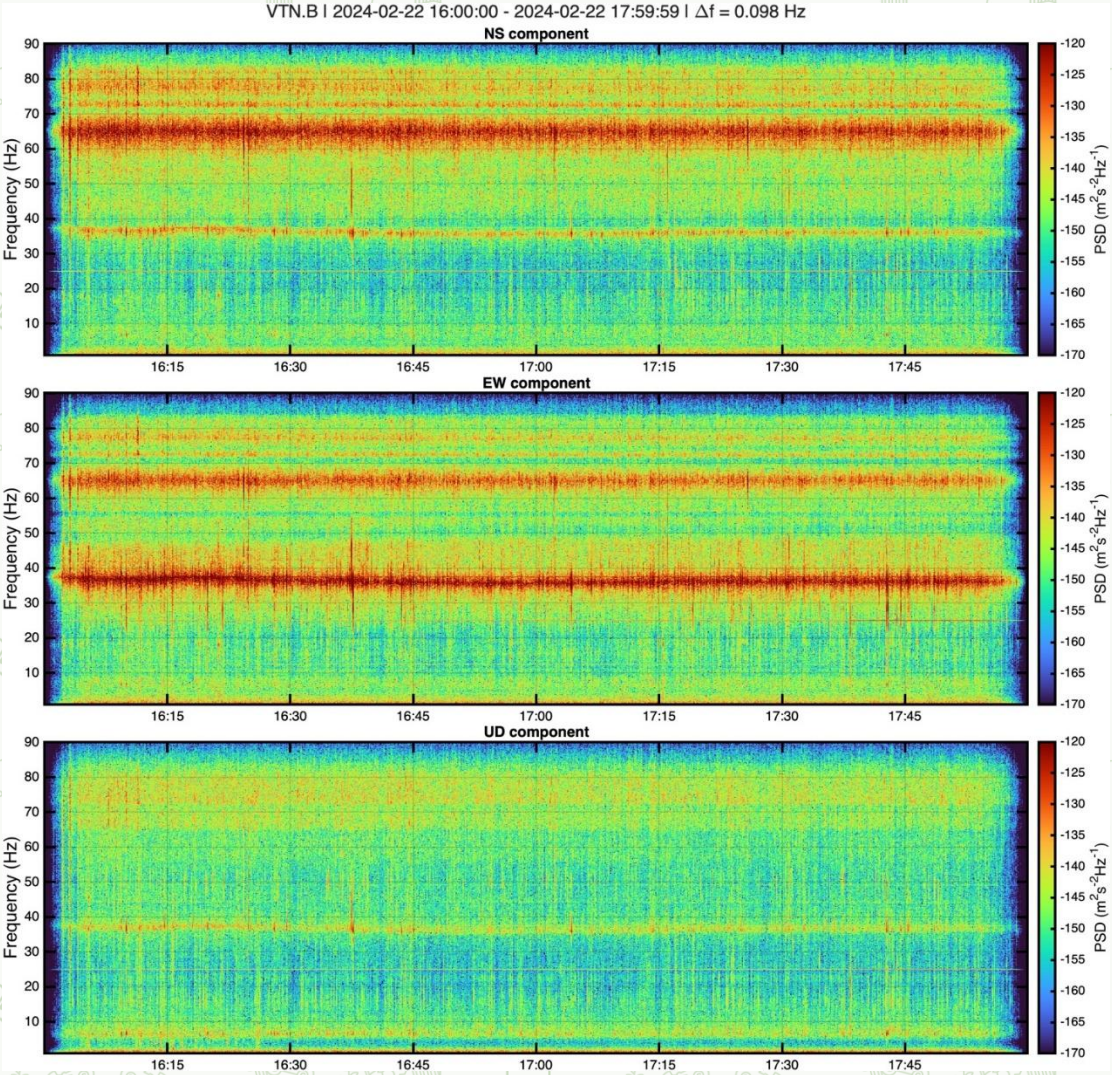

Figure 69: Spectrograms of all components of ambient vibrations at station VTN.B.

Polarization attributes can then be automatically extracted and plotted on a stereographic projection to evaluate possible relationships with the local structural conditions of the rock block. In fact, by extracting polarization degrees and angles using the SAT, the user can create a synthetic plot along with a .txt file containing all info for the selected spectral peaks (Fig. 71).

The here presented example clearly highlights the efficacy of sparse ambient vibration measurements in providing key insights into the preliminary modal characterization of potentially unstable rock elements.

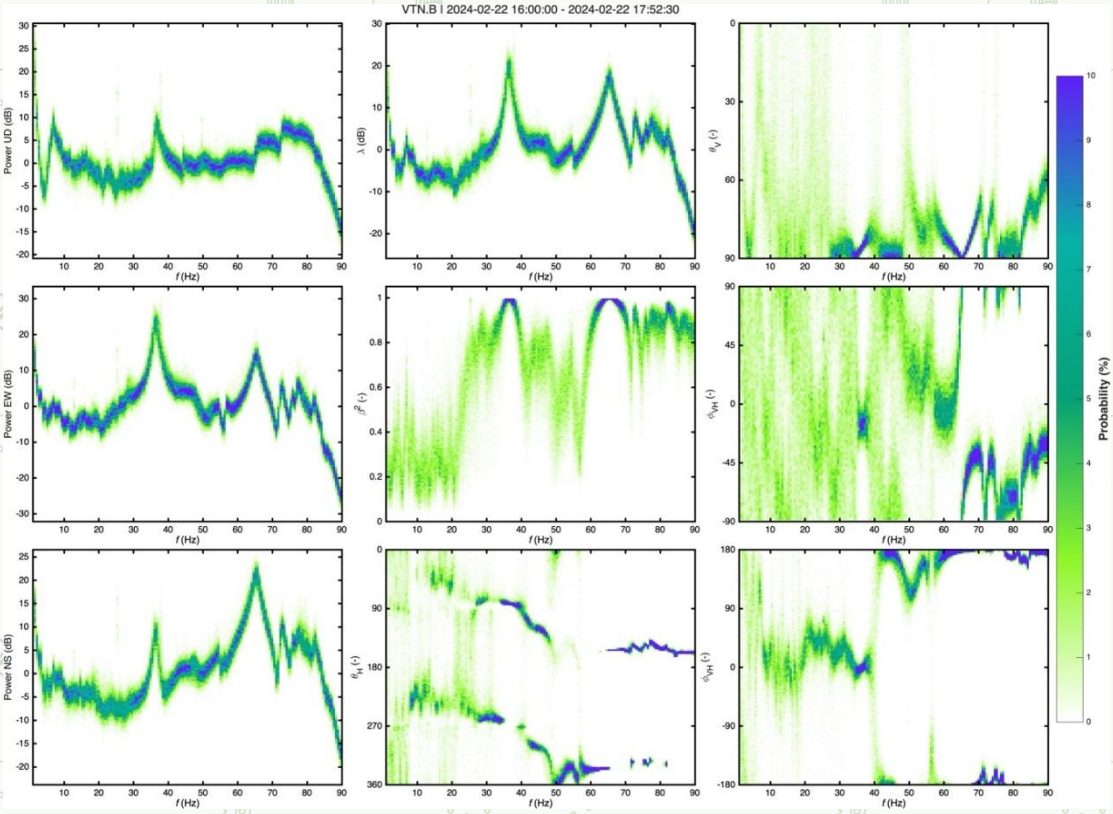

Figure 70: Probability density plot of spectral and polarization attributes derived from ambient vibration measurements at station VTN.B. Power spectra for the horizontal and vertical components (left column panels); the principal eigenvalue spectrum(λ), the degree of polarization (β^2) and the azimuth of polarization ellipsoid (θ_H) (central column panels); incidence angle of the polarization ellipsoid (θ_V), along with phase differences between the vertical and principal horizontal components (ϕ_{VH}) and the two horizontal components (ϕ_{HH}) (left column panels).

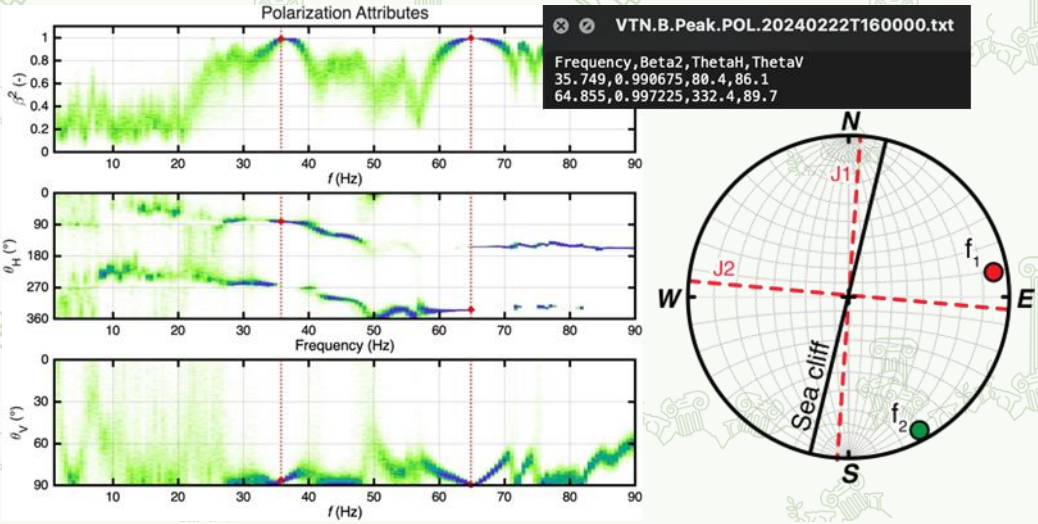

Figure 71: Synthetic plot of polarization attributes at station VTN.B: degree of polarization (upper panel), polarization azimuth (central panel) and polarization incidence angle (lower panel). Lower hemisphere stereographic projection (equal angle) shows measured polarization vectors for the first (red circle) and second (green circle) resonance mode of the analyzed rock block. The black line represents the direction of the sea cliff, whereas dotted red lines indicate the main joint sets in the area (J1 – 275N/85°, J2 – 05N/85°).

20.5. References

Bessette-Kirton, E. K., Moore, J. R., Geimer, P. R., Finnegan, R., Häusler, M., & Dzubay, A. (2022). Structural Characterization of a Toppling Rock Slab From Array-Based Ambient Vibration Measurements and Numerical Modal Analysis. Journal of Geophysical Research: Earth Surface, 127(8). https://doi.org/10.1029/2022JF006679

Clinton, J. F., Bradford, S. C., Heaton, T. H., & Favela, J. (2006). The observed wander of the natural frequencies in a structure. Bulletin of the Seismological Society of America, 96(1), 237–257. https://doi.org/10.1785/0120050052

Feliziani, F., Marmoni, G. M., Gianni, V., Ferrandes, A. F., Pegurri, A., Grechi, G., Giulia Felli, Ciampi, P., Bozzano, F., Delpino, C., Arrighi, C., & Martino, S. (2024). Engineering-geological modelling as a tool for archaeological site preservation strategies. Italian Journal of Engineering Geology and Environment, 115–126. https://doi.org/10.4408/IJEGE.2024-01.S-13

Geimer, P. R., Finnegan, R., & Moore, J. R. (2022). Meteorological Controls on Reversible Resonance Changes in Natural Rock Arches. Journal of Geophysical Research: Earth Surface, 127(10). https://doi.org/10.1029/2022jf006734

Kleinbrod, U., Burjánek, J., & Fäh, D. (2019). Ambient vibration classification of unstable rock slopes: A systematic approach. Engineering Geology, 249(January 2018), 198–217. https://doi.org/10.1016/j.enggeo.2018.12.012

Koper, K. D., & Hawley, V. L. (2010). Frequency dependent polarization analysis of ambient seismic noise recorded at a broadband seismometer in the central United States. Earthquake Science, 23(5), 439–447. https://doi.org/10.1007/s11589-010-0743-5

Larose, E., Carrière, S., Voisin, C., Bottelin, P., Baillet, L., Guéguen, P., Walter, F., Jongmans, D., Guillier, B., Garambois, S., Gimbert, F., & Massey, C. (2015). Environmental seismology: What can we learn on earth surface processes with ambient noise? Journal of Applied Geophysics, 116, 62–74. https://doi.org/10.1016/j.jappgeo.2015.02.001

McNamara, D. E., & Buland, R. P. (2004). Ambiente noise levels in the continental United States. Bulletin of the Seismological Society of America, 94(4), 1517–1527. https://doi.org/10.1785/012003001

Wathelet, M., Chatelain, J.-L., Cornou, C., Giulio, G. D., Guillier, B., Ohrnberger, M., & Savvaidis, A. (2020). Geopsy: A User-Friendly Open-Source Tool Set for Ambient Vibration Processing. Seismological Research Letters, 91(3), 1878–1889. https://doi.org/10.1785/0220190360

Welch, P. (1967). The use of fast Fourier transform for the estimation of power spectra: A method based on time averaging over short, modified periodograms. IEEE Transactions on Audio and Electroacoustics, 15(2), 70–73. https://doi.org/10.1109/TAU.1967.1161901

20.6. Contributors

Developed by: Sapienza University of Rome (SUR)

Date of last update: 10/11/2025

Lead contributors:

- Guglielmo Grechi
- Federico Feliziani
- Gian Marco Marmoni
- Mattia Montagnese
- Salvatore Martino
- Francesca Bozzano
- Gabriele Scarascia Mugnozza

21. Slope Stability Toolbox (SST)

21.1. Overview

Slope Stability Toolbox (SST) has been developed to evaluate the stability conditions of rock walls interested by toppling kinematics. A Factor of Safety (FS) is defined as the physical index describing the stability condition of a specific rock-block under different driving (destabilizing) actions. The FS value, in facts, indicates how close the considered rock-block is to collapse, offering a quantitative description of the stability condition of such geological system.

The magnitude of the driving actions implemented in the SST are related to the recurrence time of the considered natural processes, i.e. the average time interval within a natural process can occur with a certain magnitude. In other words, the recurrence time is related to the definition of natural “hazard”, thus the probability that a natural event (e.g., seismic action caused by an earthquake, heavy rainfall), characterized by a specific magnitude, will strike an exposed element (e.g., a rock-block) in a defined time window.

For these reasons, a forward scenario analysis based on the SST can be performed. By determining the probability of occurrence of the driving actions incorporated in the SST, it becomes feasible to assess the stability condition of the rock-blocks under specific scenarios where certain magnitudes of natural processes (i.e., driving forces) occur.

21.2. Methodological Description

21.2.1. Theory and Background

Landslides are among the most important natural processes interesting the TRIQUETRA project pilot sites. In order to assess the geological risk related to such phenomena it is necessary to perform a so-called “slope stability analysis”. This latter represents an essential tool to evaluate the stability conditions of a specific

portion of a slope, and to understand which are the destabilizing actions (e.g., seismic action, water pressure increase related to rainfall) that can lead the slope to instability.

The scientific literature is constantly updated with application examples of slope stability analysis to a wide variety of case studies. In such context, all the applied slope stability analysis are essentially based on analytical or numerical approaches.

Analytical approaches are those that were developed first, marking the beginning of the slope stability sciences (e.g., Fellenius, 1936; Taylor, 1937; Bishop, 1955; Morgensten & Price, 1965; Spencer, 1967; Janbu, 1968). All the methods that are based on analytical approaches implies several assumptions, the most important of which is to consider the slope (be it constituted of earth or rock) as a rigid mass characterized by instant movements. On the other hand, numerical approaches have been developed later, since they are based on numerical calculations that can be performed only via computers. Among other things, the algorithmic basis of this family of approaches is able to return the stress-strain distribution within the slope and to model the time-dependent slope deformation. The choice between the two approaches depends on the objective of the study being conducted.

Analytical approaches are traditionally used in professional and research practice for analyzing homogeneous, modest-size slopes characterized by instantaneous displacement, and for which it is easy to infer the rupture surface position and geometry. The greatest advantage of applying the analytical approach to slope stability analysis is that it is easy and fast to manage.

Numerical models are instead used for complex-geometry slopes characterized by non-instantaneous rupture dynamics. Even if the results of these approaches are more advanced in terms of returned information, their application is very time-consuming and, therefore, is limited to the analysis of a single specific slope at time.

In order to offer a tool as practical as possible for the T4.3 TRIQUETRA project deliverable, the SUR working group has decided to use an analytical approach for the slope stability analyses. The employed method is the Global Limit Equilibrium Method (GLEM). The use of a GLEM is based on the assumptions that i) the rupture surface (i.e., its position and geometry) is well known, ii) the rupture conditions are reached simultaneously along the slip surface, and iii) during the failure, the maximum strength is recalled along the entire rupture plane. To define the stability condition of the analyzed slope, a Factor of Safety (FS) is calculated. FS is a dimensionless number defined by the ratio of the resisting forces of moments (RF) (which prevent the failure) to the driving forces (DF) or moments (which promote the failure) along a potential failure surface. Mathematically, the FoS can be expressed as:

$$FS = \frac{RF}{DF}$$

A Factor of Safety greater than 1 indicates that the slope is stable, meaning the resisting forces exceed the driving forces. Conversely, a Factor of Safety less than 1 indicates that the slope is unstable, as the driving forces exceed the resisting forces. An FS equal to 1 signifies that the slope is on the verge of failure.

The GLEM has been applied, taking into account a rigid rock-block prone to a toppling-type failure, sensu Hungr et al. (2014). Most of the non-submerged TRIQUETRA pilot sites (i.e., Ventotene, Aegina, Choirokoitia) are, in fact, characterized by the presence of sub-vertical rock-walls susceptible to rock-toppling. The kinematic compatibility to toppling failure is analyzed using the Markland (1972) approach. The bare minimum to describe a block prone to topple is that:

- A dip value of the joint set that releases the rock-block must be higher than the opposite of the average dip value of the slope face;
- A bisector of the angle formed by the strike direction of two joint sets delimiting the rock-block must shape a maximum angle of ±10° with respect to all dip directions of the slope.

A rock block susceptible to a toppling failure is thus located along the sub-vertical rock wall, and it is isolated from the stable portion of the rock mass by a set of joints. Additionally, it can be characterized by the presence of a cantilever projection over the sustaining bedrock. The FS is calculated considering different static (i.e., weight force) and pseudostatic (i.e., seismic force, hydrostatic pressure within the joints).

According to Martino & Mazzanti (2014) and Mazzanti et al. (2018), two types of analysis can be performed, considering the presence of projecting and non-projecting blocks.

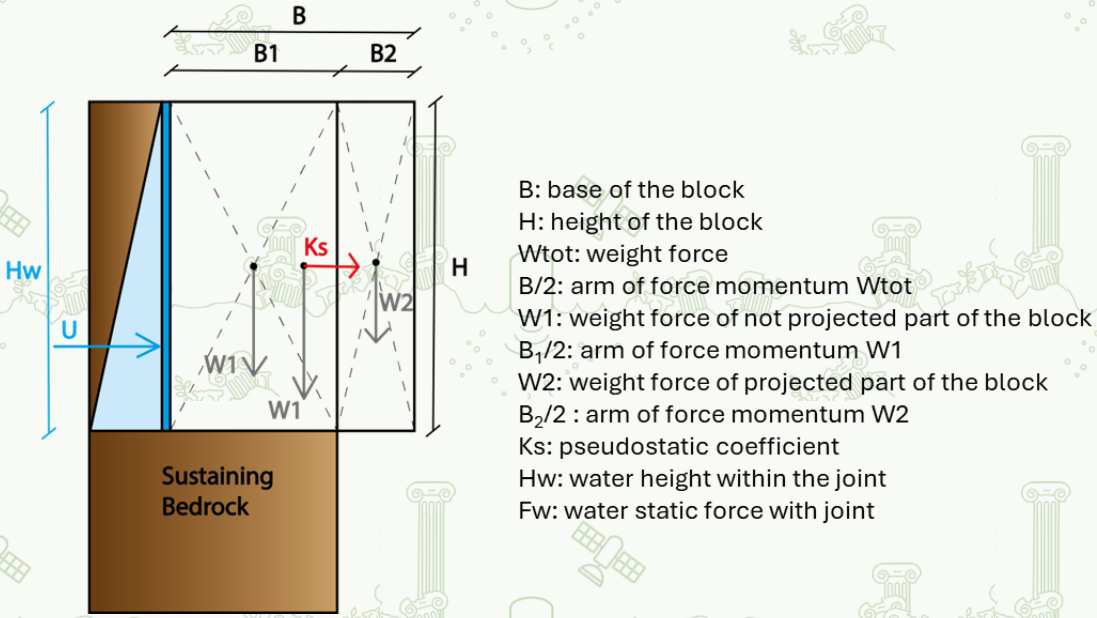

Figure 72: Two-dimensional scheme of projecting block subjected to weight force, seismic pseudo-static force and water static force within the joints.

In natural conditions, the resisting forces (RF) preventing failure depend only on the weight of the portion of the block located above the non-projecting block. Different combinations of driving forces can instead be considered. In the presented *Slope Analysis Toolbox,* it is possible to account for seismic action (SA) and hydrostatic pressure (HP) related to the water filling of the detaching joints. The FS can thus be expressed as follows:

$$FS = \frac{RF}{PB + SA + HP}$$

Where:

$$RF = W_1 * \frac{B_1}{2}$$

$$PB = W_2 * \frac{B_2}{2}$$

$$SA = W_{tot} * K_s * \frac{h}{2}$$

$$HP = \frac{1}{6} * \gamma_w * {h_w}^3$$

As reported in the equations, the driving actions are expressed in terms of momentum. These latter are referred to as a center of rotation (fulcrum) located at the base of the detected rock block. The position of the center of rotation is therefore controlled by the dimensions of the blocks and, eventually, by the presence of a cantilever (i.e., of a projected rock-block).

In addition to the FS, the model is able to run sensitivity analyses returning the conditions required to reach the disequilibrium for block toppling, considering the simultaneous and not-simultaneous action of the destabilizing forces. In particular, a sensitivity analysis of a slope involves assessing how changes in various input parameters affect the slope's stability. This type of analysis identifies critical factors that influence the slope's behavior and determines the robustness of the slope's stability under different conditions. By systematically varying parameters such as soil properties, slope geometry, and external loads, it is possible to evaluate the impact of each factor on the slope's safety and performance (i.e., on the FS variability).

Seismic action is computed as a pseudostatic action. In this way, the dynamic effect of the transient event (seismic shaking) is converted into a static term expressed by an equivalent force. This technique is beneficial for simplifying calculations and obtaining a preliminary estimate of the analyzed action. However, it cannot replace detailed dynamic analysis when a more precise and accurate evaluation is required.

21.2.2. Workflow

The Slope Stability Toolbox is constituted by a MATLAB script called “SST.mat”. The script comprises several sections that can be run separately or collectively,

depending on the analysis's goal. Each section is anticipated by some descriptive lines of code that introduce to the user the main features of the model's branch.

A. Input section

The Slope Stability Toolbox requires different types of input for its operation. These inputs refer to the characteristics of the geological system being studied and the destabilizing factors that need to be considered. The analyzed slope must first be characterized in terms of its geostructural setting, meaning a geomechanical (in situ and/or remote) survey must be conducted to identify rock blocks that are susceptible to toppling. For inputs related to destabilizing factors, they can be obtained from specific catalogs or direct measurements. All input parameters are compiled into a .csv file that the MATLAB script can easily access read.

1. Geomechanical properties and geometrical characteristics

A detailed study of the area of interest has to be performed. The main goal of this stage of territorial analysis is to reconstruct the geostructural setting of the slope, and to achieve information about the rock-mass joint sets, i.e. the geometric features of each separated rock-block. Direct and remote geomechanical analysis can be performed in order to define the fracture network characteristics of the rock-mass according to the ISRM (2007). The combination of both the methods gives the best results. Laboratory determinations are also necessary to define the density of the rock-material (i.e., weight per unit volume, **gamma**). The following geometrical entities are defined for each detected rock-block:

- block ID (***ID***)
- Base of the block (***B***)
- base of the not-projected portion of the block (***B1***)
- base of the projected block of the block (***B2***)
- height of the block (***H***)
- Length of the block (***L***)
- Water height into the disjoining fracture located behind the rock-block (***Hw***)

The collected data have to be reported in the input .csv file.

2. Seismic action

To characterize seismic action as a pseudostatic force, the model requires a parameter representing the seismic shaking. This is provided by the Peak Ground Acceleration (PGA, g), which offers useful information to quantify seismic hazard across different TRIQUETRA pilot sites. This parameter reflects the probability that seismic shaking of a specific intensity will occur over a certain return period in a given area. The PGA is referenced to seismic bedrock and therefore does not consider potential seismic amplification effects. PGAs can be obtained from various

catalogs referencing European or national scales. The 2020 European Seismic Hazard Model (ESHM20) (Danciu et al., 2021) serves as a source for each of the TRIQUETRA pilot sites. Countries like Germany, Switzerland, and Italy also have more detailed catalogs. For example, the Italian Seismic Hazard Model MPS04-S1, provided by the Istituto Nazionale di Geofisica e Vulcanologia (INGV) (Stucchi et al., 2004), allows visualization and querying of the probabilistic seismic hazard model for Italy, which uses shaking parameters on a regular grid spaced at 0.05°. These maps display two shaking parameters, PGA (horizontal peak ground acceleration) and Sa (spectral acceleration), with the unit of measurement being g, representing gravity acceleration at 9.8 m/s^2. The chosen PGA value is incorporated into the Slope Stability Toolbox as a pseudostatic coefficient called "Ks," which is included in the input .csv file. The Ks remains consistent across all rock blocks.

B. Data importing

As already mentioned, the SST works using a .csv file as input. This file contains all the input data related to the geometrical characteristics of the identified rock blocks and to the driving actions. It essential to preserve this nomenclature to make the SST work. Some of the input .csv file columns are filled with the input data, while others are empty because they will contain different numerical results of the SST. An example of input .csv file is showed in Fig 73.

The script's section dedicated to the input .csv file is the following:

```
%.csv input file import
table = readtable("input.csv",
"LeadingDelimitersRule","ignore");
```

The .csv file is returned to a table named "table". Then, the input data are stored as new MATLAB variables:

```
%variables definition
B1 = table.B1;
B2 = table.B2;
H = table.H;
L = table.L;
gamma = table.gamma;
Ks = table.Ks;
Hw = table.Hw;

table.Bb1 = B1./2;
Bb1 = table.Bb1;
table.Bb2 = B2./2;
Bb2 = table.Bb2;
table.V1 = B1.*H.*L;
V1 = table.V1;
table.V2 = B2.*H.*L;
V2 = table.V2;
table.W1 = V1.*gamma;
W1 = table.W1;
```

```
table.W2 = V2.*gamma;
W2 = table.W2;
table.Wtot = W1 + W2;
Wtot = table.Wtot;
```

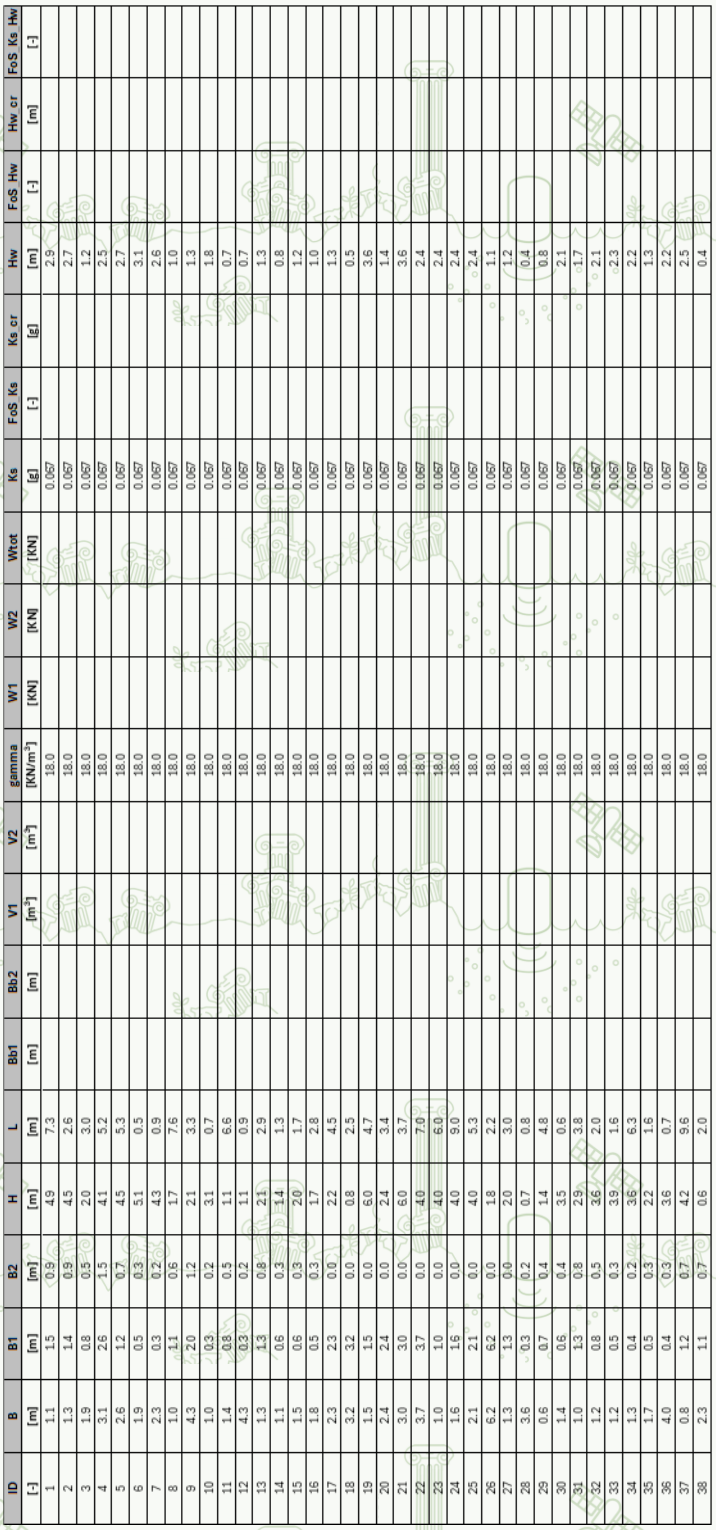

ID	B	B1	B2	H	L	Bb1	Bb2	V1	V2	gamma	W1	W2	Wtot	Ks	FoS Ks	Ks cr	Hw	FoS Hw	Hw cr	FoS Ks Hw
[-]	[m]	[m]	[m]	[m]	[m]	[m]	[m]	[m³]	[m³]	[KN/m³]	[KN]	[KN]	[KN]	[g]	[-]	[g]	[m]	[-]	[m]	[-]
1	1.1	1.5	0.9	4.9	7.3					18.0				0.057			2.9			
2	1.3	1.4	0.9	4.5	2.6					18.0				0.057			2.7			
3	1.9	0.8	0.5	2.0	3.0					18.0				0.057			1.2			
4	3.1	2.6	1.5	4.1	5.2					18.0				0.057			2.5			
5	2.6	1.2	0.7	4.5	5.3					18.0				0.057			2.7			
6	1.9	0.5	0.3	5.1	0.5					18.0				0.057			3.1			
7	2.3	0.3	0.2	4.3	0.9					18.0				0.057			2.6			
8	1.0	1.1	0.6	1.7	7.6					18.0				0.057			1.0			
9	4.3	2.0	1.2	2.1	3.3					18.0				0.057			1.3			
10	1.0	0.3	0.2	3.1	0.7					18.0				0.057			1.8			
11	1.4	0.8	0.5	1.1	6.6					18.0				0.057			0.7			
12	4.3	0.3	0.2	1.1	0.9					18.0				0.057			0.7			
13	1.3	1.3	0.8	2.1	2.9					18.0				0.057			1.3			
14	1.1	0.6	0.3	1.4	1.3					18.0				0.057			0.8			
15	1.5	0.6	0.3	2.0	1.7					18.0				0.057			1.2			
16	1.8	0.5	0.3	1.7	2.8					18.0				0.057			1.0			
17	2.3	2.3	0.0	2.2	4.5					18.0				0.057			1.3			
18	3.2	3.2	0.0	0.8	2.5					18.0				0.057			0.5			
19	1.5	1.5	0.0	6.0	4.7					18.0				0.057			3.6			
20	2.4	2.4	0.0	2.4	3.4					18.0				0.057			1.4			
21	3.0	3.0	0.0	6.0	3.7					18.0				0.057			3.6			
22	3.7	3.7	0.0	4.0	7.0					18.0				0.057			2.4			
23	1.0	1.0	0.0	4.0	6.0					18.0				0.057			2.4			
24	1.6	1.6	0.0	4.0	9.0					18.0				0.057			2.4			
25	2.1	2.1	0.0	4.0	5.3					18.0				0.057			2.4			
26	6.2	6.2	0.0	1.8	2.2					18.0				0.057			1.1			
27	1.3	1.3	0.0	2.0	3.0					18.0				0.057			1.2			
28	3.6	0.3	0.2	0.7	0.8					18.0				0.057			0.4			
29	0.6	0.7	0.4	1.4	4.8					18.0				0.057			0.8			
30	1.4	0.6	0.4	3.5	0.6					18.0				0.057			2.1			
31	1.0	1.3	0.8	2.9	3.8					18.0				0.057			1.7			
32	1.2	0.8	0.5	3.6	2.0					18.0				0.057			2.1			
33	1.2	0.5	0.3	3.9	1.6					18.0				0.057			2.3			
34	1.3	0.4	0.2	3.6	6.3					18.0				0.057			2.2			
35	1.7	0.5	0.3	2.2	1.6					18.0				0.057			1.3			
36	4.0	0.4	0.3	3.6	0.7					18.0				0.057			2.2			
37	0.8	1.2	0.7	4.2	9.6					18.0				0.057			2.5			
38	2.3	1.1	0.7	0.6	2.0					18.0				0.057			0.4			

Figure 73: Example of input .csv file.

C. Factor of Safety Computation

The first operative section is represented by the Factor of Safety (FS) calculation. This step of analysis can be performed taking into account the action of a single driving force or considering simultaneous actions.

Considering only the seismic force alone, the pseudostatic coefficient **Ks** contained in the input file is assumed to calculate the FS of all the detected rock-blocks (**FS_Ks**). The calculated FS is implemented in corresponding column of the **table**.

```
%% FoS with seismic action only
%The FS is calculated only considering the seismic action only
table.FoS_Ks = (Bb1.*W1)./((Bb2.*W2)+(Wtot.*Ks.*(H./2)));
```

It is possible to find also the so-called “critical pseudostatic seismic coefficient” (Ks_cr), i.e. the value of pseudostatic force that cause the disequilibrium of the system. The Ks_cr can be obtained by setting the FS = 1 and solving the equation:

```
% To find the critical Ks (i.e., Ks_cr):
table.Ks_cr = (2.*((W1.*Bb1)-(W2.*Bb2)))./(Wtot.*H);
```

Another possibility is to run the model returning a Factor of Safety (FS) under the assumption of the hydrostatic pressure due to the water filling of the joint disjoining the rock-block. The water height **Hw** contained in the input file is thus assumed to calculate the FS of all the detected rock-blocks (**FS_Hw**). The calculated FS is implemented in corresponding column of the **table**.

```
%% FoS with hydrostatic action only
%The FS is calculated only considering the hydrostatic action
only
table.FoS_Hw                                                    =
(W1.*Bb1)./((W2.*Bb2)+((1/6).*9.81.*(Hw.^3)));
```

It is possible to find also the so-called “critical water height” (**Hw_cr**), i.e. the value of water height that cause the disequilibrium of the system. The **Hw_cr** can be obtained by setting the FS = 1 and solving the equation:

```
%To find the critical Hw (i.e., Hw_cr):
table.Hw_cr = ((((W1.*Bb1)-(W2.*Bb2)).*6)./9.81).^(1/3);
```

The FS calculation can be also advanced considering the concurrency of the seismic and hydrostatic actions. **Ks** and **Hw** are both considered in the FS calculation as follows:

```
%The FS is calculated considering both the seismic and
hydrostatic actions
table.FoS_Ks_Hw
=(W1.*Bb1)./((W2.*Bb2)+((1/6).*9.81.*(Hw.^3))+(Wtot.*Ks.*
(H./2)));
```

D. Sensitivity Analysis

SST can perform a sensitivity analysis thanks to which is possible to visualize how the FS varies depending on one of the driving forces. In particular, this analysis is referred to a single rock-block (defined by a specific **ID**) and returns a sensitivity chart. This latter reports on the x-axis the value of the investigated parameter related to the destabilizing factor (e.g., **Hw** or **Ks**) and on the y-axis the FS value.

The generation of a sensitivity chart referred to the water height in the SST is derived as follows:

```
Hw = (0:1:Hw_cr(1))'; % Generate a column vector that goes
from 0 to Hw_cr (referred to a
% specific ID block), with spacing = 1

Hw_H = Hw./H(1); % Normalization of the Hw
FoS_Hw_I =
(W1(1).*Bb1(1))./((W2(1).*Bb2(1))+((1/6).*9.81.*(Hw.^3))); %
Note that Hw is not indexed

plot(Hw_H, FoS_Hw_I, 'b--', "LineWidth", 2)
```

While, referring to the seismic action:

```
Ks = (0:0.005:Ks_cr(1))'; % Generate a column vector that goes
from 0 to Ks_cr (referred to a
% specific ID block), with spacing = 1

FoS_Ks_I =
(Bb1(1).*W1(1))./((Bb2(1).*W2(1))+(Wtot(1).*Ks.*(H(1)./2))); %
Note that Ks is not indexed

plot(Ks, FoS_Ks_I, 'r--', "LineWidth", 2)
```

Exemplary sensitivity charts are presented in Figure 74:

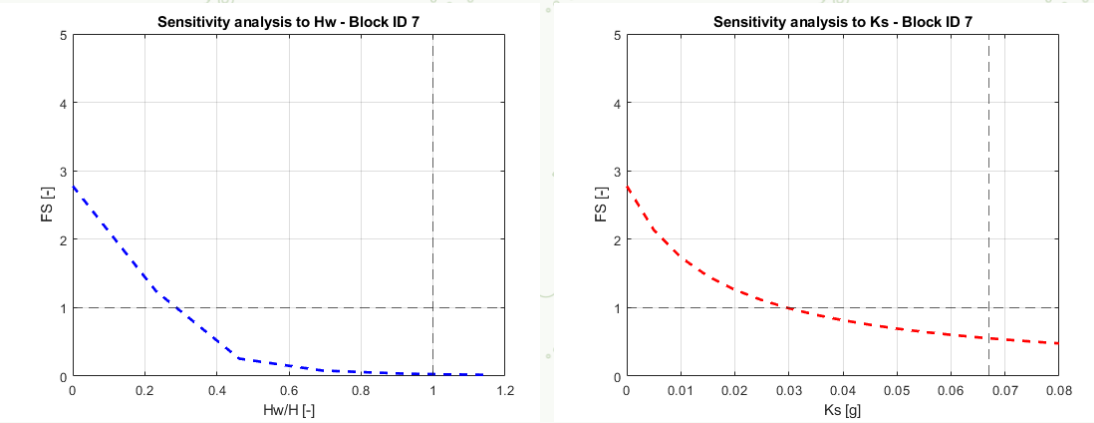

Figure 74: Example of sensitivity charts referred to the water static force (left) and to the seismic action (right).

E. Stability Charts

A stability chart conceptualizes a hazard approach in a conventional sensitivity analysis output. The chart illustrates the potential for a slope to fail if two events occur, each with a different and independent probability of occurrence. Each point

of the line corresponds to a couple of values representing the values of driving actions that, coupled together (i.e., co-occurring), cause the disequilibrium of the slope leading the FS = 1.

SST provides a dedicated section in the MATLAB script for generating a stability chart. This latter is generated for all the rock blocks described in the input .csv file.

```
%% STABILITY DIAGRAMS GENERATION
%This part of the script returns a diagram thanks to which it
is possible
%to visualize the combination of two driving forces able to
produce a
%disequilibrium (i.e., to generate a FS = 1).

n_points = 100; % the higher the number of this value, the
smoother is the curve

% calculates the number of rows
numRows = height(table);

% for each row
for i = 1:numRows
    % parameters definition
    W1 = table.W1(i);
    Bb1 = table.Bb1(i);
    W2 = table.W2(i);
    Bb2 = table.Bb2(i);
    Wtot = table.Wtot(i);
    H = table.H(i);

    % call the function that you will be define later
    plotKsHw(W1, Bb1, W2, Bb2, Wtot, H, n_points, i);

end

function plotKsHw(W1, Bb1, W2, Bb2, Wtot, H, n_points, row)

     % Sets the equation FoS_Ks_Hw - 1 = 0 as a function
handle (that is, you basically define a tFoS_Ks_Hw_eqn' object
that when called performs the operations)
     FoS_Ks_Hw_eqn = @(Ks, Hw) (W1.*Bb1)./
W2.*Bb2)+((1/6).*9.81.*(Hw.^3))+(Wtot.*Ks.*(H./2))) - 1;
     % Find Ks_max by solving for Hw = 0 (if you already know
the value, simply do Ks_max=...)
     Ks_max = fsolve(@(Ks) FoS_Ks_Hw_eqn(Ks, 0), 1); % Initial
guess for Ks = 1

     % Generate n_points values uniformly distributed Ks
between 0 and Ks_max, and initialises the values of Hw
     Ks_values = linspace(0, Ks_max, n_points);
     Hw_values = zeros(size(Ks_values));
```

```
        % For each value of Ks, find the corresponding Hw
        options = optimoptions('fsolve', 'Display', 'none');
        for i = 1:length(Ks_values)
            [Hw_values(i), ~, exitflag, ~] = fsolve(@(Hw)
FoS_Ks_Hw_eqn(Ks_values(i), Hw), 1, options);
            if exitflag ~= 1
                Hw_values(i) = NaN; % Mark as NaN if no solution
found
            end
        end

        % plot the values
        figure;
        plot(Ks_values, Hw_values, 'LineWidth', 2, 'Color',
'#F4A261');
        xlabel('Ks [-]');
        ylabel('Hw [m]');
        title(sprintf('Stability diagram of Ks vs. Hw, Block ID:
%d', row));
        grid on;
        xlim([0, Ks_max*1.1]);
        ylim([0, max(Hw_values)+1]);
end
```

An exemplary stability chart is presented in Figure 75.

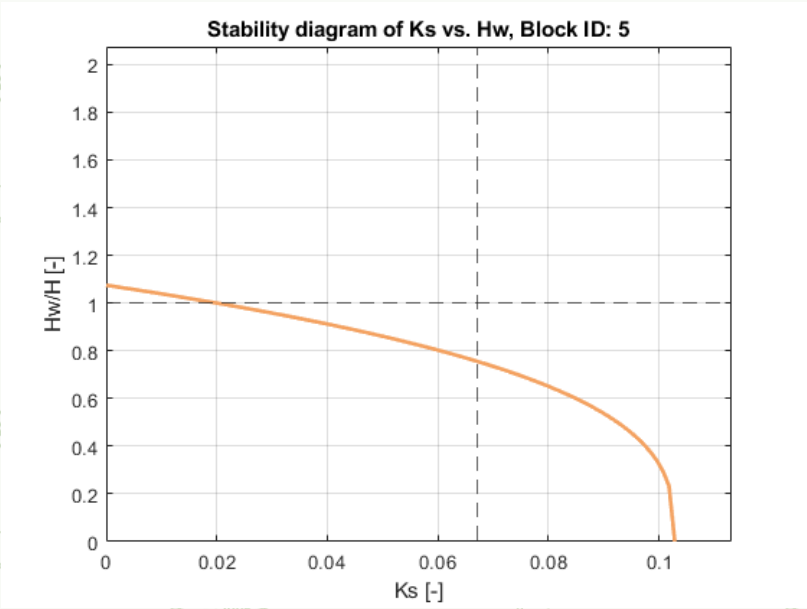

Figure 75: Example of Stability Chart.

21.3. Application Example

The SUR working group used the SST to perform a stability analysis of the Ventotene sea cliff. This pilot site was selected as a training site because, at the time of drafting this document, Ventotene has the most available data. The magnitude of the considered driving actions relates to the recurrence time of natural processes, which

is the average time interval during which a natural process of a certain magnitude occurs. In other words, the recurrence time defines a natural "hazard," representing the probability that a natural event (such., seismic activity caused by an earthquake or heavy rainfall) with a specific magnitude will impact an exposed element (e.g., a rock block) within a given time frame. A forward scenario analysis based on the SST has been performed and is presented here for the Ventotene case study. Specifically, the seismic action magnitude (i.e., Ks) was related to a return period of 475 years. Since hazard data pertaining to water height saturating the joints is unavailable for Ventotene, the initial value of Hw was arbitrarily fixed at 0.1 m for all blocks. Consequently, the stability condition analysis considered a natural hazard scenario where hydrostatic water action and seismic activity are likely representative of the next 475 years. Field and remote surveys identified all the rock blocks around Ventotene that threaten the CH-site of the Roman Villa Giulia. A total of 38 blocks were recognized. The geometrical properties of each block, kinematically compatible with toppling failure per Markland (1972), were measured (Fig. 76), stored in a .csv file (Fig. 77), and imported into the model via the SST.

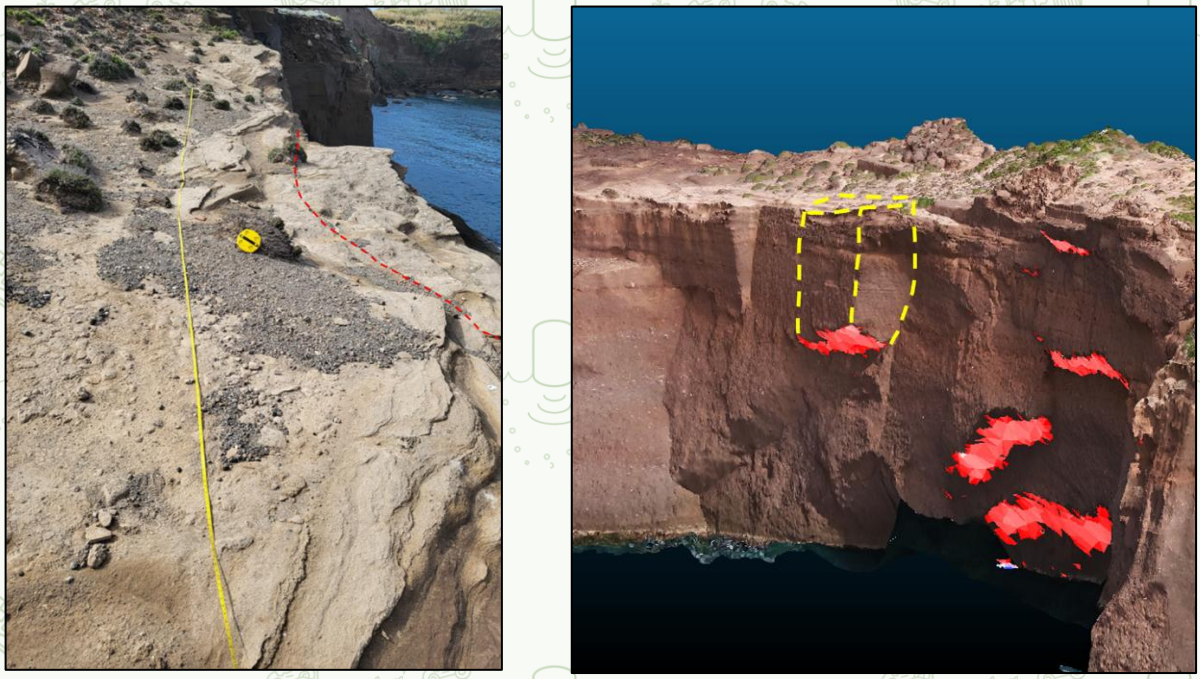

Figure 76: Rock-block detection geometrical characterization carried out in Ventotene via in situ (left panel) and remote analyses (right panel).

ID	B	B1	B2	H	L	Bb1	Bb2	V1	V2	gamma	W1	W2	Wbot	Ks	FoS_Ks	Ks_cr	Hw	FoS_Hw	Hw_cr	FoS_Ks_Hw
[-]	[m]	[m]	[m]	[m]	[m]	[m]	[m]	[m^3]	[m^3]	[KN/m^3]	[KN]	[KN]	[KN]	[g]	[-]	[g]	[m]	[-]	[m]	[-]
1	1.09	1.50	0.90	4.90	7.30	0.75	0.45	53.80	32.28	18.00	968.37	581.02	1549.38	0.067	1.41	0.12	0.10	2.78	6.58	1.41
2	1.27	1.44	0.86	4.50	2.60	0.72	0.43	16.85	10.11	18.00	303.26	181.96	485.22	0.067	1.44	0.13	0.10	2.78	4.40	1.44
3	1.94	0.80	0.48	2.00	3.00	0.40	0.24	4.80	2.88	18.00	86.40	51.84	138.24	0.067	1.59	0.16	0.10	2.78	2.38	1.59
4	3.1	2.58	1.55	4.10	5.20	1.29	0.77	54.92	32.95	18.00	988.57	593.14	1581.71	0.067	1.88	0.25	0.10	2.78	7.93	1.88
5	2.57	1.15	0.69	4.50	5.30	0.58	0.35	27.48	16.49	18.00	494.55	296.73	791.29	0.067	1.28	0.10	0.10	2.78	4.81	1.28
6	1.91	0.48	0.29	5.10	0.50	0.24	0.14	1.22	0.73	18.00	22.03	13.22	35.25	0.067	0.67	0.04	0.10	2.78	1.27	0.67
7	2.3	0.32	0.19	4.30	0.90	0.16	0.10	1.24	0.74	18.00	22.29	13.37	35.67	0.067	0.56	0.03	0.10	2.77	1.12	0.56
8	0.98	1.07	0.64	1.70	7.60	0.54	0.32	13.85	8.31	18.00	249.30	149.58	398.89	0.067	1.89	0.25	0.10	2.78	3.74	1.89
9	4.34	2.00	1.20	2.10	3.30	1.00	0.60	13.86	8.32	18.00	249.48	149.69	399.17	0.067	2.12	0.38	0.10	2.78	4.61	2.12
10	1.04	0.32	0.19	3.10	0.70	0.16	0.10	0.69	0.42	18.00	12.50	7.50	20.00	0.067	0.72	0.04	0.10	2.77	0.92	0.71
11	1.44	0.85	0.51	1.10	6.60	0.42	0.25	6.16	3.69	18.00	110.82	66.49	177.31	0.067	2.00	0.31	0.10	2.78	2.64	2.00
12	4.3	0.32	0.19	1.10	0.90	0.16	0.10	0.32	0.19	18.00	5.70	3.42	9.12	0.067	1.37	0.12	0.10	2.76	0.71	1.37
13	1.25	1.28	0.77	2.10	2.90	0.64	0.38	7.80	4.68	18.00	140.31	84.19	224.50	0.067	1.87	0.24	0.10	2.78	3.28	1.87
14	1.05	0.58	0.35	1.40	1.30	0.29	0.17	1.05	0.63	18.00	18.87	11.32	30.19	0.067	1.61	0.16	0.10	2.78	1.29	1.61
15	1.47	0.58	0.35	2.00	1.70	0.29	0.17	1.96	1.18	18.00	35.25	21.15	56.40	0.067	1.37	0.12	0.10	2.78	1.58	1.37
16	1.8	0.48	0.29	1.70	2.80	0.24	0.14	2.28	1.37	18.00	41.13	24.68	65.80	0.067	1.35	0.11	0.10	2.78	1.57	1.35
17	2.27	2.27	0.00	2.20	4.50	1.14	0.00	22.47	0.00	18.00	404.51	0.00	404.51	0.067	15.40	1.03	0.10	2.81E+05	6.55	15.40
18	3.2	3.20	0.00	0.80	2.50	1.60	0.00	6.40	0.00	18.00	115.20	0.00	115.20	0.067	59.70	4.00	0.10	1.13E+05	4.83	59.67
19	1.5	1.50	0.00	6.00	4.70	0.75	0.00	42.30	0.00	18.00	761.40	0.00	761.40	0.067	3.73	0.25	0.10	3.49E+05	7.04	3.73
20	2.38	2.38	0.00	2.40	3.40	1.19	0.00	19.42	0.00	18.00	349.57	0.00	349.57	0.067	14.80	0.99	0.10	2.54E+05	6.34	14.80
21	3.02	3.02	0.00	6.00	3.70	1.51	0.00	67.04	0.00	18.00	1206.79	0.00	1206.79	0.067	7.51	0.50	0.10	1.11E+06	10.37	7.51
22	3.72	3.72	0.00	4.00	7.00	1.86	0.00	104.16	0.00	18.00	1874.88	0.00	1874.88	0.067	13.88	0.93	0.10	2.13E+06	12.87	13.88
23	1.03	1.03	0.00	4.00	6.00	0.52	0.00	24.72	0.00	18.00	444.96	0.00	444.96	0.067	3.84	0.26	0.10	1.40E+05	5.19	3.84
24	1.59	1.59	0.00	4.00	9.00	0.80	0.00	57.24	0.00	18.00	1030.32	0.00	1030.32	0.067	5.93	0.40	0.10	5.01E+05	7.84	5.93
25	2.07	2.07	0.00	4.00	5.30	1.04	0.00	43.88	0.00	18.00	789.91	0.00	789.91	0.067	7.72	0.52	0.10	5.00E+05	7.84	7.72
26	6.23	6.23	0.00	1.80	2.20	3.12	0.00	24.67	0.00	18.00	444.07	0.00	444.07	0.067	51.66	3.46	0.10	8.46E+05	9.46	51.66
27	1.34	1.34	0.00	2.00	3.00	0.67	0.00	8.04	0.00	18.00	144.72	0.00	144.72	0.067	10.00	0.67	0.10	5.93E+04	3.90	10.00
28	3.63	0.32	0.19	0.70	0.80	0.16	0.10	0.18	0.11	18.00	3.23	1.94	5.16	0.067	1.68	0.18	0.10	2.75	0.59	1.67
29	0.64	0.69	0.41	1.40	4.80	0.34	0.21	4.62	2.77	18.00	83.22	49.93	133.15	0.067	1.73	0.20	0.10	2.78	2.24	1.73
30	1.43	0.64	0.38	3.50	0.60	0.32	0.19	1.34	0.81	18.00	24.19	14.52	38.71	0.067	1.06	0.07	0.10	2.78	1.45	1.06
31	1.04	1.28	0.77	2.90	3.80	0.64	0.38	14.11	8.46	18.00	253.90	152.34	406.24	0.067	1.66	0.18	0.10	2.78	3.99	1.66
32	1.2	0.80	0.48	3.60	2.00	0.40	0.24	5.76	3.46	18.00	103.68	62.21	165.89	0.067	1.19	0.09	0.10	2.78	2.53	1.19
33	1.2	0.51	0.31	3.90	1.60	0.26	0.15	3.19	1.92	18.00	57.51	34.50	92.01	0.067	0.85	0.05	0.10	2.78	1.79	0.85
34	1.25	0.40	0.24	3.60	6.30	0.20	0.12	9.07	5.44	18.00	163.30	97.98	261.27	0.067	0.75	0.04	0.10	2.78	2.34	0.75
35	1.7	0.48	0.29	2.20	1.60	0.24	0.14	1.69	1.01	18.00	30.41	18.25	48.66	0.067	1.17	0.09	0.10	2.78	1.42	1.17
36	4	0.45	0.27	3.60	0.70	0.22	0.13	1.13	0.68	18.00	20.32	12.19	32.51	0.067	0.82	0.05	0.10	2.78	1.21	0.82
37	0.8	1.18	0.71	4.20	9.60	0.59	0.36	47.74	28.64	18.00	859.30	515.58	1374.88	0.067	1.35	0.11	0.10	2.78	5.84	1.35
38	2.3	1.12	0.67	0.60	2.00	0.56	0.34	1.34	0.81	18.00	24.19	14.52	38.71	0.067	2.40	0.75	0.10	2.78	1.74	2.39

Figure 77: Output table resulting from SST (Ventotene cliff study). The SST model compiles the rows corresponding to the FS values.

When running the Factor of Safety calculation section of the SST, the Factor of Safety is computed for each block by considering the seismic action, the hydrostatic pressure within the joints, and the combination of both. For the seismic action, a Ks

= 0.067g was used as the pseudostatic seismic coefficient, corresponding to a return period of 475 years. Since it was not possible to measure the water level within the joints, the initial water height (Hw) was arbitrarily fixed at 0.1m for all blocks. This value represents a reasonable water height related to the presence of water within the joints caused by a coastal cliff repeatedly wetted by sea waves impacts.

Considering the seismic action, a Ks value of 0.067g is able to destabilize n.7 blocks (ID: 5, 6, 7, 10, 33, 34) producing a negative value of the FS (FoS_Ks < 1). The pseudostatic coefficient (Ks_cr) is calculated and reported in the corresponding column.

All the blocks are in a stable condition (FoS_Hw > 1) if only the hydrostatic action is contemplated. This means that a 0.1m water height is not able to destabilize any block. The critical water height (Hw_cr) is thus calculated and reported in the corresponding column.

The combination of seismic and water action is not capable of destabilizing additional blocks to the n.7 already destabilized by the seismic action. The Factor of Safety (FoS_Ks_Hw) decreases without reaching values below 1 (except for the blocks named 5, 6, 7, 10, 33, 34).

Sensitivity charts can be then produced considering a specific block (i.e., spcifing the block ID) (Fig 78):

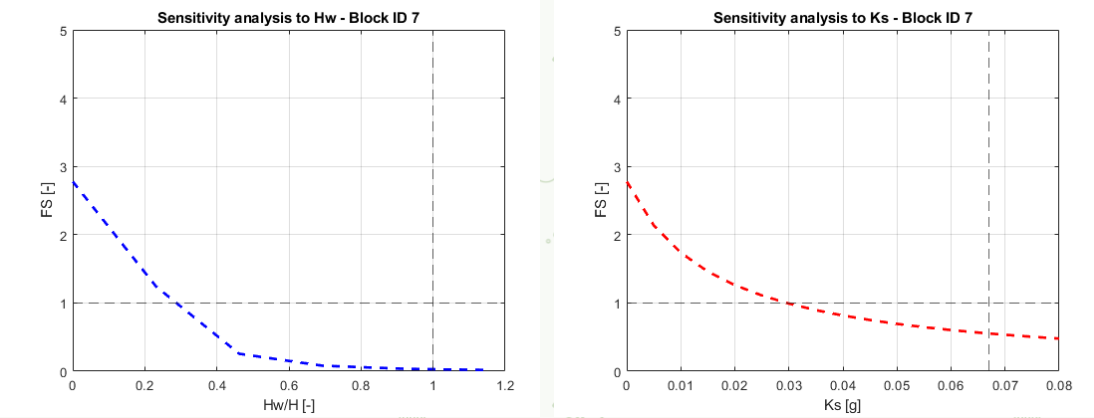

Figure 78: Block type sensitivity charts in Ventotene for the block ID 7.

The water height within the joints value (Hw) is normalized with respect to the block height (H). The sensitivity charts reveal that block 7 reaches a disequilibrium condition (i.e., FS < 1) with water height filling more than 30% of the block height (Hw/H = 0.3) and of the occurrence of a Ks = 0.03g.

A stability chart can be produced thanks to the Stability chart section of the SST (Fig. 79).

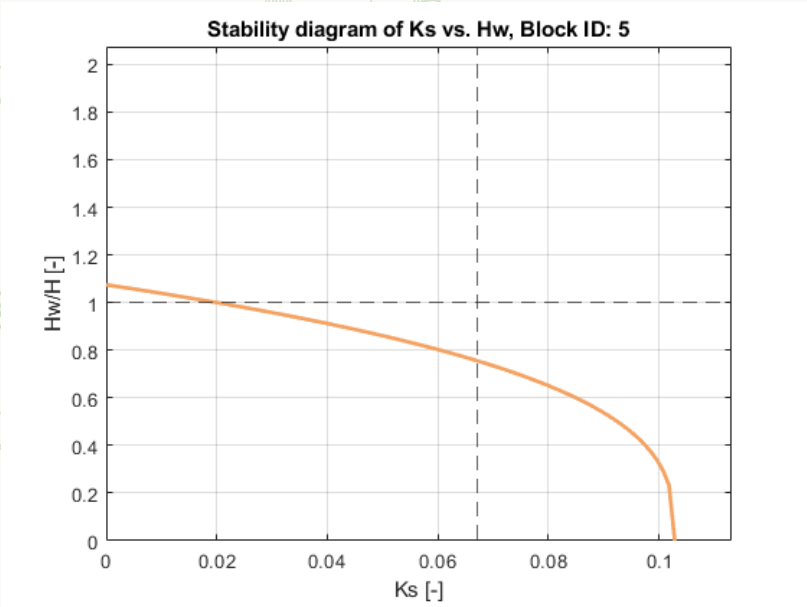

Figure 79: Stability chart of the block ID 5 for the Ventotene case study.

For the analyzed block (ID = 7), there are several realistic combinations of water height within the joints and seismic actions capable of destabilizing the slope. The combinations that can decrease the Factor of Safety (FS) below 1 (i.e., FS < 1) occur when seismic activity happens while the water height in the joints is between 100% of the block height (Hw/H = 1) and 75%. Pseudostatic seismic coefficients greater than the input Ks of 0.067g do not represent the seismic hazard in the Ventotene area for a return period of 475 years.

21.4. References

Bishop, A. W. (1955). The use of the slip circle in the stability analysis of slopes. Geotechnique, 5(1), 7-17.

Danciu, L., Nandan, S., Reyes, C. G., Basili, R., Weatherill, G., Beauval, C., ... & Giardini, D. (2021). The 2020 update of the European Seismic Hazard Model-ESHM20: model overview. EFEHR Technical Report, 1.

Fellenius, W. (1936). Calculation of the stability of earth dams. In Proc. of the second congress on large dams (Vol. 4, pp. 445-463).

Hungr, O., Leroueil, S., & Picarelli, L. (2014). The Varnes classification of landslide types, an update. Landslides, 11, 167-194.

Janbu, N. (1968). Slope stability computations, soil mechanics and foundation engineering report. Technical University of Norway, Trondheim.

Markland, J. T. (1972). A useful technique for estimating the stability of rock slopes when the rigid wedge slide type of failure is expected. Interdepartmental Rock Mechanics Project, Imperial College of Science and Technology.

Martino, S., & Mazzanti, P. (2014). Integrating geomechanical surveys and remote sensing for sea cliff slope stability analysis: the Mt. Pucci case study (Italy). Natural Hazards and Earth System Sciences, 14(4), 831-848.

Mazzanti, P., Schilirò, L., Martino, S., Antonielli, B., Brizi, E., Brunetti, A., ... & Scarascia Mugnozza, G. (2018). The contribution of terrestrial laser scanning to the analysis of cliff slope stability in Sugano (Central Italy). Remote Sensing, 10(9), 1475.

Morgenstern, N. U., & Price, V. E. (1965). The analysis of the stability of general slip surfaces. Geotechnique, 15(1), 79-93.

Spencer, E. (1967). A method of analysis of the stability of embankments assuming parallel inter-slice forces. Geotechnique, 17(1), 11-26.

Stucchi, M., Akinci, A., Faccioli, E., Gasperini, P., Malagnini, L., Meletti, C., ... & Valensise, G. (2004). Redazione della Mappa di Pericolosità Sismica prevista dall'Ordinanza PC del 20 marzo 2003, n. 3274, All. 1 Rapporto Conclusivo.

Taylor, D. W. (1937). “Stability of earth slopes.” J. Boston Soc. Civ. Eng., 24, 197–246.

Ulusay, R. (2014). The present and future of rock testing: highlighting the ISRM suggested methods. The ISRM Suggested Methods for Rock Characterization, Testing and Monitoring: 2007-2014, 1-22.

21.5. Contributors

Developed by: Sapienza University of Rome (SUR)

Date of last update: 31/07/2024

Lead contributors:

- Federico Feliziani
- Guglielmo Grechi
- Gian Marco Marmoni
- Mattia Montagnese
- Stefano Rivellino
- Salvatore Martino
- Francesca Bozzano
- Gabriele Scarascia Mugnozza

22. Structural Seismic Response Analysis

22.1. Overview

The Structural Analysis Model is designed to quantify the seismic response of the Temple of Apollo through detailed nonlinear simulations. The model captures the complex dynamic behaviour of the monument under earthquake loading by

incorporating material nonlinearity, geometric effects, and realistic boundary conditions. Five real ground motion records were selected to represent a range of seismic scenarios, each scaled to four peak ground acceleration (PGA) levels to assess performance under increasing seismic intensity.

A total of 26 distinct structural frames were analysed to reflect the variability in geometry, boundary constraints, and local damage patterns within the temple. The simulations produce comprehensive outputs, including full-field displacement maps, displacement cuts along key sections, and time-history responses at critical points. These outputs collectively provide a spatially resolved picture of the structure's deformation and stress distribution.

The resulting dataset offers a robust basis for evaluating the structural performance, identifying critical regions of vulnerability, and assessing overall resilience. By systematically varying the seismic input and capturing nonlinear responses across multiple frames, the model supports a detailed understanding of how the Temple of Apollo would behave under different earthquake intensities, thereby contributing to informed conservation and risk mitigation strategies.

22.2. Methodological Description

This section describes the methodological framework adopted for developing and analyzing the structural model of the Temple of Apollo at Aegina Kolonna. The process involved several key stages, including 3D mesh pre-processing, geometric cleaning and preparation, finite element model generation, material characterization, and nonlinear dynamic analysis under seismic loading.

22.2.1. Geometry Acquisition from Point-Cloud

The initial dense meshes obtained from the photogrammetry were post-processed to create a clean and structurally meaningful model suitable for finite element analysis. The raw meshes contained both structural and non-structural components, as well as surrounding terrain and archaeological remains not relevant to the present study.

Non-structural elements, such as the surrounding ground surfaces and detached fragments (depicted in red in Figure 80), were removed. This process ensured that only the primary structure of interest, the Temple of Apollo, was retained. The cleaning process was performed in Blender, where unwanted mesh components were carefully isolated and deleted. This step was essential to obtain a geometrically consistent and interpretable model focused exclusively on the temple.

Figure 80: The mesh was cleaned from the non-structural parts that are indicated with red.

Following the removal of non-structural features, the area of interest was cropped to include solely the Temple of Apollo, which represents the most significant and structurally complex monument within the Aegina Kolonna archaeological site. This targeted approach reduced the computational load and ensured that the subsequent analysis concentrated on the structural behaviour of the temple itself.

After cropping, the resulting surface mesh was checked for topological consistency and repaired where necessary. The mesh was made manifold, meaning that all surfaces were closed and watertight, allowing for a valid transformation into a solid model suitable for finite element meshing. This process involved fixing non-manifold edges, removing duplicate vertices, and ensuring the correct surface orientation.

o balance computational efficiency with geometric precision, the cleaned and manifold mesh was remeshed to a voxel size of 0.2 m (see Figure 81). This voxelization provided a uniform mesh density appropriate for large-scale structural simulations, ensuring adequate representation of the temple's geometry while maintaining manageable model size and computational cost.

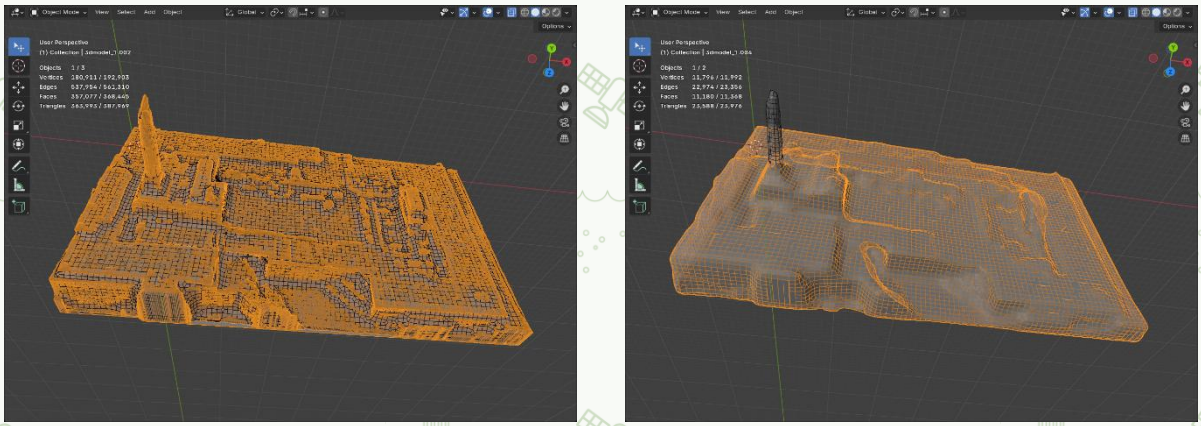

Figure 81: Remeshed 3D model of the Temple of Apollo at Aegina Kolonna, showing the voxel representation with a resolution of 0.2 m and the original mesh (right), and the final voxel mesh (left).

22.2.2. Numerical Modelling

The processed mesh was imported into Abaqus and converted into solid tetrahedral elements (C3D4 or C3D10), which are particularly suited for irregular geometries. No direct experimental data were available for the limestone from Aegina; therefore, material properties were adopted from literature. Greek limestone typically exhibits an average density of ρ = 2750 kg/m^3, an elastic modulus of E = 70 GPa, and a Poisson's ratio of ν = 0.25 (Dasiou et al. 2024).

Appropriate boundary conditions were defined to represent realistic support and interaction with the foundation substrate. These constraints ensured that the numerical model captured the physical behaviour of the temple under seismic loading.

A. Seismic Loading and Dynamic Analysis

Five real ground motion records with a return period of 475 years were selected to represent a range of plausible seismic scenarios. Each record was scaled to four peak ground acceleration (PGA) levels: 0.2 g, 0.4 g, 0.6 g, and 0.8 g. This scaling allowed for the evaluation of the temple's performance across increasing levels of seismic intensity.

The dynamic analysis was carried out using the dynamic implicit procedure within Abaqus/Standard. This approach employs an implicit time integration scheme to solve transient dynamic problems governed by inertia, damping, and stiffness forces. The fundamental equation of motion solved at each time step is:

$$\boldsymbol{M\ddot{u}}(t) + \boldsymbol{C\dot{u}}(t) + \boldsymbol{Ku}(t) = \boldsymbol{F_{ext}}(t)$$

where $\mathbf{M}$ is the mass matrix, $\mathbf{C}$ the damping matrix, $\mathbf{K}$ the stiffness matrix, $\mathbf{u}(t)$ is the displacement vector, and $\boldsymbol{F_{ext}}(t)$ is the external force vector.

The implicit method requires solving nonlinear equations at each time increment, using Newton-Raphson iteration:

$$\boldsymbol{K}^i \boldsymbol{\Delta u}^i = \boldsymbol{F}_{ext} - \boldsymbol{F}_{int}^i$$

where $\mathbf{K}^i$ is the tangent stiffness matrix at iteration i, and $\mathbf{F}_{\text{int}}^i$ are internal forces.

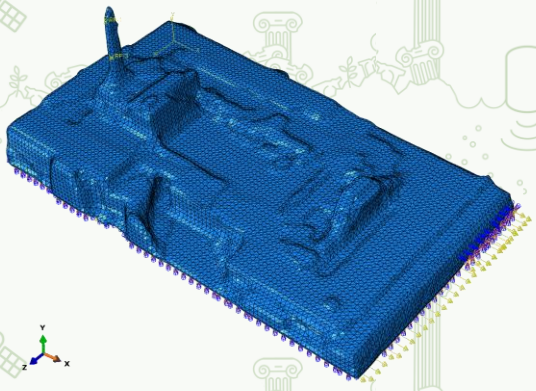

Figure 82: Finite element model of the Temple of Apollo at Aegina Kolonna, generated from the volumetric mesh. The applied boundary conditions (blue and orange lines) and loading conditions (yellow arrows) are indicated for the numerical simulation.

22.3. Outputs and Interpretation of Results

The nonlinear dynamic analyses provided detailed insight into the structural behavior of the Temple of Apollo under seismic excitation. The outputs include full-field displacement maps, sectional displacement cuts, and point-based time histories of stress and strain, allowing both global and local evaluation of the structural response.

22.3.1. Global Structural Displacement

Figure 83 right and Figure 83 left illustrate the spatial distribution of resultant displacements for the realistic seismic scenario. The maximum displacements occur at the upper regions of the surviving column and adjacent structural remnants, reaching values on the order of 3.2×10^{-5} mm. This indicates that the upper sections of the temple experience the largest dynamic amplification due to their height and relative flexibility. In contrast, the lower foundation and stylobate regions exhibit minimal displacements, confirming that these zones act as rigid supports during seismic loading.

The displacement cut provides a clearer visualization of the deformation gradient through the height of the structure. It reveals that most of the deformation is concentrated in the vertical elements, particularly in the surviving column shaft, while the horizontal structural components show comparatively minor relative motion. This pattern suggests that bending and rocking effects dominate the dynamic behaviour rather than significant translational motion of the base.

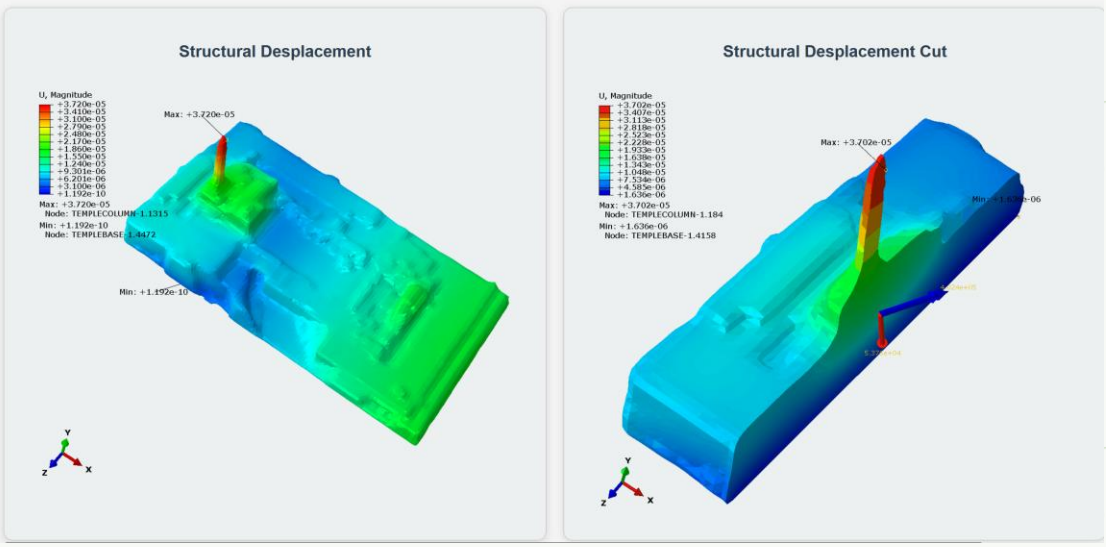

Figure 83: Seismic resultant displacement for the realistic scenario magnitude. The values are in mm.

22.3.2. Local Stress and Strain Response

Figure 84 presents the time-series data for selected monitoring points distributed across the temple's structure. The plotted histories include normal stresses (S11), von Mises equivalent stresses, maximum principal stresses, and corresponding strain components (EE11 and EE:MaxPrincipal). The oscillatory nature of these

responses reflects the dynamic loading cycles imparted by the ground motion records.

At the representative point highlighted in Figure 5, the time histories reveal that stress peaks coincide with the main acceleration pulses of the input motion. The von Mises and maximum principal stress values remain within the expected range for the material's elastic regime, suggesting that no extensive cracking or plastic deformation is likely to occur under the examined seismic intensity. However, localized amplification near slender elements and discontinuities indicates that stress concentrations could become critical at higher PGA levels.

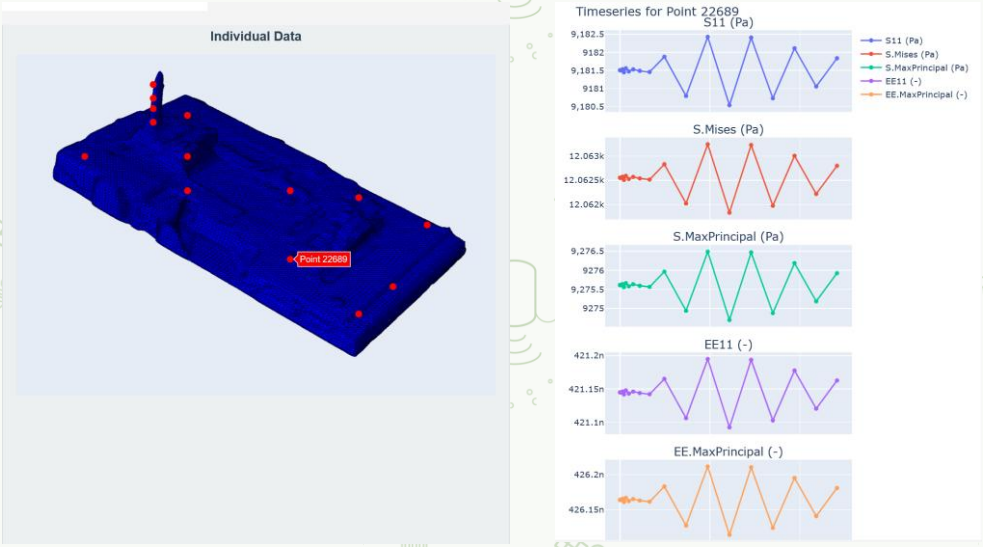

Figure 84: Timeseries of stresses and strains for specified points.

22.3.3. Conclusions and Structural Implications

The overall displacement and stress distributions demonstrate that the Temple of Apollo retains a predominantly elastic response under the considered seismic scenarios, with deformations remaining small relative to the structure's dimensions. The combination of high stiffness and limited height contributes to this stable behaviour. Nonetheless, the concentration of stresses around the surviving column and interface regions highlights potential zones of vulnerability where damage initiation could occur under stronger seismic events.

These results provide a quantitative basis for evaluating the structural integrity and resilience of the monument. They also establish a framework for future parametric studies involving material degradation, soil-structure interaction, and progressive damage modelling, to better understand the long-term seismic vulnerability of the site.

22.4. References

Dasiou, M.-E., Lachanas, C. G., Melissianos, V. E., & Vamvatsikos, D. (2024). Seismic performance of the temple of Aphaia in Aegina island, Greece. Earthquake Engineering & Structural Dynamics, 53(2), 573–592.

22.5. Contributors

Developed by: National Technical University of Athens

Date of last update: 10/11/2025

Lead contributors:

- Paraskevi Modé
- Denis Istrati

23. Ship Induced Waves

23.1. Overview

The model simulates the generation and propagation of ship–induced waves in coastal waters with fixed slope bathymetry, aiming to evaluate the hydrodynamic risk posed by vessel traffic to nearshore environments, coastal structures, and cultural heritage sites. It assesses risks associated with increased wave heights and potential erosion driven by ship wakes. The modelling framework operates in two stages: first, it calculates the ship–induced wave field using the linear pressure–patch formulation and solves the full dispersion relation numerically to describe wave propagation until the depth where linear theory remains valid. Beyond this limit, the model estimates the transformation of wave height due to shoaling as the wave travels toward shallower regions, continuing until the point of breaking. Considering the most frequent vessel types—namely a passenger ferry operating along the route to Aegina and three representative sizes of boats navigating around Epidaurus—the model uses ship parameters (length, beam, draft, speed, and pressure patch width) together with site–specific bathymetry slopes as inputs. The outputs include spatial distributions of free–surface elevation, Kelvin and [Equation]wave angles, validity line position (h/L< 0.05), and time–dependent maximum wave heights, ultimately providing an estimate of the wave height over the historical site and a quantitative basis for evaluating exposure, wave impact intensity, and potential nearshore instability caused by ship–induced waves.

23.2. Methodological Description

The modelling framework is composed of two modules: (1) ship–induced wave generation and propagation, and (2) wave shoaling and breaking. Together, they provide a depth–aware estimate of the wave height near coastal heritage sites by linking offshore vessel motion to nearshore hydrodynamic transformation.

The first module calculates the free–surface response generated by a moving vessel represented as an elliptical Gaussian pressure patch, following a linearized formulation of the surface wave problem. The model numerically solves the linear dispersion relation:

$$\omega^2 = gk \tanh(kh)$$

For every local depth h, where ω is the wave angular frequency, k the wave number, and g the gravitational acceleration. The ship speed V is compared to the phase velocity $c = \sqrt{\frac{g}{k}\tanh(kh)}$ to ensure that the model remains within subcritical conditions.

The input data include ship geometry and motion parameters—length, beam, draft, speed , and pressure–patch width—together with depth measurements at three locations (offshore, ship position, and shoreline). A fixed–slope bathymetry is defined in the primary propagation direction (x or y).

A numerical integration over wavenumber and propagation angle reconstructs the spatial field of free–surface elevation ζ(x,y), including characteristic Kelvin angles (≈19.47°) and the maximum–energy angle $\left(\varphi_{max} = \frac{0.224}{Fr}\right)$, where $Fr = \frac{V}{\sqrt{g(pressure\ patch\ width)}}$ is the local Froude number.

To ensure physical validity, the model automatically detects the limit of linear theory by monitoring the depth–to–wavelength ratio. The validity line is defined by the threshold

$$\frac{h}{L} > 0.05,$$

Beyond which nonlinear and breaking effects are expected. The wave height along this line is extracted as

$$H_{valid} = 2\ max\ |\zeta|,$$

And recorded together with the corresponding depth h_{valid} and period $\left(T_{wave} = \frac{2\pi}{\omega}\right)$. The model also generates a time history of the maximum wave height at the validity line as the ship moves forward, providing temporal information on the wave evolution.

The second module uses the output from the previous step—specifically the wave height and period at the validity line—to estimate the transformation of wave height as it propagates toward the shore over a known slope. A linear depth profile between the validity line and the shoreline is discretized, and at each location the dispersion relation is solved iteratively to obtain the local wavenumber k(h).

The group velocity is computed as

$$c_g = \frac{1}{2}c\left[1 + \frac{2kh}{\sinh(2kh)}\right],$$

And the shoaling law based on energy–flux conservation is applied:

$$H(x) = H_{valid}\sqrt{\frac{c_g(h_{valid})h_{valid}}{c_g(h)h}}$$

This formulation accounts for the gradual increase of wave height as the depth decreases. The model continuously checks for wave breaking using the empirical criterion

H/h=0.78,

Which defines the onset of breaking in shallow water. Once this threshold is reached, the computation stops and the breaking point—including breaking height Hb, depth hb, and distance from the validity line—is reported.

The methodological framework developed in this work combines bathymetric representation, ship characterization, and wave propagation modeling to simulate ship–induced wakes in coastal environments. The approach begins with the definition of shoreline orientation relative to the ship direction and water depth simplified profile, which is constitute by water depth at the ship location and the average slope. Ship parameters, including principal dimensions, operating speed, and pressure distribution width, are then introduced to generate the forcing conditions that give rise to the wave field.

Wave transformation across the domain is resolved using a depth–aware formulation of linear wave theory, which accounts for variations in local depth and ensures that characteristic features such as Kelvin and ϕ_max angles are consistently reproduced. A dedicated detection routine identifies the validity line, marking the transition beyond which linear theory no longer applies. The output of the framework includes spatial maps of free–surface elevation, time series of maximum wave height at the validity line, and log files summarizing dispersion solutions and depth-to-wavelength ratios.

As shown in Fig. 1, the user specifies ship and depth conditions through simple inputs, after which the code estimates wave characteristics over a computational grid defined by the user.

Together, these components form a structured methodology for investigating ship–induced wave generation, propagation, and nearshore impact. The following subsections describe each component in detail.

23.2.1. Ship Parametrization

The ship is represented in the framework through a set of input parameters that define its principal characteristics and operating conditions. These include length L, beam B, draft T, and the vessel speed V. A pressure distribution width b is also specified to control the spatial extent of the forcing that generates the wave field. Together, these parameters establish the scale and intensity of the ship–induced wake.

For flexibility, the framework allows different ship sizes and speeds to be introduced, enabling systemic exploration of how vessel characteristics influence wake generation. By structuring the ship in this parametric form, the model avoids

the complexity of full geometric hull representation while retaining the ability to capture key dependencies on vessel dimensions and operating conditions. This provides a consistent basis for comparing results across a range of scenarios and applications.

Table 10: Ship sizes used in this study as representative cases in the area of interest (Epidaurus)

characteristics	Big yacht	Medium yacht	Small yacht
Length	60 m	40 m	20 m
Beam	12 m	8 m	5 m
Draft	5 m	3 m	2 m
Speed	6.6 m/s	5.6 m/s	5.5 m/s

23.3. Output and Interpretation of Results

From the first module, the model provides spatial maps of free–surface elevation $\zeta(x,y)$, Kelvin and φ_{max} wake angles, and the position of the validity line (h/L<0.05), together with the maximum wave height and its time evolution along that limit. From the shoaling module, the results include the variation of wave height due to energy–flux conservation and the point of wave breaking, defined by the empirical criterion H/h=0.78.

The second module output consists of a shoaling–transformed wave height profile, the breaking location, and graphical visualization of H(x) versus distance.

These results, when combined, yield a depth aware estimate of the maximum expected wave height over the historical site, representing the cumulative effects of ship–wake generation offshore and nearshore amplification by shoaling. The wave height profiles and time histories can be interpreted as indicators of potential exposure intensity, while the detected breaking point marks the limit beyond which the model no longer applies, and wave energy would dissipate through breaking or turbulence.

The model assumes linear wave theory up to the validity limit and one–dimensional bathymetric variation beyond it. Nonlinear effects such as wave breaking dynamics, bottom friction, and wave reflection are not explicitly simulated. The shoreline is treated as a fixed slope, and the pressure distribution representing the ship is idealized as a smooth Gaussian patch. Consequently, the results provide a physically consistent but simplified representation of ship–induced hydrodynamics, suitable for comparative risk assessment and preliminary site evolution, rather than for detailed local flow modeling.

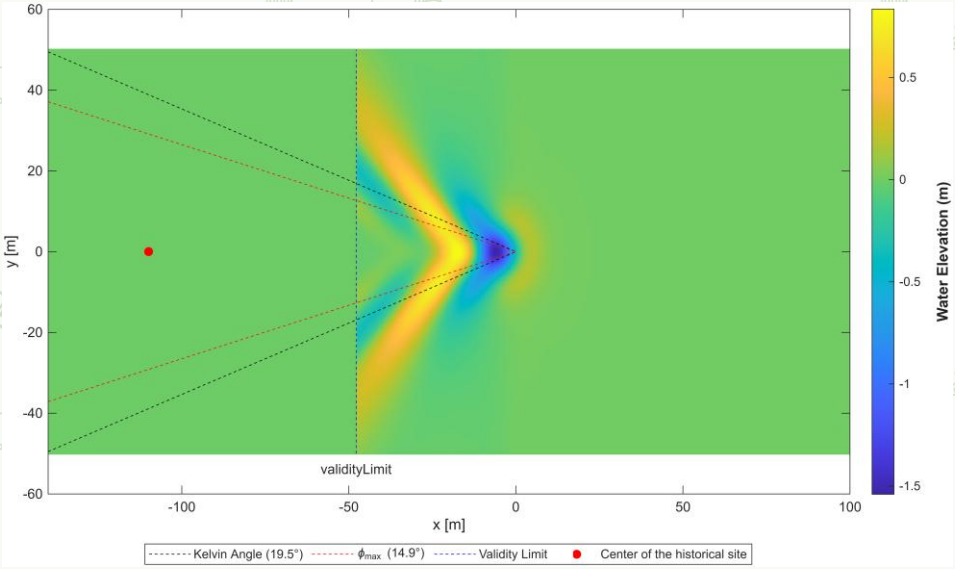

Figure 85: Ship-induced waves generated behind a ship.

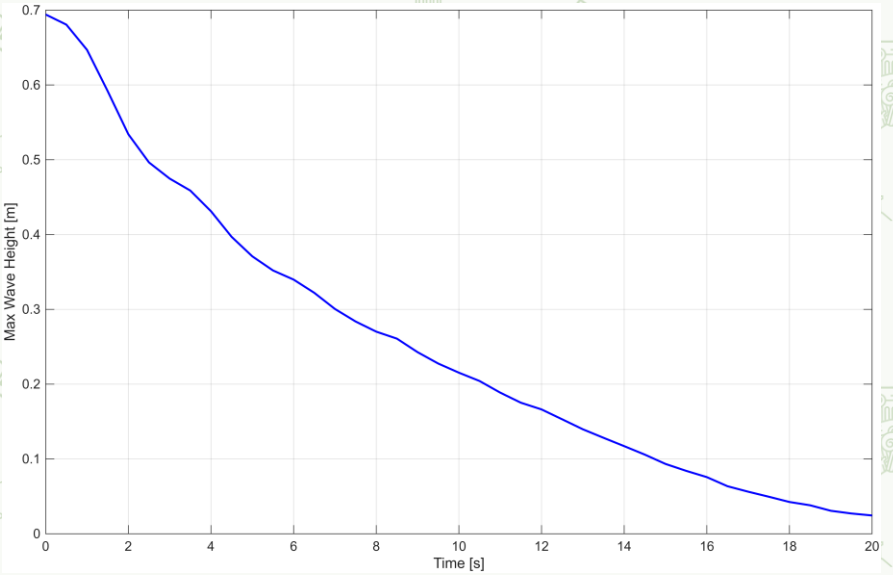

Figure 86: Time history of wave height on the validity.

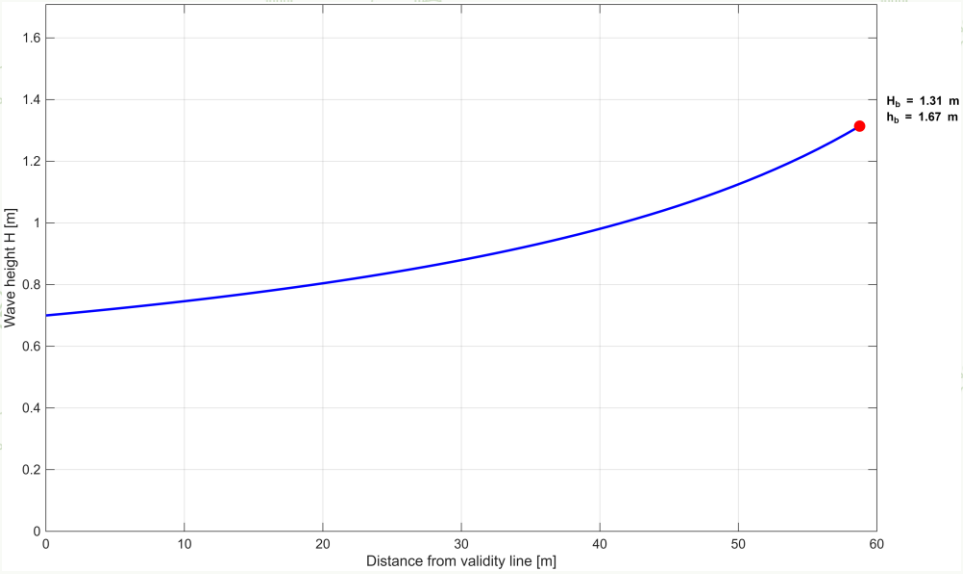

Figure 87: Wave height changes due to shoaling in the shallow water region.

23.4. References

Torsvik, T., Kalisch, H., & Dutykh, D. (2015). Ship waves on shallow water. Wave Motion, 56, 129–142. https://doi.org/10.1016/j.wavemoti.2015.03.003

23.5. Contributors

Developed by: National Technical University of Athens

Date of last update:

Lead contributors:

- Raouf Sobhani
- Denis Istrati

24. Wave Impacts

24.1. Overview

This numerical framework predicts wave–cliff interactions under future sea–level rise (SLR) scenarios driven by climate change. The significance of this work lies in the fact that numerous coastal cliffs worldwide—particularly across the Mediterranean basin—host ancient settlements and cultural landmarks. Rising sea levels can amplify the erosive and destabilizing effects of wave impacts on such cliffs. Therefore, identifying how future SLR scenarios influence wave interaction patterns and potential damage mechanisms is essential for developing effective preservation and mitigation strategies for these heritage sites. SLR projections follow IPCC AR6 (2022) scenarios (SSP2-4.5 and SSP 5-8.5) (Chalkidou et al., 2024).

To address this need, a series of high–fidelity numerical models have been developed to simulate extreme, high–energy wave events over site–specific bathymetry, which is derived from detailed terrestrial and aerial site surveys. The

model incorporates several representative cliff configurations, including vertical, 85° and 65° inclined, and partially damaged (notched) profiles, to capture the range of possible morphological conditions observed at the site. Simplified yet physically consistent cliff geometries, derived from detailed bathymetric and topographic surveys, are used to isolate the influence of features such as basal notches or varying cliff inclinations.

The simulations are performed using a Computational Fluid Dynamics (CFD) solver capable of resolving wave transformation, runup processes, and impact dynamics along solid boundaries. Key model inputs include offshore wave height, site-specific geometric and topographic data, and boundary conditions representative of current and future sea–level scenarios. The main outputs comprise free–surface elevations, time-varying pressure fields, and integrated hydrodynamic forces on the cliff face. Together, these outputs provide a detailed quantification of the magnitude and spatial distribution of wave–induced loading under various SLR conditions, supporting assessment of potential damage, erosion risk, and protective interventions for future planning.

24.2. Methodological Description

The methodological framework integrates bathymetric and topographic representations with high-fidelity Computational Fluid Dynamics (CFD) simulations to assess wave–cliff interactions under present and future sea-level rise (SLR) conditions. The model solves the incompressible Navier–Stokes equations for mass and momentum conservation, accounting for the combined effects of pressure, gravity, and viscous stresses, and is implemented in OpenFOAM® using the interFoam solver. This three-dimensional two-phase solver employs the Volume of Fluid (VOF) method to capture the air–water interface by advecting the phase fraction field, ensuring accurate representation of wave transformation, run-up, and impact dynamics.

$\nabla . \boldsymbol{u} = 0$ (conservation of mass)

$\frac{\partial \boldsymbol{u}}{\partial t} + \boldsymbol{u} \cdot \nabla \boldsymbol{u} = -\frac{1}{\rho} \nabla p + \nu \nabla^2 \boldsymbol{u} + \boldsymbol{g}$ (conservation of momentum)

Where $\boldsymbol{u}$ is the velocity vector, p is the pressure, ρ is the fluid density, ν is the kinematic viscosity, and $\boldsymbol{g}$ is the gravitational acceleration vector.

The equations are discretized with a finite-volume scheme on structured or unstructured meshes, using the PISO algorithm for pressure–velocity coupling. Turbulence closure is introduced through RANS or LES formulations depending on grid resolution and study objectives. The computational domain includes an inlet boundary prescribing Boussinesq-type solitary waves. Post-processing of each simulation yields free-surface elevations, pressure time histories, and integrated hydrodynamic forces along the face of the cliff, which collectively describe the spatial and temporal distribution of wave loading and support the analysis of multi-

hazard scenarios affecting the stability and exposure of coastal cliffs and nearby cultural heritage sites.

24.2.1. Three–Dimensional Two–Phase Solver

This approach is implemented using the OpenFOAM framework, specifically the interFoam solver, which is validated against experimental data in a considerable number of previous studies (L. F. Chen et al., 2014; Pablo Higuera et al., 2014), resolveing two–phase incompressible flow through the Volume of Fluid (VOF) method. The free surface is tracked by advecting a phase–fraction field α:

$$\frac{\partial \alpha}{\partial t} + \boldsymbol{u} \cdot \nabla \alpha = 0$$

Where $\alpha = 1$ denotes the water phase, $\alpha = 0$ denotes the air phase, and intermediate values represent the interface region.

The governing Navier-Stokes equations are discretized with a finite–volume scheme on both structured and unstructured meshes, allowing flexibility in capturing complex cliff and structure geometries. Pressure–velocity coupling is handled by PISO algorithm for transient simulations.

Turbulence closure can be introduced through either RANS models or LES approaches, depending on the spatial resolution of the grid and objectives of the simulation. Viscosity is explicitly included in the momentum equation and can be specified as constant, laminar, or modeled through turbulence formulations.

All these governing equations are being solved in all cells inside the mesh grid using FVM method at every time step, which is adaptive in this case, i.e., keeping the CFL number below a threshold, which is 0.5 in this case.

$$CFL = \frac{U \Delta x}{\Delta t}$$

1. Computational Domain

In this study, the two–phase solver is applied primarily for local wave–cliff interactions, where high spatial resolution is required to resolve spikes and transient pressures. The most important boundary conditions are the inlet, where prescribed wave conditions are imposed; the opposite boundary, which represents a solid surface where a no–slip condition is assigned, similar to the seabed boundary at the bottom; and the outlet, where wave energy is allowed to dissipate. Although the solver is 3D inherently, it is possible to employ a 2D configuration, achieved by assigning empty condition on the sides of the domain. This setup reduces computational cost while retaining the ability to reproduce the key hydrodynamic processes governing local loading on cliffs and structures. In the present application, the computational domain extends over 150 m meters, which is sufficient to generate and propagate waves within the domain without reflections

at the inlet boundary, while still allowing mesh refinement to capture rapid transient phenomena.

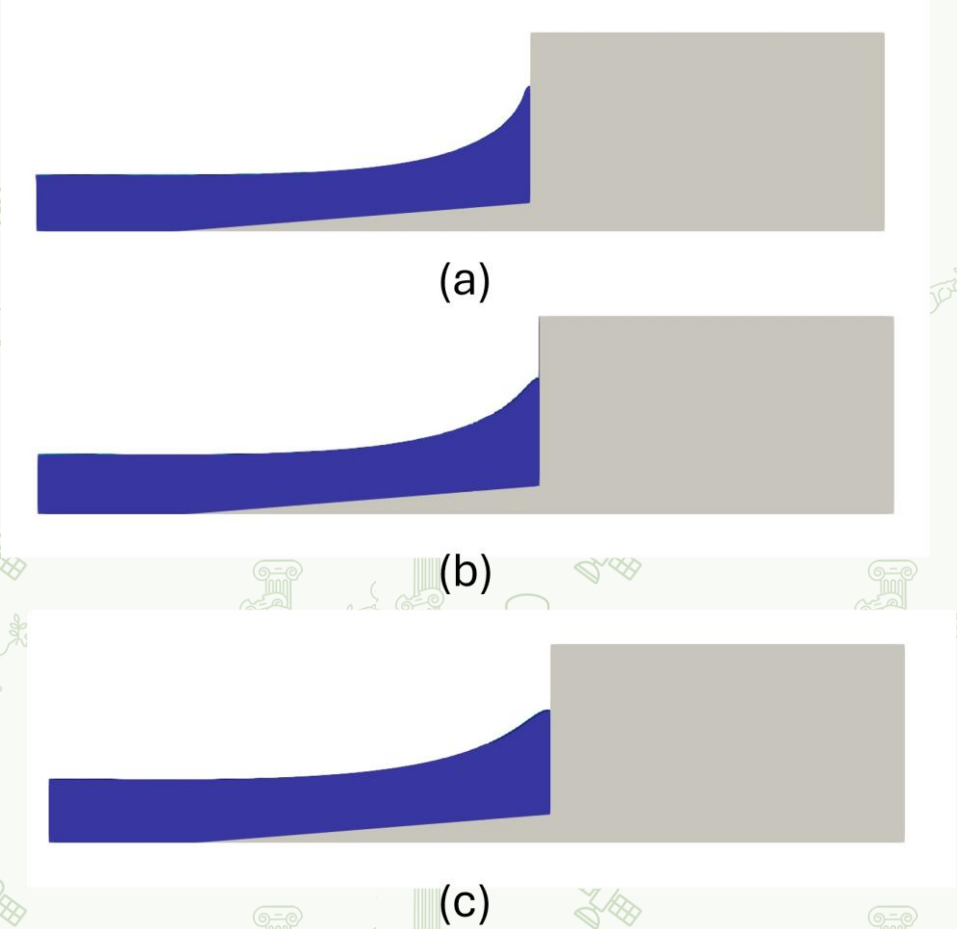

Figure 88: This figure clearly shows how increasing initial water level can alter wave impact process along a vertical normal cliff, which is evident looking at the shape of water elevating the cliff face. (a) no SLR, (b) SLR=0.5m, and (c) SLR=1.0m

24.3. Output and Interpretation of Results

The model examines the combined effects of extreme waves, sea–level rise scenarios, and varying cliff geometries under different projections of future sea–level rise conditions (Figure 88). It provides plot containing precise, location–specific data on the water elevations, pressure fields, and hydrodynamic forces acting on the cliff face—parameters essential for evaluating the immediate hazard posed to coastal cliffs and associated heritage sites. The interpretation of these outputs is highly case–specific. Under small to moderate wave regimes, SLR increases the maximum water exposure level on the cliff, and although it consistently amplifies impact forces, the effect is more pronounced in smaller–wave conditions.

24.4. References

Chalkidou, S., Georgiadis, C., Roustanis, T., & Patias, P. (2024). A methodology for identifying coastal cultural heritage assets exposed to future sea level rise scenarios. Applied Sciences, 14(16), 7210.

Chen, L. F., Zang, J., Hillis, A. J., Morgan, G. C., & Plummer, A. R. (2014). Numerical investigation of wave–structure interaction using OpenFOAM. Ocean Engineering, 88, 91-109.

Higuera, P., Lara, J. L., & Losada, I. J. (2014). Three-dimensional interaction of waves and porous coastal structures using OpenFOAM®. Part I: Formulation and validation. Coastal Engineering, 83, 243-258.

24.5. Contributors

Developed by: National Technical University of Athens

Date of last update:

Lead contributors:

- Raouf Sobhani
- Denis Istrati

25. AI Forecasting for EVI Prediction

25.1. Overview

This tool implements a Long Short-Term Memory (LSTM) neural network designed to predict future values of a univariate time series representing the Enhanced Vegetation Index (EVI). LSTMs are well-suited for this application because they learn temporal dependencies and nonlinear behaviors inherent in vegetation phenology and ecosystem dynamics.

The forecasting setup follows a sequence-to-one architecture. Historical EVI observations are normalized and divided into input windows, each consisting of 12 consecutive months of past values. This sliding-window approach preserves temporal structure and enables the network to learn lagged relationships associated with vegetation growth cycles. The core architecture includes a single LSTM layer with 100 hidden units feeding into a fully connected output layer. The prediction is generated from the final hidden state, ensuring that the model leverages temporally integrated information from the full input window.

Model parameters are optimized using the Adam optimizer with a mean squared error (MSE) loss function, appropriate for continuous biophysical indices. During training, hidden and cell states are reset for each batch to maintain consistent gradient flow and stabilize learning. Once trained, the model produces forecasts by processing the most recent six months of EVI data. Predictions are then inverse-transformed to restore values to the original EVI scale. This LSTM-based framework

offers a reliable method for capturing vegetation dynamics and supports applications in ecosystem monitoring and environmental assessment.

25.2. Methodological Description

25.2.1. Data Preparation

Accurate forecasting with LSTM models requires careful preparation and preprocessing of the input time series data. In this implementation, the data consists of univariate environmental indicators, such as the Enhanced Vegetation Index (EVI), recorded at regular monthly intervals.

The preprocessing workflow begins by **normalizing** the raw data using a **Min-Max scaler**, which maps all values into the [0, 1] range. Normalization ensures numerical stability during training and facilitates gradient-based optimization in PyTorch. Next, the normalized time series is segmented into **overlapping sequences** of one year fixed length to create supervised learning pairs. Each sequence consists of a window of consecutive past observations, which serves as the input, while the subsequent value acts as the target output. In this framework, a sequence length of 12 months is used to predict the following month, enabling the model to capture short- to medium-term temporal dependencies. The sequences and their corresponding targets are then converted into **PyTorch tensors**, reshaped to match the expected input dimensions of the LSTM network: **[batch size, sequence length, number of features]** for inputs, and **[batch size, 1]** for targets. These tensors are wrapped in a **TensorDataset** and loaded into a **PyTorch DataLoader**, which facilitates efficient batch processing and shuffling during training. The use of DataLoader also ensures seamless integration with GPU acceleration when available. This systematic preprocessing pipeline guarantees that the LSTM model receives consistently structured, scaled, and temporally organized data, thereby optimizing learning and predictive performance for vegetation index forecasting tasks.

25.2.2. Model Training

The LSTM model is trained using a supervised learning framework, where the objective is to minimize the discrepancy between predicted and observed time series values. Prior to training, the input series is normalized using a Min-Max scaling procedure to constrain all values within the [0, 1] interval. This normalization facilitates efficient gradient-based optimization and mitigates issues arising from differing variable magnitudes. Training data are organized into sequences of fixed length, with each sequence paired with the subsequent observation as the target output. This sequence-to-one formulation allows the network to learn temporal dependencies and capture the dynamics inherent to vegetation index variations. The model is trained using the **Adam optimizer**, which adaptively adjusts learning rates for each parameter based on first- and second-order moments of the gradients. The **mean squared error (MSE)** is employed as the loss function,

providing a smooth and differentiable measure of prediction error suitable for continuous environmental variables. During each training epoch, the hidden and cell states of the LSTM are initialized for each batch, ensuring stable gradient propagation and preventing the accumulation of state across unrelated sequences. Batches of 16 sequences are fed into the network, predictions are generated, and the loss is backpropagated to update network weights iteratively. Training proceeds for 100 epochs, with intermediate loss monitoring to track convergence and detect potential overfitting. Once training is complete, the model weights are saved, allowing for future reuse without retraining. This process ensures that the LSTM network is capable of generating accurate forecasts for future EVI values based on recent historical observations.

25.3. Inference and Prediction

After training, the LSTM model can be employed to generate forecasts for future time series values, concerning the Enhanced Vegetation Index (EVI). The inference process begins by selecting the most recent **sequence of observations** from the historical dataset, corresponding to the model's predefined input window length (12 months in the present implementation). A typical one-step forecast is illustrated in Figure 1, where the last 12 observations (blue) form the input window and the network predicts the next month (red) against the observed value (green). This sequence is normalized using the same Min-Max scaler applied during training to ensure consistency in data representation. The normalized input sequence is then converted into a three-dimensional tensor compatible with the LSTM input requirements, where the dimensions correspond to **batch size**, **sequence length**, and **number of features**. During prediction, the model's hidden and cell states are initialized to zero, and the sequence is passed through the LSTM and fully connected output layer. The prediction for the next time step is obtained from the last output of the LSTM, which encapsulates the learned temporal dependencies across the input window. For multi-step forecasting, the predicted value can be appended to the input sequence and the process repeated iteratively. The resulting normalized forecast is **inverse-transformed** using the original scaler to return the prediction to the original physical scale, allowing direct interpretation in units of EVI. This procedure enables reliable short-term prediction while preserving the temporal patterns captured during training. The LSTM-based inference framework is particularly suitable for applications requiring continuous environmental monitoring and anticipatory decision-making.

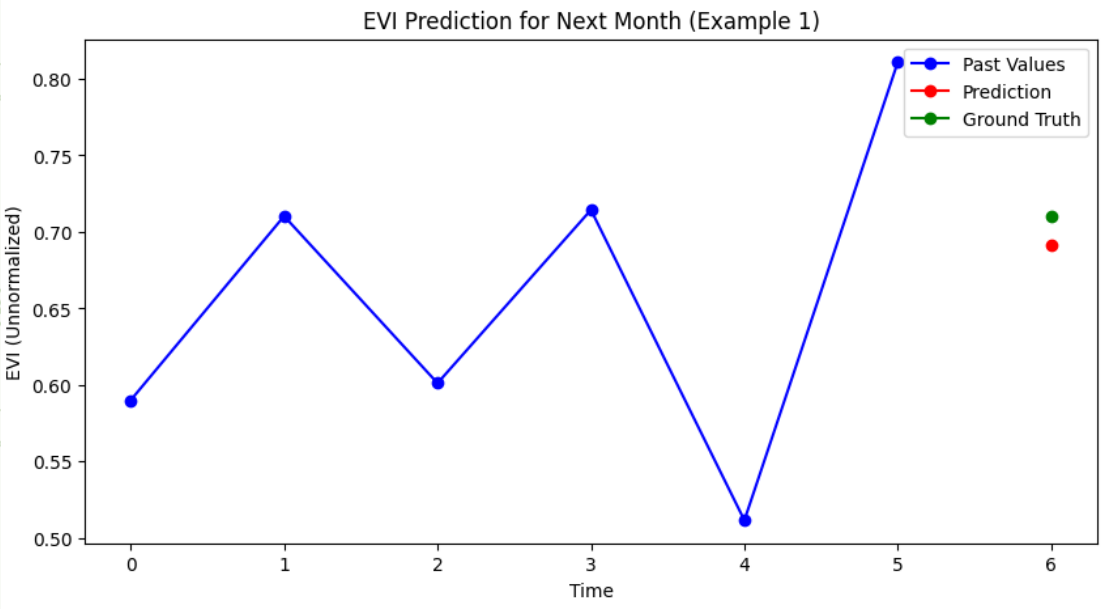

Figure 89: Example one-step forecast for monthly EVI. Blue: past values (model input window). Red: model prediction. Green: ground truth.

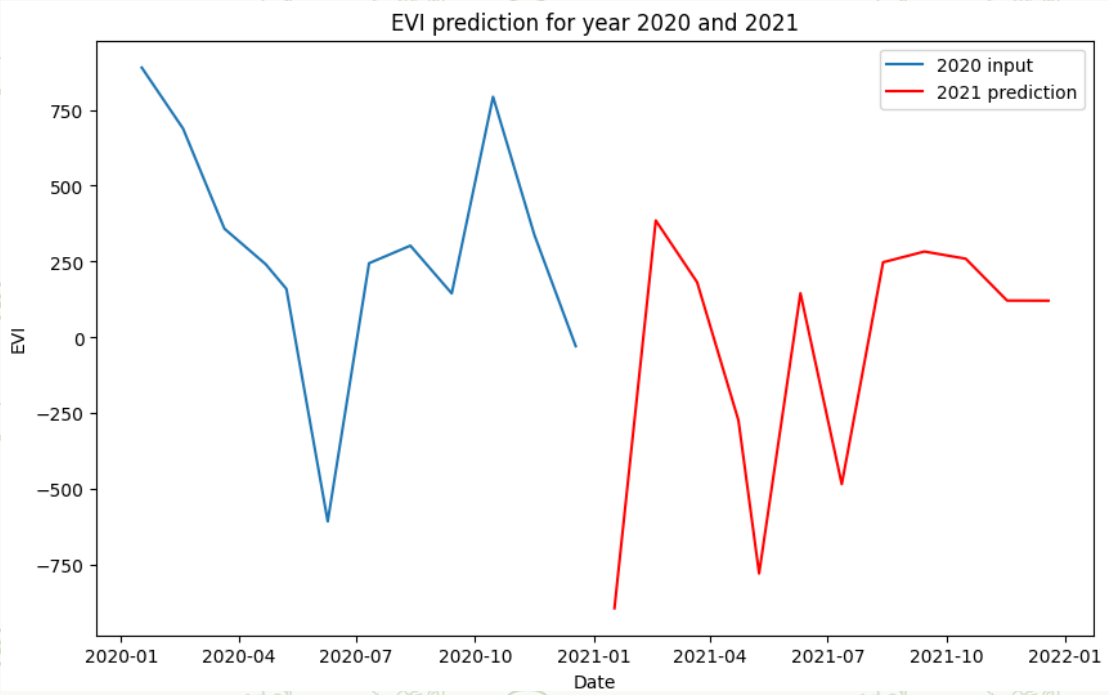

Figure 90: By combining multiple single predictions for Figure 1, a one-year prediction of the EVI for 2021 is accumulated.

25.4. References

Duan, S., Ullrich, P., Risser, M., & Rhoades, A. (2024). Using temporal deep learning models to estimate daily snow water equivalent over the Rocky Mountains. Water Resources Research, 60(4), e2023WR035009. https://doi.org/10.1029/2023WR035009

Hochreiter, S., & Schmidhuber, J. (1997). Long short-term memory. Neural Computation, 9(8), 1735–1780. https://doi.org/10.1162/neco.1997.9.8.1735

Kartal, S., Iban, M. C., & Sekertekin, A. (2024). Next-level vegetation health index forecasting: A ConvLSTM study using MODIS Time Series. Environmental Science and Pollution Research, 31(12), 18932-18948. https://doi.org/10.1007/s11356-024-32430-x

Kingma, D. P., & Ba, J. L. (2015). Adam: A method for stochastic optimization. In Proceedings of the 3rd International Conference on Learning Representations (ICLR). https://arxiv.org/abs/1412.6980

Paszke, A., Gross, S., Massa, F., Lerer, A., Bradbury, J., Chanan, G., … Chintala, S. (2019). PyTorch: An imperative style, high-performance deep learning library. In Advances in Neural Information Processing Systems 32 (NeurIPS 2019) (pp. 8026–8037).

Song, Y., Tsai, W. P., Gluck, J., Rhoades, A., Zarzycki, C., McCrary, R., ... & Shen, C. (2024). LSTM-based data integration to improve snow water equivalent prediction and diagnose error sources. Journal of Hydrometeorology, 25(1), 223-237. https://doi.org/10.1175/JHM-D-22-0220.1

Zhao, F., Yang, G., Yang, H., Zhu, Y., Meng, Y., Han, S., & Bu, X. (2021). Short and medium-term prediction of winter wheat NDVI based on the DTW–LSTM combination method and MODIS time series data. Remote Sensing, 13(22), 4660. https://doi.org/10.3390/rs13224660

25.5. Contributors

Developed by: NTUA

Date of last update: 30 June 2025

Lead contributor:

Ilias Chamatidis

26. AI Forecasting for Snow Cover Prediction

26.1. Overview

This tool implements a Long Short-Term Memory (LSTM) neural network designed to forecast future values of a univariate environmental time series related to snow cover. LSTM architectures are particularly suitable for this task because they capture temporal dependencies and nonlinear dynamics characteristic of snow accumulation, melt cycles, and seasonal variability.

The model uses a sequence-to-one prediction setup. Historical snow cover observations are normalized and segmented into fixed-length input windows, where each window represents 4 months for the monthly snow cover and 6 days for the daily snow cover of past values. This sliding-window design preserves temporal context and enables the network to learn short- and medium-term lag relationships that influence snowpack evolution. The architecture consists of a single LSTM layer

with 100 hidden units followed by a fully connected output layer. The prediction is derived from the final hidden state of the sequence, allowing the model to focus on aggregated temporal patterns.

Training is performed using the Adam optimizer and a mean squared error (MSE) loss function, which is appropriate for continuous environmental variables. Hidden and cell states are re-initialized for each batch to maintain stable gradient flow and ensure consistent learning across epochs. After the model is trained, new forecasts are generated by inputting the most recent six months of snow cover data. The resulting normalized predictions are then inverse-transformed to return values to their original physical scale. Overall, this LSTM framework provides a robust approach for modeling temporal variability in snow cover and supports applications in seasonal monitoring and climate-related decision making.

26.2. Methodological Description

26.2.1. Data Preparation

Accurate forecasting with LSTM models requires careful preparation and preprocessing of the input time series data. In this implementation, the data consists of univariate environmental indicators, such as snow cover, recorded at regular monthly intervals.

The preprocessing workflow begins by **normalizing** the raw data using a **Min-Max scaler**, which maps all values into the [0, 1] range. Normalization ensures numerical stability during training and facilitates gradient-based optimization in PyTorch. Next, the normalized time series is segmented into **overlapping sequences of** 4 months for monthly snow covers and 6 days for daily snow cover of fixed length to create supervised learning pairs. Each sequence consists of a window of consecutive past observations, which serves as the input, while the subsequent value acts as the target output. In this framework, a sequence length of four months for the monthly prediction and six days for the daily prediction is used to predict the following month or day, respectively, enabling the model to capture short- to medium-term temporal dependencies. The sequences and their corresponding targets are then converted into **PyTorch tensors**, reshaped to match the expected input dimensions of the LSTM network: **[batch size, sequence length, number of features]** for inputs, and **[batch size, 1]** for targets. These tensors are wrapped in a **TensorDataset** and loaded into a **PyTorch DataLoader**, which facilitates efficient batch processing and shuffling during training. The use of DataLoader also ensures seamless integration with GPU acceleration when available. This systematic preprocessing pipeline guarantees that the LSTM model receives consistently structured, scaled, and temporally organized data, thereby optimizing learning and predictive performance for snow cover forecasting tasks.

26.2.2. Model Training

The LSTM model is trained using a supervised learning framework, where the objective is to minimize the discrepancy between predicted and observed time series values. Prior to training, the input series is normalized using a Min-Max scaling procedure to constrain all values within the [0, 1] interval. This normalization facilitates efficient gradient-based optimization and mitigates issues arising from differing variable magnitudes. Training data are organized into sequences of fixed length (4 consecutive monthly observations in this implementation for monthly snow cover prediction and 6 consecutive daily observations for daily snow prediction), with each sequence paired with the subsequent observation as the target output. This sequence-to-one formulation allows the network to learn temporal dependencies and capture the dynamics inherent to snow cover variations. The model is trained using the **Adam optimizer**, which adaptively adjusts learning rates for each parameter based on first- and second-order moments of the gradients. The **mean squared error (MSE)** is employed as the loss function, providing a smooth and differentiable measure of prediction error suitable for continuous environmental variables. During each training epoch, the hidden and cell states of the LSTM are initialized for each batch, ensuring stable gradient propagation and preventing the accumulation of state across unrelated sequences. Batches of 16 sequences are fed into the network, predictions are generated, and the loss is backpropagated to update network weights iteratively. Training proceeds for 100 epochs, with intermediate loss monitoring to track convergence and detect potential overfitting. Once training is complete, the model weights are saved, allowing for future reuse without retraining. This process ensures that the LSTM network is capable of generating accurate forecasts for future snow cover based on recent historical observations.

26.3. Inference and Prediction

After training, the LSTM model can be employed to generate forecasts for future time series values, concerning snow cover. The inference process begins by selecting the most recent **sequence of observations** from the historical dataset, corresponding to the model's predefined input window length (4 months for monthly snow cover prediction and 6 days for daily snow cover prediction in the present implementation). Typical one-step forecasts are illustrated in Figure 1 and Figure 2. This sequence is normalized using the same Min-Max scaler applied during training to ensure consistency in data representation. The normalized input sequence is then converted into a three-dimensional tensor compatible with the LSTM input requirements, where the dimensions correspond to **batch size**, **sequence length**, and **number of features**. During prediction, the model's hidden and cell states are initialized to zero, and the sequence is passed through the LSTM and fully connected output layer. The prediction for the next time step is obtained from the last output of the LSTM, which encapsulates the learned temporal dependencies across the input window. For multi-step forecasting, the predicted value can be appended to the input sequence and the process repeated iteratively.

The resulting normalized forecast is **inverse-transformed** using the original scaler to return the prediction to the original physical scale, allowing direct interpretation in units of snow cover. This procedure enables reliable short-term prediction while preserving the temporal patterns captured during training. The LSTM-based inference framework is particularly suitable for applications requiring continuous environmental monitoring and anticipatory decision-making.

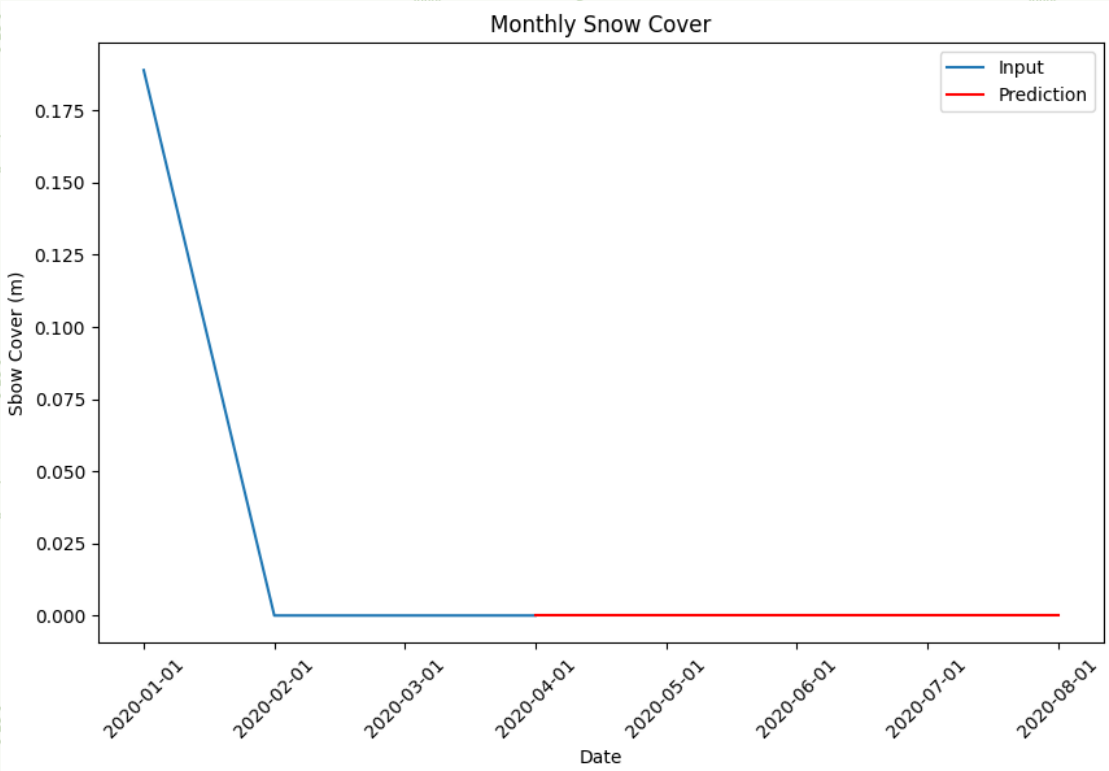

Figure 91: Monthly snow cover prediction of 4 months in 2020.

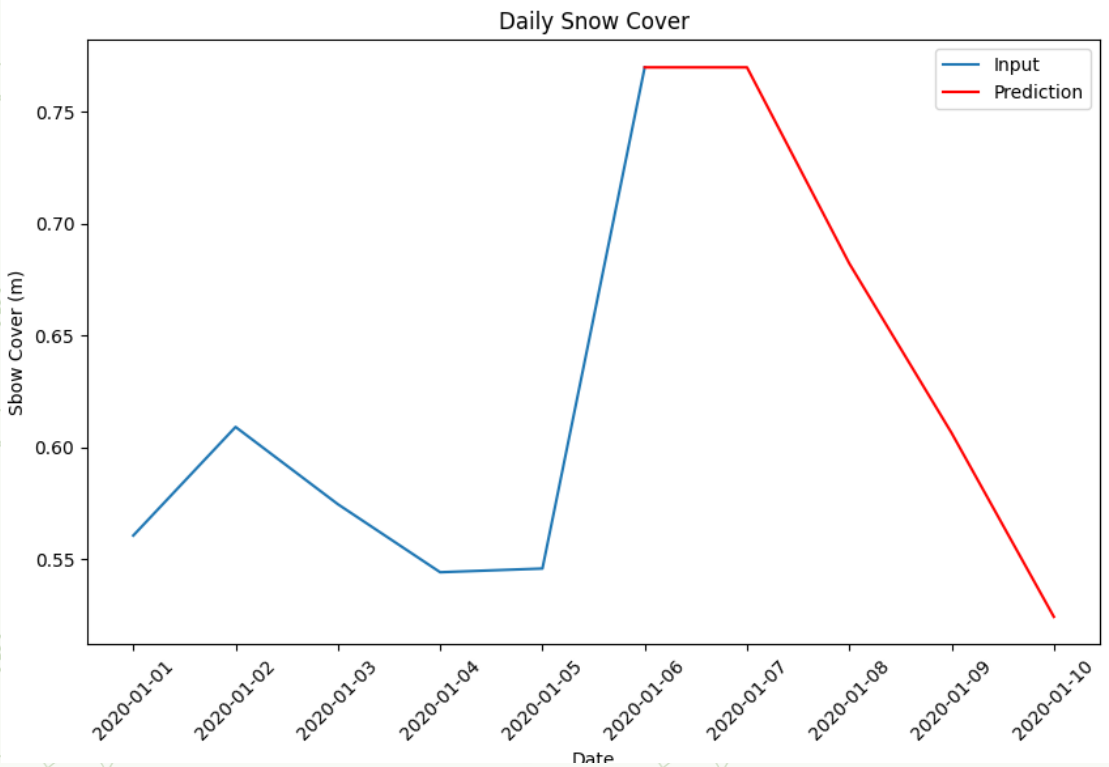

Figure 92: Daily snow cover prediction of 6 days using an input sequence of 6 days.

26.4. References

Duan, S., Ullrich, P., Risser, M., & Rhoades, A. (2024). Using temporal deep learning models to estimate daily snow water equivalent over the Rocky Mountains. Water Resources Research, 60(4), e2023WR035009. https://doi.org/10.1029/2023WR035009

Hochreiter, S., & Schmidhuber, J. (1997). Long short-term memory. Neural Computation, 9(8), 1735–1780. https://doi.org/10.1162/neco.1997.9.8.1735

Kartal, S., Iban, M. C., & Sekertekin, A. (2024). Next-level vegetation health index forecasting: A ConvLSTM study using MODIS Time Series. Environmental Science and Pollution Research, 31(12), 18932-18948. https://doi.org/10.1007/s11356-024-32430-x

Kingma, D. P., & Ba, J. L. (2015). Adam: A method for stochastic optimization. In Proceedings of the 3rd International Conference on Learning Representations (ICLR). https://arxiv.org/abs/1412.6980

Paszke, A., Gross, S., Massa, F., Lerer, A., Bradbury, J., Chanan, G., … Chintala, S. (2019). PyTorch: An imperative style, high-performance deep learning library. In Advances in Neural Information Processing Systems 32 (NeurIPS 2019) (pp. 8026–8037).

Song, Y., Tsai, W. P., Gluck, J., Rhoades, A., Zarzycki, C., McCrary, R., ... & Shen, C. (2024). LSTM-based data integration to improve snow water equivalent prediction

and diagnose error sources. Journal of Hydrometeorology, 25(1), 223-237. https://doi.org/10.1175/JHM-D-22-0220.1

Zhao, F., Yang, G., Yang, H., Zhu, Y., Meng, Y., Han, S., & Bu, X. (2021). Short and medium-term prediction of winter wheat NDVI based on the DTW–LSTM combination method and MODIS time series data. Remote Sensing, 13(22), 4660. https://doi.org/10.3390/rs13224660

26.5. Contributors

Developed by: NTUA

Date of last update: 30 June 2025

Lead contributor:

Ilias Chamatidis

27. Multi-Criteria Decision Analysis

27.1. Overview

This tool implements a **Multi-Criteria Decision Analysis (MCDA)** framework for assessing natural hazard risks based on geohazard severity charts. The methodology integrates **likelihood** and **intensity** metrics for each identified hazard to provide a quantitative evaluation of potential impacts across the study area.

The input data consists of the intensity and likelihood extracted from the geohazards severity charts. For each hazard, two key parameters are evaluated:

1. **Likelihood (L)** – the probability or frequency of occurrence of the hazard in the specified area.
2. **Intensity (I)** – the potential severity or impact level of the hazard, considering both magnitude and expected consequences.

The MCDA process combines these parameters using multiple aggregation approaches, including **combination** (e.g., maximum likelihood or sum of intensities) and **weighted scoring** (e.g., linear combination of L and I with user-defined weights). The resulting scores facilitate the ranking of hazards and scenarios, highlighting areas or events of highest potential risk. This framework allows for **systematic comparison** across hazards and scenarios, supporting informed decision-making and prioritization in hazard mitigation, emergency planning, and environmental management. By quantifying both likelihood and intensity, the approach provides a robust, reproducible basis for evaluating multi-hazard exposure, the data extracted from the geohazard severity chart.

A growing body of research applies Multi-Criteria Decision Analysis (MCDA) to assess natural hazard risks across diverse environments. The reviewed studies illustrate how MCDA frameworks integrate hazard likelihood, intensity, and spatial indicators to support disaster risk management.

Ibrahim et al. (2025) developed a GIS-MCDA approach for flood risk assessment in a flood-prone region of Pakistan. The authors combined hydrological, topographic, and land-use variables, weighted through an Analytic Hierarchy Process (AHP), to derive a flood-hazard index. Their work demonstrates the effectiveness of integrating spatial datasets with MCDA to produce interpretable hazard maps that assist local decision-making. Ladas et al. (2007) applied GIS-based MCDA to landslide susceptibility mapping in the Messinia region of Greece. By weighting geomorphological and geological criteria using AHP, the study produced landslide susceptibility zones that were later validated against historical landslide records. This early work remains influential in demonstrating how MCDA supports region-specific hazard assessments. Nefros and Loupasakis (2023) expanded MCDA applications by integrating climate models, remote sensing, and GIS to evaluate landslide risk in areas previously affected by wildfires and floods. Their methodology highlights the importance of combining environmental change indicators (e.g., vegetation loss) with traditional susceptibility factors for dynamic hazard environments. Soldati et al. (2022) proposed a PROMETHEE-based MCDA model to evaluate combined seismic and flood risks at the regional scale in Italy. Their multi-hazard strategy moves beyond single-hazard mapping, demonstrating how multiple hazard dimensions (e.g., intensity, exposure, frequency) can be simultaneously evaluated to support comprehensive regional-planning decisions. Zhou and Zhai (2023) introduced a multi-hazard risk assessment framework for urban disaster-prevention planning in Xiamen, China. Their study integrates hazard intensity, exposure, and vulnerability indicators within a spatial MCDA system to support urban resilience planning. By focusing on urban environments, their framework captures complex interactions between hazards and socio-economic factors, offering a strong example of multi-hazard analysis tailored to densely populated regions.

Collectively, these studies demonstrate that MCDA provides a robust foundation for multi-hazard risk mapping. They also underscore the flexibility of MCDA methods (AHP, PROMETHEE, weighted linear combination) in addressing both single-hazard and multi-hazard contexts.

27.2. Methodological Description

27.2.1. Data Description

The input data for the MCDA framework consists of **geohazard severity chart** for each cultural heritage site, and extracting the intensity and likelihood based on the color coding of the geohazard severity chart.

Each hazard within the image is characterized by two primary attributes:

1. **Likelihood (L):** Represents the probability of hazard occurrence, based on the geohazard severity charts. Likelihood values are typically normalized to a standardized scale to facilitate comparison across hazards.

2. **Intensity (I):** Reflects the potential severity or magnitude of the hazard, capturing the expected impact if the hazard occurs. Intensity is derived from the geohazard severity charts, and is similarly standardized for consistency.

In Figure 93, there is an example of a geohazard severity chart that was used as an input. Based on the color for each hazard, the intensity (1-4) and likelihood (1-4) are derived.

By representing hazard information in a spatially explicit format, the image provides a **comprehensive and high-resolution basis** for calculating combined risk scores. This enables the MCDA framework to generate quantitative assessments of hazard exposure and vulnerability across the landscape, facilitating informed planning and mitigation strategies.

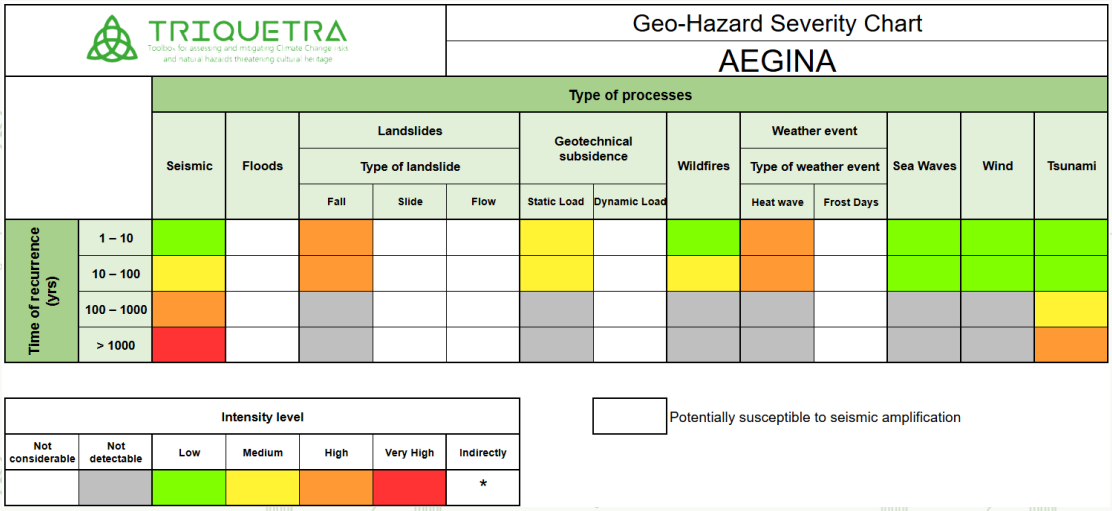

Figure 93: Example of the data used to calculate MCDA.

27.2.2. MCDA Calculation

The Multi-Criteria Decision Analysis (MCDA) framework combines hazard-specific **likelihood** and **intensity** metrics to generate a composite risk score for each spatial unit (pixel) in the study area. Let $L_h(x,y)$ denote the likelihood of hazard h at location (x,y), and $I_h(x,y)$ denote the corresponding intensity. Both variables are normalized to a comparable scale, typically [0,1].

A. Naïve Combination Approaches

Two simple aggregation approaches are employed to provide baseline risk scores:

1. **Maximum Likelihood Score:**

$$S_L(x,y) = L_h(x,y)$$

This method identifies the most probable hazard at each location, focusing on hazard occurrence regardless of intensity.

2. **Sum of Intensity Scores:**

$$S_I(x,y) = \sum_{h_h^I} (x,y)$$

This approach accumulates the potential impact of all hazards at each location, emphasizing the combined severity.

B. Weighted Linear Combination

To integrate both likelihood and intensity into a single metric, a **weighted sum** is calculated for each hazard or spatial unit:

$$S_w(x,y) = w_L \cdot L_h(x,y) + w_I \cdot I_h(x,y)$$

where w_L and w_I are user-defined weights reflecting the relative importance of likelihood and intensity. In practice, weights are chosen such that $w_L + w_I = 1$.

For example, a common configuration uses $w_L = 0.4 \; and \; w_I = 0.6$, emphasizing hazard severity over probability.

C. Ranking and Risk Prioritization

Once the composite scores $S_W(x,y)$ are computed across the spatial domain, pixels or regions can be **ranked** according to their risk magnitude:

$$Rank(x,y) = argsort\big(S_W(x,y)\big)$$

This ranking enables the identification of **high-risk zones**, informing mitigation strategies and decision-making. The MCDA framework is flexible, allowing for different scoring schemes, multiple hazards, and customizable weightings to suit the requirements of specific environmental or emergency planning applications.

27.3. Outputs and Interpretation of the results

The single-hazard MCDA evaluates each natural hazard independently by calculating naïve combined scores and weighted risk scores. Table 1 summarizes the results across the study area, including likelihood (L), intensity (I), and weighted aggregation.

In Figure 94 an example MCDA for Figure 1 is shown based on a single hazard. From the analysis, seismic events emerge as the highest-risk single hazard, with both maximum likelihood and intensity scores of 4, resulting in a weighted score of 4.0. Wildfires and tsunamis follow closely, with weighted scores of 3.4 and 3.2, respectively, reflecting a balance between their probability of occurrence and potential severity. Less impactful hazards, such as frost days, receive lower scores due to negligible intensity, despite moderate likelihood.

This single-hazard evaluation highlights which hazards individually pose the greatest threat, providing a baseline for risk prioritization and resource allocation.

Multi-Criteria Decision Analysis (Single Hazard)

Scenario	Maximum Likelihood Score (L)	Intensity Score (I)	Weighted Sum Score (0.4×L+0.6×I)	Rank
Seismic	4	4	(0.4x4)+(0.6x4)=4.0	1
Wildfires	4	3	(0.4x4)+(0.6x3)=3.4	2
Tsunami	2	4	(0.4x2)+(0.6x4)=3.2	3
Floods	3	3	(0.4x3)+(0.6x3)=3.0	4
Landslides (Fall)	3	3	(0.4x3)+(0.6x3)=3.0	5
Weather event (Heat Wave)	3	3	(0.4x3)+(0.6x3)=3.0	6
Geotechnical Subsidence	3	2	(0.4x3)+(0.6x2)=2.4	7
Sea Waves	4	1	(0.4x4)+(0.6x1)=2.2	8
Wind	4	1	(0.4x4)+(0.6x1)=2.2	9
Frost Days	3	0	(0.4x3)+(0.6x0)=1.2	10

Figure 94: Intensity and likelihood for a single hazard based on the input data of Figure 93.

The multi-hazard MCDA considers **combined scenarios**, where two or more hazards may co-occur, potentially amplifying overall risk. For each scenario, the **maximum likelihood** among constituent hazards is retained, while the **sum of intensities** reflects cumulative impact. The weighted score integrates both components:

$$S_w = 0.4 \cdot (L_h) + 0.6 \cdot \sum_{i}^{n} I_h$$

In Figure 95, an example of multi multi-hazard is given based on Figure 1. The results indicate that scenarios involving **tsunamis triggered by offshore seismic events** present the highest combined risk, with a weighted score of 6.4, due to both high intensity and significant likelihood. Other critical scenarios include **major seismic events coupled with landslides** (5.8) and **prolonged heatwaves with large wildfires** (5.2), demonstrating the amplified risk when hazards interact. Lower-risk combinations, such as coastal storms involving sea waves and high winds, have reduced weighted scores (2.8), reflecting limited intensity despite moderate likelihood.

Multi-Criteria Decision Analysis (Multi-Hazard)

Combined Hazards	Maximum Likelihood Score (L)	Intensity Score (I)	Weighted Sum Score (0.4×L+0.6×I)	Rank
4. Tsunami triggered by Offshore Seismic Event	max(2,4)=4	4+4=8	(0.4x4)+(0.6x8)=6.4	1
1. Major Seismic Event & Landslides	max(4,3)=4	4+3=7	(0.4x4)+(0.6x7)=5.8	2
3. Prolonged Heatwave & Large Wildfire	max(3,4)=4	3+3=6	(0.4x4)+(0.6x6)=5.2	3
2. Extreme Rainfall & Flash Floods & Debris Flows	max(3,3)=3	3+2=5	(0.4x3)+(0.6x5)=4.2	4
5. Coastal Storm (Sea Waves & High Winds)	max(4,4)=4	1+1=2	(0.4x4)+(0.6x2)=2.8	5
6. Urban Subsidence during Flood	max(3,3)=3	3+2=5	(0.4x3)+(0.6x5)=4.2	6

Figure 95: Intensity and likelihood for multi-hazard based on the input data of Figure 93.

Overall, the multi-hazard analysis provides a **more comprehensive assessment of systemic risk**, identifying areas and scenarios where hazard interactions may lead to the greatest potential impacts. These results support **decision-making for mitigation, emergency planning, and resource prioritization**, emphasizing both individual hazard severity and cumulative effects in multi-hazard contexts.

27.4. References

Ibrahim, M., Huo, A., Ullah, W., Ullah, S., & Xuantao, Z. (2025). An integrated approach to flood risk assessment using multi-criteria decision analysis and geographic information system: A case study from a flood-prone region of Pakistan. Frontiers in Environmental Science, 12. https://doi.org/10.3389/fenvs.2024.1476761

Ladas, I., Fountoulis, I., & Mariolakos, I. (2007). Using GIS & multicriteria decision analysis in landslide susceptibility mapping — A case study in Messinia prefecture area (SW Peloponnesus, Greece). Bulletin of the Geological Society of Greece, 40(4), 1973–1985. https://doi.org/10.12681/bgsg.17240

Nefros, C., & Loupasakis, C. (2023). Landslide risk management in areas affected by wildfires or floods: A comprehensive framework integrating GIS, remote sensing techniques, and regional climate models. Bulletin of the Geological Society of Greece, 60(1), 27–68. https://doi.org/10.12681/bgsg.35629

Soldati, A., Chiozzi, A., Nikolić, Ž., Vaccaro, C., & Benvenuti, E. (2022). A PROMETHEE multiple-criteria approach to combined seismic and flood risk assessment at the regional scale. Applied Sciences, 12(3), 1527. https://doi.org/10.3390/app12031527

Zhou, S., & Zhai, G. (2023). A Multi-Hazard Risk Assessment Framework for Urban Disaster Prevention Planning: A Case Study of Xiamen, China. Land, 12(10), 1884. https://doi.org/10.3390/land12101884

27.5. Contributors

Developed by: National Technical University of Athens

Date of last update: 28/06/2025

Lead contributors:

Ilias Chamatidis

28. Indicative list of mitigation measures per hazard

In this section, a brief overview of proposed mitigation measures referring to certain of the most common hazards posed upon the CH sites is given.

28.1. Forest fires

A wildfire or forest fire is an unplanned and uncontrolled process in an area of combustible vegetation like trees or bushes. When a wet period that produced substantial fuels is followed by a prolonged drought and heat, it can result in a severe event of fire. The severity and magnitude of a wildfire depend on the combustible material present and the effect of weather on the fire.

Fire detection, monitoring and early warning system can play a crucial role in the management of a fire event. Fixed forest fire monitoring facilities and communication systems for detection are the main adaptive measure to be taken. Satellite imagery, the use of local scale smoke detectors or drones can yield real – time information. The use of drones before a fire event can acquire high resolution date on the forest structure, composition, growth, produced biomass and during the event can give information on fire location, dimension and progress.

Other adaptive measures include the reduction and management of combustible materials or planned burning programs during appropriate weather conditions.

Moreover, the establishment and maintenance of fire breaks and forest tracks can aid during a fire event. Regular water supply points and close collaboration with the local fire brigade station will also play an important role. Finally, land use planning to avoid construction within the forested areas or urban expansion, watering systems to reduce dryness of trees and ground, planting trees and hedges can all lead to better results.

28.2. Drought

Drought is a prolonged dry period leading to the dryness of the ground and depletion of water reservoirs. Nature-based solutions are preferred and can be effective by the management of channels and water retention basins. Adaptive measures refer to the increase of water storage facilities such as recharge aquifers by surface infiltration and injection or by the construction of artificial streams and ponds creating local systems for the collection of rainwater.

28.3. Heat waves

A heat wave is a long period of at least 5 days of extremely hot weather and increases the risk of wildfires in areas with drought. Adaptive measures include the change of operational hours of a site for visitors and the working hours for the staff, the provision of shades, installation of ventilation systems, watering devices and artificial constructions of ponds and fountains. It can also refer to the replacement or the covering of artificial surfaces with reflective materials.

28.4. Heavy rainfall

Heavy rainfall refers to high amounts of precipitation in a short period of time that usually falls spatially limited and is accompanied by short warning times due to its convective origin. The temperature rise leads to the increase of air capacity to absorb water, triggering heavy rain events by the upward movement and the resulting cooling of warm, humid air. Large amounts of rainfall can cause a rise in water levels in small rivers and streams, leading to flooding. Flash floods occur even without bodies of water due to the enormous amount of rain, especially on slopes.

Adaptive measures for heavy rainfall include sheltering of assets, the provision of water retention areas and regular maintenance and cleaning of the water waste and sewage system.

28.5. Floods

Flood refers to the overflow of water that submerges usually dry land. Flooding may occur as an overflow of water from rivers, lakes, sea or ocean, resulting in some of that water escaping its usual boundaries. Flooding may also occur due to an accumulation of rainwater on saturated ground.

Nature based adaptive measures may involve the widening of natural flood plains, protecting and expanding wetlands, developing large-scale buffer strips combined

with conservation agriculture techniques and investing in green spaces to reduce run – off and develop a retention area. This type of measures is effective for low level flooding and to slow the flow of rainwater through the landscape into streams and rivers. Other measures may include the plantation in the greater area of the site of trees and hedges to increase water absorption, the cover of soil with plants to reduce water run-off, installation of water reservoirs to store water and leaky barriers to slow water flow in streams and ditches.

28.6. Landslides

Landslides are forms of downward ground movements, such as rockfalls, mudflows, shallow or deep-seated slope failures and debris flows under the influence of gravity, which occur in a variety of environments, characterized by either steep or gentle slope gradients. They occur when the condition of a slope (or a portion of a slope) changes due to a variety of factors from stable to unstable. The effects of climate change on landslides need to be adapted on a regional scale.

Adaptive measures may include the construction of retaining walls designed to hold the slope and prevent sliding, incorporating drainage systems to prevent water built up. Furthermore, the application of synthetic materials, geotextiles and geomembranes, and soil nailing, introducing metal rods into slopes, are all used to reinforce the soil and maintain slope stability. Finally, terracing, the making of stepped slopes providing agricultural areas and prevent erosion. Planting deep rooted plants can be particularly effective in holding the slopes stable. The combination of vegetation with engineered structures, like live staking and vegetated geogrids, offer eco-friendly solutions.

28.7. Frost

Frost forms when an outside surface cools past the dew point, where the air gets so cold, and the water vapor in the atmosphere turns into liquid which freezes.

Covering of the CH site or sensitive earthen elements can be an adaptive measure for the protection against frost.